

NOVEL METHODS TO CHARACTERISE  
ATMOSPHERICALLY RELEVANT  
ORGANIC RADICALS AND REACTIVE  
OXYGEN SPECIES



**Steven John Campbell**

Hughes Hall

Centre for Atmospheric Science

Department of Chemistry

University of Cambridge

This dissertation is submitted for the degree of *Doctor of Philosophy*

September 2017



*“Curiously, the chiming of the hour seemed to have put new heart into him. He was a lonely ghost uttering a truth that nobody would ever hear. But so long as he uttered it, in some obscure way the continuity was not broken. It was not by making yourself heard, but by staying sane that you carried on the human heritage. He went back to the table, dipped his pen and wrote:”*

*--George Orwell*





## DECLARATION

This dissertation is the result of my own work and includes nothing, which is the outcome of work done in collaboration except where specifically indicated in the text. It has not been previously submitted, in part or whole, to any university or institution for any degree, diploma, or other qualification.

In accordance with the Department of Engineering guidelines, this thesis is does not exceed 60,000 words, and it contains less than 150 figures.

Signed:\_\_\_\_\_

Date:\_\_\_\_\_

Steven John Campbell

September 2017



# ABSTRACT

**Candidate Name:** Steven John Campbell

**Thesis title:** Novel Methods to Detect Atmospherically Relevant Organic Radicals and Reactive Oxygen Species

A key reaction in the troposphere involves the oxidation of biogenic and anthropogenic alkenes with ozone, which contributes to local photochemical smog. It is generally accepted that this reaction proceeds *via* a reactive intermediate often called the Criegee intermediate (CI). This reaction is known to produce a plethora of oxidised organic compounds, which contribute to ozone formation and secondary organic aerosol production, two of the main characteristics of a polluted atmosphere. Furthermore, epidemiological studies have shown a close correlation between exposure to ambient organic aerosol and adverse human health effects. The toxicological mechanisms leading to this observation are still poorly characterised, although studies suggest that reactive oxygen species present in organic aerosol are a major contributor. Reactive oxygen species and reactive intermediates represent a large uncertainty in tropospheric chemistry, and pose an analytical challenge due to their high reactivity and typically low concentrations. This emphasises the need for the development of new methods to characterise the chemistry of these species.

In this thesis, several novel laboratory based techniques have been developed in order to characterise and quantify reactive intermediates and reactive oxygen species. New methods to facilitate the detection of CIs in both the gas and particle phase are presented. Spin trap molecules are used to scavenge CIs to form stable 1:1 adducts which are subsequently detected and quantified using mass spectrometry. The chemistry of CIs with spin traps is extensively investigated. The unique capability of this technique to simultaneously characterise multiple CIs generated from a variety of atmospherically relevant organic precursors in the gas phase is demonstrated. This technique was further developed to facilitate the detection of CIs in secondary organic aerosol, representing the development of a method capable of characterising low-volatility CIs and other reactive intermediates in the condensed phase.

Furthermore, two new chemical fluorescence assays have been developed to quantify both organic radicals and reactive oxygen species in organic aerosol. A novel profluorescent spin trap assay was applied to quantify radical concentrations in organic aerosol. A series of experiments were then devised to investigate the lifetime of organic radicals in secondary organic aerosol. A second assay, based on physiologically relevant ascorbic acid chemistry, was also developed to measure the concentrations of toxicologically relevant reactive oxygen species in secondary organic aerosol. The quantitative capability of this assay was extensively characterised. The assay was incorporated into a prototype instrument capable of measuring particle-bound reactive oxygen species on-line, and the assays' sensitivity to secondary organic aerosol was demonstrated.



## ACKNOWLEDGEMENTS

First and foremost, I would like to thank my supervisor Professor Markus Kalberer for providing me with the opportunity to work in his group. His good natured, humorous approach to science, invaluable support, and knowledgeable insights have made this a very enjoyable research project.

I would like to extend thanks to the various members of the Kalberer group I have had the pleasure of working with over the years. This PhD has been made more enjoyable through working with such enthusiastic and friendly colleagues. Particular thanks to Dr Chiara Giorio, whose support and guidance during my research project has been invaluable, and has instilled in me a passion for research. I would also like to acknowledge Dr Pete Gallimore for his continued advice, and to Arthur Zielinski for his help during the many “boring lab tasks” we had to endure. Extended thanks to others who I have had the pleasure of collaborating with in this project including Daniel Leinhardt, Battist Uttinger and Suzanne Paulson. I would also like to thank Svetlana Stevanovic, Branka Miljevic, Zoran Ristovski and Steven Bottle of Queensland University of Technology for providing the BPEA spin trap, and for their help in initially setting up the assay.

Special thanks go to my family for being so supportive throughout this PhD. Particular acknowledgement to my grandparents, John and Doreen Campbell, for their constant support throughout my enduring time in higher education. Their faith in me has been a key driver during my time in academia, and I hope that this thesis is worth the investment.

To my girlfriend, Charlotte; your support has been absolutely key during the dark times in my PhD. Listening to me constantly complain about broken science over the last 3 years must have been tough, but your humour, companionship and support has been truly invaluable. If we can make it through this, we can conquer anything.

Thanks to Hughes Hall for providing me with the platform to meet so many dear friends for life during my time in Cambridge.

To all those mentioned above, and more, I am extremely grateful.



# CONTENTS

<b>1 INTRODUCTION.....</b>	<b>19</b>
1.1 ATMOSPHERIC AEROSOL: SOURCES, SIZES AND COMPOSITION .....	20
1.1.1 An Overview of Atmospheric Aerosol.....	20
1.1.2 Organic Aerosol Sources.....	22
1.2 OXIDATION MECHANISMS LEADING TO SOA FORMATION.....	26
1.2.1 Criegee Intermediates.....	29
1.3 HEALTH EFFECTS OF EXPOSURE TO PARTICULATE MATTER .....	33
1.3.1 Epidemiological studies .....	33
1.3.2 Health Relevant Physical and Chemical Properties of Aerosol .....	36
1.3.3 Current Methods of ROS Detection in Aerosol .....	40
1.3.4 On-line Measurement of Particle Bound ROS .....	43
1.3.5 Spin Trap Reagents: Mechanisms and Applications.....	45
1.4 ANALYTICAL METHODS .....	51
1.4.1 Overview of Mass Spectrometry .....	51
1.4.2 Scanning mobility particle sizer .....	58
1.4.3 Fluorescence Spectroscopy .....	60
1.5 CHAPTER SUMMARY .....	62
1.6 THESIS STRUCTURE AND OUTLINE .....	63
<b>2 AIMS OF THIS THESIS.....</b>	<b>65</b>
<b>3 ONLINE QUANTIFICATION OF CRIEGEE INTERMEDIATES IN THE GAS PHASE .....</b>	<b>67</b>
3.1 INTRODUCTION.....	68
3.2 METHODOLOGY.....	70
3.2.1 Reagents and Materials .....	70
3.2.2 Liquid Phase Ozonolysis.....	70
3.2.3 HPLC-ESI-HRMS.....	71
3.2.4 NMR Sample Preparation .....	72
3.2.5 Electron Paramagnetic Resonance Spectroscopy.....	73
3.2.6 PTR-ToF-MS measurements.....	74
3.2.7 Set-up for Gas Phase Ozonolysis .....	75
3.2.8 Optimisation of the Flow Tube Set-up.....	76
3.2.9 MCM modelling.....	78
3.3 RESULTS AND DISCUSSION .....	78
3.3.1 Characterisation of CI-spin trap adduct structure.....	78

3.3.2 Quantification of $\alpha$ -pinene CI-DMPO Adducts in the Gas Phase .....	86
3.3.3 Simultaneous Quantification of Various CI-DMPO Adducts from Multiple VOC Precursors .....	90
3.3.4 Comparison between Experimental Results and MCM modelling .....	98
3.4 CONCLUSIONS AND FUTURE OUTLOOK .....	101
<b>4 NOVEL METHOD TO DETECT CRIEGEE INTERMEDIATES IN THE PARTICLE PHASE.....</b>	<b>105</b>
4.1 INTRODUCTION.....	106
4.2 METHODOLOGY.....	109
4.2.1 Reagents.....	109
4.2.2 Bulk ozonolysis .....	109
4.2.3 Flow tube experiments.....	111
4.2.4 PTR-ToF-MS Measurements.....	115
4.2.5 HPLC-ESI-HRMS Analyses.....	116
4.3 RESULTS AND DISCUSSION .....	116
4.3.1 Initial Method Tests: Detection of CIs in $\alpha$ -pinene SOA .....	116
4.3.2 Formation Mechanism of $\beta$ -caryophyllene CI-Spin Trap Adducts .....	119
4.3.3 Characterisation of $\beta$ -caryophyllene CI Adducts using HPLC-ESI-HRMS .....	121
4.3.4 Quantification of $\beta$ -caryophyllene CI-DMPO Adducts in the Gas Phase .....	123
4.3.5 Detection of CIs in SOA generated from $\beta$ -caryophyllene Ozonolysis.....	125
4.3.6 Quantification of $\beta$ -caryophyllene CIs in SOA using HPLC-ESI-HRMS.....	130
4.4 CHAPTER SUMMARY .....	132
<b>5 QUANTIFICATION OF ORGANIC RADICALS IN SECONDARY ORGANIC AEROSOL .....</b>	<b>135</b>
5.1 INTRODUCTION.....	136
5.2 METHODOLOGY.....	137
5.2.1 Reagents.....	137
5.2.2 Flow tube Set-up.....	137
5.2.3 Fluorescence Measurements .....	138
5.3 RESULTS AND DISCUSSION .....	139
5.3.1 ESI-HRMS Characterisation of BPEA fluorescent products.....	139
5.3.2 Characterisation of the Fluorescent Set-up .....	143
5.3.3 Proof-of-Principle: Quantification of Radicals in SOA.....	146
5.3.4 Estimating the Radical Lifetime in $\alpha$ -pinene SOA .....	149
5.3.5 Radical Concentrations in SOA formed from different VOCs .....	153
5.4 CHAPTER SUMMARY .....	157



<b>6 DEVELOPMENT OF AN ON-LINE CHEMICAL ASSAY TO MEASURE PARTICLE- BOUND ROS .....</b>	<b>159</b>
6.1 INTRODUCTION .....	160
6.2 METHODOLOGY .....	162
6.2.1 Reagents .....	162
6.2.2 Development of an Ascorbic Acid Chemical Assay .....	162
6.2.3 Experimental set-up.....	165
6.3 RESULTS AND DISCUSSION .....	169
6.3.1 Calibration of the On-line Ascorbic Acid Assay.....	169
6.3.2 Calibration of the On-line Ascorbic Acid Assay with Metal Salts .....	173
6.3.3 Assessment of Sensitivity towards Secondary Organic Aerosol.....	180
6.3.4 Investigating the Assay Response to an Iron Sulphate – SOA mixture .....	185
6.4 CHAPTER SUMMARY .....	189
<b>7 CONCLUSIONS AND FUTURE WORK .....</b>	<b>192</b>
7.1 INTRODUCTION .....	192
7.2 SUMMARY OF RESEARCH FINDINGS .....	193
7.2.1 Online Quantification of Criegee Intermediates in the Gas Phase .....	193
7.2.2 Novel Method to Detect Criegee Intermediates in the Particle Phase.....	194
7.2.3 Quantification of Radicals in Secondary Organic Aerosol .....	195
7.2.4 Development of an On-line Chemical Assay to Measure Particle Bound ROS.....	196
7.3 POTENTIAL IMPLICATIONS AND FUTURE RECOMMENDATIONS .....	198
7.4 CLOSING REMARKS .....	202
<b>8 REFERENCES.....</b>	<b>203</b>
<b>9 APPENDICES .....</b>	<b>226</b>
<b>APPENDIX 1 – EXTENSIVE NMR ANALYSIS OF CI-PBN ADDUCTS .....</b>	<b>227</b>
<b>APPENDIX 2 – DENSITY FUNCTIONAL THEORY CALCULATIONS.....</b>	<b>239</b>
9.1.1 Density Functional Theory Calculations: Optimisation.....	239
9.1.2 DFT calculations of $\alpha$ -pinene – PBN Adducts .....	240
9.1.3 DFT Calculation of CI-DMPO Proton Reaction Rate Constants .....	243
9.1.4 DFT calculations of Various CI-DMPO Adducts. ....	244
<b>APPENDIX 3– MATHEMATICA MODEL FOR B-CARYOPHYLLENE MODELLING STUDY .....</b>	<b>247</b>

## LIST OF ABBREVIATIONS AND ACRONYMS

AA	Ascorbic Acid
BVOC	Biogenic Volatile Organic Compound
CI	Criegee Intermediate
CI*	Excited Criegee Intermediate
Da	Dalton
DFT	Density Functional Theory
DHA	Dehydroascorbic acid
DMA	Differential Mobility Analyser
DMPO	5,5-dimethylpyrroline- <i>N</i> -oxide
DMSO	Dimethyl Sulfoxide
ELVOC	Extremely low Volatile Organic Compound
EPR	Electron Paramagnetic Resonance
ESI	Electrospray Ionisation
HO <sub>2</sub>	Hydroperoxyl radical
HPLC	High performance Liquid Chromatography
HRMS	High Resolution Mass Spectrometry
IR	Infrared
LOD	Limit of Detection
MCM	Master Chemical Mechanism (v3.1.1)
<i>m/z</i>	Mass-to-Charge Ratio

NMR	Nuclear Magnetic Resonance
NVOC	Non-volatile Organic Compound
$O_2^{\cdot -}$	Superoxide
$O_3$	Ozone
OH	Hydroxyl Radical
OPROSI	On-line Particle-bound ROS Instrument
ppb	Parts per Billion
ppm	Parts per Million
PBN	<i>N-tert-butyl-<math>\alpha</math>-phenylnitron</i>
PM	Particulate Matter
PM <sub>2.5</sub>	PM < 2.5 $\mu$ m diameter
PM <sub>10</sub>	PM < 10 $\mu$ m diameter
POA	Primary Organic Aerosol
PTR-ToF-MS	Proton Transfer Reaction Time-of-Flight Mass Spec
R $\cdot$	Radical Species (S $\cdot$ , C $\cdot$ , O $\cdot$ )
ROS	Reactive Oxygen Species
RO <sub>2</sub>	Peroxy Radicals
RTLFL	Respiratory Tract Lining Fluid
SMPS	Scanning Mobility Particle Sizer
SOA	Secondary Organic Aerosol
SVOC	Semi-Volatile Organic Compound
VOC	Volatile Organic Compound



## LIST OF APPENDICES

APPENDIX 1 – EXTENSIVE NMR ANALYSIS OF CI-PBN ADDUCTS.....	227
APPENDIX 2 – DENSITY FUNCTIONAL THEORY CALCULATIONS.....	239
APPENDIX 3– MATHEMATICA MODEL FOR B-CARYOPHYLLENE MODELLING STUDY ....	247



# 1 INTRODUCTION

The effects of airborne particulate matter (aerosol) in the atmosphere, on climate, and public health are among some of the central topics in modern environmental research. Aerosol particles interact with solar and terrestrial radiation through both absorption and scattering, they are central to the formation of cloud condensation nuclei and precipitation, and they affect the abundance of trace gas species through various heterogeneous and multiphase processes.<sup>1,2</sup> Furthermore, aerosol particles play an important role in observed adverse human health effects associated with exposure to urban air pollution such as respiratory and cardiovascular disease. Airborne particles can also act as a transport mechanism for biological organisms, pathogens and biological material such as bacteria, viruses and pollen.<sup>1</sup> The extent of these impacts are closely related to the size, physical properties, and chemical composition of the aerosol. Organic compounds constitute a large fraction of the total atmospheric aerosol mass, and therefore are of crucial importance to understand the role of aerosol in the atmosphere.

However, large uncertainties remain regarding the formation mechanisms and chemical evolution of organic aerosol in the atmosphere, as well as the toxicological mechanisms leading to observed adverse human health effects upon exposure to organic particulate matter. Understanding the reaction mechanisms associated with organic aerosol formation is of crucial importance if we are to determine the composition, and therefore health effects, of organic aerosol.

This introductory chapter will summarise the field at present, discussing our current mechanistic understanding of the formation of organic aerosol, as well as the current analytical techniques employed to probe the composition and formation of organic aerosol. The mechanisms of the gas phase oxidation of volatile organic compounds (VOCs) in the troposphere, which are a substantial source of organic aerosol, will be summarised. The knowledge gaps still associated with the field will also be discussed, in order to contextualise the aims of this work. The array of analytical techniques and

---

instruments used in this work, as well as their physical principles of operation will also be described.

This thesis focusses on the development of novel methods to characterise reactive intermediates relevant to the formation of organic aerosol, as well as developing new chemical assays capable of determining the health-relevant effects of organic aerosol. The methods developed in this thesis have shown considerable promise for further developing our understanding of certain aspects of the chemistry governing the composition and health relevant components of organic aerosol.

## **1.1 Atmospheric Aerosol: Sources, Sizes and Composition**

### **1.1.1 An Overview of Atmospheric Aerosol**

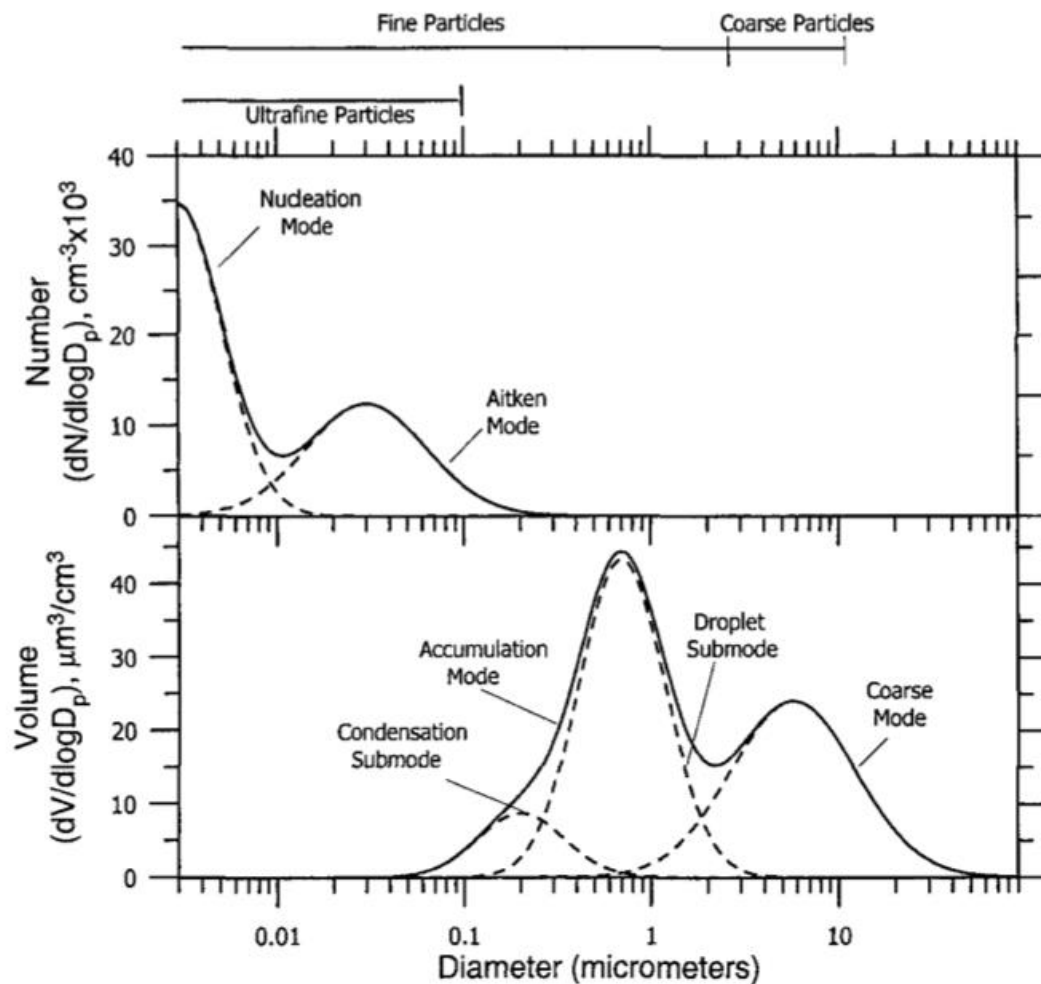
Aerosol is defined as being a gaseous suspension of liquid, solid or multiphase particles. The term aerosol refers to both the suspended particles and the gaseous medium; however, in atmospheric science this term conventionally refers to the particle component alone, and encompasses particulates spanning orders of magnitude in size, ranging from small nano-scale (nm) clusters to bioaerosol such as pollen, which can be up to 100  $\mu\text{m}$  in diameter. In the atmosphere, primary aerosol is generated from processes that emit condensed phase material directly into the atmosphere, through naturally occurring and anthropogenic sources. Secondary aerosol is formed from gas-to-particle conversion mechanisms, such as condensation or adsorption of vapours onto existing aerosol, or gas phase reactions that form semi-volatile and non-volatile products, which can homogeneously nucleate to form new particles.

Figure 1.1 demonstrates that the size of the aerosol is closely dependant on the source of atmospheric aerosol. Coarse particles (aerodynamic diameter  $> 1\text{-}2\ \mu\text{m}$ ) are generally formed from anthropogenic and natural mechanical processes such industry, sea spray, resuspension of dust by wind, erosion and volcanic activity. Coarse particles have sufficiently large gravitational sedimentation velocities that they settle out of the atmosphere at a relatively fast rate. Fine particles (aerodynamic diameter  $< 1\text{-}2\ \mu\text{m}$ ) have three separate modes: the nucleation mode (2-3 up to 10 nm), the Aitken mode (up to 0.1  $\mu\text{m}$ ) and the accumulation mode (from 0.1 to 1-2  $\mu\text{m}$ ). From a policy perspective, aerosol is often defined in terms of their health relevant properties: An EU directive (EU 2008/50/EC, directive 2008/50/EC of the European Parliament and of the council of 21



May 2008 on ambient air quality and cleaner air for Europe) broadly defines particles in terms of their diameter;  $PM_{10}$  ( $< 10 \mu\text{m}$  diameter) and  $PM_{2.5}$  ( $< 2.5 \mu\text{m}$ ). The health relevance of these terms will be discussed in detail in Section 1.3.

Removal mechanisms for atmospheric aerosol are also dependant on the mode of the aerosol. Typically, coarse mode particles are lost *via* gravitational sedimentation and impaction onto surfaces. Smaller, fine aerosol are primarily washed out by precipitation, in-cloud scavenging, by acting as cloud condensation nuclei or *via* uptake into rain droplets (washout). Nucleation mode particles are typically lost through diffusion onto surfaces; in the atmosphere, nucleation mode particles are predominantly lost to the surfaces of other aerosol, particularly accumulation mode aerosol, as this mode of aerosol constitutes a large proportion of available surface area in the atmosphere.



**Figure 1.1** - Diagram illustrating the distribution of particle number and particle volume of atmospheric aerosol. Principal modes are included. Reproduced from Seinfeld and Pandis.<sup>1</sup>

---

The composition of organic aerosol in the atmosphere varies greatly depending on the source of the particles, as well as their respective formation mechanisms. Meteorological conditions (including wind/sunlight) greatly affect the transport and chemical ageing of the aerosol, further complicating their chemistry. Aerosol in the lower atmosphere, in particular the troposphere, can be composed of inorganic species such as nitrates, sulphates and metals, as well as other materials including elemental (black) carbon and mineral dust.

However, organic compounds constitute a substantial, and sometimes dominant, contribution to the total mass of atmospheric aerosol.<sup>3,4,5</sup> Despite vast amounts of research into the chemistry of organics in the atmosphere, large uncertainties remain regarding the mechanisms of organic particle formation, as well as their sources, formation pathways and chemical reaction (ageing) in the atmosphere.

This thesis will largely focus on understanding the reactive intermediates that play a crucial role in defining the reaction pathways of organics found in aerosol. A firmer understanding of the fundamental processes governing organic aerosol formation provides the foundation for gaining further insight into the physical and chemical properties of aerosol, and hence their effects in the atmosphere.

### **1.1.2 Organic Aerosol Sources**

Organic compounds in the atmosphere are defined as molecules containing carbon, except for elemental/black carbon and carbonates generally found in mineral dust, synonymous with the definition in the field of organic chemistry. Carbon based compounds have a large and complex chemistry which makes understanding their role and chemical evolution in the atmosphere challenging. At present, it is estimated that at least  $10^4$ - $10^5$  organic compounds have been detected in the atmosphere, a substantial amount of these being observed in the particle phase.<sup>6</sup>

With regards to organic aerosol, they are broadly defined as two separate classes based on their source and formation mechanisms; primary organic aerosol (POA), which is directly emitted into the atmosphere, and secondary organic aerosol (SOA) which is formed from gas-to-particle conversion mechanisms.<sup>1</sup>

## Emission Sources of Primary Organic Aerosol

Primary organic aerosol (POA) originate from both anthropogenic and biogenic sources. A study by Rogge et al.<sup>7</sup> calculated that on average 28.9 tonnes of organic carbon are globally emitted per day, originating from 32 sources, the most important of which include meat cooking (21.2 %), paved road dust (15.9%) and fireplaces (14%). POA can contain a mix of low-volatility compounds, which permanently reside in the condensed phase, and semi-volatile species, which can desorb from the particle surface into the gas phase depending on environmental condition (e.g. temperature). Some of the more typical constituents of POA include polycyclic aromatic hydrocarbons from combustion sources, as well as oleic acid from the cooking of meat.<sup>8</sup>

Several hundreds of individual organic compounds have been detected in POA, but this represents a small fraction of the total organic complexity of organic aerosol with respect to its source. Certain species within POA can be indicative of its source, for example levoglucosan is a common tracer associated with POA generated from biomass burning.<sup>1</sup> Despite recent advancements in our knowledge of the composition of POA, a greater understanding would allow the detection of more tracer species, which could shed light on POA sources.

## Formation of Secondary Organic Aerosol

Secondary organic aerosols (SOA) are formed in the atmosphere by the mass transfer to the aerosol phase of low volatility products from the oxidation of volatile organic compounds (VOCs). SOA contributions to the total organic aerosol budget can vary from 20-80% depending on climate and location.<sup>9-11</sup>

In the troposphere, VOC processing can be initiated *via* reaction with hydroxyl radicals ( $\cdot\text{OH}$ ), ozone ( $\text{O}_3$ ), nitrate radicals ( $\cdot\text{NO}_3$ ), and chlorine radicals ( $\text{Cl}\cdot$ ).<sup>12</sup> The relative importance of these competing atmospheric oxidants is dependent on the VOC structure and the ambient conditions at any given point in space and time. The initial oxidation step can lead to the generation of a variety of oxygenated functional groups such as ketones ( $\text{RR}'\text{-C=O}$ ), aldehydes ( $\text{HR-C=O}$ ), alcohols ( $\text{R-OH}$ ), carboxylic acids ( $\text{R-C(=O)-OH}$ ) and hydroperoxides ( $\text{R-C-OOH}$ ) amongst many others. The addition of these functional groups lowers the vapour pressure of the organic compound. The change in vapour pressure associated with the addition of common functional groups is displayed in Table 1.1. The addition of any oxygen-containing functional group has a greater effect on the

vapour pressure of an organic compound compared to the increase in the carbon skeleton size by one additional carbon atom. This change is moderate for ketones and aldehydes, given their relatively non-polar nature. The change is more substantial upon the addition of hydroxyl, hydroperoxyl, nitrate and acid groups, each of which can lower the volatility of an organic compound by as much as two orders of magnitude.

Further processing of the newly formed oxidised species can also occur, resulting in a second generation of more oxygenated products, which themselves can partition into the condensed phase, contributing to SOA mass. Various oxidation mechanisms can also lead to the fragmentation of the parent VOC, leading to the formation of lower molecular weight species and, potentially, lower volatility compounds. The mechanisms of VOC oxidation are discussed in detail in Section 1.2.

**Table 1.1** – Approximate changes in vapour pressure of an organic compound upon addition of common functional groups, based upon the contribution method predictions of Pankow and Asher (2007)<sup>13</sup>. Table reproduced from Kroll *et al.*<sup>14</sup>

Functional Group	Structure	Change in Vapour Pressure (298K) <sup>a</sup>
<b>Ketone</b>	-C(O)-	0.10
<b>Aldehyde</b>	-C(O)-H	0.085
<b>Hydroxyl</b>	-OH	$5.7 \times 10^{-3}$
<b>Hydroperoxyl</b>	-OOH	$2.5 \times 10^{-3}$
<b>Nitrate</b>	-ONO <sub>2</sub>	$6.8 \times 10^{-3}$
<b>Carboxylic Acid</b>	-C(O)OH	$3.1 \times 10^{-3}$
<b>Peroxyacid</b>	C(O)OOH	$3.2 \times 10^{-3}$
<b>Acyl Peroxynitrate</b>	C(O)OONO <sub>2</sub>	$2.7 \times 10^{-3}$
<b>Extra Carbon</b>	-CH <sub>2</sub> -	0.35

<sup>a</sup> Represents a multiplicative factor regarding the decrease in vapour pressure upon addition of the functional group.

The phase partitioning and generation of SOA can be described using the theoretical basis of aerosol phase partitioning developed by Pankow *et al.*<sup>15</sup> and then further developed for SOA by Odum *et al.*<sup>16</sup> The main concept of this theory is that SOA is comprised of semi-volatile organic compounds that can partition between the gas and particle phase. Partitioning of each compound can be described by an equilibrium-partitioning coefficient  $K_p$  ( $\text{m}^3 \mu\text{g}^{-1}$ ), defined as:

$$K_p = \frac{P}{GM} \quad (1.1)$$

where  $P$  is the mass concentration ( $\mu\text{g m}^{-3}$ ) of the semi-volatile species in the particle phase,  $G$  is the mass concentration ( $\mu\text{g m}^{-3}$ ) of the semi-volatile species in the gas phase and  $M$  is the mass concentration ( $\mu\text{g m}^{-3}$ ) of the total absorbing particle phase.  $M$  only refers to the particulate matter actively participating in the absorption process (*i.e.* particulate matter onto which semi-volatile organics can absorb). Thus,  $K_p$  is inversely proportional to the saturated vapour pressure,  $c^*$ , of the pure semi-volatile VOC based on Equation (1.1). So long as any particulate mass is available to enable adsorption of a semi-volatile compound (even if the gas phase concentration is below the saturated vapour pressure), the fraction  $F$  of a semi-volatile compound in the particle phase can be estimated by:

$$F = \frac{P}{P + G} = \frac{MK_p}{1 + MK_p} = \frac{1}{1 + c^*/M} \quad (1.2)$$

Therefore, as the amount of  $M$  (absorbing material) increases, compounds of higher volatility (higher  $c^*$  and lower  $K_p$ ) can partition into the condensed phase. Odum *et al.*<sup>16</sup> further developed this theorem to show that the SOA yield  $Y$  (defined as  $\Delta M/\Delta \text{HC}$ , the mass of aerosol formed per the mass of hydrocarbon reacted) can then be calculated:

$$Y = \frac{\Delta M}{\Delta \text{HC}} = M \sum \frac{\alpha_i K_{p i}}{1 + MK_{p i}} \quad (1.3)$$

Where  $\alpha_i$  and  $K_{p i}$  are the mass yield and the equilibrium partitioning coefficient respectively for compound  $i$ . Equation 1.3 demonstrates that  $Y$  can be expressed in terms

---

of a large collection of different semi-volatile compounds. Theoretically, SOA formation can be calculated by summation of equation 1.3 over all semi-volatile products formed in a given reaction. However, given the complexity of atmospheric oxidation of VOCs this method only provides an estimate of the SOA yield. Often in SOA studies, the two-product model is used, where two surrogate compounds are selected to describe volatility distribution of SOA. The two compounds are usually one of low volatility and one of higher volatility, and this method has a good degree of skill in representing laboratory based SOA growth studies.<sup>16,17</sup> Semi-volatile organic compounds (SVOCs) can further react to produce non-volatile organic compounds (NVOCs) that reside fully in the condensed phase.<sup>18</sup>

Recent measurements of laboratory generated organic aerosol have shown that SVOC monomers, and potentially organic radicals, can react to produce a series of dimers and trimers which can contribute to the total NVOC mass.<sup>19–21</sup> Due to the variety of monomeric species formed, oligomers of this type can show great complexity, for example, oligomers derived from the ozonolysis of  $\alpha$ -pinene exhibit over 1000 unique elemental formulas in the ~ 300-1000 Dalton (Da) range.<sup>22,23</sup> Another class of compounds termed extremely low volatile organic compounds (ELVOC) were recently detected in both laboratory and field SOA, and shown to contribute substantially to the SOA mass fraction.<sup>24–27</sup>

## 1.2 Oxidation Mechanisms Leading to SOA Formation

The gas phase oxidation of VOCs is one of the most important process in the lower atmosphere, contributing to poor visibility, photochemical smog and global climate.<sup>28</sup> This section will largely focus on the oxidation of VOCs that largely contribute to the formation of SOA. It is generally regarded that a narrow class of VOCs dominate SOA formation in the troposphere, most notably; isoprene, monoterpenes ( $\alpha$ -pinene,  $\beta$ -pinene, limonene, etc), highly reactive sesquiterpenes such as  $\beta$ -caryophyllene, and aromatic compounds.<sup>14</sup>

Biogenic volatile organic compounds (BVOCs) account for ~90% of VOC emissions<sup>6</sup>, and have been estimated to contribute up to 90% to the current SOA load<sup>29</sup>. The mechanisms by which VOCs are converted into low-volatility oxidised compounds depends on both the organic compound and the oxidant. Table 1.2 shows a list of common

VOCs in the atmosphere, and their respective lifetime in the atmosphere with respect to the oxidant.

**Table 1.2** – Estimated tropospheric lifetimes of key atmospheric organic compounds. Reproduced from Seinfeld and Pandis (2006).<sup>1</sup>

	Lifetime Against Reaction with			<i>hν</i>
	OH <sup>a</sup>	O <sub>3</sub> <sup>b</sup>	NO <sub>3</sub> <sup>c</sup>	
<i>n</i> -Butane	5.7 days	—	1.7 months	
Propene	6.6 h	1.6 days	5.9 h	
Benzene	12 days	—	—	
Toluene	2.4 days	—	1.1 month	
<i>m</i> -Xylene	7.4 h	—	10 days	
Formaldehyde	1.5 days	—	4 days	4 h
Acetaldehyde	11 h	—	20 h	5 days
Acetone	66 days	—	—	38 days
Isoprene	1.7 h	1.3 days	0.8 h	
α-Pinene	3.4 h	4.6 h	6 min	
β-Pinene	2.3 h	1.1 days	15 min	
Camphene	3.5 h	18 days	1.8 h	
2-Carene	2.3 h	1.7 h	1.8 min	
3-Carene	2.1 h	10 h	3.3 min	
<i>d</i> -Limonene	1.1 h	1.9 h	2.7 min	
Terpinolene	49 min	17 min	0.4 min	

<sup>a</sup>12-h daytime OH concentration of  $1.5 \times 10^6$  molecules cm<sup>-3</sup> (0.06 ppt).

<sup>b</sup>24-h average O<sub>3</sub> concentration of  $7 \times 10^{11}$  molecules cm<sup>-3</sup> (30 ppb).

<sup>c</sup>12-h average NO<sub>3</sub> concentration of  $4.8 \times 10^8$  molecules cm<sup>-3</sup> (20 ppt).

The lifetime of these VOCs, respective of each oxidant, can be estimated by assuming a constant concentration of each oxidant in the atmosphere. As is clear from the Table 1.2, each VOC has a highly variable lifetime with respect to each oxidant. For instance, predominantly anthropogenic alkanes such as *n*-butane are unreactive towards O<sub>3</sub> but are readily removed from the atmosphere on average in ~ 6 days by ·OH and ~ 1.7 months by nitrate radicals, meaning that ·OH is the dominant sink of these species. OH, O<sub>3</sub> and NO<sub>3</sub> readily remove monoterpene species such as β-pinene and α-pinene, and the rate of reaction is sufficient with O<sub>3</sub> and NO<sub>3</sub> that these oxidants are often the dominant sinks for monoterpenes in the troposphere.

There is an obvious distinction between the oxidation mechanisms associated with O<sub>3</sub> and ·OH. ·OH-initiated reactions can initially proceed *via* the abstraction of a hydrogen atom by ·OH from the VOC, producing H<sub>2</sub>O and a carbon-centred radical. ·OH can also add across a C=C double bond or aromatic ring, adding a hydroxyl group and generating a carbon centred radical, as illustrated in Figure 1.2.

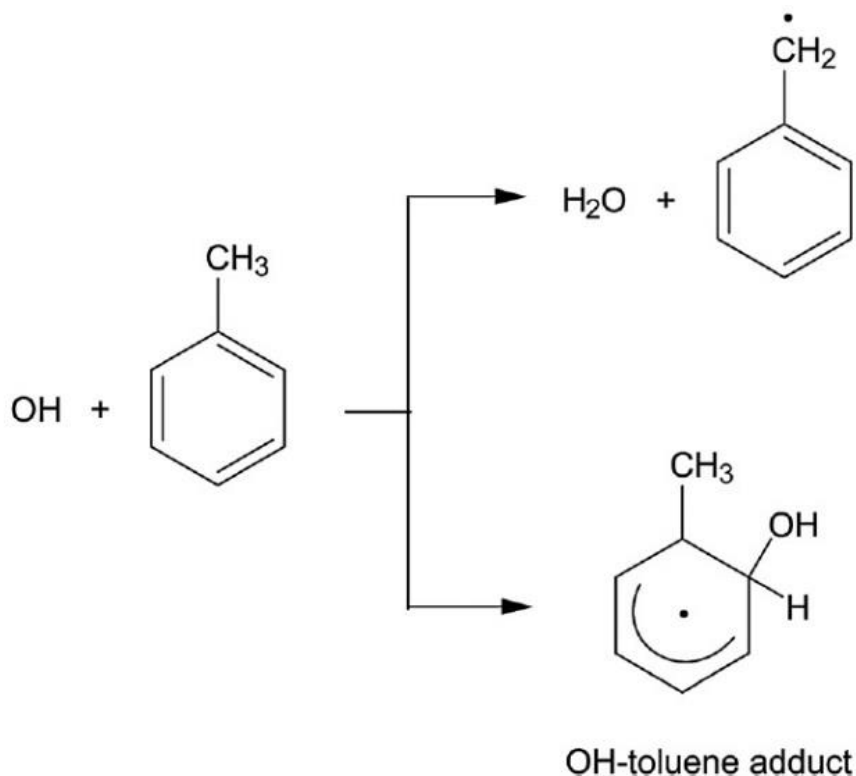


**Figure 1.2** – OH initiated oxidation of toluene, proceeding *via* proton abstraction or addition of OH to the aromatic ring. Reproduced from Ziemann and Atkinson (2012).<sup>30</sup>

The carbon centred radical produced in this reaction predominantly reacts with O<sub>2</sub> to form peroxy radicals (RO<sub>2</sub>). Peroxy radicals play a crucial role in the formation of lower volatility compounds<sup>31</sup>, and through reaction with HO<sub>2</sub> substantially contribute towards the formation of potentially low-volatility hydroperoxides, species which are postulated to be a major component of SOA.<sup>32–34</sup> Nitrate radical initiated oxidation constitutes an important night time sink for VOCs, and its chemistry with alkenes is synonymous with that of OH.<sup>1</sup>

O<sub>3</sub> reacts rapidly with monoterpenes due to the presence of a C=C unsaturated double bond. The reaction between alkenes and O<sub>3</sub> proceeds through a generally accepted mechanism first proposed by Rudolf Criegee<sup>35</sup>; O<sub>3</sub> adds across the double bond of the alkene *via* a 1,3-cycloaddition, initially forming a primary ozonide which then promptly decomposes to form a carbonyl compound, and a so called Criegee intermediate (CI), as depicted in Figure 1.3. Criegee intermediates are one of the main focusses of this thesis, and their chemistry and current methods of detection will now be discussed in detail in Section 1.2.1.



### 1.2.1 Criegee Intermediates

The chemistry associated with Criegee Intermediates (CIs) is central to many aspects of tropospheric chemistry. The chemistry and reaction mechanisms of alkene-ozone reactions has been known for decades<sup>35</sup>, but despite this, it is only in recent years that direct measurement of their reaction kinetics has become possible.

Decomposition of the primary ozonide on average leaves the CI with substantial internal excitation<sup>36,37</sup>; at this stage, the CI either rapidly undergoes unimolecular decomposition (“hydroperoxide channel”) or can be collisionally stabilised to form the stabilised Criegee intermediate (SCI) (Figure 1.3). The SCI can then undergo bimolecular reaction with a number of trace gasses including CO, H<sub>2</sub>O, SO<sub>2</sub>, NO and NO<sub>2</sub>, as well as VOCs, the dominant stable products of which are usually ketones, aldehydes, carboxylic acids and hydroperoxides.<sup>30</sup>

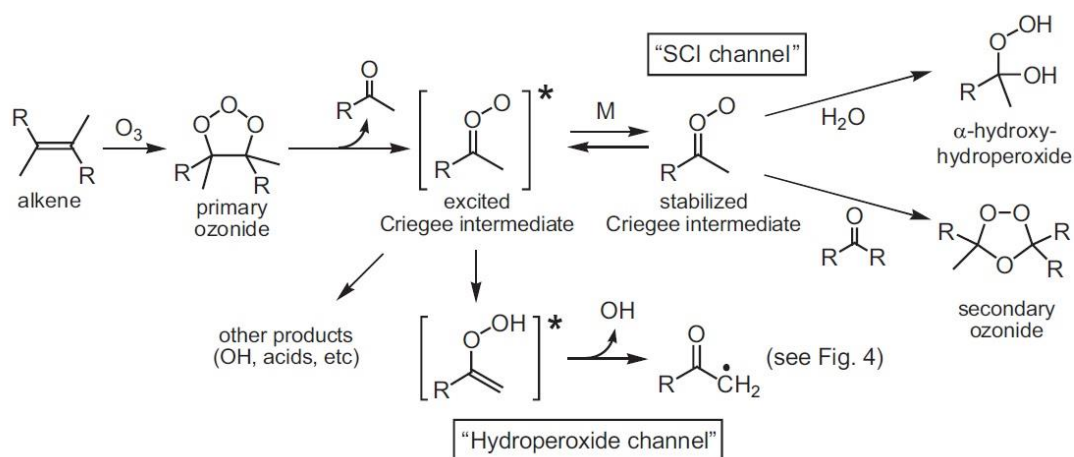
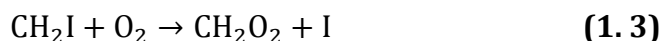
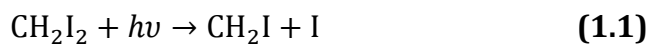


**Figure 1.3** – Simplified mechanism of alkene ozonolysis. The CI initially formed is termed thermally hot, and either undergoes rapid decomposition (hydroperoxide channel) or collisional stabilisation to form the stabilised Criegee intermediate (SCI). Figure reproduced from Kroll and Seinfeld (2008).<sup>14</sup>

Recent advancements in instrumentation have allowed research into the unimolecular and bimolecular kinetics of simple CIs, therefore improving our understanding of their role in tropospheric chemistry. Synchrotron photoionisation mass spectrometry has been demonstrated as a mean to identify and probe the kinetics of CIs; tuneable photoionisation energy generated from a synchrotron allows the identification of different CI isomers, as well as distinguishing CIs from isomeric compounds formed from ozonolysis such as the dioxirane, vinyl hydroperoxide and bis(oxy) forms.<sup>38,39</sup>

However, this technique was not applied to the detection of CIs generated from ozonolysis; the relatively low rate coefficients of ozone-olefin reactions, as well as the high reactivity of CIs, results in a low steady-state concentration of CIs in an ozonolysis reaction system.

Welz *et al.*<sup>40</sup> demonstrated that photolysis of diiodoalkanes generates an iodomethyl radical, which can subsequently react with O<sub>2</sub> to produce the CI (Equations 1.1-1.4), where the atomic iodine channel has been found to be dominant<sup>41</sup> (Equation 1.4), and the CH<sub>2</sub>OO was formed in sufficient quantities to carry out kinetic studies, with yields of CH<sub>2</sub>OO reported between 0.72-0.78<sup>42</sup>



This powerful technique, coupled with a novel method of generating CIs, has allowed substantial advancement in our understanding of the kinetics of simple CIs. This was first applied to probe the reaction of CH<sub>2</sub>OO with SO<sub>2</sub> (Figure 1.4), where it was found that the rate coefficient associated with the reaction was considerably fast ( $k = (3.9 \pm 0.7) \times 10^{-11} \text{ cm}^3 \text{ s}^{-1}$ ), far larger than previous estimates which were on the order of  $k \sim 1 \times 10^{-16} \text{ cm}^3 \text{ s}^{-1}$ <sup>43</sup>.

This enhanced reactivity of CH<sub>2</sub>OO towards SO<sub>2</sub> means it is likely competitive with ·OH oxidation of SO<sub>2</sub>, and could substantially contribute towards global H<sub>2</sub>SO<sub>4</sub> budgets.<sup>44</sup> Rate constants have also been determined for CH<sub>2</sub>OO + NO ( $k = \sim 6 \times 10^{-14} \text{ cm}^3 \text{ s}^{-1}$ , an upper limit estimate) and CH<sub>2</sub>OO + NO<sub>2</sub> ( $k = \sim 7 \times 10^{-12} \text{ cm}^3 \text{ s}^{-1}$ ).<sup>44</sup> Direct measurements made on the reactions of CH<sub>3</sub>CHOO by Taatjes *et al.*<sup>45</sup> represented an important step forward regarding our understanding of the conformer-dependant chemistry of CIs. CH<sub>3</sub>CHOO can exist either as a *syn* or *anti* conformer. The products generated from the ozonolysis of olefins is dependent on the conformer of the CI formed, as summarised in Figure 1.5:

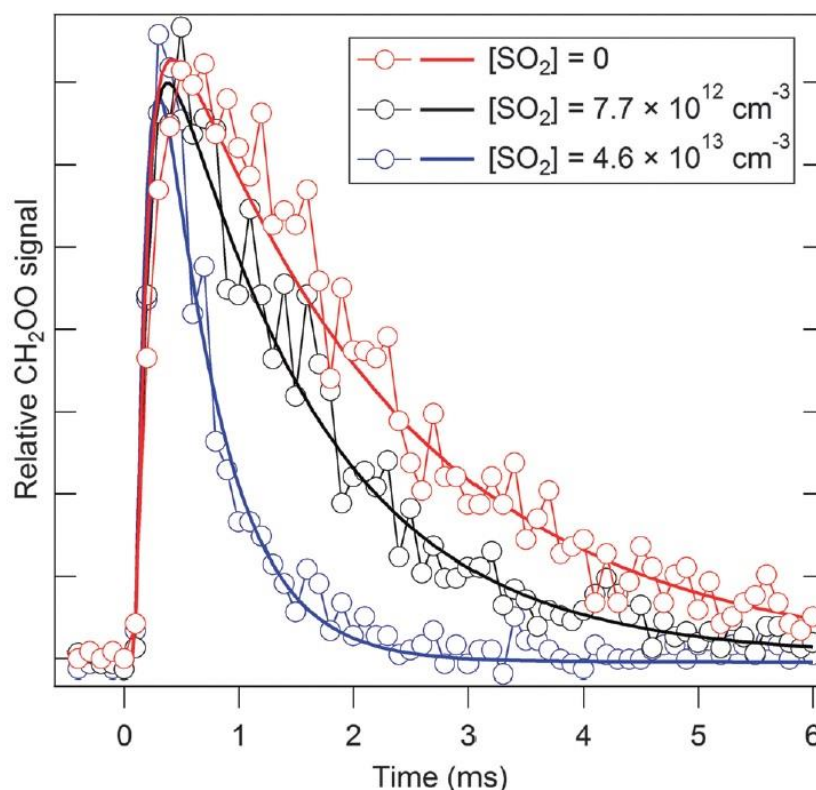


**Figure 1.4** – First-order decays of  $\text{CH}_2\text{OO}$  as a function of sulphur dioxide ( $\text{SO}_2$ ) concentration. Reproduced from Welz *et.al.* (2012)<sup>46</sup>

Theoretical calculations have indicated that the dominant ground state of smaller Criegee intermediates is that of a zwitterionic configuration, where the molecule contains both a positive and negative charge (see Figure 1.5).<sup>47,48</sup> Due to the  $\text{C}=\text{O}$  character in the zwitterionic configuration of the CI there is a substantial enthalpic barrier between the *syn* and *anti* conformer and therefore their interconversion is slow. Photoionisation spectra of the two conformers were different enough to distinguish both the *syn* and *anti* conformer of  $\text{CH}_3\text{CHOO}$ , allowing the determination of the kinetics of bimolecular reactions of  $\text{CH}_3\text{CHOO}$  with  $\text{SO}_2$ ,  $\text{NO}_2$  and  $\text{H}_2\text{O}$ .

Bimolecular reactions of CIs with water are important for the formation of organic acids in the troposphere. Recent experimental studies by Leather *et al.*<sup>49</sup> revealed that the yield of formic acid ( $\text{HC}(\text{O})\text{OH}$ ) from the ozonolysis of ethene has a strong dependence on water concentration, with the yield substantially increasing upon the addition of water to the reaction system. The results of this work suggest that reaction between the simplest CI,  $\text{CH}_2\text{OO}$ , could be responsible for a large fraction of observed ambient formic acid. However, a recent study by Sheps *et al.*<sup>50</sup> found that the reaction between  $\text{CH}_2\text{OO}$  and the water dimer  $(\text{H}_2\text{O})_2$  is  $\sim 4$  orders of magnitude faster than that of the water monomer.

The main products formed between  $\text{CH}_2\text{OO}$  and  $(\text{H}_2\text{O})_2$  were found to be formaldehyde and hydroxymethyl hydroperoxide, also indicating that the formaldehyde yield from this reaction is  $\sim 10\%$ , in contrast with previous studies. There is also growing evidence to suggest that products of CI reaction with water form low-volatility species that can also contribute to SOA formation.<sup>22,40,51</sup>

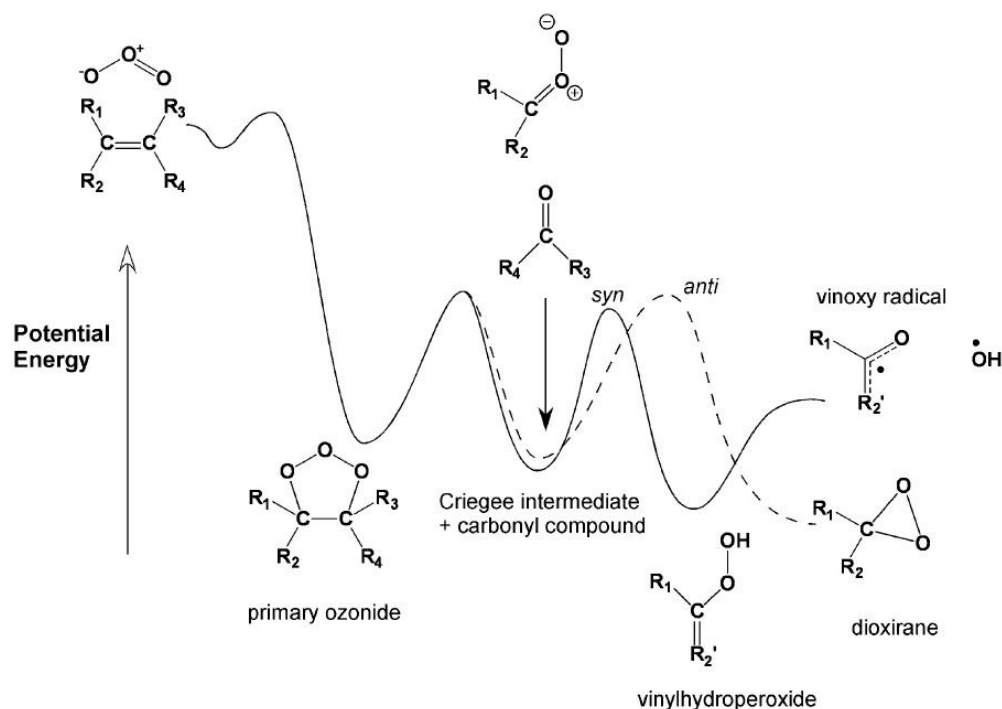


**Figure 1.5** – Schematic of the potential energy diagram illustrating the formation of Criegee Intermediates from alkene-olefin reactions. The initial pathways the CI can follow is dependent on the conformation of the CI. Reproduced from Taatjes *et.al.*<sup>44</sup>

Recent advancements in the detection of CIs using photoionisation mass spectrometry<sup>38,40,45</sup>, ultraviolet spectroscopy<sup>53,54</sup> and infrared absorption<sup>55</sup> (recently, used to directly measure large CIs generated from  $\beta$ -pinene ozonolysis<sup>56</sup>) have rapidly expanded the field of Criegee chemistry. Despite this, large uncertainties remain in understanding the chemistry of larger CIs in complex ozonolysis regimes. However, probing CIs generated from ozonolysis is challenging due to the relatively small rate coefficient for ozone-olefin reactions and fast rate of loss of the CI, as steady-state CI concentrations will be low.

Producing large, atmospherically relevant CIs from the photolysis of diiodoalkane precursors is problematic due in part to the lack of commercial availability. There is still

a requirement for novel techniques that are capable of characterising, and ideally, quantifying direct yields of CIs generated from the ozonolysis of alkenes.

## 1.3 Health Effects of Exposure to Particulate Matter

The adverse human health effects associated with exposure to ambient particulate matter (PM) have been well documented in epidemiological studies, and further supported by *in vivo* and *in vitro* cell culture studies. It is widely accepted that there is an association between exposure to ambient PM and increases in hospital admissions as well as overall mortality due to respiratory disease, cardiovascular disease and cancer.<sup>57–66</sup>

Despite these correlations, the specific toxicological mechanisms, which lead to observed adverse human health effects, are at present poorly characterised. The following Section will outline past and current epidemiological studies, which have improved our understanding of the adverse health effects observed upon exposure to ambient particulate matter, as well as discussing our current knowledge of the physical and chemical properties that affect the toxicological effects of PM.

### 1.3.1 Epidemiological studies

In the UK, one early example of a detailed study of an air pollution event occurred due to pollution generated from both coal power stations and the combustion of coal for residential heating in London. A particularly intense, yet brief, episode of pollution occurred on 5<sup>th</sup> - 9<sup>th</sup> December 1952, followed by ~2 months of elevated pollution levels. During this period, the mortality rate for the week ending 13<sup>th</sup> December was roughly a factor of 2.5 greater than that of the weekly average observed for the same period between 1947-1951 (Figure 1.6).

There is a strong correlation between the observed concentration of SO<sub>2</sub> and increased mortality in greater London as evidenced in Figure 1.6. SO<sub>2</sub> can be considered as a reliable proxy for aerosol concentration, given its close relationship to the concentration of H<sub>2</sub>SO<sub>4</sub> particles formed, and the likely high concentrations of black carbon generated from coal combustion. The UK has since imposed strict regulations regarding the burning of fossil fuels; in particular, the need for a reduction in the burning of coal in close proximity to populated areas resulted in the UK Clean Air Act 1956.

There have since been several large-scale and long-term epidemiological studies, which have correlated exposure of PM to adverse human health effects. A study by Dockery *et al.*<sup>57</sup> is one of the first examples of such a large-scale study. An investigation of 8111 adults in six different U.S. cities between 1975 – 1991 was conducted, with controls in place for other risk factors such as smoking status, gender and age. The study found a distinct correlation between exposure to ambient PM<sub>2.5</sub> and increased mortality due to lung cancer and cardiopulmonary disease. They also observed a correlation between total ambient PM exposure and increased mortality, although the correlation was strongest when considering PM<sub>2.5</sub> alone. The Europe APHEA-2 (Air pollution and health: a European approach) was conducted in the mid-1990s, studying 29 European cities with a combined population > 43 million.<sup>67</sup> There was again a correlation between exposure to ambient PM<sub>10</sub> and hospital admissions for asthma, chronic obstructive pulmonary disease and cardiovascular disease.<sup>59</sup>

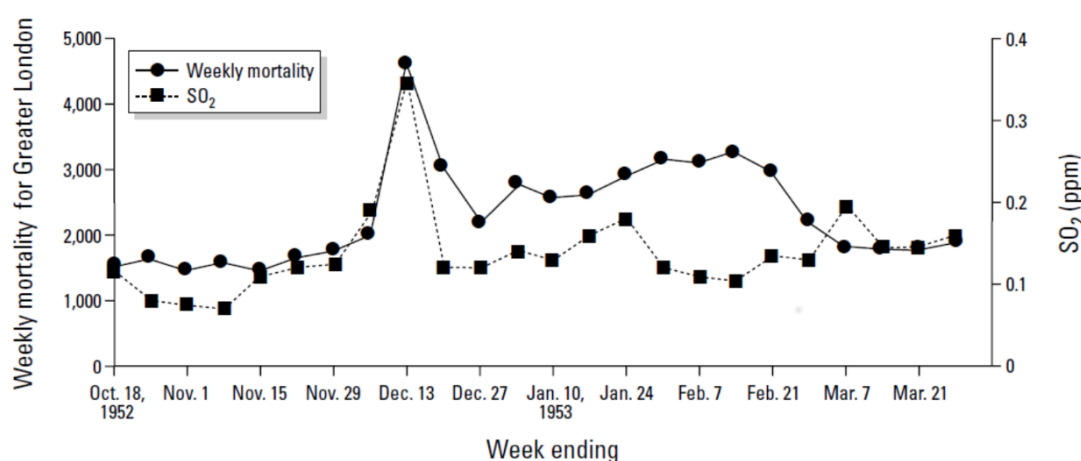


**Figure 1.6** – Weekly mortality rate and measured concentrations of SO<sub>2</sub> in Greater London from October 1952 - March 1953. Observed mortality rates were significantly greater following the great London Smog event in December 1952, with an average increase ~50% for the following two months compared to the weekly average in 1947 – 1952. Reproduced from Bell and Davis (2001).<sup>68</sup>

Laden *et al.*<sup>64</sup> and Lepeule *et al.*<sup>65</sup> revisited the study by Dockery *et al.*<sup>57</sup> to apply modern statistical methods to the entire dataset gathered by the study. Laden compared the mean levels of PM<sub>2.5</sub> between 1980-1985 and 1990-1998, represented in Figure 1.7 by the bold letters (1980-1985) and italicised letters (1990-1998) respectively.

A correlation was found between a reduction in PM<sub>2.5</sub> between the two time-periods and a reduction in the overall rate of mortality, implying that the mortality rates due to

exposure to PM are partially reversible if  $\text{PM}_{2.5}$  concentrations can be reduced. This effect may be due in part to the exacerbation of underlying conditions upon exposure to  $\text{PM}_{2.5}$ , an effect that would subside given a reduction in the concentration of  $\text{PM}_{2.5}$ . Despite this, there is still evidence to suggest that  $\text{PM}_{2.5}$  enhances the development of chronic diseases, which are less likely to respond to a short-term reduction in  $\text{PM}_{2.5}$ .

Lepeule *et al.*<sup>65</sup> further analysed the dataset and extended it up to 2009, showing further reductions in the annual mean concentration of  $\text{PM}_{2.5}$ . They showed that the response in mortality to  $\text{PM}_{2.5}$  is linear above a concentration of  $8 \mu\text{g m}^{-3}$ , and that for every increase in  $\text{PM}_{2.5}$  by  $10 \mu\text{g m}^{-3}$ , there was an increase in the overall mortality rate (14 %), mortality due to cardiovascular disease (26 %) and lung cancer mortality (37%).

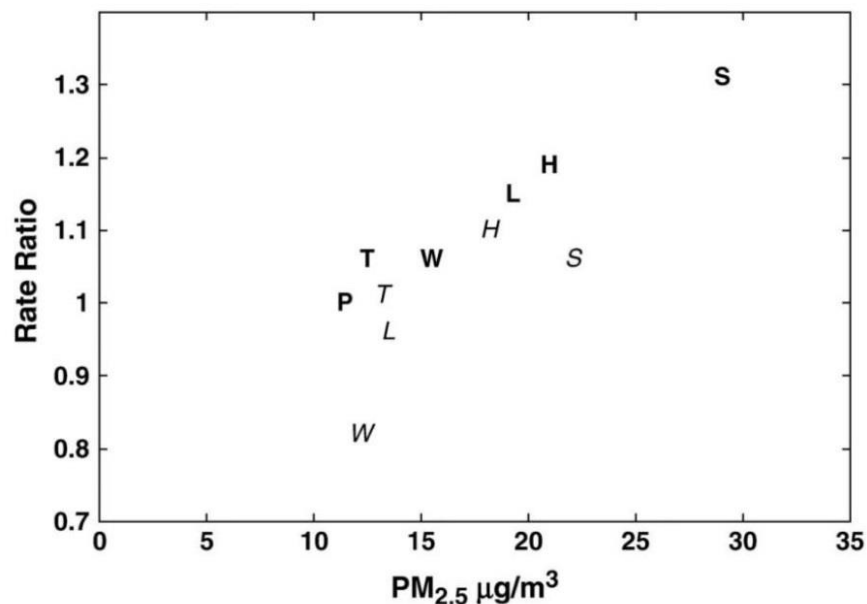


**Figure 1.7** - Estimated adjusted rate ratios for total mortality and  $\text{PM}_{2.5}$  levels in the Six Cities Study by period. P denotes Portage (reference for both periods); T Topeka; W Watertown; L St. Louis; H Harriman; S Steubenville. Bold letters represent Period 1 (1980–1985) and italicised letters represent Period 2 (1990–1998). Reproduced from Laden *et al.*<sup>64</sup>

These studies clearly correlate an increase in exposure to ambient particulate matter with an increase in respiratory disease, cardiovascular disease and overall mortality. To improve our understanding of this correlation, one must gain a firm grasp on the fundamental physical and chemical properties of PM that cause the observed adverse human health effects.

### 1.3.2 Health Relevant Physical and Chemical Properties of Aerosol

The composition of ambient PM varies both spatially and over time. Due to this inherent complexity, it is challenging to isolate the specific physical and chemical properties of PM that lead to the toxicological response observed in epidemiological studies. Several studies have suggested that particle size, the concentration of transition metals and oxidative potential of aerosol are more accurate markers of PM toxicity, as opposed to just measuring the total PM mass. The manner in which particles can affect the lung is strongly dependant on their diameter, as illustrated in Figure 1.8. The human respiratory system can be crudely separated into three sections: The nasal airway (including mouth and nasal passage), the tracheobronchial region and the alveolar region. The nasal airway contains fine cilia hairs to collect particles, and a mucociliary system to direct particles towards the mouth for expulsion from the body.

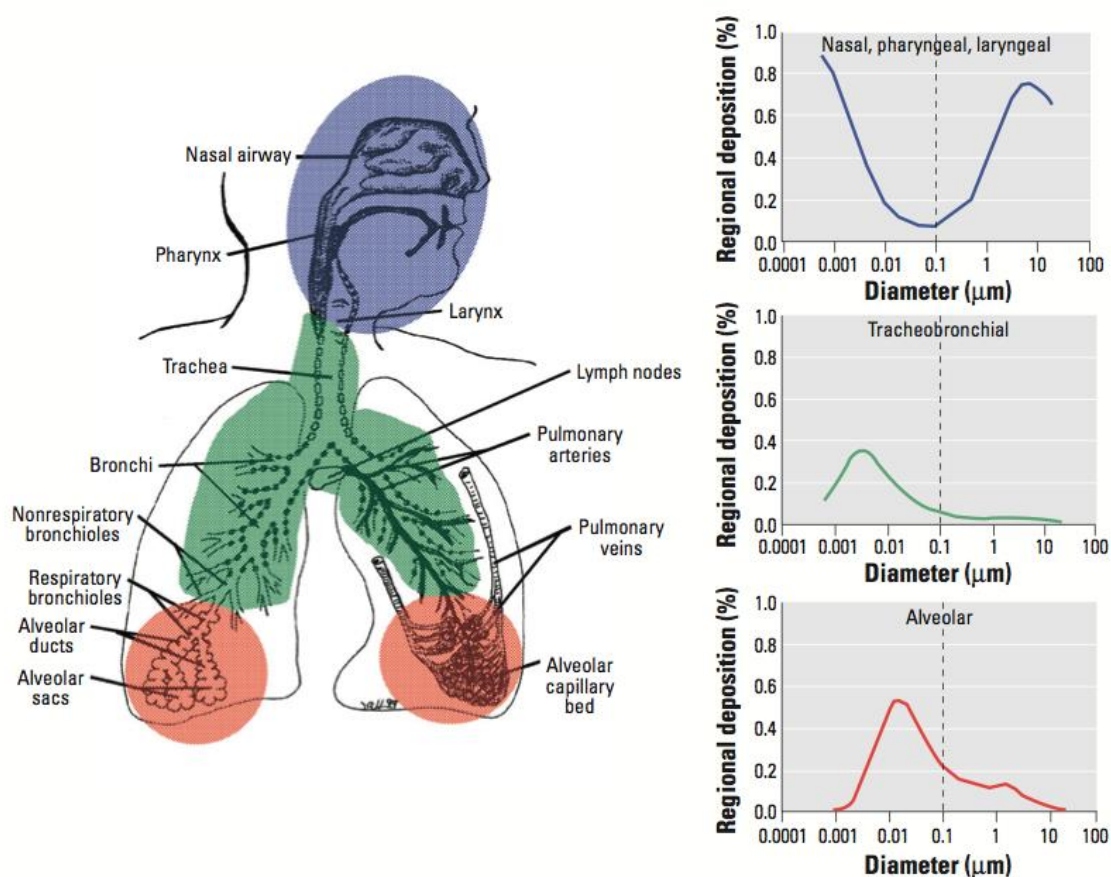


**Figure 1.8** - Depiction of the deposition of airborne particles in the lung as a function of particle diameter. Larger particles ( $> 0.1 \mu\text{m}$ ) are largely removed in the nasal airway (blue region). Sub-micron particles ( $< 0.1 \mu\text{m}$ ) can penetrate much deeper into the lungs to the tracheobronchial (green) and alveolar (red) regions and deposit on the respiratory tract wall *via* gravitational sedimentation, due to the reduced airflow in these regions. Reproduced from Oberdorster *et al.*<sup>69</sup>



The bronchial region consists of many branched airways, often experiencing rapid changes in airflow, and contains a mucociliary system for removing particles. The alveolar region is where the gaseous exchange of air between the lung lining fluid and the cardiovascular system occurs, and has no mucociliary defence in place. Therefore, the alveolar region could be more susceptible to the toxicological effects of PM, given the lack of mucociliary or fibrous defence in this region. As illustrated in Figure 1.8, smaller particles in the range 0.01-0.1  $\mu\text{m}$  in diameter deposit more efficiently in this region. Typically, PM<sub>2.5</sub> and ultrafine particles are most efficient at penetrating deep into the lung as evidenced by the alveolar deposition (red curve) in Figure 1.8. The smallest ( $<0.001 \mu\text{m}$ ) and largest ( $\sim > 4 \mu\text{m}$ ) particles are efficiently removed in the upper lung *via* efficient diffusion and impaction respectively. Particles in the accumulation mode are not efficiently removed in the upper lung, and can deposit in the alveolar region *via* diffusion mechanisms as these regions restrict rapid changes in airflow so that air can be more efficiently absorbed, therefore inherently improving the rate of diffusion of particles in this region. Damaging components of PM can therefore more efficiently promote a response in this region due to the inefficient removal of particles. It has also been shown that smaller particles can cross the lungs membrane and enter the cardiovascular system.<sup>70</sup> Therefore, it is more likely that smaller particles ( $< 4 \mu\text{m}$ ) are more relevant to the toxicological effects of PM as opposed to the total PM mass.<sup>69</sup>

The oxidative potential of particles has been identified as a suitable marker for the toxicological impact of PM. Oxidative potential is defined as the potential of PM to oxidise target molecules of biological relevance. Particle-bound reactive oxygen species (ROS) are one particular class of compounds that are widely believed to substantially contribute towards observed adverse human health effects upon exposure to PM. The term ROS in general refers to organic species with oxidative properties (*e.g.* peroxides), ionic species such as  $\text{OH}^-$  and free radical species ( $\cdot\text{OH}$ ,  $\cdot\text{OOH}$ ,  $\cdot\text{RO}_2$ ).<sup>71-75</sup> These oxidising species could therefore substantially contribute to the observed oxidative potential of PM observed in ambient studies. The exogenous delivery and deposition of particle-bound ROS in the lung, or endogenous generation of ROS in the lung lining fluid by particle-bound components, has been proposed to reduce the concentration of naturally occurring anti-oxidants present in the lung. Anti-oxidants present in lung lining fluid include (but are not limited to) ascorbic acid (vitamin C), tocopherol (vitamin E), uric acid and glutathione. Depletion of these anti-oxidants leads to an imbalance of the anti-oxidant vs oxidant concentration in the lung in favour of the oxidants, known as oxidative stress.

This can result in ROS inducing an immune response, inflammation of the lung surface or lysis of cells. The inflammatory response and cellular damage induced by ROS can induce or exacerbate conditions observed in epidemiological studies such as chronic obstructive pulmonary disorder, cardiovascular disease, asthma, and cancer.<sup>50, 58,62,69</sup> This stress mechanism is not only present at the point of deposition in the lung; ROS species such as hydrogen peroxide have been shown to penetrate cell membranes, and therefore can be transported beyond the point of initial deposition, and can damage other cells throughout the body.<sup>73</sup> ROS species can also damage DNA and cause mutagenesis, contributing towards tumour formation and growth.<sup>58,72</sup> There are various complex mechanisms associated with the promotion of oxidative stress by PM upon uptake into the lung. Figure 1.9 summarises 5 key interrelating mechanisms which can lead to oxidative stress in the lung, as described in detail by Kelly *et al.*<sup>62</sup>

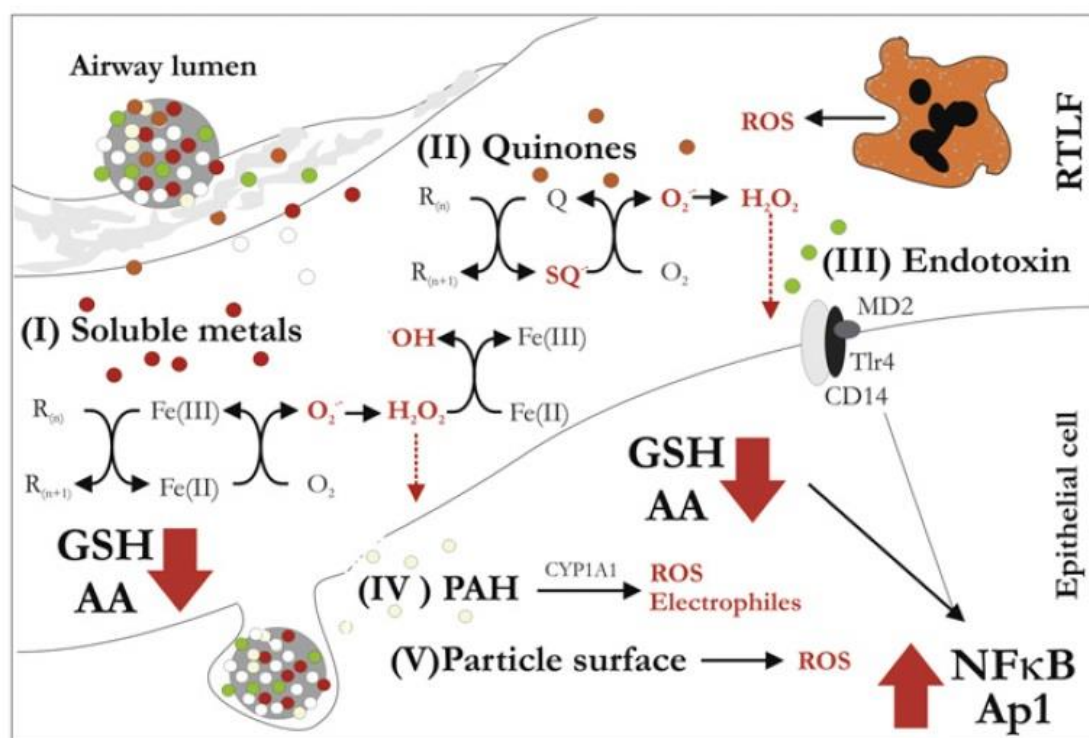


**Figure 1.9** – Pathways of particle induced toxicity at the lung-air surfaces through 5 interrelated mechanisms: (I) Through the introduction of redox active metals which can generate ROS in the lung. (II) Quinones on the particle surface which participate in redox-active chemistry. (III) Bacterial endotoxins associated with the particle surface can trigger inflammatory responses. (IV) Polycyclic aromatic hydrocarbons have no inherent redox activity, but they can undergo biotransformation *in vivo* into quinone species. (V) The particle surface itself has been shown to cause oxidative stress *in vivo*, but the mechanisms of this is ill defined. Figure reproduced from Kelly *et al.*<sup>62</sup>

The Figure shows a close relationship between the 5 different pathways to oxidative stress, involving both exogenous delivery of ROS directly to the lung surface, the endogenous generation of ROS in the lung, as well as biotransformation of particle-bound components *in vivo* which can lead to the generation of redox active species.

Pathway (I) involves the introduction of redox active metals, such as iron and copper, into the lung. These metals then participate in redox active chemistry in the presence of oxygen and biological reductants (*e.g.* anti-oxidants such as ascorbic acid and glutathione) to yield superoxide radicals ( $O_2^{\cdot-}$ ), hydrogen peroxide ( $H_2O_2$ ) and  $\cdot OH$  radicals. The metals can be recycled, and in some cases, the generation of these ROS species can be considered catalytic, causing even more damage to cells on the lung surface. (II) The introduction of quinones from the particle surface can also participate in redox chemistry in the presence of anti-oxidants to form the semi-quinone radical, which can react further to yield the superoxide radical and hydrogen peroxide. (III) Bacterial endotoxins, components of bacterial membranes, which can be present on the particle surface, can promote inflammation and oxidative stress *via* interaction with receptors on endothelial cell membranes. (IV) Polycyclic aromatic hydrocarbons have no redox reactivity of their own. However, they can undergo biotransformation *in vivo*, through the action of metabolising enzymes, to form quinones and ROS, which can induce oxidative stress. (V) Illustrates that ROS components bound to the particle surface can be directly delivered to the lung surface, where they can directly induce oxidative stress. The particle surface itself has been shown to induce oxidative stress in the lung, although the mechanisms of this process are not entirely clear.

The function of macrophage cells in the lung is to remove particulates before they can damage other cell membranes or even DNA. As illustrated in Figure 1.9, ROS can disrupt the biological mechanism of the NF $\kappa$ B (Nuclear Factor) and Ap1 (activation protein). Upregulation of these transcription factors can lead to the increase in the number of macrophages, which themselves generate a substantial amount of ROS, therefore contributing to oxidative stress.

Figure 1.9 demonstrates the chemical complexity associated with the induction of oxidative stress in the lung; therefore, distinguishing individual chemical species responsible for observed adverse health effects upon exposure to ambient aerosol is challenging. *In vitro* cell culture studies have shown a correlation between the total oxidative capacity of aerosol and their negative effect on human health.<sup>59,77,78</sup> Despite

this, large uncertainties remain on both the quantity and composition of ROS species present in organic aerosol. Novel analytical techniques are required to probe ROS concentration in organic aerosol, both in the lab and the field, to corroborate the data gathered from *in vitro* studies, and to elucidate specific reaction mechanisms responsible for promoting oxidative stress.

### 1.3.3 Current Methods of ROS Detection in Aerosol

A number of chemical assays have been developed to probe ROS concentrations in ambient aerosol. Given the breadth of species that are believed to cause oxidative stress, leading to observed adverse human health effects, no one assay is likely capable of quantifying the total health relevant ROS in aerosol. Most assays in use focus on determining the oxidative potential of the aerosol, which serves as a proxy for the likelihood that the particles will induce a toxic response in the lung. Several methods have recently been developed to quantify ROS in PM using on-line, off-line and *in vitro* methods.<sup>79–85</sup>

Two common assays used for measuring organic ROS in ambient aerosol are the dithiothreitol (DTT) assay and the 2,7-dichlorofluorescein (DCFH) assay. DTT is a strong reducing species, the consumption of which is assumed proportional to the concentration of oxidising species in a given sample of aerosol. DTT has been employed in several studies, and has shown a particular sensitivity towards transition metals and quinones in PM.<sup>77,79,86–88</sup> Oxidising species are quantified by monitoring the concentration of unreacted DTT.

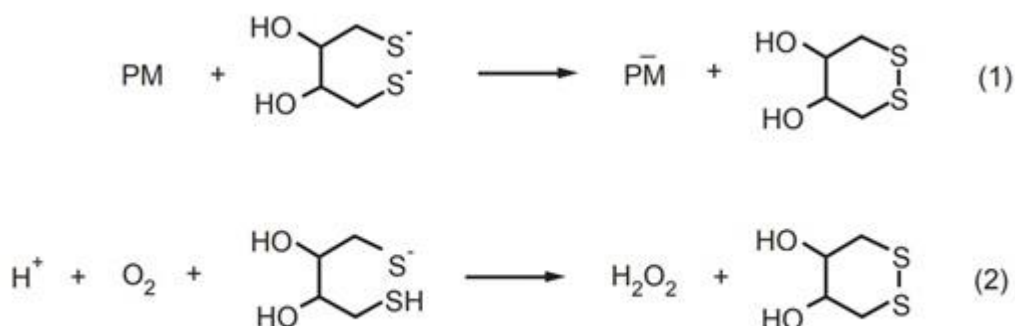


**Figure 1.10** – Schematic illustrating the chemistry associated with the PM enhanced oxidation of DTT. The oxidative potential of PM can then be estimated by quantifying the remaining concentration of unreacted DTT. Reproduced from Cho *et al.*<sup>79</sup>

The excess DTT reacts with 5,5-dithio-bis-2-nitrobenzoic acid to produce the product 2-nitro-5-thiobenzoic acid (TNB). TNB is more stable than DTT, and can be measured using absorbance spectroscopy, which eventually yields the concentration of oxidising species in the reaction system.<sup>89</sup> There are still some caveats regarding use of the DTT assay; contradictory results regarding the assays sensitivity to transition metals have been reported, and the assays generally slow and laborious mode of operation.<sup>89</sup> However, recent advancements including the development of microfluidic electrochemical sensors<sup>87</sup> and on-line microfluidic chips<sup>88</sup> using DTT have sought to overcome the slow operating speed of this analytical technique.

DCFH assays have been applied to a variety of off-line and on-line methods to detect ROS in ambient aerosol.<sup>80,83,85,90</sup> The assay uses DCFH in the presence of a catalytic electron-accepting enzyme hydrogen peroxidase (HRP), which yields the fluorescent product dichlorofluorescein (DCF), which can be subsequently measured using fluorescence spectroscopy.<sup>91</sup> This peroxidase cycle is particularly sensitive to  $\text{H}_2\text{O}_2$ , organic peroxides and peroxy acids.<sup>85,90</sup>

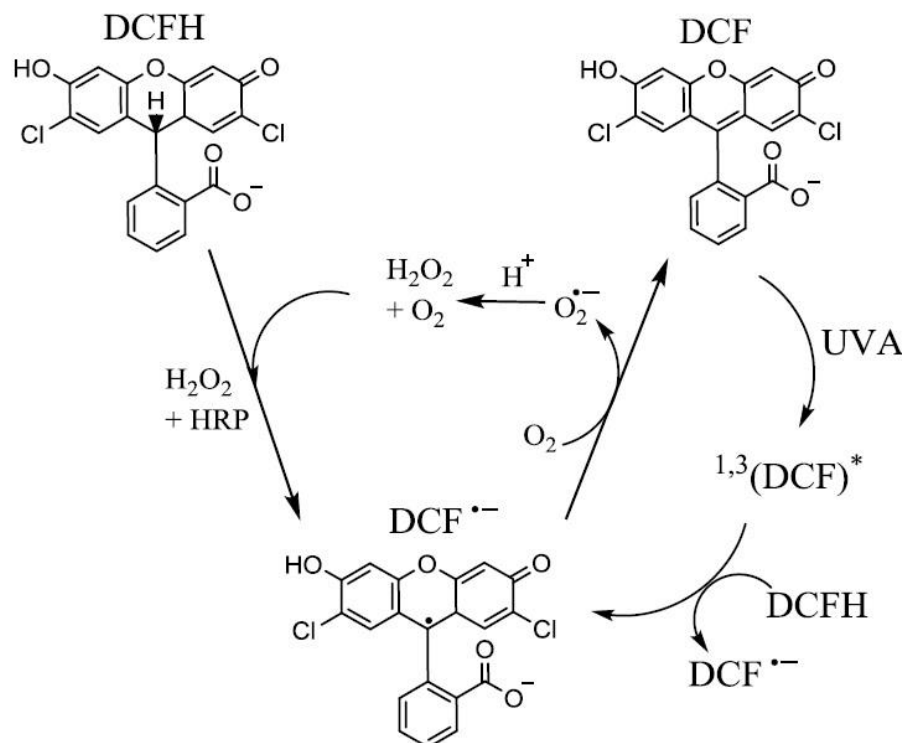


**Figure 1.11** – Scheme illustrating the conversion of DCFH to the fluorescent compound DCF in the presence of the catalytic enzyme HRP. Reproduced from Chigwell and Sik (2003).<sup>92</sup>

---

The DCFH assay is widely employed due to its relative lack of chemical specificity and interaction with a variety of oxidants; however, its full interaction with species such as  $\cdot\text{OH}$  and  $\text{O}_2^-$  is currently unclear.<sup>93</sup> Recent studies by Wragg *et al.*<sup>85</sup> and Gallimore *et al.*<sup>94</sup> have shown that the DCFH assay is sensitive to organic peroxides such as peracetic acid, and particle-bound ROS generated from both  $\alpha$ -pinene and limonene ozonolysis.

Radical components of PM have been investigated and quantified using a profluorescent nitroxide probe 9-(1,1,3,3-tetramethylisindolin-2-yl)oxyl-5-ethynyl-10-(phenylethynyl)anthracene (BPEA).<sup>75,95–97</sup> This particular assay is utilised in this work to measure particle-bound radicals in secondary organic aerosol (Chapter 5), and the chemistry of BPEA is discussed in detail in Section 1.3.5.

The aforementioned assays try to define and quantify a certain subset of the oxidising components in particles, or processes in cells that result from particle deposition in the lung. Therefore, each technique only quantifies a certain range of ROS species, although in most cases large uncertainty remains on the specific compounds inducing the observed response. Thus, observing the decrease in naturally occurring anti-oxidants may serve as an alternative strategy to characterise the oxidative potential of particulate matter from a health perspective.

One such assay involves the use of naturally occurring anti-oxidants in the lung using synthetic respiratory tract lining fluid (RTLFL); this comprises of ascorbic acid (AA), glutathione (GSH) and uric acid (UA). This assay has been used to detect ROS generated from redox-active transition metals.<sup>98</sup> AA concentrations are depleted as a response to oxidising species present in the reaction mixture; the extent of AA oxidation can then be determined using fluorescence spectroscopy. This assay is employed in this thesis, and the chemistry will be discussed in more detail in Chapter 6. As the aforementioned chemical assays show differing levels of sensitivity to different species that may all constitute ROS, health relevant ROS systems should be probed with a variety of assays simultaneously.<sup>99</sup>

In order to determine the full impact of ROS concerning adverse health effects, compact, cost effective, on-line instruments capable of being readily deployed in the field are required. On-line instruments for measuring ROS are particularly advantageous:

- They allow the more accurate quantification of short-lived species, due to the much faster time resolution compared to traditional filter studies. This has been evidenced in studies such as Fuller *et al.*<sup>90</sup>, Wragg *et al.*<sup>85</sup> and Gallimore *et al.*<sup>94,100</sup>
- They allow the monitoring of fast compositional changes in organic aerosol, providing insight into the chemistry occurring, and can determine the rates of loss of short-lived species (Gallimore *et al.*<sup>94,100</sup>)
- Many other methods of atmospheric measurement typically have a fast time resolution as well as operating on-line. A method to detect ROS on-line would potentially allow the identification of ROS sources, or insights into the formation pathways or ROS in the atmosphere by correlating data with other on-line measurements.

There are several practical and chemical challenges associated with the development of such instruments. This next section will briefly summarise current instruments that have been developed with various chemical assays to probe ROS in atmospherically relevant aerosol.

### 1.3.4 On-line Measurement of Particle Bound ROS

Instruments capable of making on-line measurements of particle bound ROS require several components. A system capable of sampling aerosol continuously into solution so ROS components can react with a given chemical assay (which is typically a liquid), a continuous flow-through reaction system, and a continuous flow-through detection method that is specific to ROS. Fluorescence spectroscopy is commonly used detection technique, particularly with assays such as DTT or DCFH.

Initial designs to improve the time-resolution of aerosol sampling compared to traditional off-line filter sampling techniques were made by Wang *et al.*<sup>83</sup> where they used a particle-into-liquid-sampler (PILS) to sample aerosol on-line, with the ROS components of aerosol subsequently analysed using the DCFH assay. However, PILS requires an operating temperature of 100 °C and the introduction of steam to grow the particles for collection. Due to the highly reactive nature of ROS species, this elevated temperature and increased humidity could result in the decomposition of ROS species present in the particle, or could in fact artificially generate species that may affect quantification. King *et al.*<sup>80</sup> developed a similar technique in which a mist chamber is used to collect particles

instead of a PILS. However, this technique has a comparatively poor time resolution, as the aerosol must be extracted into water before ROS analysis with the DCFH assay.

Recently, two studies by Fuller *et al.*<sup>78</sup> and Wragg *et al.*<sup>85,90</sup> developed a new on-line instrument called the Online Particle-bound ROS Instrument (OPROSI). A schematic of the instrument design is depicted in Figure 1.12. This instrument is advantageous as it uses an alternative particle collection system, whereby the aerosol is sampled onto a wetted filter containing HRP, reacting with ROS almost immediately after introduction of the particles into the instrument. The aerosol is then dissolved in the reaction mixture, where the ROS concentration is analysed using fluorescence spectroscopy. The instrument allows a fast-response measurement of particle-bound ROS, and extended field operation whereby it needs maintenance ~ twice a day. The instrument has been shown to be sensitive to peroxides, but also ROS (likely peroxides) present in aerosol generated in a smog chamber. This instrument design was the basis of a novel instrument developed in this thesis, as described in Chapter 6.

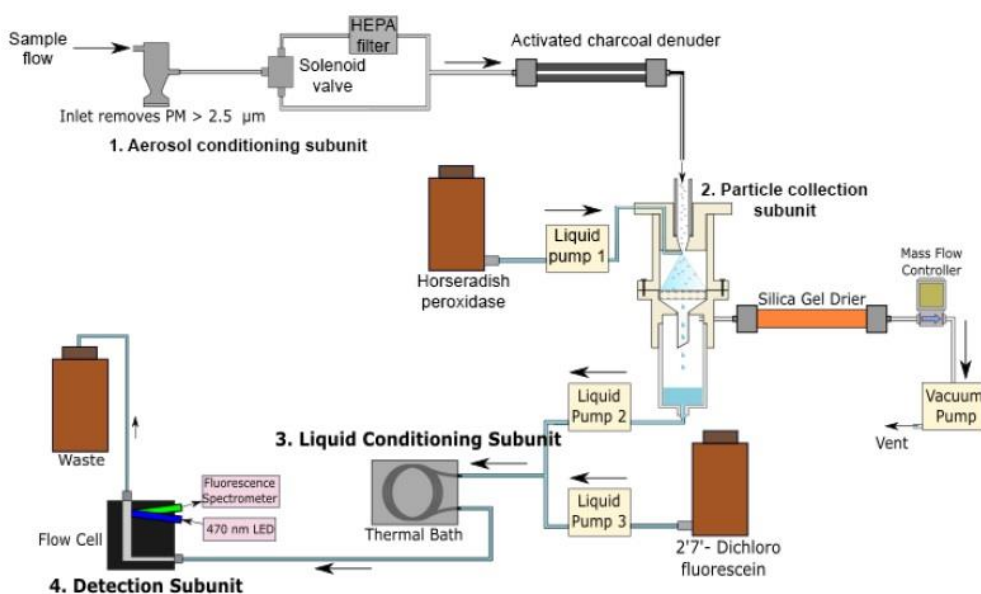


**Figure 1.12** – Schematic of the Online Particle-bound ROS Instrument (OPROSI), which comprises of four labelled subunits: (1) the aerosol-conditioning subunit enables the removal of particles > 2.5 μm, automated blank measurement and removal of gases such as VOCs and ozone. (2) The particle collection subunit allows collection of the particles into liquid phase, allowing soluble ROS to be extracted. (3) The liquid-conditioning subunit provides suitable time and temperature for the reaction between the DCFH-HRP assay and extracted ROS and (4) the detection subunit records fluorescence intensity as a function of ROS concentration. Reproduced from Wragg *et al.*<sup>85</sup>



### 1.3.5 Spin Trap Reagents: Mechanisms and Applications

As previously mentioned, ROS is a term that encapsulates a wide range of oxidising species. Organic radical species also often have oxidising character, and therefore could act as ROS, contributing to the oxidative potential of particles and therefore oxidative stress in the lung.

Spin trapping, a term initially coined by Janzen *et al.*<sup>101</sup> involves the scavenging of reactive radical or reactive intermediate species by a spin trap molecule, which generates a more stable radical or non-radical adduct. This technique has been widely applied to study biologically relevant radicals *in vivo* and *in vitro* for decades.<sup>102–109</sup> The most common method of detecting the stabilised radical adducts is using a technique called electron paramagnetic resonance (EPR) spectroscopy, which again has been widely applied to the study of radicals in various fields.<sup>102,104,110–113</sup> Given the inherent high reactivity of radicals, they are a challenge to characterise in both biological assays and other environments; spin traps offer a unique way to scavenge and stabilise radicals in complex chemical and biological environments, and facilitate the indirect quantification of radicals using conventional methods.

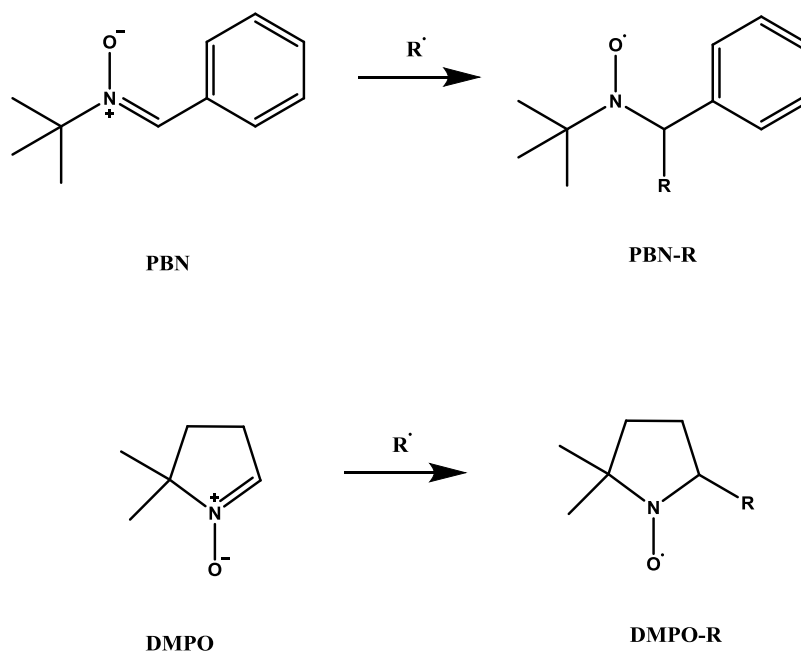


**Figure 1.13** - Mechanism for the reaction of the spin trap PBN and DMPO with a radical,  $R^\cdot$  to produce a more stable spin trap product, which itself is a radical species. R can typically be a carbon, oxygen, nitrogen, chlorine or fluorine centred radical. EPR can be used to measure the concentration of radicals indirectly, by measuring the concentration of spin trap- adduct radicals.

---

Two commonly applied spin traps are *N-tert*-butyl- $\alpha$ -phenylnitrone (PBN, C<sub>11</sub>H<sub>15</sub>NO) and 5,5-dimethyl-pyrroline-*N*-oxide (DMPO, C<sub>6</sub>H<sub>11</sub>NO).<sup>114–118</sup> These species fall into the nitron class of spin traps, due to the C=N-O nitron functionality that reacts with radicals. DMPO and PBN have been widely applied to trap a variety of radical species including R· = C $\equiv$ N-C(CH<sub>3</sub>)<sub>3</sub>, CH<sub>3</sub>-C(O)-C(CH<sub>3</sub>)<sub>2</sub>, methyl, ethyl, *n*-butyl, fluoro, chloro, succinimidyl, alkoxy, hydroxyl and peroxy radicals.<sup>119</sup> These species react with a radical to produce a stable nitroxide (N-O·) functionality (Figure 1.13), which can subsequently be studied using EPR.

EPR is capable of distinguishing the trapped radical species based on the hyperfine splitting observed when probing the radical on the spin trap – radical adduct, as well as quantifying the radicals indirectly *via* quantification of the radical-spin trap adducts themselves, assuming sufficient lifetime of the adducts.<sup>111</sup> Studies have also used the spin traps PBN and DMPO to probe radicals formed from the oxidation of organics, with the radical-spin trap adducts qualitatively assigned using electrospray ionisation high resolution mass spectrometry (ESI-HRMS).<sup>120,121</sup>

The spin trap PBN is used in this work for solution-phase trapping of radicals due to its commercial availability, low-volatility and extensive application in the literature. DMPO is also utilised in this research to scavenge radicals in the gas phase. DMPO is functionally synonymous with PBN, sharing the same nitron functionality, although DMPO has a higher volatility and can therefore be introduced into the gas phase.

Using such spin traps, it is possible to scavenge radical intermediates in complex organic chemical systems, such as the ozonolysis of VOCs, and with analysis using a variety of conventional techniques, gain both a qualitative and quantitative insight into the radicals formed in these oxidation regimes. Both of these species are used in this work to scavenge Criegee intermediates in both the gas and particle phase, as described in Chapter 3 and Chapter 4.

Another class of spin traps, known as nitroxide spin traps, have been used to probe radicals in aerosol generated from the combustion of biomaterial. One particular spin trap, 9-(1,1,3,3-tetramethyl-*iso*-indolin-2-yl)oxy-5-ethynyl)-10-(phenylethynyl)anthracene (BPEA), synthesised for the first time by Fairfull-Smith *et al.*<sup>122</sup>, has been used in several studies to probe radicals in cigarette smoke<sup>97,95</sup>, biomass burning<sup>75,95</sup> and the combustion of transport-relevant fossil fuels<sup>96,123,124</sup>.

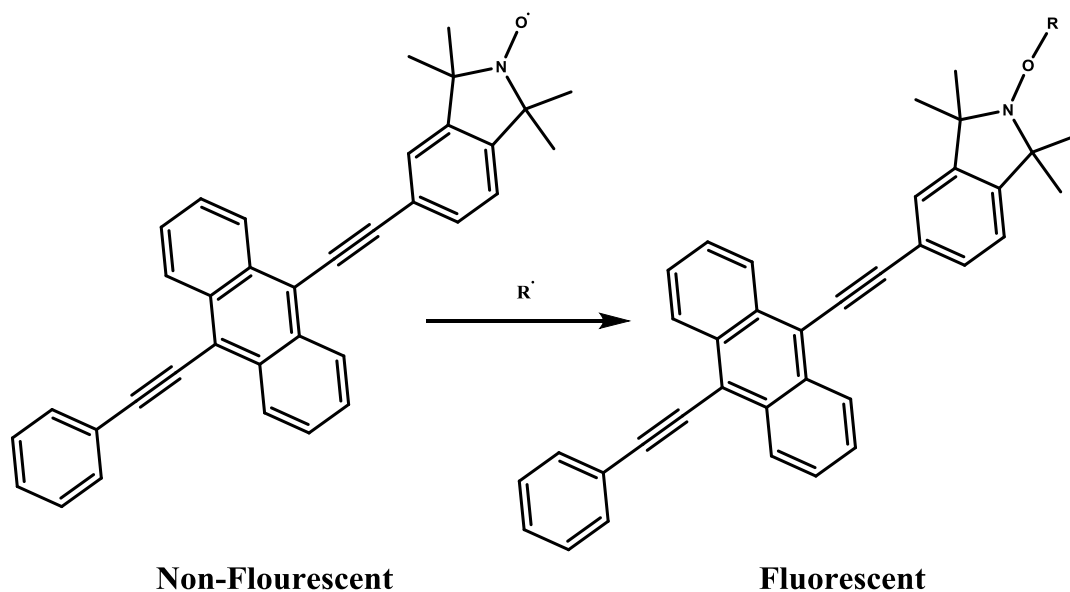


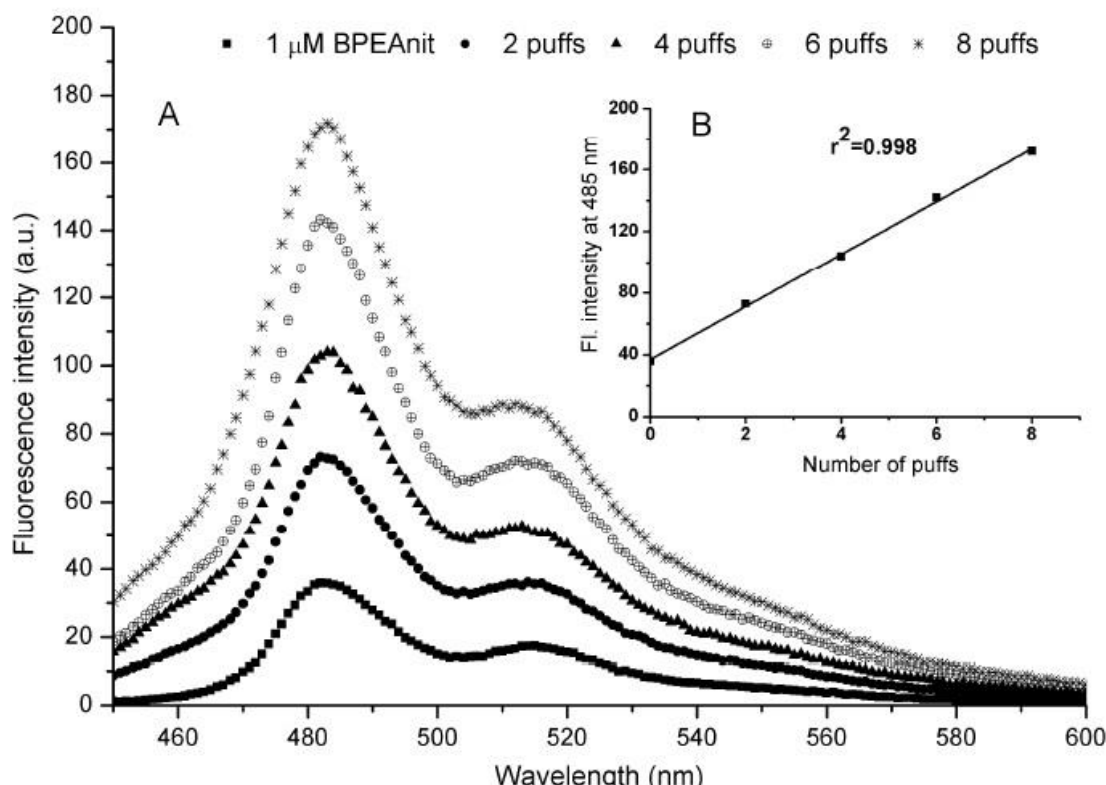
**Figure 1.14** – BPEA reaction with a radical species,  $R^\bullet$ . The radical reacts directly with the oxygen-centred radical on BPEA to produce a non-radical spin trap-radical adduct. BPEA is particularly sensitive to carbon-centred and sulphur-centred radicals, and particularly insensitive to oxygen-centred radicals due to the instability of the N-O-O-R bond formed.

BPEA is a profluorescent spin trap containing a nitroxide ( $N-O^\bullet$ ) functional group bound to a large conjugated fluorophore. The paramagnetic nature of the unpaired electron substantially suppresses the fluorescent properties of the aromatic fluorophore, so BPEA itself is relatively non-fluorescent.

The mechanisms of this suppression are not entirely clear, however it is hypothesised that exchange induced relaxation processes (intersystem crossing and internal conversion)<sup>125</sup>, electron transfer<sup>126</sup> or other energy exchange mechanisms<sup>84</sup> could lead to fluorophore suppression by the unpaired electron on  $N-O^\bullet$ . As depicted in Figure 1.14, the  $N-O^\bullet$  group reacts with a radical species,  $R^\bullet$  *via* a radical termination step to form  $N-O-R$ . The formation of the  $N-O-R$  bond, and therefore the quenching of the unpaired electron, results in a highly fluorescent molecule BPEA-R. The highly fluorescent spin trap is excited at  $\lambda_{\text{excitation}} = 430 \text{ nm}$  and has strong peak emissions at  $\lambda_{\text{emission}} = 485 \text{ nm}, 510 \text{ nm}$ .

Therefore, this spin trap can probe radical concentrations using this fluorescent response and due to the 1:1 BPEA-Radical reaction stoichiometry. BPEA has a particularly strong affinity towards carbon-centred and sulphur-centred radicals. When dissolved in DMSO, it is capable of detecting peroxy and hydroxyl radicals.<sup>97</sup> It is known that oxygen and carbon centred radicals can react with DMSO to in turn produce either sulfur centred

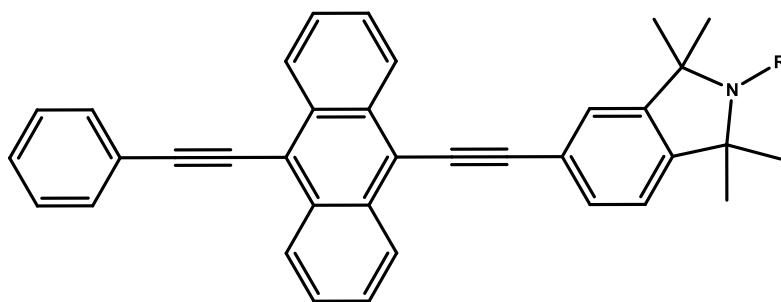
(sulfoxyl) or carbon centred (methyl) radicals, which can be subsequently scavenged by BPEA.



**Figure 1.15** - Fluorescence intensity measurements of BPEA exposed to increasing concentrations (“puffs”) of cigarette smoke. A linear increase in fluorescence intensity is observed as the puffs of cigarette smoke, and therefore combustion generated ROS, are increased. Figure Reproduced from Miljevic *et al.*<sup>95</sup>

This method, dissolving BPEA in DMSO before sampling, has been used to probe the concentration of particle bound radicals from a number of sources. One particular study by Miljevic *et al.*<sup>95</sup>, which sought to probe the particle-bound radical load from cigarette smoke, illustrates the quantitative potential of the BPEA/DMSO assay.

Figure 1.15 demonstrates a linear increase in the fluorescence intensity observed upon increasing “puffs” of cigarette smoke sampled into an impinger containing BPEA/DMSO. This study established that introducing increasing concentrations of PM into the BPEA/DMSO assay leads to an increased fluorescence response, and with an appropriate calibration standard, could allow one to quantify the concentration of radicals in PM.

1: R = O $\cdot$ 

4: R = H

2: R = OH

5: R = S(=O)-CH<sub>3</sub>3: R = S(=O)<sub>2</sub>-CH<sub>3</sub>6: R = OCH<sub>3</sub>

**Figure 1.16** – Products identified which are believed to be responsible for the observed fluorescent response of the BPEA/DMSO assay using HPLC-ESI-HRMS, NMR and IR.<sup>84</sup>

A follow up study by Stevanovic et al.<sup>84</sup> aimed to probe the reaction mechanisms associated with the observed fluorescent response of the BPEA/DMSO assay, as well as determine the dominant products responsible for the fluorescent response. Using a combination of high performance liquid chromatography electrospray ionisation high-resolution mass spectrometry (HPLC-ESI-HRMS), nuclear magnetic resonance spectroscopy (NMR), and infrared spectroscopy (IR), they identified several products responsible for the fluorescent response, summarised in Figure 1.16.

It was found that methanesulfonamide **3** (Figure 1.14), formed from the reaction of a sulfoxyl radical with subsequent internal re-arrangement, was the dominant product formed which subsequently leads to a fluorescent response upon exposure of the assay to PM. A tentative reaction mechanism leading to the formation of methanesulfonamide **3** was derived from the information from this study, and is illustrated in Figure 1.17. The postulated mechanism proceeds through the nitroxide probe scavenging a sulfoxyl radical (**5**). After this formation, the N-O bond of (**5**) cleaves, generating a nitrogen-centred radical coupled to the aromatic fluorophore, and sulfoxide radical respectively. These two radical species then react *via* a radical termination step, to produce methanesulfonamide **3**.

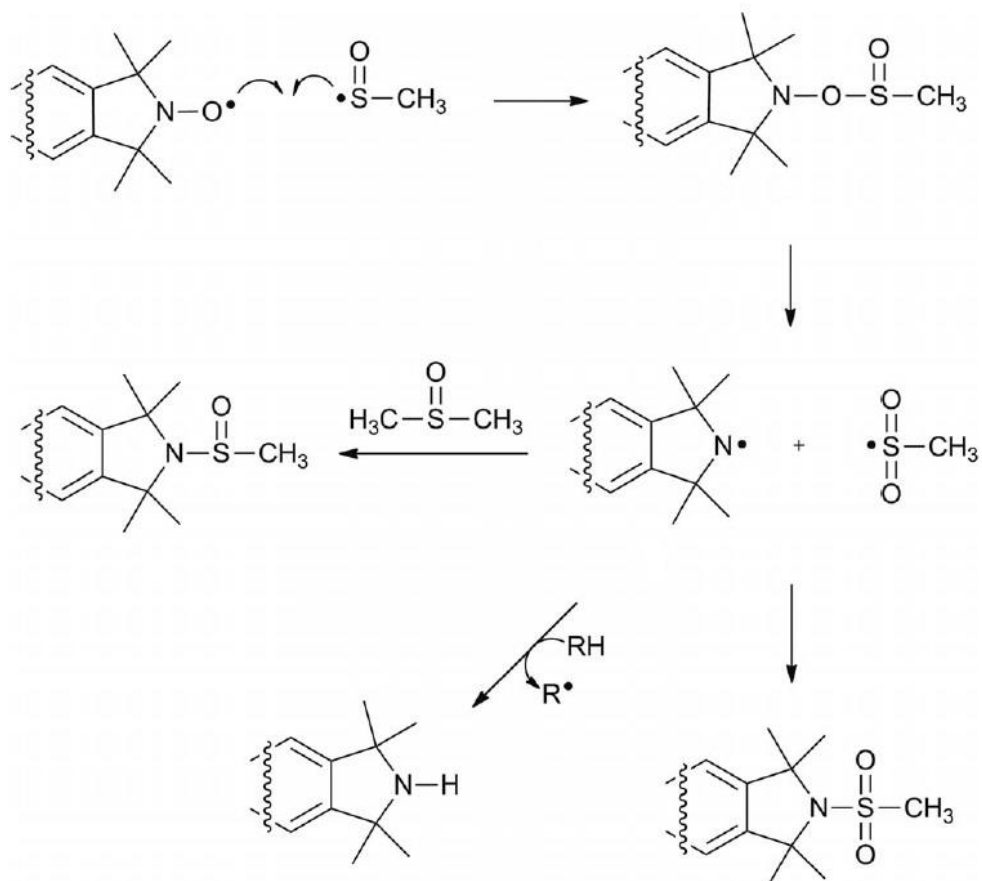


**Figure 1.17** - Reaction scheme showing the formation of methanesulfonamide **3**. Initially, the nitroxide radical scavenges a sulfoxyl radical (**5**). After this formation, the N-O bond cleaves, generating a nitrogen-centred radical and sulfoxide radical respectively. These two radical species then react via a radical termination step, to produce methanesulfonamide **3**. The nitrogen-centred radical can also deprotonate any adjacent organic molecules to produce amine **4**, or product **5** via reaction with another DMSO molecule. This process also generates another radical species,  $R^\bullet$ . Scheme adapted from Stevanovic *et al.*<sup>84</sup>.

The nitrogen-centred radical can also deprotonate any adjacent organic molecules (RH) to produce amine **4**, or produce **5** via reaction with another DMSO molecule. This process also generates another radical species,  $R^\bullet$ . Furthermore, DMSO is known to interact with  $\cdot\text{OH}$  and other oxygen-centred radicals to produce methyl radicals ( $\cdot\text{CH}_3$ ) and sulfoxyl radicals ( $\cdot\text{S}(=\text{O})\text{-CH}_3$ ).<sup>127</sup>

Although the mechanisms of formation of fluorescent products in the BPEA/DMPO assay are at present not entirely clear, these studies have demonstrated that this assay is capable of quantifying particle-bound radicals generated from a series of combustion processes. Therefore, in principle this technique could be applied to probe particle-bound radicals in

atmospherically relevant aerosol, including SOA generated from the oxidation of alkenes. The BPEA/DMSO assay demonstrates a large response to combustion generated PM, although radical concentrations generated in pyrolysis are likely to be higher than those expected for typical ozone-alkene reactions. The BPEA/DMSO assay is used in this work to probe radical concentrations in SOA generated from the ozonolysis of a variety of VOCs, as described in Chapter 5.

## 1.4 Analytical Methods

This section will discuss the underlying principles of the instrumentation and analytical techniques used in this thesis to characterise the size and composition of organic aerosol, measure the concentration of species in the gas and solution phase and probe the concentration of chemical species of interest.

### 1.4.1 Overview of Mass Spectrometry

Mass spectrometry has been widely applied to characterise the composition of organic aerosol.<sup>19,20,94,100,128,129</sup> This technique is particularly advantageous in this application due to its high sensitivity and ability to identify multiple compounds in complex organic mixtures. There are multiple mass spectrometer designs with a wide range of applications. Mass spectrometers measure the mass-to-charge ratio ( $m/z$ ), and mass spectrometers used to measure organic composition of aerosol are typically composed of:

- An ion source, which generates ions from neutral analyte molecules and introduces them into the gas phase.
- A mass analyser, which separates the ions based on their mass-to-charge ratio, typically using an electric or magnetic field.
- A detector, which converts the information taken from the mass analyser (current, for example) and converts it into an intensity for each compound with a unique  $m/z$ .

The performance of various mass spectrometers depends on the performance of the ion source, resolution, mass accuracy of the mass spectrometer, ion transmission and detector sensitivity. In order to probe the composition of organic aerosol, which can contain many thousands of individual organic compounds, mass spectrometers require a high resolution to detect individual compounds. In the following, aspects of mass spectrometry, which were applied in this study, are discussed in more detail.

---

## Electrospray Ionisation sources

There are many types of ionisation sources used to study the composition of organic aerosol; one applied in this research is electrospray ionisation (ESI). ESI is said to be a “soft” ionisation technique, in that there is limited fragmentation of the compounds being introduced into the mass spectrometer.<sup>128</sup> This is advantageous when considering the analysis of complex organic aerosol samples; “hard” ionisation sources such as electron ionisation or laser-desorption ionisation sources involve high-energy processes, and readily fragment organics.

Despite the fact that this can produce fragments that are characteristic of certain molecular structures or functionalities, it provides limited molecular information. Indeed, the complexity associated with organic aerosol samples is great, and extensive fragmentation would further complicate analysis. One potential drawback of ESI is a lower efficiency of ionisation, which means that it can be problematic to detect trace amounts of a particular compound of interest. ESI can often exhibit compound-specific ionisation efficiencies, which may make quantification problematic when no suitable calibration standards are available.

Figure 1.18 illustrates the droplet formation and physical principles behind the operation of an ESI source (Gaskell *et al.*<sup>130</sup>). The solution containing the sample analyte is introduced into a narrow diameter capillary tube. A positive or negative potential difference is then generated at the tip of the capillary, with an applied voltage of typically 3-5 kV. Assuming positive potential, positive ions will accumulate at the surface, which is then drawn to form a so-called “Taylor cone”.

At high enough potential, the cone is drawn to a filament *via* a “budding” process when the surface tension is exceeded by the applied electrostatic force. Evaporation of solvent from the initially formed droplets, as they travel across a pressure gradient towards the analyser of the mass spectrometer, leads to a reduction in the diameter of the droplets, with collisional warming stopping the freezing of the droplets. Coulomb explosions will occur at the point at which the magnitude of the charge is sufficient to overcome the surface tension of the droplet, and charge transfer occurs from the solvent to the analyte. The analyte ions are then introduced to the mass analyser, and the  $m/z$  determined for each species.



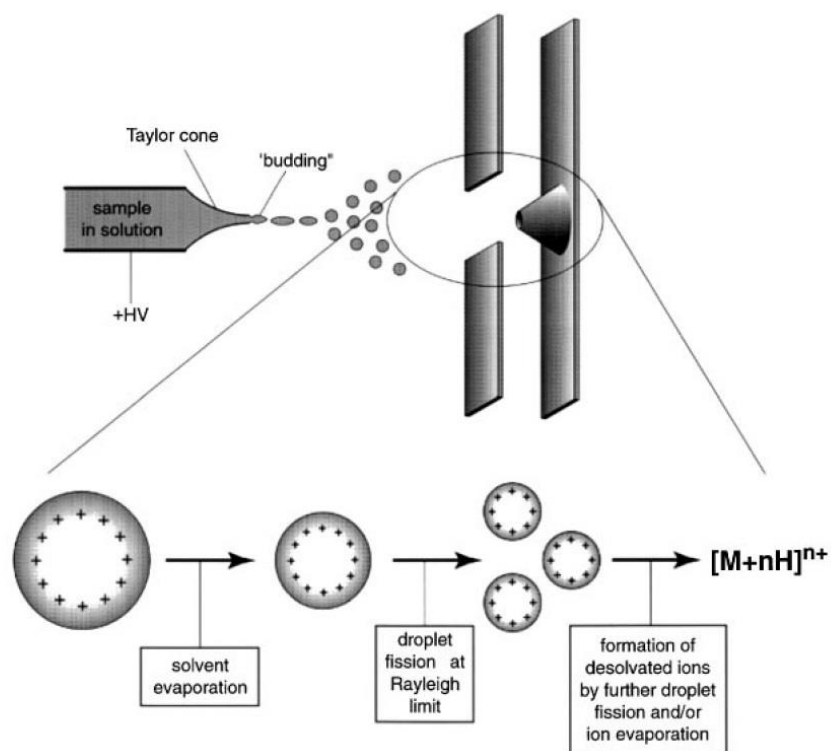


**Figure 1.18** – Principle operation and droplet and ion formation from an ESI source. Reproduced from Gaskell *et al.*<sup>130</sup>

ESI can be operated in either positive or negative mode, depending on the species of interest.<sup>131</sup> Depending on the potential applied at the tip of the capillary, either positively charged, protonated  $[M+H]^+$  or negatively charged, mainly de-protonated  $[M-H]^-$  ions will be formed. The mode in which ESI is run depends on the compounds of interest. Negative mode ionisation requires species with a sufficiently acidic proton to be lost; otherwise, they will not be detected by the mass analyser. In the positive mode, organics can form adducts with cations present in solution such as sodium  $[M+Na]^+$ , ammonium  $[M+NH_4]^+$  and potassium  $[M+K]^+$  which may also be detected at the mass analyser.<sup>130</sup> The formation of  $Na^+$  and  $K^+$  adducts with species is often unavoidable, as trace concentrations in typical solvents are often sufficient enough that these species can compete with  $H^+$  with regards to analyte ionisation.

ESI-MS has been widely applied to probe organic aerosol composition of species collected in a filter from the field improving our understanding of the composition of biogenic SOA. ESI-MS has also been coupled to high performance liquid chromatography (HPLC) which provides quantitative information on species of interest, as well as qualitative assignment.

Of late, ESI has been further developed; an extractive ESI was developed by Gallimore et al.<sup>100</sup> where aerosol can be sampled on-line by colliding an aerosol sample flow with charged solvent droplets. On-line in this context refers to the analyte being constantly introduced into the mass spectrometer using an extractive ESI, which can directly sample aerosol from smog chamber studies into the mass spectrometer. This has shown great potential for probing the evolution of organic species over time in smog chamber studies.<sup>94</sup> An alternative ESI source, Nano-ESI, provides substantially improved sensitivity as well as reduced interference from inorganic salts.<sup>132</sup>

### High resolution Mass Spectrometry

One such high-resolution mass spectrometer applied in this thesis is the Orbitrap (Thermo Scientific, Waltham, MA, USA), an example of a Fourier-transform high resolution mass spectrometer.

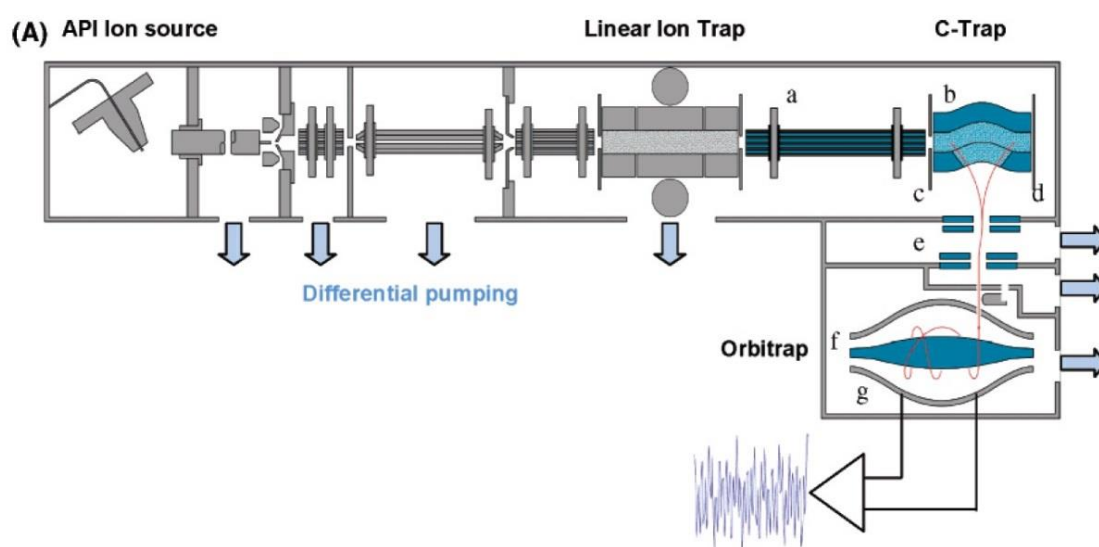


**Figure 1.19** - The hybrid Velos Orbitrap mass spectrometer (Thermo Scientific) combines a linear ion trap mass spectrometer with an ultra-high resolution Orbitrap mass spectrometer. The Orbitrap measures ion mass by measuring harmonic oscillations along a central electrode as the ions orbit the electrode in the Orbitrap. The linear ion trap can be used to conduct MS/MS analysis of individual ions. Image reproduced from Makarov *et al.*<sup>133</sup>

This is part of a hybrid set-up with an LTQ Velos linear ion trap as depicted in Figure 1.19. The linear ion trap can be used to fragment selected ions and help to identify their structure. The Orbitrap contains a cylindrical ion trap with a central electrode. Ions are injected into the cylindrical ion trap and briefly orbit around the central electrode. As the ions orbit around the central electrode, the shape of the electrode causes them to oscillate

along the length of the electrode, with a frequency that is dependent on the ion mass. Therefore, different ions have different oscillation frequencies. It is the frequency of these axial oscillations, which is measured by recording an image current at the detector plate surrounding the central Orbitrap electrode. This axial frequency is independent of the energy and spatial spread of the ions.<sup>134</sup> Ion frequencies are measured non-destructively by acquisition of time-domain image current transients, with subsequent fast Fourier transforms being used to obtain the mass spectra.

With regards to measurements of organic aerosol, Orbitrap MS has a much higher resolving power (>100 000) and is at least an order of magnitude higher than other conventional mass spectrometers, which typically have a resolution of 5 000 – 20 000.<sup>129</sup> Resolving power is defined as the ability of the mass spectrometer to separate two ion peaks:

$$R = \frac{M}{\Delta M} \quad (1.4)$$

Where R is the resolving power, M is the mass of the second peak with respect to the peak of interest, and  $\Delta M$  is the minimum peak separation, which allows one to distinguish between two ion peaks. Resolving power is particularly important when dealing with complex mixtures such as organic aerosol, as it allows the separation of peaks that have very similar masses, as illustrated in Figure 1.20. The mass accuracy can be determined using Equation 1.5, where the accuracy is expressed in parts per million (ppm):

$$\text{Mass Accuracy} = \frac{(1 \times 10^6) \cdot (\text{Measured Mass} - \text{Theoretical mass})}{\text{Theoretical Mass}} \quad (1.5)$$

If the mass accuracy is sufficiently high, it allows the unambiguous assignment of elemental formulae to ions present in the mass spectra. The Orbitrap's mass accuracy was determined before each experimental procedure, and was found to range from as low as 0.2 ppm to 1.5 ppm. This low mass accuracy error allows one to unambiguously assign

elemental formulae in mass spectra, and identify individual compounds in complex organic mixtures.

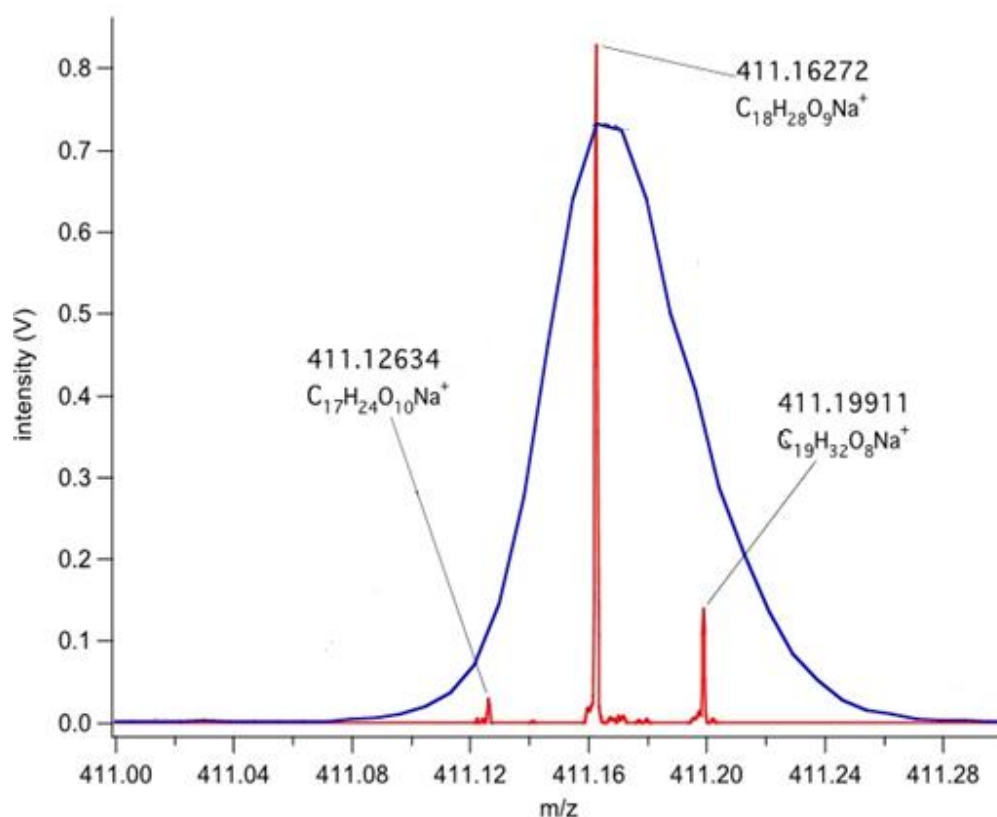


**Figure 1.20** - Comparison of a quadrupole time-of-flight mass spectrometer (blue) and a high-resolution Fourier-transform ion cyclotron mass spectrometer, (red) comparison for  $\alpha$ -pinene SOA in the mass range 411.00-411.30. The quadrupole mass spectrometer with a resolution of 5000 measures the  $m/z$  at 411.16 and it appears to be due to one compound. The higher resolving power of the cyclotron mass spectrometer (400 000) reveals that actually 3 individual peaks from 3 individual compounds occupy this region that can't be distinguished by the Q-TOF. Figure reproduced from Reinhardt *et al.*<sup>135</sup>

### Proton Transfer Reaction Time-of-Flight Mass Spectrometry

Proton transfer reaction mass spectrometry (PTR-MS) is an analytical technique that allows the study of multiple organic compounds in the gas phase using “soft” ionisation.<sup>136</sup> Scientists in Innsbruck initially developed this instrument by combining a PTR drift tube with a quadrupole mass spectrometer, which allows the fast detection of volatile organic compounds.<sup>137,138</sup> There are several PTR instruments available, but one widely used in this thesis is the proton transfer time-of-flight mass spectrometer (PTR-ToF-MS 8000, Ionicon Analytik, Innsbruck, Austria), illustrated in Figure 1.21.

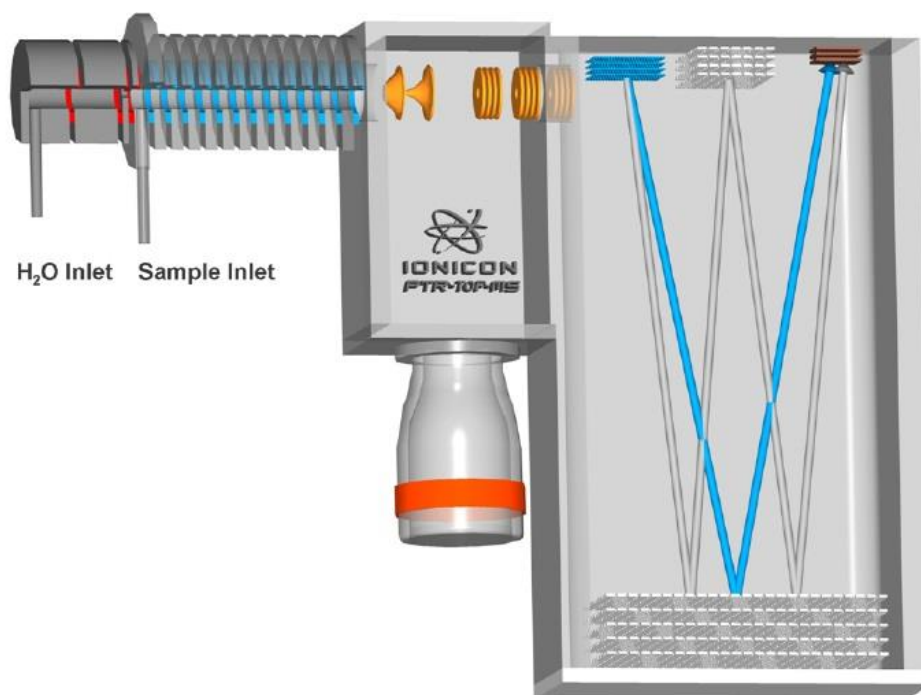


**Figure 1.21** – Schematic representation of the PTR-ToF-MS (8000, Ionicon Analytik, Innsbruck, Austria). The instrument is broadly composed of three main parts: An ion source where  $\text{H}_3\text{O}^+$  is produced at high purity. A PTR drift tube, where continuously sampled gas phase VOCs undergo mostly non-dissociative (with respect to other ESI, etc..) proton transfer and an mass analysing system where species are separated according to their  $m/z$  ratio. Figure reproduced from the instrument manual.

The PTR-ToF-MS is broadly composed of three sections:

- **Ion source:** Produces  $\text{H}_3\text{O}^+$  ions at high purity level (up to 98%) from water vapour *via* hollow cathode discharge.
- **PTR drift tube:** The continuously introduced sample gas containing VOCs undergoes mostly non-dissociative proton transfer from  $\text{H}_3\text{O}^+$  ions, which are injected into the drift tube *via* a Venturi-type inlet (typical operating pressure  $\sim 2.22$  mbar).
- **Analysing system:** A high-resolution time-of-flight mass spectrometer separates the ions according to their mass to charge  $m/z$  ratio. The resolution of 5000 is sufficient to distinguish between isobaric molecules at low molecular masses and makes unambiguous identification possible.

This design allows the simultaneous on-line monitoring of volatile organics at concentrations down to  $< 1$  pptv in ambient air. Using  $\text{H}_3\text{O}^+$  as an ionisation source is advantageous; it offers very efficient ionisation of most VOCs which have proton affinity rate coefficients on the order of  $\sim 2 \times 10^{-9}$  molecules  $\text{cm}^3 \text{s}^{-1}$ , close to the gas phase kinetic

---

limit, offering a very broad ionisation technique.<sup>137</sup> Since proton transfer is a soft method, fragmentation is kept relatively low compared to other conventional ionisation techniques such as electron impact ionisation.

The  $\text{H}_3\text{O}^+$  generation and reaction conditions are strictly controlled in the system, allowing for the calculation of gas phase VOC concentrations using the  $\text{H}_3\text{O}^+$  concentrations, negating the need for gas phase standards to obtain concentration estimates.<sup>137</sup> Furthermore,  $\text{H}_3\text{O}^+$  does not react with any of the major components of clean air due to their low proton affinity, allowing the PTR-ToF-MS to be selective to trace gases present in ambient air.

### 1.4.2 Scanning mobility particle sizer

There are multiple instrumental techniques capable of determining the size and number concentration of airborne particles, but the one used routinely in this thesis is a Scanning Mobility Particle Sizer (SMPS, TSI, St. Paul, MN, USA). The SMPS allows the on-line and *in situ* measurement of the size and number of particles in a gas. The SMPS uses the electrical mobility of particles to select them as a function of their size (Knutson *et al.*<sup>139</sup>), and the model used in this thesis is comprised of three major components:

- A model 3087 advanced aerosol neutraliser (TSI), which forms a well-defined charge distribution across a sample of particles in a gas.
- A model 3081 differential mobility analyser (DMA) (TSI), which sizes particles based on their mobility diameter
- A model 3776 ultrafine condensation particle counter (CPC) (TSI), which counts the number of particles of a given size selected by the DMA.

Particles are first introduced into the neutraliser where they undergo a large number of collisions from charged carrier gas molecules. This imposes an equilibrium charge distribution across the particles. The charge distribution across the particles can then be determined by a numerical method developed by Wiedensohler.<sup>140</sup> Neutralisers typically ionise air by using an X-ray source or a radioactive source (e.g. Kr-85 or Am-241). Figure 1.22 illustrates the construct of the DMA. A central cylindrical electrode that is connected to a negatively charged power supply (0 – 10 000 V DC) provides a precise negative potential. Particles with a negative charge are repelled towards and deposited on the outer wall of the DMA, neutral particles exit the DMA with excess sheath flow air, and

positively charged particles are attracted towards the central electrode and one particular size is extracted at the monodisperse aerosol outlet.

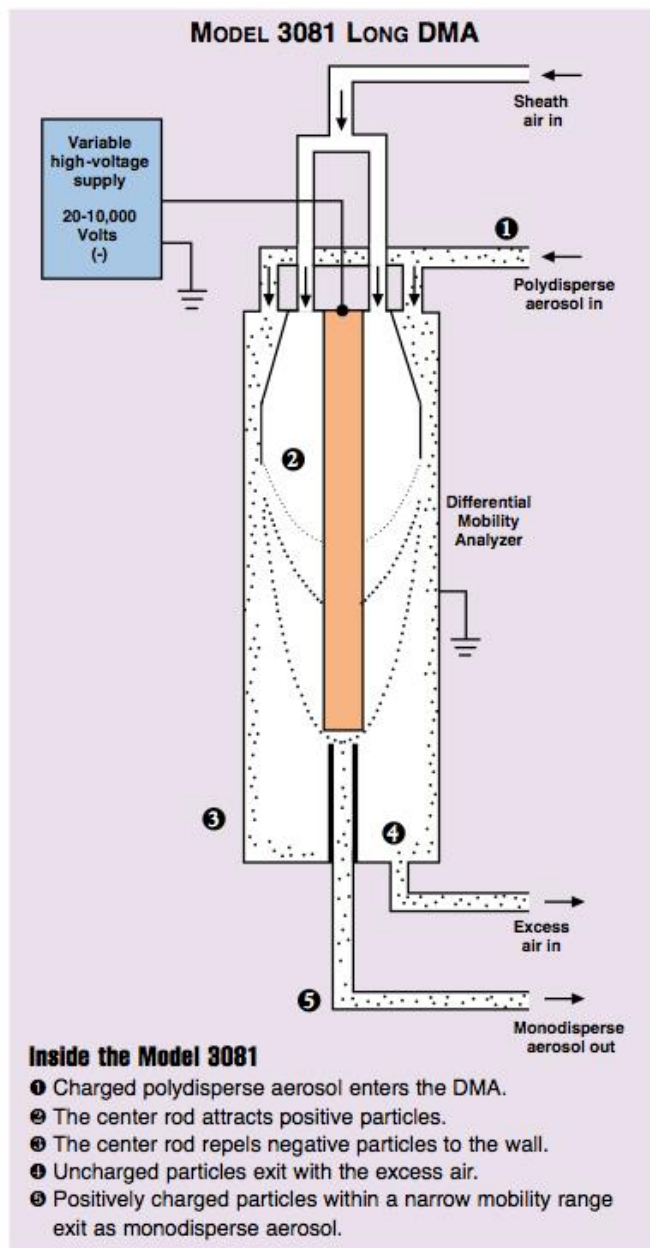


**Figure 1.22** - Schematic of the model 3081 differential mobility analyser (DMA). Reproduced from the TSI SMPS instrument manual.

Varying the voltage applied to the inner electrode alters the particle extracted at the monodisperse outlet, and thus by varying the voltage from low to high, particles from small to larger diameters can be sequentially extracted, allowing one to construct an aerosol size distribution. This particular model of DMA allows selection of particles with a diameter range of 10 – 1000 nm in diameter.

Upon selection of a uniform (monodisperse) particle diameter by the DMA, aerosol is passed through into the condensation particle counter (CPC). In this instrument, the selected particles are drawn through a heated saturator where butan-1-ol is evaporated and diffuses into the sample stream. The aerosol and alcohol vapour then both pass through a cooled condenser, where the alcohol vapour becomes super saturated, whereupon the aerosol act as condensation nuclei, with the aerosol particles growing as the butan-1-ol condenses onto them.

The activated particles then pass through an optical counter. The SMPS therefore generates particle number as a function of diameter as the DMA voltage is ramped, as the CPC determines the amount of particles passing through for each size bin. The mass concentration ( $\mu\text{g m}^{-3}$ ) of the aerosol particles generated can also be calculated by the software associated with the SMPS, assuming spherical particles and uniform particle density. (Aerosol Instrument Manager, TSI).

### 1.4.3 Fluorescence Spectroscopy

Fluorescence spectroscopy is a detection technique applied in this work, and the physical principles behind this technique will be described in brief here. Fluorescence involves the excitation of a molecule in its ground electronic state *via* absorption of a photon of light at a specific wavelength.

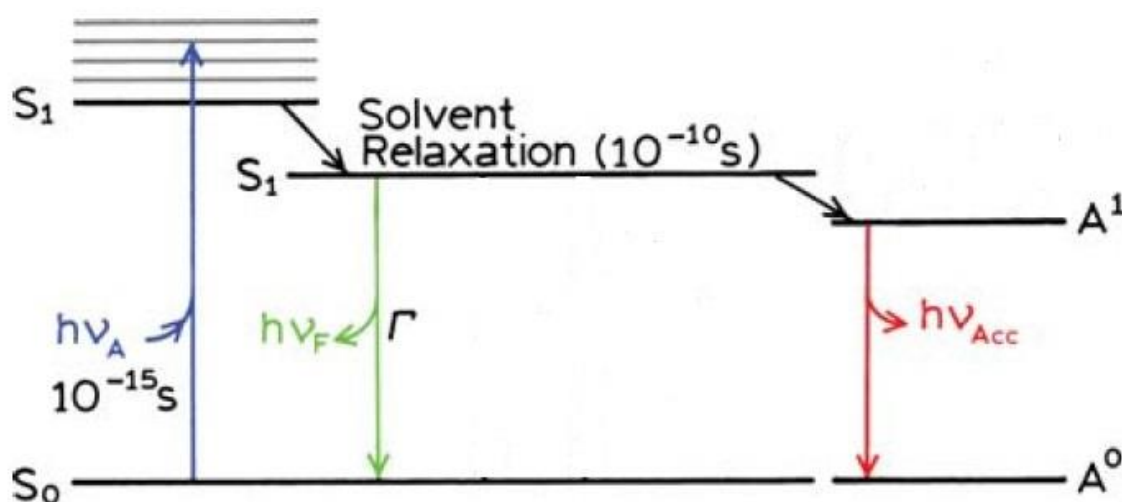


**Figure 1.23** – Jablonski diagram with collisional quenching via solvent relaxation and fluorescent resonance energy transfer, which leads to the emission of a photon at a different wavelength of that of the absorbed photon. The diagram represents a transition from the ground electronic state ( $S_0$ ) to a higher energy state ( $S_1$ ). Light grey lines represent accessible vibrational states. Figure reproduced from Principles of Fluorescence Spectroscopy (2006).<sup>141</sup>



This excited state molecule can then decay back to its ground state configuration, but in doing so, it spontaneously emits a photon. The physical processes occurring during fluorescence are often displayed in a typical Jablonski diagram, as illustrated in Figure 1.23. Examination of Figure 1.23 reveals that the energy of emission is typically less than that of absorption. Fluorescence typically occurs at a lower energy or longer wavelength than the excitation. The singlet ground, first and second electronic states are depicted by  $S_0$ ,  $S_1$  and  $S_2$  respectively. At each of these electronic energy levels, the fluorophores can exist in a number of vibrationally excited energy levels, depicted by the grey lines in Figure 1.23.

The transitions between different states are depicted by vertical lines to illustrate the instantaneous mechanism of light absorption. Following light absorption, several processes can then occur. Usually, in the condensed and liquid phase, there is rapid relaxation of the molecule to the ground vibrational state in the  $S_1$  electronic state. The timescale of this ( $\sim 10^{-12}$  s) is much more rapid than that typical of fluorescence ( $10^{-8}$  s), and therefore fluorescence emission generally occurs from the ground vibrational state of the  $S_1$  electronic state.

According to the Frank-Condon principle, re-distribution of electron density upon an electronic transition from  $S_0$  to  $S_1$  can subsequently lead to an unfavourable orientation. The system then relaxes from this state to a lower energy state, in a process known as solvent relaxation. The timescale of this relaxation is often faster than that of electronic relaxation from  $S_1$  to  $S_0$  which results in the emission of a photon. Therefore, the energy of the photon emitted is often lower than that of the absorbed photon, leading to a shift in wavelength.

The difference in wavelength between the incident absorbed photon and emitted photon is known as the Stokes shift. Energy losses between excitation and emission are observed universally for fluorescent molecules in solution. One common cause of the Stokes shift is the rapid decay to the lowest vibrational energy state in  $S_1$ , followed by relaxation back to the  $S_0$  electronic energy level (Figure 1.23). Further to this, fluorophores can display further Stokes shifts due to solvent effects, excited-state reactions complex formation and/or energy transfer.<sup>141</sup> An illustration of the Stokes shift, using fluorescein and DFC excitation and emission as an example, is displayed in Figure 1.24.

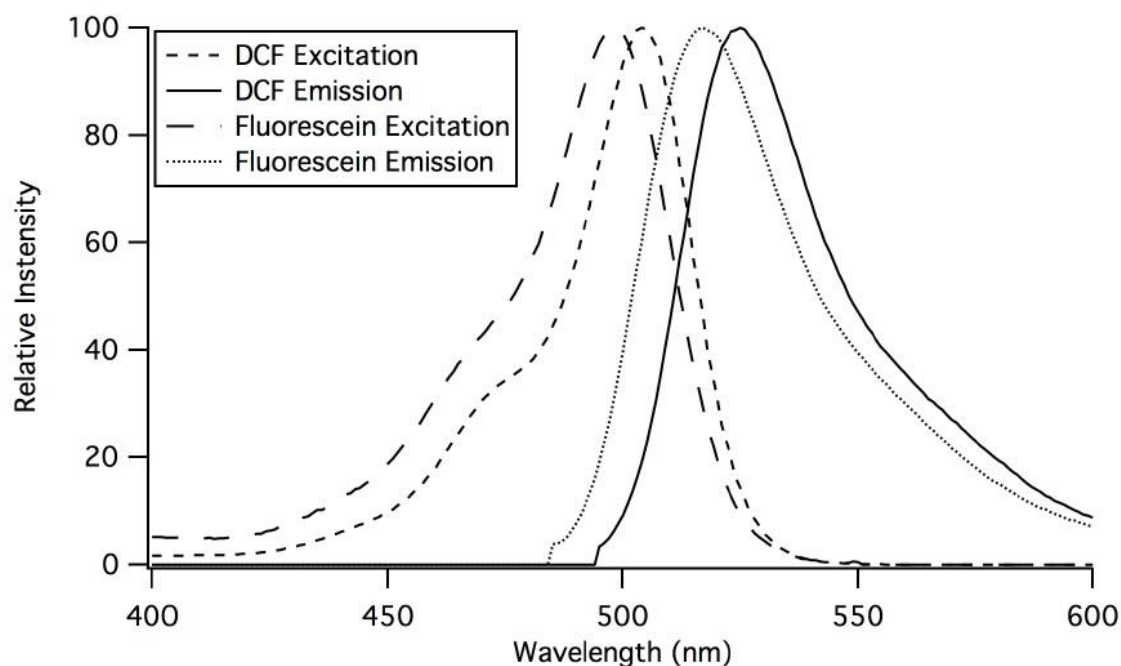


**Figure 1.24** – Excitation and emission spectra for fluorescein and DCF at pH 7.2. The Stokes shift, the difference in wavelength between incident photons and emitted photons, is indicated for both fluorescein and DCF. Reproduced from Fuller (2013).<sup>142</sup>

At low concentrations, the intensity of the emission spectra is proportional to the concentration of the fluorescent molecule in solution. This phenomenon can be exploited to probe the concentration of certain species using a fluorescent dye, or a reaction leading to a fluorescent product, and quantify a particular species of interest. However, at elevated concentrations of the fluorescent molecule in solution, self-absorption and quenching phenomena may become significant, leading to the decay of a species from the excited state to the ground state without emission of a photon, complicating quantification. The fluorescent measurement is typically at 90° to the incident beam of light, to reduce interference from transmitted or reflected incident light.

## 1.5 Chapter Summary

This chapter has outlined some of the key open questions motivating the work presented in this thesis. The physical and chemical principles involved in the formation of secondary organic aerosol has been discussed, as well as the analytical techniques currently available to measure reactive intermediate species such as Criegee Intermediates. The evidence for adverse human health effects upon exposure to PM was summarised, as well as the physical and chemical properties of PM that are of particular interest from a health

perspective. Finally, the analytical methods and operational principles of instruments applied routinely in this thesis were detailed.

## **1.6 Thesis Structure and Outline**

The fundamental aims of this research will be summarised in Chapter 2. Results from this work are discussed in Chapters 3-6. Each chapter is written in the form of a manuscript, which either have been published in the literature or are currently in preparation for submission to journals. Chapter 3 comprises of two manuscripts, which have been published in the literature. Each Chapter begins with an explicit outline of any collaborators or contributors to the work within this thesis.

The conclusions in Chapter 7 will integrate and contextualise the key results and conclusions in this thesis. The major outcomes of the research presented, as well as key questions approached and open questions remaining, will be contextualised. Furthermore, suggestions of key steps for future improvement and development are also discussed.

---

## 2 AIMS OF THIS THESIS

Large uncertainties remain regarding the chemical pathways and mechanisms leading to the production of organic compounds in aerosol, as well as the impact these organic species have on both aerosol ageing and observed adverse health human health effects upon organic aerosol exposure. One defining feature is the need to understand reactive intermediates in the gas phase and in organic aerosol; these species have a significant impact on the stable product distribution, which affects organic aerosol composition and therefore their potential implications for health-relevant studies upon uptake into the lung. Current analytical techniques struggle to characterise and quantify many of these organic reactive intermediates, making it difficult to assess the effect of these reactive intermediates on organic compound oxidation and aerosol formation.

Therefore, there remains a requirement for new and innovative chemical and analytical techniques capable of qualitatively and quantitatively describing these species in organic aerosol. The work in this thesis describes the development and application of four such chemical assays, all of which are capable of probing various reactive intermediates, which all have potentially crucial impacts on various aspects of tropospheric chemistry. The aims of each individual assay are broadly summarised below:

### **Chapter 3: Online Quantification of Criegee Intermediates in the Gas Phase**

- Develop a novel, laboratory-based technique capable of characterising and quantifying Criegee intermediates produced from the ozonolysis of VOCs.
- Apply said method to various VOC ozonolysis regimes, to simultaneously characterise multiple CIs generated from the ozonolysis of atmospherically relevant VOCs.

### **Chapter 4: Novel Method to Measure Criegee Intermediates in the Particle Phase**

- Develop a novel technique uniquely capable of characterising low-volatility, particle-bound Criegee intermediates generated from the ozonolysis of atmospherically relevant VOCs in the particle phase.

- 
- Apply this method to estimate, for the first time, the concentrations of particle-bound CIs in secondary organic aerosol.

### **Chapter 5: Novel Method to Quantify Radicals in Organic Aerosol**

- Develop a fluorescent assay uniquely capable of quantifying organic radical species in secondary organic aerosol
- Determine the sensitivity of this assay towards particle-bound radicals generated from the ozonolysis of a variety of atmospherically relevant VOCs, and determine the quantitative potential of the technique.

### **Chapter 6: Development of an On-line Chemical Assay to Measure Particle-bound ROS**

- Develop a novel on-line assay capable of quantifying physiologically relevant particle-bound reactive oxygen species
- Optimise the chemistry in this assay, and generate a series of calibration curves to assess the assay's sensitivity to common transition metals found in ambient aerosol.
- Determine the assay's sensitivity towards both organic aerosol and a mixture of iron/organic aerosol, and compare the assay's sensitivity to both metals and aerosol with concentrations typically observed in the field, in order to assess the prototype instruments potential applicability to field studies.

# 3 ONLINE QUANTIFICATION OF CRIEGEE INTERMEDIATES IN THE GAS PHASE

---

**This manuscript is based on work in the following publications:**

**Chiara Giorio, Steven J. Campbell, Maurizio Bruschi, Francesco Tampieri, Antonio Barbon, Antonio Toffoletti, Andrea Tapparo, Peter Grice, Duncan J. Howe, and Markus Kalberer** *J. Am. Chem. Soc.*, 2017, *139* (11), pp 3999–4008

**Chiara Giorio, Steven J. Campbell, Maurizio Bruschi, Alexander T. Archibald and Markus Kalberer** *Faraday Discuss*, 2017 *Advance Article* DOI: 10.1039/C7FD00025A. Presented at Faraday Discussions by Steven J. Campbell.

## **Author Contributions**

Steven J. Campbell wrote this manuscript except for Section 3.3.4 (p. 90-92), where the MCM model calculations were performed and discussed by Chiara Giorio, with additional analysis from Alexander T. Archibald. Chiara Giorio designed the initial experimental set-up, and conducted the ESI-HRMS analysis in Section 3.3.1 (Figure 3.2 and Figure 3.3). Steven J. Campbell performed further optimisations of the gas phase set-up. Francesco Tampieri, Antonio Barbon, Antonio Toffoletti and Andrea Tapparo conducted the EPR analysis in Section 3.3.1 (Figure 3.4). Maurizio Bruschi performed the DFT calculations discussed in Section 3.3.2 and 3.3.3 (largely displayed in Appendix 2), and was analysed and interpreted by Chiara Giorio and Steven J. Campbell. Peter Grice and Duncan J. Howe performed the NMR analysis and aided in interpretation of this data. Steven J. Campbell conducted all other experiments in this manuscript.

---

### 3.1 Introduction

One of the key processes governing tropospheric chemistry and composition is the oxidation of biogenic and anthropogenic VOCs by a number of oxidants including hydroxyl radicals ( $\cdot\text{OH}$ ), ozone ( $\text{O}_3$ ) and nitrate radicals ( $\cdot\text{NO}_3$ )<sup>143</sup>. One crucial oxidation reaction involves the ozonolysis of alkenes, which contributes to photochemical smog, visibility issues and global climate change.<sup>144</sup> The mechanisms of this reaction, postulated for the first time by Rudolf Criegee<sup>35</sup> and described in detail in Section 1.5.1, proceeds *via* the 1-3 cycloaddition of ozone across an olefinic bond to produce a primary ozonide, which promptly decomposes to form a carbonyl compound, and a short-lived carbonyl oxide often called the Criegee Intermediate (CI). This reactive intermediate can be construed as biradical or zwitterionic in character, as the CI can adopt multiple resonance structures.<sup>4-7</sup>

The reaction pathways that CIs follow, after their formation from ozonolysis and subsequent collisional stabilisation, play a pivotal role in determining the composition of the troposphere. CI chemistry represents one of the largest uncertainties in tropospheric chemistry, playing a potentially crucial role in several key tropospheric processes. The CI can undergo bimolecular reaction with species such as hydrocarbons,  $\text{SO}_2$ ,  $\text{NO}_x$  and a variety of other trace gasses.<sup>144,148,149</sup> Reaction of CIs with  $\text{SO}_2$  leads to the production of  $\text{H}_2\text{SO}_4$ , which has been the subject of intense investigation as sulphuric acid is a key component regarding the initiation of particle nucleation, and therefore aerosol production in the troposphere, affecting global climate.<sup>143,150</sup>

A key metric in shaping the composition of the lower atmosphere is the oxidising capacity. The oxidising capacity can determine the lifetime of some key greenhouse gasses and pollutants, as well as influencing the formation of organic aerosol.  $\cdot\text{OH}$  is a key player in determining the oxidising capacity, as it is responsible for initiating the oxidation of most VOCs in the troposphere.  $\text{OH}$  can be formed from the photolysis of  $\text{O}_3$  with subsequent reaction with water vapour:



This mechanism for the generation of  $\text{OH}$  depends on sufficient levels of sunlight and concentrations of water vapour. Field measurements have shown that  $\text{OH}$  levels are very



similar during both winter and summer campaigns in UK urban environments<sup>151–154</sup>. However, in winter, the efficiency of Reaction 3.1 drops dramatically and it is believed that CI decomposition chemistry makes up for this difference, as well being the dominant source of night-time  $\cdot\text{OH}$  (Figure 1.3). In playing such an important role in the formation of  $\text{OH}$ , as well as their own bimolecular reactivity, CI chemistry has important implications for our understanding of urban air chemistry.

Analysing CIs in the gas phase poses an analytical challenge due to their inherent short lifetime and low ambient concentrations. Current techniques to detect CIs, some of which are described in Section 1.5.3, have provided kinetic data on the bimolecular reaction of small, simple CIs with a range of species including the water dimer,  $\text{SO}_2$ ,  $\text{NO}_x$  and organics. IR-spectroscopy has also been used to investigate the fate of larger CIs from  $\beta$ -pinene ozonolysis, with potential application to a range of other CIs. There remains a large uncertainty regarding the fate of CIs from the ozonolysis of VOCs; it is challenging for current methods of CI detection to probe CIs in these chemically complex, atmospherically relevant systems.

In this chapter, the development of a novel cost-effective, laboratory-based technique for characterising CIs in complex VOC ozonolysis systems will be presented. CIs are characterised by first reacting them with spin trap molecules (Section 1.3.5) compounds that have been used to characterise radical species in biological assays for decades<sup>155–158</sup>. Initially, CIs, generated from a model VOC ozonolysis system involving the reaction of the monoterpene  $\alpha$ -pinene and  $\text{O}_3$ , are synthesised in the liquid phase and reacted with the spin trap DMPO. The structure of the adducts formed between the CI and DMPO are extensively characterised using an array of powerful analytical techniques and theoretical calculations, and used to postulate a reaction mechanism. A set up was then designed and fully optimised to characterise CIs from  $\alpha$ -pinene ozonolysis in the gas phase, by analysing the CI-DMPO adducts using PTR-ToF-MS. The technique's quantitative potential was evaluated using this model chemical system.

This study was then expanded on further, where CIs generated from the ozonolysis of a variety of biogenic and anthropogenic VOC precursors such as  $\beta$ -pinene, limonene, methacrolein, styrene and *cis*-2-hexene were characterised. DFT calculations were performed to ascertain the energetics associated with various CIs with DMPO, to gain a firmer understanding of the chemistry. Experimentally observed concentrations of CIs were compared to theoretical calculations using the Master Chemical Mechanism (MCM

---

v3.1.1.) to validate the results. This chapter demonstrates that this novel technique is uniquely capable of characterising multiple CIs simultaneously in complex, atmospherically relevant chemical systems.

## 3.2 Methodology

### 3.2.1 Reagents and Materials

For bulk and gas phase experiments  $\alpha$ -pinene (98% (+/-)- $\alpha$ -pinene, Aldrich) and oleic acid ( $\geq 99\%$ , GC grade, Sigma-Aldrich) were reacted with ozone produced by a UV lamp (185/254 nm, Appleton Woods®). The spin traps 5,5-dimethyl-pyrroline N-oxide (DMPO) ( $\geq 97\%$ , GC grade, Sigma) and N-*tert*-butyl- $\alpha$ -phenylnitrone (PBN) ( $\geq 98\%$ , GC grade, Sigma) were used in this study to capture and stabilise the Criegee intermediates. Acetonitrile ( $>99.9\%$  Optima™ LC/MS grade, Fisher Chemical) was used as solvent for bulk reaction. Water with 0.1% formic acid (Optima™ LC/MS grade, Fisher Chemical) and methanol ( $>99.9\%$  Optima™ LC/MS grade, Fisher Chemical) were used for HPLC separation, and deuterated acetonitrile (Acetonitrile D3  $\geq 99.80\%$ , NMR solvent, Euriso-Top) was used for NMR measurements.

### 3.2.2 Liquid Phase Ozonolysis

The olefinic precursor  $\alpha$ -pinene and the spin trap (DMPO or PBN) were dissolved in 100 mL of acetonitrile (solvent used in previous ozonolysis studies<sup>159</sup>) at room temperature (16-18°C) at a concentration of 1 mM for the olefinic compound and 2 mM for the spin trap. The solution was placed in an ice bath for the reaction as the spin trap adducts are more stable at lower temperatures and to minimise solvent evaporation.<sup>160</sup>

The UV lamp used for ozone production was switched on and equilibrated for at least 20 min with a flow of synthetic air (Zero grade, BOC) at 0.3 L/min before the start of the reaction. Subsequently, ozone was bubbled at 0.3 L/min through the solution *via* a Teflon tube connected to a Pasteur pipette tip for 1h (concentration of 600 ppm ozone in air). The flow rate was controlled with a mass flow controller (20-2000 cm<sup>3</sup>/min MKS 1179A Mass-Flo® controller). Throughout the reaction, the reaction flask was covered completely with aluminium foil to prevent photolysis, and closed with parafilm to minimise evaporation and keep ozone concentrations in solutions as close as possible to saturation. The ozone concentration in solution was  $1.3 \pm 0.7$  mM on average, as measured by iodometric titration.<sup>161,162</sup>

Control experiments of ozonolysis of only the spin traps (DMPO+O<sub>3</sub> and PBN+O<sub>3</sub>) or the olefinic precursors ( $\alpha$ -pinene+O<sub>3</sub>, and oleic acid+O<sub>3</sub>) were also performed under the same experimental conditions. All solutions were analysed with electrospray ionisation high-resolution mass spectrometry (ESI-HRMS), electron paramagnetic resonance (EPR) and nuclear magnetic resonance (NMR) following the procedures described in the following sections.

A strict control of reagent concentrations seems necessary to ensure efficient production of CI-spin trap adducts, including stabilisation of ozone output from the UV lamp prior to the start of the reactions. As the spin trap also reacts with ozone, the starting concentrations of reagents and reaction times have to be carefully optimised to assure efficient CI-spin trap adduct formation. Traces of water dissolved in solution do not seem to affect the efficiency of the reaction. Tests performed with up to 1% of water in acetonitrile showed no significant decrease of the CI-spin trap signals in direct infusion ESI-HRMS.

### 3.2.3 HPLC-ESI-HRMS

The reaction mixtures were analysed with direct infusion in ESI in positive ionisation (flow rate 5  $\mu$ L/min, spray voltage 3.0 kV, transfer capillary temperature 275°C, Sheath flow 12 L/min, S-Lens RF Level 60%) coupled to a high-resolution mass spectrometer (LTQ Velos Orbitrap, Thermo Scientific, Bremen, Germany) with a resolution of 100 000 at  $m/z$  400 and a typical mass accuracy within  $\pm 2$  ppm. Data were acquired in full scan in the  $m/z$  range 100-600 and in MS/MS with a collision-induced dissociation (CID) energy of 30 (normalized collision energy). The instrument was calibrated routinely with a Pierce LTQ Velos ESI Positive Ion Calibration Solution (Thermo Scientific).

The  $\alpha$ -pinene CI adducts with DMPO and PBN were analysed with HPLC-HRMS using an Accela system HPLC (Thermo Scientific, San Jose, USA) coupled with a LTQ Velos Orbitrap. A T3 Atlantis C18 column (3  $\mu$ m; 2.1 $\times$ 150 mm; Waters, Milford, USA) was used for chromatographic separation. Injection volume was 50  $\mu$ L. Mobile phases were (A) water with 0.1% formic acid and (B) methanol.

#### Elution Programme for HPLC-ESI-HRMS Analysis

$\alpha$ -pinene CI-DMPO and CI-PBN adducts were separated at room temperature and with a flow rate of 200  $\mu$ L/min. For the DMPO adduct, elution gradient was: 0–44 min linear

---

gradient from 20% to 80% B, 44-44.01 min linear gradient to 100% B, 44.01-47 min 100% B, 47-48 min linear gradient from 100% to 20 % B, 48-60 min 20% B. Retention time of the adduct was 49.0 minutes. For the PBN adduct, elution gradient was: 0–30 min linear gradient from 50% to 90% B, 30-30.01 min linear gradient to 100% B, 30.01-36 min 100% B, 36-37 min linear gradient from 100% to 50 % B, 37-39 min 50% B. Retention time of the adduct was 35.2 minutes. Heated ESI parameters were: 150°C source temperature, 40 L/min sheath gas flow rate, 5 L/min auxiliary gas flow rate, 3.20 kV needle voltage, 300°C transfer capillary temperature, S-Lens RF Level (%) 69.2. MS spectra were collected in full scan with a resolution of 100 000 in the mass ranges  $m/z$  80–600 and  $m/z$  100–900, and in auto MS/MS with a collision induced dissociation (CID) energy of 35 (normalised collision energy) on the three most intense ions.

### 3.2.4 NMR Sample Preparation

The Criegee-spin trap adduct was separated with HPLC using the methods described in Section 3.2.3. Fractions containing the separated adduct have been collected (4 times, 50  $\mu$ L of sample injected in HPLC), combined, evaporated to dryness, and recovered with 1 mL of deuterated acetonitrile.

Direct analysis of the reaction mixture without prior HPLC separation resulted in an NMR spectrum dominated by signals from unreacted reagents and secondary products, which made the identification of key signatures from the CI-DMPO adducts difficult. HPLC-ESI-HRMS has therefore been used to isolate the  $\alpha$ -pinene CI-DMPO adducts, however, probably due to the volatility of the adducts, it was not possible to concentrate the solution enough for NMR detection. For this reason, NMR has been conducted on the CI-PBN adducts only. PBN is non-volatile, but has the same nitron functional group as DMPO, and is expected to react in the same way as DMPO as supported by ESI-HRMS analysis.

The NMR spectra were acquired on a 500 MHz Bruker Avance III HD, with Dual Cryoprobe (carbon observe). The software Topspin3.2 was used to acquire and Topspin 3.5pl5 to process the data. Full characterisation including  $^1\text{H}$ ,  $^{13}\text{C}$ , HMBC (heteronuclear multiple-bond correlation), HSQC (heteronuclear single quantum coherence), and COSY (homonuclear correlation spectroscopy) was conducted to confirm molecular structures.

## NMR Acquisition Protocol

$^1\text{H}$ -NMR was recorded with a zg30 pulse program, size of FID 64K points (3.28s acquisition), D1=1s, no. scans 32 and processed with 1 Hz exponential multiplication.

$^{13}\text{C}$ -NMR was acquired with a UDEFT pulse program,<sup>163</sup> size of FID 25170 (0.36s acquisition), D1=5s (used 600s pre-acquisition delay, no delay scans), no. scans 1024 and processed with forwards linear prediction to 256K points (4K coefficients) and using 2 Hz exponential multiplication.

HMBC-NMR was acquired with hmbcetgpl3nd pulse program, which employs a 3-fold J-filter to suppress one-bond correlations, using 4096x512 points in F2 and F1, 40% non-uniform sampling and, a Poisson-gap sampling schedule<sup>164</sup> (algorithm by Scott Robson at Harvard Medical School, modified in-house to compile under Microsoft windows). Scan acquisition time was 0.36s with a 1.6s D1, 16 scans per increment; total experiment time was 49 minutes. Spectra were processed to 8192x1024 points in F2 and F1, using a sine window function (ssb=2); zero-filled to 1024 points in F1. NUS reconstruction used the Bruker Topspin standard mdd\_mod=cs method.

HSQC-NMR was acquired with DEPT135 editing, hsqcedetgsp.3 pulse program, using 1816x256 data points in F2 and F1, 128 scans per increment, acquired using 25% non-uniform sampling using the Bruker standard schedule, with 54321 as the random seed (0.14s scan acquisition time, D1=0.8s; 2hrs 11 minutes total experiment time). Spectra were processed to 2048x2048 data points using linear prediction in F2 (number coefficients=32) and a QSINE window function (SSB=2). NUS reconstruction used the Bruker Topspin standard mdd\_mod=cs method.

COSY-NMR was acquired using cosygpmfqf pulse program to give a double quantum filtered result. Used 4096x256 data points in F2 and F1, 8 scans per increment. (0.31s scan acquisition time, D1=2s, total acquisition time 1hr 20 minutes). Processed to 8192x2048 points in F2 and F1, using a sine window function (ssb=2), linear forwards prediction (to 1024 points, no. coefficients=100) and zero filling.

### 3.2.5 Electron Paramagnetic Resonance Spectroscopy

Samples were kept in dry ice overnight before analysis. Under these conditions, no significant degradation of CI-DMPO adducts occurred as shown by ESI-HRMS analysis. Prior to EPR analysis, solutions were transferred into quartz tubes (ID=3 mm) and

---

subsequently deoxygenated by passing N<sub>2</sub> through the solution. The EPR spectra were obtained by a Bruker ECS spectrometer operating at X-band equipped with a TMH resonator. Typical acquisition conditions were: microwave power 6 mW, acquisition time 40 ms/point, modulation amplitude 0.3 G (0.03 mT), number of scans 10. The spectra were fitted with the standard software PEST package from NIEHS.<sup>165</sup>

### 3.2.6 PTR-ToF-MS measurements

Online gas phase concentrations of  $\alpha$ -pinene, DMPO and CI-DMPO adducts were measured using a proton transfer reaction time-of-flight mass spectrometer (PTR-ToF-MS 8000, Ionicon Analytik, Innsbruck, Austria) in the  $m/z$  range 10-500, with a time resolution of 10 s and a mass resolution  $m/\Delta m$  of 5000 (full width at half maximum) at the mass of protonated acetone. Source settings were: drift tube voltage 510 V, drift tube pressure  $\sim 2.22$  mbar, and drift tube temperature: 90°C, resulting in an  $E/N$  of  $\sim 127$  Td ( $1 \text{ Td} = 10^{-17} \text{ V cm}^2$ ). The PTR-ToF-MS inlet (1 m long inert peek tube ID=1 mm, OD=1.59 mm) was kept at 100°C and the sampling flow rate was 100 cm<sup>3</sup>/min. Data analysis was conducted using PTR-MS Viewer 3.1 (Ionicon Analytik).

The mixing ratio of  $\alpha$ -pinene was estimated on the basis of the rate constant ( $k = 2.44 \cdot 10^{-9} \text{ cm}^3 \text{ molecule}^{-1} \text{ s}^{-1}$ ) of the proton transfer reaction<sup>166</sup> considering both the protonated molecular ion ( $m/z$  137.133) and its main fragment ( $m/z$  81.070). For DMPO and the CI-DMPO adducts the rate constant is unknown and therefore a default rate constant ( $k$ ) of  $2 \cdot 10^{-9} \text{ cm}^3 \text{ molecule}^{-1} \text{ s}^{-1}$  was used, and only the protonated molecular ion was considered for quantification. DMPO and  $\alpha$ -pinene signals are often in saturation during the experiments and therefore the corresponding <sup>13</sup>C isotopes were used for quantification. CI-DMPO adducts concentrations were quantified using a Gaussian multi-peak fitting with the PTR-Viewer v3.1 software (Ionicon) to integrate the peak and back out the adduct concentration.

For quantification of the initial mixing ratio  $s$  of  $\beta$ -pinene and limonene, both the protonated molecular ion C<sub>10</sub>H<sub>17</sub><sup>+</sup> and the fragment C<sub>6</sub>H<sub>9</sub><sup>+</sup> were used. For *cis*-2-hexene, both the protonated molecular ion C<sub>6</sub>H<sub>13</sub><sup>+</sup> and the main fragment C<sub>3</sub>H<sub>7</sub><sup>+</sup>, for methacrolein the protonated molecular ion C<sub>4</sub>H<sub>7</sub>O<sup>+</sup> and the fragments C<sub>3</sub>H<sub>7</sub><sup>+</sup> and C<sub>3</sub>H<sub>5</sub><sup>+</sup> while for styrene only the protonated molecular ion C<sub>8</sub>H<sub>9</sub><sup>+</sup> was used for quantification.

### 3.2.7 Set-up for Gas Phase Ozonolysis

#### Set-up for capturing $\alpha$ -pinene CIs

Ozonolysis of  $\alpha$ -pinene was selected as a proof-of-principle model for the detection of CI-spin trap adducts in the gas phase. The ozonolysis reaction was conducted in a flow tube reactor maintained at ambient temperature ( $\sim 16^\circ\text{C}$ ) and pressure and dry conditions (relative humidity  $< 2\%$ ) shown in Figure 3.1. The experimental set-up comprised a 2.5 L glass flow tube in which  $\alpha$ -pinene reacts with ozone, a mixing point (T-fitting) in which the spin trap is mixed with the sample flow from the flow tube, and a heated PTFE tube in which the spin trap reacts with the CI before quantification in the PTR-ToF-MS. Additional instruments (ozone analyser and SMPS) were also connected in some experiments sampling from the exhaust flow (Figure 3.1).

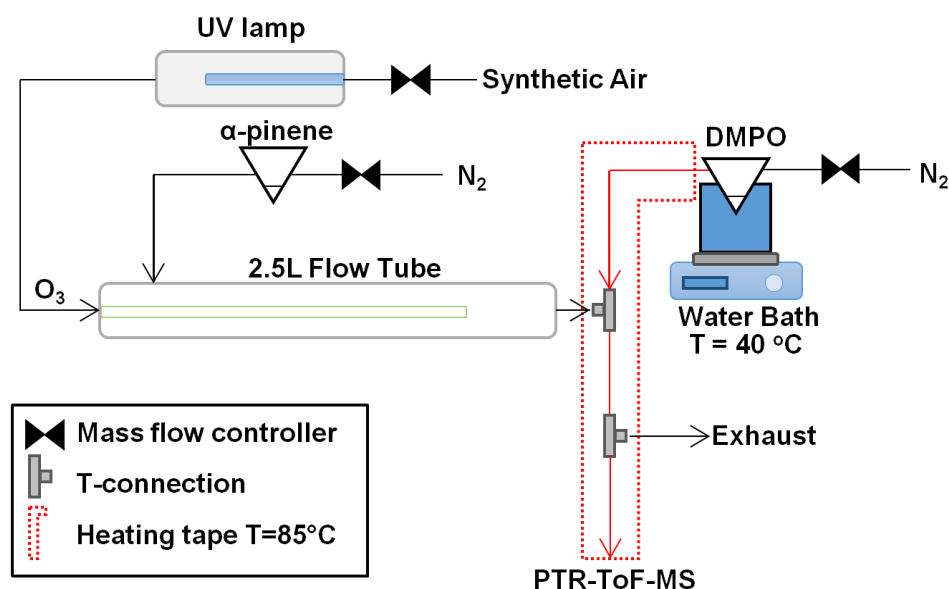


**Figure 3.1** – Experimental set-up comprising of a 2.5 L glass flow tube, in which  $\alpha$ -pinene and ozone react, with an approximate reaction time of 3s. DMPO is introduced after this initial reaction volume given the fact that  $\text{O}_3$  reacts efficiently with the spin trap. The PTFE line downstream of the DMPO towards the PTR-ToF-MS is heated to  $85^\circ\text{C}$  to limit wall losses of the DMPO, as well as the CI-DMPO adduct before analysis using the PTR-ToF-MS.

$\alpha$ -pinene was vaporised from a 25 mL pear-shaped flask filled with 0.5 mL of pure  $\alpha$ -pinene with a  $175\text{ cm}^3/\text{min}$  flow of  $\text{N}_2$  (oxygen-free nitrogen, BOC) regulated via a  $20\text{--}2000\text{ cm}^3/\text{min}$  mass flow controller (MKS 1179A Mass-Flo® controller). Ozone was produced from a UV lamp (185/254 nm, Appleton Woods®) by flowing synthetic air (Zero grade, BOC) at  $150\text{ cm}^3/\text{min}$  ( $20\text{--}2000\text{ cm}^3/\text{min}$  MKS 1179A Mass-Flo® controller). The outlet of the flow tube is then mixed into a T connection (stainless-steel

---

1/4'' (~6.35 mm) T-fitting, Swagelok®) with a 310 cm<sup>3</sup>/min flow (50-5000 cm<sup>3</sup>/min MKS 1179A Mass-Flo® controller) of DMPO in N<sub>2</sub> (oxygen-free nitrogen, BOC) evaporated from a 25 mL flask filled with 0.5 mL of pure DMPO and held in a water bath at 40°C.

Connecting tubes and the T-connection were kept at 85°C to minimise condensation of DMPO. The reaction time between the spin trap and the CIs was controlled by varying the length of a 1/4'' (OD=6.35 mm, ID=3.17 mm) polytetrafluoroethylene (PTFE) tube kept at 85°C, connecting the mixing point in which DMPO is added with the PTR-ToF-MS. Ozone was measured using a UV photometric ozone analyser (Thermo Scientific model 49i) and particle concentration was measured using a TSI scanning mobility particle sizer (SMPS) composed of TSI 3080 electrostatic classifier (X-ray neutraliser and differential mobility analyser TSI model 3081) and a condensation particle counter (TSI model 3775).

### 3.2.8 Optimisation of the Flow Tube Set-up

Concentrations of the reagents were varied by changing the amount of pure reactant in evaporating flask, by changing the flow rate of N<sub>2</sub>/synthetic air, or by increasing coverage of the UV lamp with aluminium foil to reduce the mixing ratio of [O<sub>3</sub>] produced *via* O<sub>2</sub> photolysis. Initially, relatively low reagent mixing ratios of  $\alpha$ -pinene (~2 ppm) and DMPO (~3 ppm) were used to ensure that the PTR-ToF-MS was measuring efficiently, avoiding saturation of the detector and excess consumption of the primary ion (H<sub>3</sub>O<sup>+</sup>) during ionisation. Within these experimental conditions, it was observed that higher mixing ratios of ozone (~20 ppm) lead to the complete consumption of DMPO due to excess ozone, therefore resulting in the inefficient trapping of the CIs by DMPO. Using lower mixing ratios of O<sub>3</sub> (~2 ppm), the speed of the reaction between  $\alpha$ -pinene and O<sub>3</sub> was too low, and no CIs were observed. Thus, reagent concentrations had to be increased significantly, and carefully balanced to avoid DMPO consumption and facilitate CI-DMPO adduct detection.

The mixing ratios in the reaction system of  $\alpha$ -pinene, DMPO and O<sub>3</sub> were optimised to 340, 150 and 290 ppm respectively in order to facilitate detection of the CI-DMPO adduct at a concentration appreciably above the instrumental detection limit (0.03 ppb). These elevated mixing ratios are not representative of ambient mixing ratios of these species, but were required in order to allow CI detection, and to perform method proof-of-



principle experiments. Furthermore, the high concentrations of these species cause the primary ion ( $\text{H}_3\text{O}^+$ ) to be depleted, which inherently affects the quantification of these species, as well as the quantification of the CI-DMPO adduct for which there is no calibration standard available. The concentrations of the reactants were measured by diluting the flow in the reaction system by a factor of 10 (from  $600\text{ cm}^3\text{ min}^{-1}$  to  $6000\text{ cm}^3\text{ min}^{-1}$ ) to avoid primary ion ( $\text{H}_3\text{O}^+$ ) depletion in the PRTMS drift tube. For  $\alpha$ -pinene and DMPO, the concentrations under dilution were measured by tracing the  $^{13}\text{C}$  isotope as the parent compounds were still saturating the detector of the PTR-ToF-MS, which in turn leads to inaccurate quantification. The concentration of  $\text{O}_3$  was measured using a UV photometric ozone analyser (Thermo Scientific model 49i) still using the same dilution factor, given that the high concentrations used here are towards the upper limit of detection for the instrument.

The temperature of the flow tube where the ozonolysis takes place was altered by changing the temperature of the lab where the experiment takes place. A reduction of lab temperature from  $20\text{ }^\circ\text{C}$  to  $16\text{ }^\circ\text{C}$  increased the concentration of the detected DMPO-CI by a factor of approximately 1.5. This is likely due to the slower decomposition of CIs at lower temperature, therefore increasing their lifetime and the probability of CIs being scavenged by DMPO. The PTFE tube carrying the DMPO to the T-connection (see Figure 3.1) was heated using heating tape wrapped around the tubing. The temperature of the tubing was varied from room temperature ( $16\text{ }^\circ\text{C}$ ) to  $95\text{ }^\circ\text{C}$  to minimise the condensation of DMPO to the tubing walls, as well as reduce the condensation of the CI-DMPO adduct. The concentration of the CI-DMPO adduct increases and plateaus at  $85\text{ }^\circ\text{C}$ , so the PTFE tubing was heated to this temperature. There was no visible evidence of thermal degradation of the CI-DMPO adduct at this temperature. The loss of low-volatility adducts is further complicated given the high secondary organic aerosol yield generated by the ozonolysis of  $\alpha$ -pinene ( $\sim 10\text{ mg m}^{-3}$  average during these experiments), and therefore high aerosol surface area, which could allow substantial loss of the CI-DMPO adducts *via* partitioning of the adduct to the condensed phase. The extent of loss of the adduct to the particle phase and this processes' effect on the accuracy of quantification is currently unclear.

The residence time of the DMPO CI reaction was optimised by varying the length of the PTFE tube connecting the T-connection, where the CI and DMPO are mixed, to the PTR-ToF-MS from 0 to 200 cm, which corresponds to an additional reaction time of 0-1.5

---

s, with an additional ~0.5 s reaction time in the PTR-ToF-MS peak inlet tubing. The concentration of the DMPO-CI increases slightly over time reaching a plateau with a residence time of ~1 s. For this reason, 200 cm PTFE tube length and a 1.5 s reaction time after the T-connection was deemed suitable for ensuring the CI and DMPO had sufficient time to react.

The inlet and drift tube temperatures of the PTR-ToF-MS were optimised in order to minimise DMPO and CI-DMPO condensation onto the walls of the inlet. The temperature was altered between 60 – 100 °C. The greatest and most reproducible signals of the PTR-ToF-MS were with a drift tube temperature of 90 °C and an inlet temperature of 100 °C. HPLC-ESI-HRMS analysis of liquid phase CI-DMPO adducts, which were initially kept at 60 °C, showed that there was no obvious degradation of the adduct over a time period of 20 minutes, far greater than the residence time in the heated reaction line and PTR-ToF-MS inlet, suggesting that the adduct is stable enough for the instrument to be run at these higher temperatures.

### 3.2.9 MCM modelling

Experimental results obtained in this chapter were compared to modelled time evolution of various products and reagents using the AtChem (<http://atchem.leeds.ac.uk>) numerical box-model. AtChem is designed to be used alongside the Master Chemical Mechanism (MCM)<sup>167</sup>. The following inputs were used in the model: Temperature = 289.15K, number density (M) =  $2.6 \times 10^{19}$  molecules cm<sup>-3</sup> and [H<sub>2</sub>O] =  $1.23 \times 10^{14}$  molecules cm<sup>-3</sup>. All other variables in AtChem were run in standard configuration. For each AtChem simulation, a specific mechanism subset was downloaded. Initial mixing ratios of  $\alpha$ -pinene and O<sub>3</sub> were 340 and 290 ppm respectively, to represent the reaction conditions described in Section 3.2.8.

## 3.3 Results and Discussion

### 3.3.1 Characterisation of CI-spin trap adduct structure

The structure of the adduct formed between CIs, generated from  $\alpha$ -pinene ozonolysis, and DMPO was probed. A series of powerful analytical techniques were applied to gain a firm understanding of the adduct structure, as well as gaining an insight into the reaction mechanism of the CI with the spin trap DMPO.

### Electrospray Ionisation High Resolution Mass Spectrometry (ESI-HRMS)

Solution phase ozonolysis of  $\alpha$ -pinene, as described in Section 3.2.2, was conducted for one hour by bubbling ozone through a solution of 1 mM  $\alpha$ -pinene and 2 mM DMPO in acetonitrile. A control experiment was conducted by bubbling ozone through a solution containing 2 mM DMPO, with no  $\alpha$ -pinene present in solution (Figure 3.2).

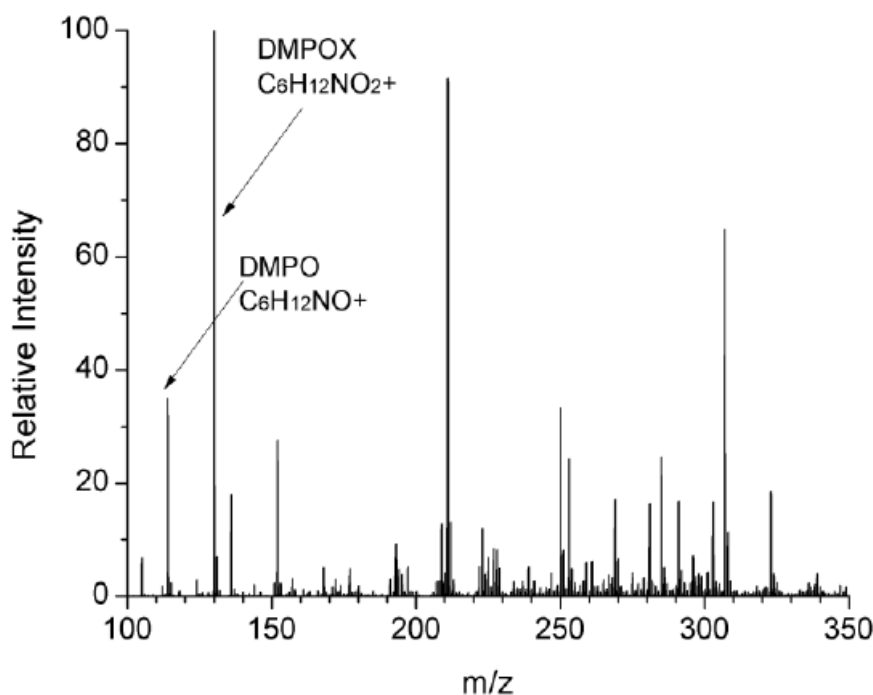


**Figure 3.2** – ESI-HRMS analysis of a control experiment, where ozone was bubbled through a 2 mM solution of DMPO in acetonitrile. No mass corresponding to CI-DMPO was detected, but the presence of unreacted DMPO, as well as the degradation product DMPOX were observed.

The resulting solutions were analysed using ESI-HRMS. Figure 3.2 shows the control experiment, where no mass corresponding to CI-DMPO was detected. Unreacted DMPO, as well as the product DMPOX were observed in the control experiment, a common degradation product of DMPO found in harsh oxidising conditions<sup>114</sup>. Figure 3.3 shows ESI-HRMS analysis, where a peak corresponding to the formation of a 1:1 adduct, CI-DMPO at  $m/z = 298.2013$  ( $C_{16}H_{27}NO_4$ ) $H^+$  was detected from a sample containing  $\alpha$ -pinene and DMPO.

It should be noted that ozonolysis of  $\alpha$ -pinene can generate two isomeric CIs, depending on the fragmentation of the alkene bond. The CIs generated in this system can contain either a carbonyl oxide with a terminal ketone, or carbonyl oxide with a terminal aldehyde, from here termed  $CI_K$  and  $CI_A$ .

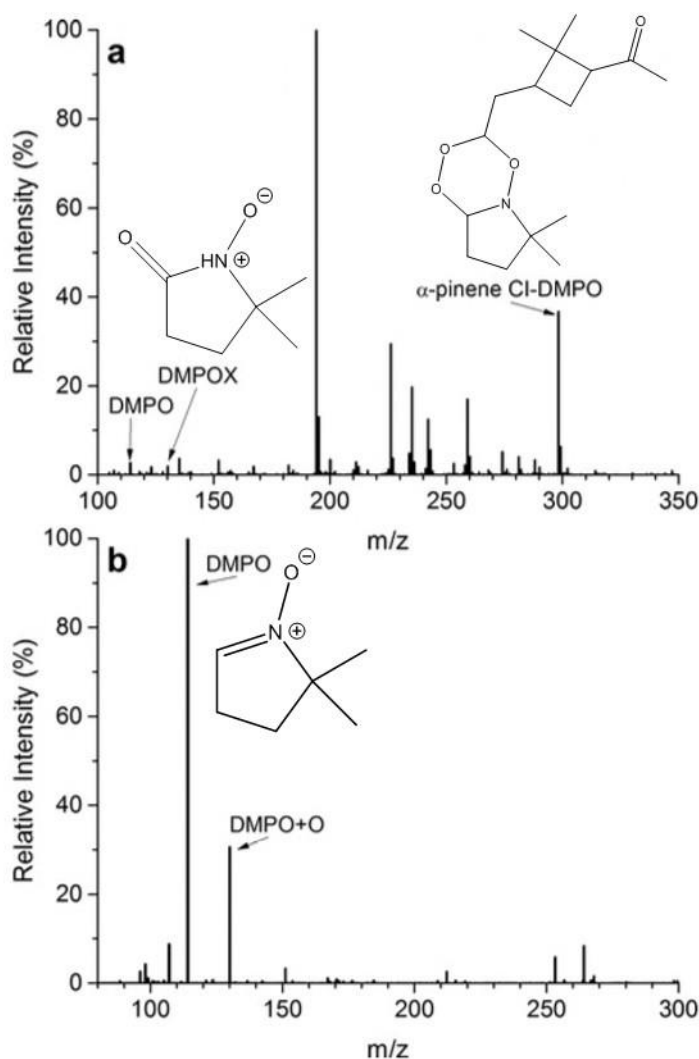


**Figure 3.3** – Initial characterisation of CI-DMPO adducts using (a) Positive mode ESI-HRMS showing the presence of the 1:1 CI-DMPO adduct at  $m/z$  298.2013, as well as unreacted DMPO and DMPOX ( $m/z$  129.0745) and (b) MS/MS analysis of CI-DMPO, with fragments corresponding to DMPO and DMPO + O.

ESI-HRMS is not capable of distinguishing which isomer is scavenged and trapped by the spin trap DMPO, due to the isomers' equivalent masses. Therefore, the adduct formed between the DMPO and either CI isomer will have an identical mass, and cannot be resolved with ESI-HRMS alone. There are also peaks corresponding to the unreacted spin trap DMPO  $m/z$  114.0845 as well as the compound DMPOX at  $m/z$  = 130.0784. MS/MS analysis (Figure 3.3 (b)) shows that the most prominent fragment has the exact mass corresponding to the spin trap DMPO. This further indicates that the compound detected at  $m/z$  = 298.2013 is indeed the 1:1 CI-DMPO adduct, although this provides limited structural information on the compound. There is also a fragment corresponding to

DMPO + O, suggesting that the oxygen centred radical of the CI attacks the carbon atom of the nitron functional group of the DMPO.

### Electron Paramagnetic Resonance (EPR)

Using the same experimental conditions described in Section 3.2.2, solution phase ozonolysis of  $\alpha$ -pinene in acetonitrile containing the spin trap DMPO was conducted in order to generate the CI-DMPO adduct for EPR analysis. A control experiment was also performed by bubbling ozone through a 2 mM solution of DMPO in acetonitrile. The EPR spectrum corresponding to both the sample and control is displayed in Figure 3.4.

Both EPR spectra are characterised by the presence of a single species with hyperfine interaction with a nitrogen ( $a_N = 6.9$  G) and two equivalent protons ( $a_H = 3.5$  G). The observed hyperfine splitting of the nitrogen is unusually low compared to those of typical DMPO adducts, which are usually on the order of  $a_N = 15\text{G}^{168}$ . The spectral features are in fact consistent with that reported in the literature for the compound 5,5-dimethyl-2-pyrrolidone-*N*-oxyl<sup>114</sup> (DMPOX, structure in Figure 3.4), a degradation product found under harsh oxidising conditions<sup>168</sup>.

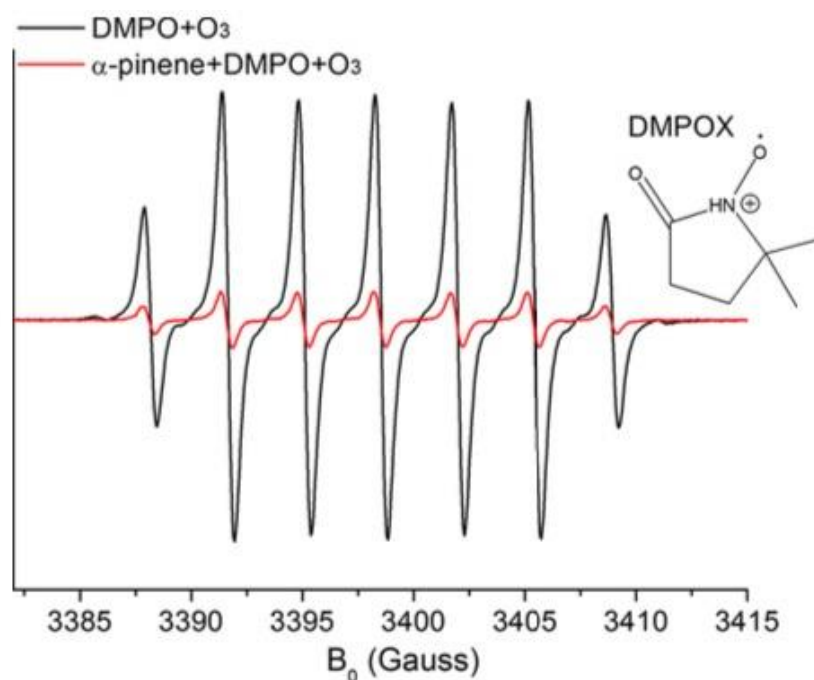


**Figure 3.4** – EPR spectrum conducted at room temperature in acetonitrile for a control (DMPO + O<sub>3</sub>) and sample ( $\alpha$ -pinene + DMPO + O<sub>3</sub>). The control experiment shows a signal corresponding to DMPOX, a product formed under harsh oxidising conditions. The sample shows no change in the hyperfine splitting, suggesting that DMPOX is still formed albeit in much lower concentrations. No other radical species were observed in the sample experiment.

---

Hyperfine coupling constants of the nitrogen and protons in this compound have been reported to be  $a_o = 6.27\text{-}6.87$  G and  $a_o = 3.18\text{-}3.65$  G respectively.<sup>168</sup> The presence of DMPOX was also confirmed in the ESI-HRMS analysis conducted on solution phase ozonolysis of  $\alpha$ -pinene in the presence of DMPO, with a peak at  $m/z = 130.0784$  (as also observed in Fig. 3.2). Other studies have associated the peak at  $m/z$  130.0784 with the adduct formed between DMPO and OH radicals<sup>115,116,121,158</sup>, although this was not detected in the EPR experiments conducted here.

For the sample experiment in which  $\alpha$ -pinene was present in solution (red spectrum, Figure 3.4), the same hyperfine splitting pattern as the control was observed, indicating the presence of DMPOX in these experiments, although at lower concentrations than that observed in the control experiment. No other radical species were detected using EPR, including those which would correspond to the typical radical spin trap adduct which would be formed with the CI. This is consistent with a previous study by Pryor *et al.*<sup>155</sup> in which spin traps have been applied to study the formation of radicals from ozone - alkene reactions at  $-78$  °C. In this study, no radical species corresponding to the CI-DMPO adducts were observed in the EPR. This potentially suggests that the CI reacts with the spin trap to form a non-radical adduct.

### Density Functional Theory (DFT) Calculations

Density Functional Theory calculations were performed in order to identify stable CI-DMPO adduct structures, as well as to postulate a reaction mechanism for this process. DFT calculations were conducted by Maurizio Bruschi at the Dipartimento di Scienze dell'Ambiente e del Territorio e di Scienze della Terra, Università degli Studi di Milano Bicocca (Italy). Extensive information regarding the calculations can be found in Giorio *et al.*<sup>169</sup>. Extensive results of this DFT study are presented in Appendix 2, and will briefly be discussed here.

The calculated  $\Delta G_r$  values for the addition of  $CI_K$  to DMPO show that the formation of a 6-membered ring is strongly exoergic. The Gibbs free reaction energy ( $\Delta G_r$ ) calculated for this, referring to the formation of the most stable stereoisomer, was  $-32$  kcal mol<sup>-1</sup>. The  $\Delta G_r$  value for the corresponding reaction between  $CI_A$  and DMPO was  $-19$  kcal mol<sup>-1</sup>. The reaction leading to a 5-membered ring between  $CI_K$  and DMPO was still exoergic at  $-13$  kcal mol<sup>-1</sup>, whereas the addition of  $CI_A$  to DMPO to form a 5-membered ring was endoergic at  $+ 5.2$  kcal mol<sup>-1</sup>. Given this information (extensively described in

Appendix 2), optimised structures and proposed cycloaddition reactions are illustrated in Figure 3.5.

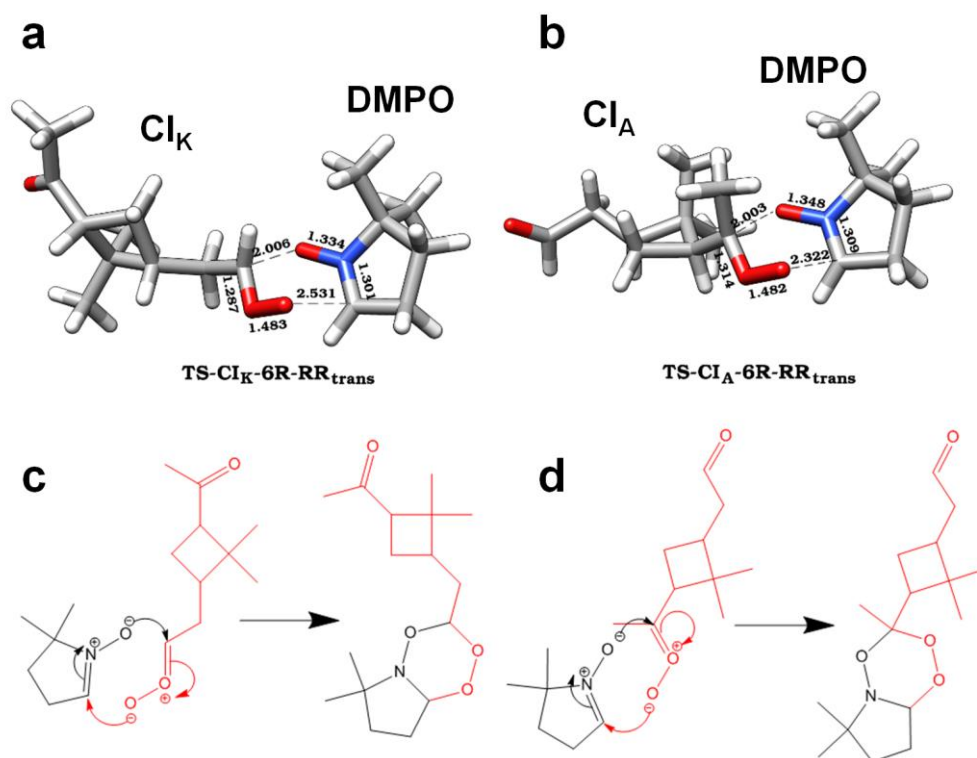


**Figure 3.5** – Optimised structures, with distances in Å, of the transition states of (a)  $\text{CI}_{\text{K}(180)} + \text{DMPO}$  and (b)  $\text{CI}_{\text{A}(180)} + \text{DMPO}$  reaction, as well as proposed cycloaddition mechanisms for (c)  $\text{CI}_{\text{K}(180)} + \text{DMPO}$  and (d)  $\text{CI}_{\text{A}(180)} + \text{DMPO}$ .

The formation of a 5-membered ring would need to proceed with substantial re-arrangement of the oxygen atom out of the C=N-O plane, likely contributing to the large activation energy barrier associated with the formation of the 5-membered ring. A summary of the reaction profiles associated with the formation of the 5- and 6-membered ring adducts are shown in Figure 3.6, demonstrating the lowest reaction energy profiles for the formation of CI-DMPO adducts.

It is clear from this diagram that the most favourable pathway to the formation of CI-DMPO leads to the formation of an adduct consisting of a 6-membered ring, produced *via* the 1,3 dipolar cycloaddition of  $\text{CI}_{\text{K}}$  with DMPO. The relatively low activation energy barrier, as well as the relatively large stability associated with the  $\text{CI}_{\text{K}}$ -DMPO adduct, suggests that the trapping of CIs by DMPO in the gas phase could be competitive with other unimolecular and bimolecular loss processes of these CI species in the gas phase.

On top of these theoretical calculations, further experimental data is required in order to probe the structure of the adduct formed between the CI and DMPO.

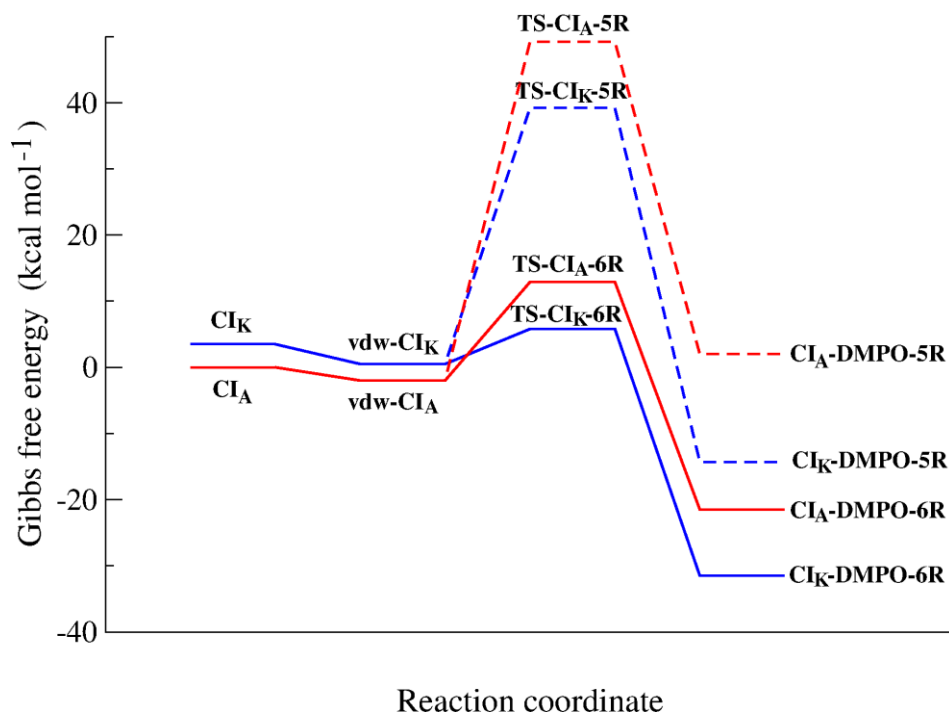


**Figure 3.6** – Reaction energy profiles of the  $\text{CI}_A$  + DMPO (red) and  $\text{CI}_K$  + DMPO (blue). These profiles were calculated considering the lowest reaction energy profile for the formation of each adduct. Pathways leading to 5-membered ring formation are shown with dashed lines.

### Nuclear Magnetic Resonance Spectroscopy (NMR)

In order to gain further insight into the structure of the adduct formed between the  $\alpha$ -pinene CI and DMPO, NMR spectroscopy was performed with the methodology described in Section 3.2.4. Initial attempts to recover the CI-DMPO adduct using HPLC separation with subsequent evaporation, and recovery in deuterated acetonitrile for NMR analysis, failed and no adduct was detected. It is likely that the CI-DMPO adduct was volatile enough to be lost to the gas phase during evaporation, and is therefore not recovered in the deuterated solvent. The spin trap *N-tert*-butyl- $\alpha$ -phenylnitrone (PBN) was used to capture CIs as opposed to DMPO, given the fact that PBN is less volatile and would therefore form a lower volatility adduct, minimising loss *via* evaporation. In this section, it is assumed that DMPO and PBN will react in the same way with the CI as they are characterised by the same nitron functional group. An extensive analysis of the NMR data can be found in Appendix 1, and will be briefly presented here. A prediction of the



$^1\text{H}$  and  $^{13}\text{C}$  signals for the NMR spectra of both  $\text{CI}_\text{K}$ -PBN and  $\text{CI}_\text{A}$ -PBN, simulated using Chemdraw v10.0, can be found in Appendix 1 (Table 9.1). NMR analysis of the purified CI-PBN adducts confirmed the presence and the structure of the theoretically postulated 6-membered ring adducts formed from the 1,3-dipolar cycloaddition between both  $\text{CI}_\text{K}$  and  $\text{CI}_\text{A}$  with the spin trap PBN.

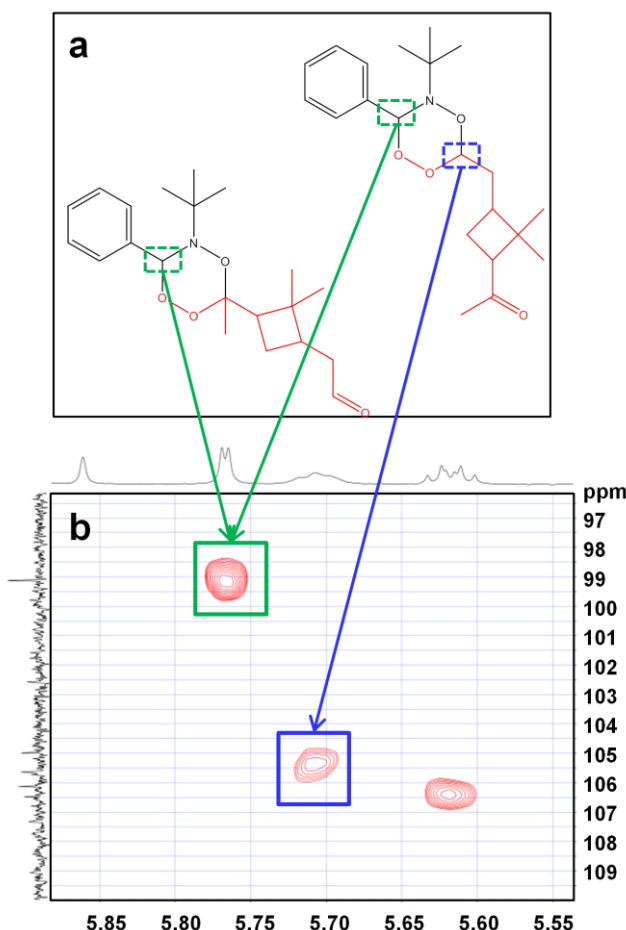


**Figure 3.7** – (a) proposed structures of the adducts formed between the CIs generated from  $\alpha$ -pinene ozonolysis ( $\text{CI}_\text{A}/\text{CI}_\text{K}$ ) and the spin trap PBN and (b) HSQC-NMR spectrum showing the correlation between the two protons with the carbon to which they are attached to in the 6-membered ring formed between  $\text{CI}_\text{K}$  and DMPO (blue) and the correlation between the proton and the carbon to which it is attached to in the 6-membered ring formed between  $\text{CI}_\text{A}$  and DMPO (green).

Figure 3.7 shows the characteristic triplet corresponding to the proton of the  $-\text{CH}-$  group between the two oxygen atoms in the heterocycle, as well as the signal corresponding to the  $-\text{CH}-$  group between the nitrogen and oxygen atom of the heterocycle. This is in good agreement with the predicted  $^1\text{H}$  shifts (Table 9.1).

The extensive NMR characterisation (Appendix 1) indicates the presence of the  $\text{CI}_\text{K}$ -PBN adduct, in which the CI reacts *via* a 1,3 cycloaddition to the nitron functional group of

---

the PBN spin trap to form a 6-membered heterocycle (mechanisms show in Figure 3.5). The presence of CI<sub>A</sub> is also shown due to the presence of two different cyclobutane groups and two different *t*-butyl groups in the HSQC-NMR depicted in Appendix 1 (Figure 9.6). The lower intensity of the peaks uniquely associated with CI<sub>A</sub>-PBN indicates a lower yield of the CI<sub>A</sub>-PBN adduct compared to that of CI<sub>K</sub>-PBN, or a more rapid degradation of the CI<sub>A</sub>-PBN adduct during the timescale of the total NMR analysis of approximately 12 hours.

### 3.3.2 Quantification of $\alpha$ -pinene CI-DMPO Adducts in the Gas Phase

Using the fully optimised flow tube set-up detailed in Section 3.2.8, Criegee intermediates generated from the ozonolysis of  $\alpha$ -pinene were trapped with DMPO, and the CI-DMPO adduct was analysed on-line using PTR-ToF-MS.  $\alpha$ -pinene ozonolysis was chosen as the model oxidation regime due to its ease of handling, as well as its extensively characterised chemistry<sup>167</sup>.

The 1:1 adduct CI-DMPO, with the elemental formula C<sub>16</sub>H<sub>28</sub>NO<sub>4</sub><sup>+</sup> was detected by PTR-ToF-MS at  $m/z$  298.20 (Figure 3.9 (a)) using the optimised experimental conditions detailed in Section 3.2.9, with an estimated reaction time of 50 s in this particular experiment. Figure 3.8 (b) shows the time trace of the peak corresponding to the  $\alpha$ -pinene CI-DMPO adduct, as well as the control experiment (O<sub>3</sub> + DMPO), which exhibits a much lower signals than that of the sample including  $\alpha$ -pinene, DMPO and O<sub>3</sub>.

Upon switching on the O<sub>3</sub> lamp after 20 minutes, the CI-DMPO adduct mixing ratio initially increases to ~2 ppb, before reaching a steady-state mixing ratio of ~1.6 ppb after 25 minutes. This initial increase before reaching a plateau is likely due to the heating-up period of the lamp, which takes ~ 30 minutes for the O<sub>3</sub> output from the lamp to plateau, and therefore the concentration and reaction conditions will vary during this time period.

The CI-DMPO signal observed is relatively stable for hours, and highly repeatable in this reaction system, with typical variations of  $\pm 0.5$  ppb as observed in multiple repeats. The observed mixing ratio of the CI-DMPO is approximately five orders of magnitude lower than that of the mixing ratio s of the reactants, which were 293, 340 and 150 ppm for O<sub>3</sub>,  $\alpha$ -pinene and DMPO respectively. The detection limit of the technique with respect to the CI-DMPO adduct was determined to be 0.03 ppb using the  $3\sigma_{bl}$  method, estimated by calculating 3 times the standard deviation of the signal from the average signal. The

quantification limit was estimated to be 0.10 ppb using the  $10_{\text{obl}}$  method, estimated by calculating 10 times the standard deviation of the signal from the average signal, with a time resolution of 10s.

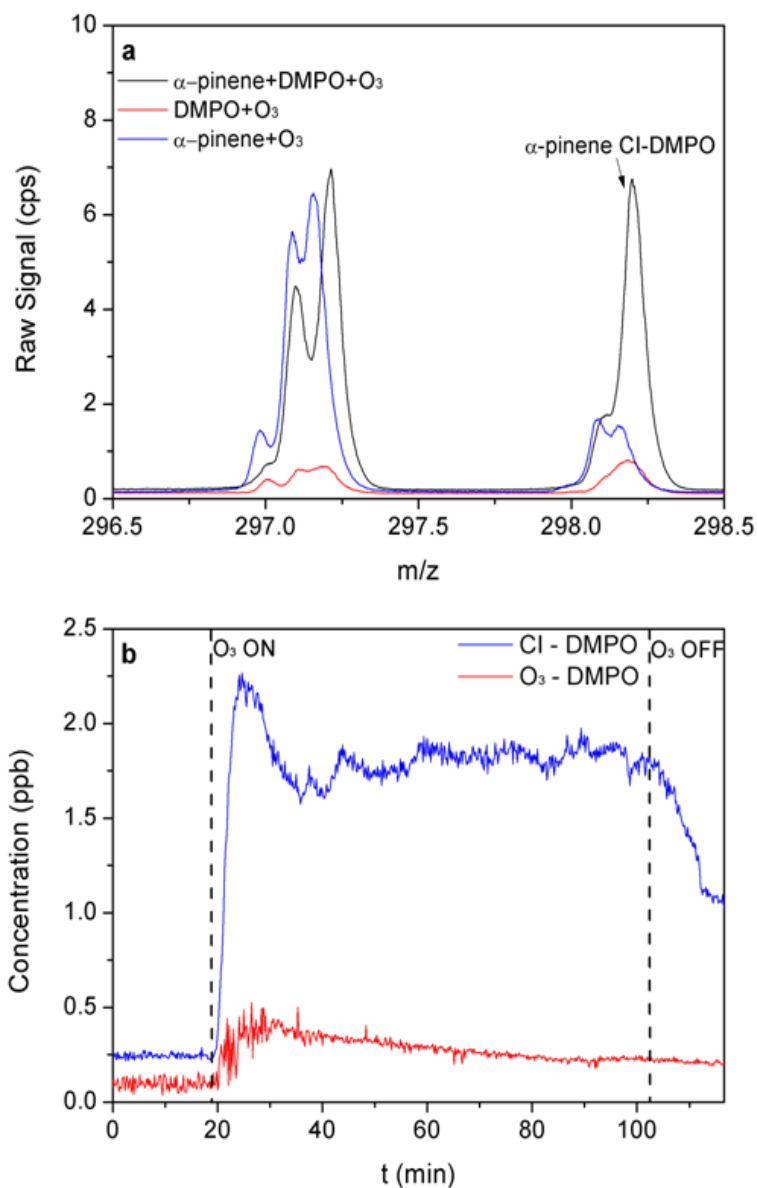


**Figure 3.8** – Detection of CI-DMPO in the gas phase using PTR-ToF-MS. (a) Mass spectrum at steady-state showing the  $m/z$  298.20 peak, as well as two control experiments (DMPO + O<sub>3</sub>,  $\alpha$ -pinene + O<sub>3</sub>). The  $m/z \sim 297$  peak is also shown, the <sup>13</sup>C of which may contribute to the  $m/z$  298.20 signal. (b) Time trace of the mass corresponding to the CI-DMPO adduct (blue) as well as the time trace of a control experiment (DMPO + O<sub>3</sub>, no  $\alpha$ -pinene present).

A simulation of this oxidation regime was performed using the Master Chemical Mechanism (MCM)<sup>170</sup> v.3.3.1 to compare measured mixing ratios of CI-DMPO adduct with theoretically expected mixing ratios of CIs. Figure 3.9 displays the time evolution

of stabilised Criegee intermediates (SCI), excited state Criegee intermediates (CI\*) as well as the change in mixing ratio of the precursors  $\alpha$ -pinene and  $O_3$ .

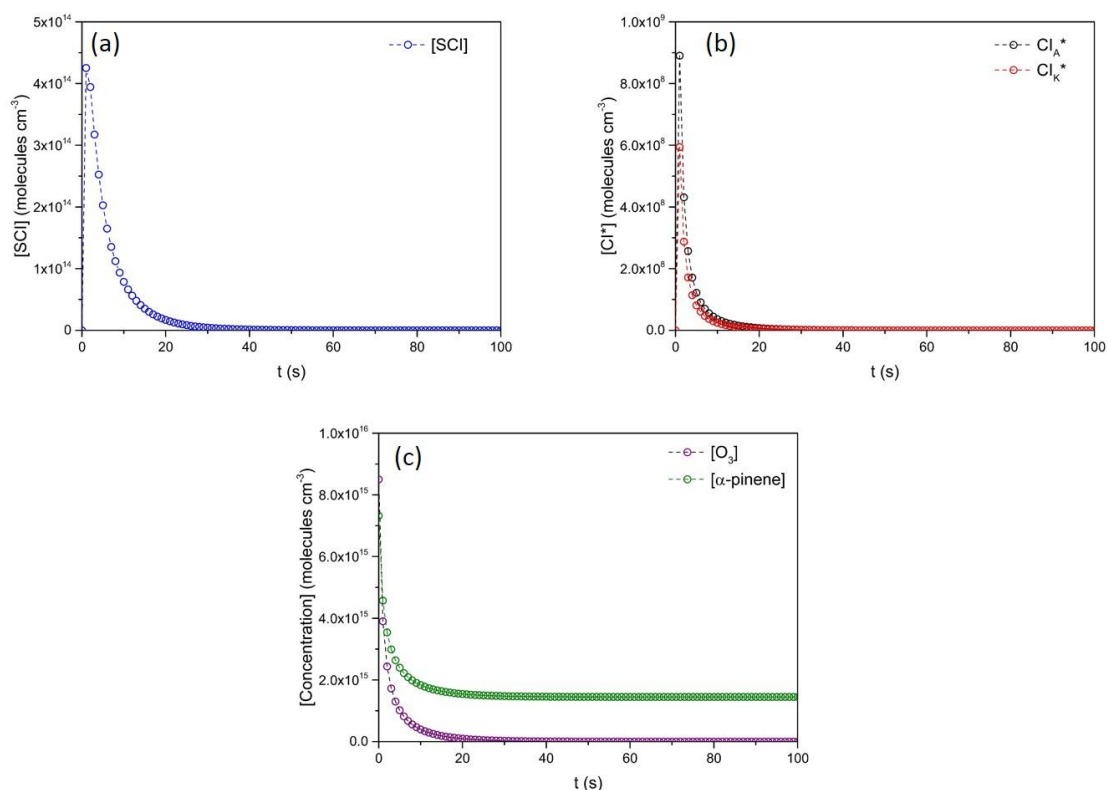


**Figure 3.9** – Modelling of the  $\alpha$ -pinene ozonolysis using the MCM v.3.3.1. Initial reactant concentrations for the modelling run were 2 ppm  $H_2O$ , 340 ppm  $\alpha$ -pinene and 290 ppm  $O_3$ . (a) mixing ratio  $s$  of the  $CI_K$  stabilised Criegee intermediate (SCI), (b) modelled output of the excited state Criegee ( $CI^*$ ) and (c) simulated decay in mixing ratio of both  $O_3$  and  $\alpha$ -pinene.

Figure 3.9 illustrates the (a) modelled mixing ratio of the collisionally stabilised Criegee intermediate (SCI), (b) thermally hot Criegee Intermediates ( $CI^*$ ) (c) the change in mixing ratio of both precursors  $\alpha$ -pinene and  $O_3$  over time. The model run under dry conditions ( $\sim 4 \times 10^{13}$  molecules  $cm^{-3}$   $H_2O$ ) suggests that within 50 s, the approximate reaction time between  $\alpha$ -pinene and DMPO before being introduced into the T-connection containing DMPO, almost all of the  $CI_A^*$  and  $CI_K^*$  excited state Criegee intermediates will have been lost either *via* unimolecular decomposition or isomerisation<sup>171</sup>, or alternatively through collisional quenching to form the SCI.

The MCM only considers SCI formed from the  $CI_K^*$  excited state Criegee, even at low humidity. This is in agreement with previous studies, which have suggested a SCI yield

of typically < 40 % from this reaction indirectly by considering the OH yield from this reaction<sup>67,172–174</sup>.

The concentration of SCI<sub>K</sub> after 50 s was estimated to be  $2.88 \times 10^{11}$  molecules cm<sup>-3</sup> in the model, in reasonable agreement with the observed steady state concentration of the CI-DMPO adduct of  $3.2 \times 10^{10}$  molecules cm<sup>-3</sup>. The discrepancies in the modelled and observed values may be due to uncertainties in the AtChem model, given the fact it assumes instantaneous mixing of all reactants in the system. As well as this, the MCM is designed to gain accurate HO<sub>x</sub> yields from such reactions, and as such, there may be certain inaccuracies associated with the estimation of SCI yields from this reaction, although this is purely speculative and will not be further discussed in this thesis.

### Potential Interferences regarding Quantification

There remain several aspects of the method that need to be properly addressed in order to improve its quantitative capabilities. To confidently quantify the mixing ratio of the CI-DMPO adduct, a suitable standard should be used to calibrate the PTR-ToF-MS. This proves difficult in practice, because the CI-DMPO adduct is not sufficiently stable overtime. The reaction kinetics between the CI and DMPO are currently unknown, and it is not known what fraction of the CI formed is actually trapped by the DMPO. It is very likely that the trapping efficiency of DMPO towards the CI is < 100 %, and therefore this technique may not fully quantify the absolute yield of CIs in this ozonolysis regime. The reaction kinetics should be further investigated in future studies, to gain a perspective on the quantitative capabilities of this technique.

The CI-DMPO adduct, once formed, will also have a lower volatility than both individual species combined, and this may lead to additional losses *via* adsorption of the adduct to the walls, or indeed to the surfaces of SOA particles generated from the ozonolysis of  $\alpha$ -pinene, therefore reducing its mixing ratio in the gas phase and affecting quantification.

In this complex chemical system, several organic compounds have the same molecular formula as the CIs, for example, pinonic acid, dioxirane and vinyl hydroperoxide, which are all produced from the ozonolysis of  $\alpha$ -pinene. If these compounds are reactive towards DMPO, then the PTR-ToF-MS traces detected might not only include the CI-DMPO adduct, but also interferences from other compounds as PTR-ToF-MS cannot distinguish between different isomers. Dioxirane can potentially react with the spin trap, but would not produce a stable adduct according to the mechanism proposed by Adam *et al.*<sup>175</sup>.

---

Vinyl hydroperoxides generated from ozonolysis are typically produced with excess internal energy, and promptly decompose to liberate  $\cdot\text{OH}$  radicals.<sup>176</sup> Due to the typically large OH yield from this reaction, with studies estimating the percentage yield relative to the reagent starting concentrations to be between  $0.76\text{--}0.81 \pm 0.23$ <sup>67,172,173</sup>, it is likely that a substantial amount of hydroperoxide will be produced. The vinyl hydroperoxide generated from this regime is isomeric with respect to the CI, and could potentially undergo reaction with the DMPO, although this effect would need to be investigated in more detail. There is also potentially interference from the peak at  $\sim 297$  Da (Figure 3.9 (a)), given the fact there could be a contribution towards the peak at  $m/z$  298.20 from the  $^{13}\text{C}$  isotope of the species at 297 Da, although a multipeak Gaussian fitting of the data and the PTR-ToF-MS resolution of  $\sim 5000$  likely minimises the impact of this effect.

Despite these potential caveats, this novel technique has been applied to unambiguously identify the CIs *via* detection of CI-DMPO adducts. This study demonstrates for the first time detection and characterisation of CIs generated from the ozonolysis of  $\alpha$ -pinene. Furthermore, the method potentially offers a novel, laboratory-based technique to study CIs in complex chemical systems. In principle, the technique can characterise CIs in even more complex organic mixtures, from VOC precursors that generate multiple CIs of differing masses, depending on how the primary ozonide formed in these ozonolysis regimes decomposes. This could offer an insight into the fate of CIs in more atmospherically relevant gas phase mixtures. The next chapter explores the range of CI structures this new method can detect and the potential of the method to detect simultaneously several CIs from multiple VOCs.

### 3.3.3 Simultaneous Quantification of Various CI-DMPO Adducts from Multiple VOC Precursors

This section will expand on the study of CI-DMPO adducts generated from the ozonolysis of  $\alpha$ -pinene, by measuring CIs from a series of biogenic and anthropogenic VOC precursors:  $\beta$ -pinene, limonene, methacrolein, cis-2-hexene, styrene and a mixture of multiple VOCs ( $\beta$ -pinene and cis-2-hexene) in the same experiment. The aim of these series of experiments was to further probe the capability of the technique developed, and described in Section 3.2.2, to characterise multiple CIs simultaneously.

DFT theoretical calculations were again performed by Maurizio Bruschi to probe the reaction mechanism, energy barriers, and adduct stability of the various CIs with DMPO.

Ozonolysis experiments with the various VOC precursors were conducted using a flow tube set-up that was re-optimised after the initial experiments detailed in Section 3.2.2. The CIs that are generated from these various VOCs, and their acronyms for reference in this section, are displayed in Figure 3.10.

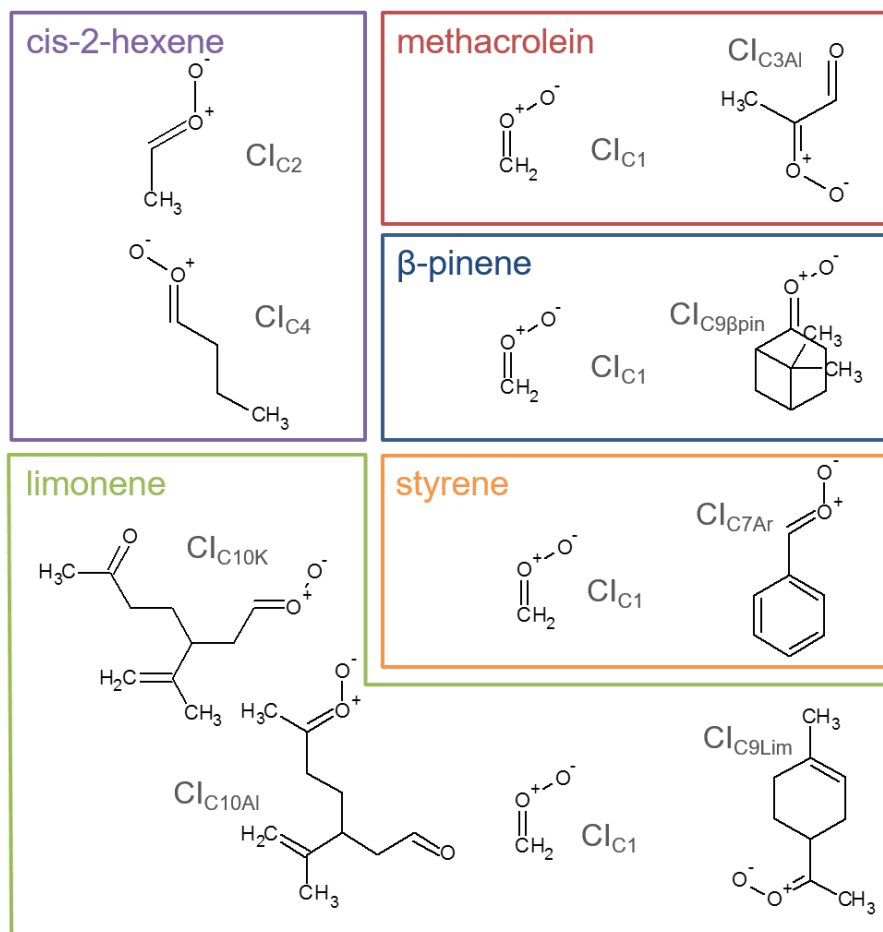


**Figure 3.10** –Molecular structures and acronyms for reference of a variety of CIs generated from the ozonolysis of cis-2-hexene, methacrolein,  $\beta$ -pinene, limonene and styrene. Reproduced from<sup>177</sup>.

### Further optimisations of the Experimental Set-up

Due to the use of some VOC precursors with different physical properties, some experimental optimisations were performed. The ozonolysis reaction takes place in a flow tube reaction vessel, which is maintained at ambient temperature ( $\sim 16\text{--}18^\circ\text{C}$ ) and pressure, and under dry conditions (relative humidity  $< 2\%$ ). The experimental apparatus is largely the same as that described in Figure 3.1, and only alterations to the set-up will be discussed here.

The olefinic precursors were evaporated from a 25 mL pear-shaped flask filled with 0.5 mL of pure compound and introduced continuously in the flow tube using  $\text{N}_2$ . For

experiments with cis-2-hexene and methacrolein, due to the fact that they are more volatile compared to the other VOC precursors, the pear shaped flask was submersed in a dry ice/acetonitrile bath ( $-41^{\circ}\text{C}$ ) in order to maintain a lower steady-state mixing ratio of these compounds in the flow tube. The other VOCs were maintained at ambient temperature. Ozone was produced in the same manner as described in Section 3.2.8. The UV lamp used in this study produced a lower amount of ozone compared with the previous study on  $\alpha$ -pinene ozonolysis, reaching a maximum mixing ratio in the reaction vessel of  $\sim 18$  ppm measured using a UV photometric ozone analyser (Thermo Scientific model 49i).

The residence time in the flow tube was previously estimated to be 50 seconds. This was an upper limit, assuming that the mixing of the reactants was occurring for the entire volume of the flow tube, and that  $\text{O}_3$  was uniformly mixed at the point of contact with the VOC precursor. This value was re-calculated: given the fact that  $\text{O}_3$  is injected into the flow tube through a narrow diameter glass tube, as illustrated in Figure 3.11.

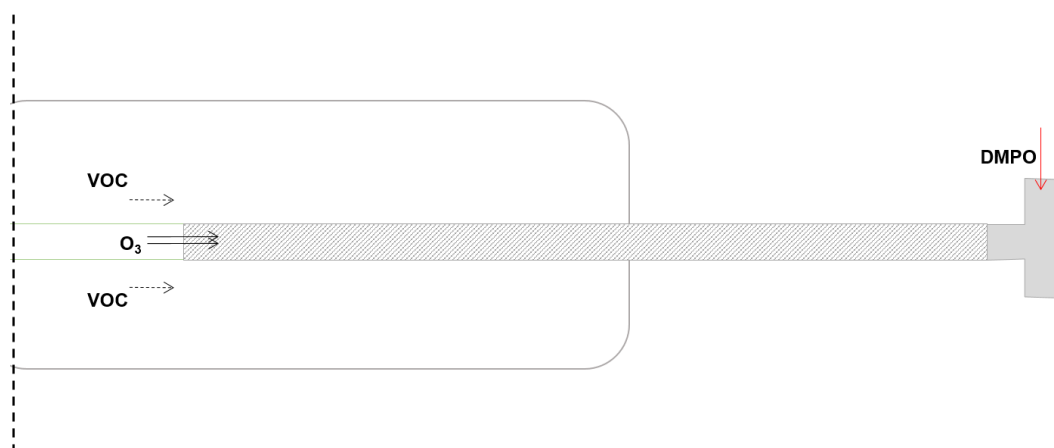


**Figure 3.11** - Schematic of the final section of the flow tube showing the point in which  $\text{O}_3$  is mixed with the olefinic VOC and the ozonolysis reaction occurs up to the mixing point with DMPO. The hatched rectangle shows the area considered for calculation of the residence time in the flow tube.

The  $\text{O}_3$  will enter the reaction vessel at a velocity approximately 50 times greater than that of the VOC, effectively creating a jet through the reaction vessel as demonstrated by the hatched area in Figure 3.11. Therefore, the  $\text{O}_3$  and VOC precursor would not be uniformly mixed, which complicates the calculation of the reaction time.

In this study, it is assumed that the lower limit for the reaction time would correspond to the hatched area in Figure 3.11, which was calculated to be  $\sim 3$  s total reaction time



between  $O_3$  and the VOC. This is only a first order estimate, as to extensively characterise the reaction time would require modelling of the flow tube set-up, which is beyond the scope of this study. This value was re-optimised after the discussion in Section 3.3.2, and will be used in this discussion.

### DFT Calculations of CI-DMPO Adducts and Proton Reaction Rate Constants

One issue encountered in Section 3.3.2 was the lack of knowledge regarding the ionisation efficiency of the CI-DMPO adducts, which can therefore lead to inaccurate quantification. Appendix 2 contains information on the calculation of proton transfer reaction rate constants of a range of CI-DMPO adduct. These values were used for quantification of the adducts using PTR-ToF-MS.

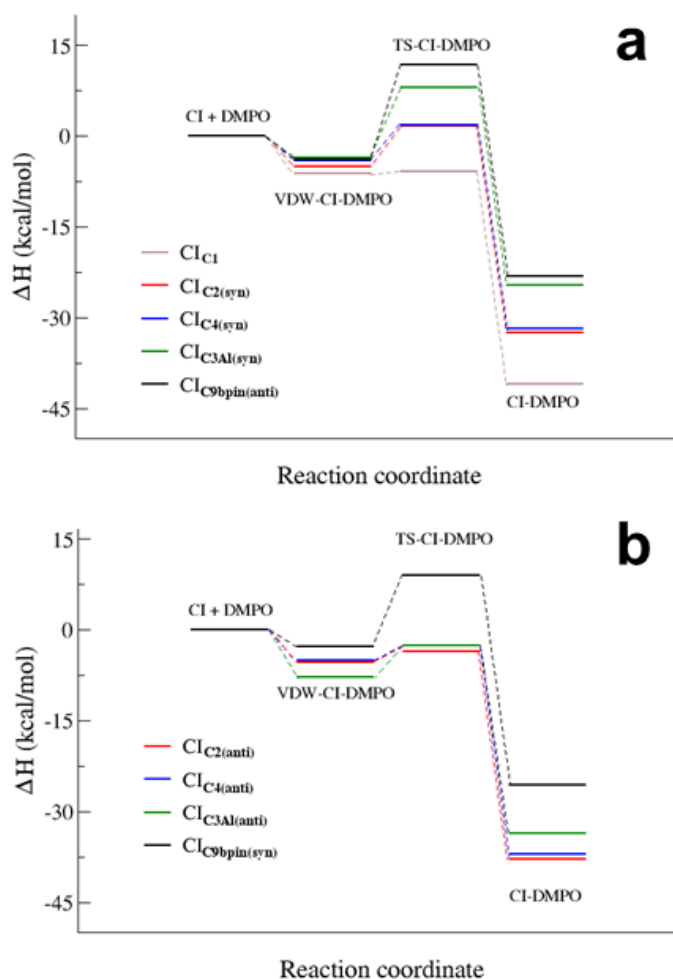


**Figure 3.12** - . Reaction energy profiles of the CI + DMPO  $\rightarrow$  CI-DMPO reactions of CI<sub>C1</sub>, CI<sub>C2</sub>, CI<sub>C4</sub>, C<sub>9βpin</sub> and CI<sub>C3Al</sub>, calculated starting from the (a) more stable and (b) the less stable conformation of each adduct.

---

The measurement method used in this study is based on the stabilisation of the highly reactive CIs using the spin trap DMPO. Assessing the quantitative capability can be challenging as the kinetics of formation of the CI-DMPO adducts and the stability of such adducts are unknown. To support and aid interpretation of experimental results, the stability of the CI-DMPO adducts generated by the ozonolysis of  $\beta$ -pinene, cis-2-hexene and methacrolein, and the mechanism and energy barriers of their formation have been investigated by DFT calculations. These are extensively presented in Appendix 2 and will be discussed in brief here. Figure 3.12 summarises the results presented in Appendix 9.1.4, showing the reaction energy profiles for the formation of the CI-DMPO adducts starting from the CIs in the more stable (Figure 3.12a) and less stable (Figure 3.12b) conformations.

These results show that the reaction of the investigated CIs with DMPO occurs very rapidly, with the exception of  $\text{CI}_{\text{C9}\beta\text{pin}}$  for which, in both conformations the activation energies are larger than those calculated for the other CIs. In addition, all reactions are strongly exothermic, but with the  $\Delta H_r$  value that becomes significantly less negative with increasing the number of substituents of the carbonyl oxide carbon atom (i.e. the  $\Delta H_r$  of the  $\text{CI}_{\text{C9}\beta\text{pin}}$ -DMPO adduct is more than  $15 \text{ kcal mol}^{-1}$  higher than that of  $\text{CI}_{\text{C1}}$ -DMPO).

It also worth noting that for all CIs investigated the less stable conformer has a more favourable energy profile. In particular,  $\text{CI}_{\text{C3Al}}$ , which is characterised by the larger difference in stability of the conformers, also features the larger change in the reactivity of such conformers. A similar behaviour has been observed experimentally by Taatjes *et al.*<sup>45</sup> who reported that the *anti* (less stable) conformer of acetaldehyde oxide is more reactive than the *syn* (more stable) conformer towards both  $\text{H}_2\text{O}$  and  $\text{SO}_2$ .

### Detection of CIs from the Ozonolysis of Biogenic and Anthropogenic VOCs

Using the experimental set-up first described in Section 3.2.8, the conditions of which were re-optimised for this study, a variety of CI-DMPO adducts were detected using PTR-ToF-MS. The adduct formed between the spin trap DMPO and  $\beta$ -pinene CIs, with the elemental formulae  $\text{C}_{15}\text{H}_{26}\text{NO}_3^+$  ( $m/z = 268.1907$ ) and  $\text{C}_7\text{H}_{14}\text{NO}_3^+$  ( $m/z = 160.0968$ ) were detected by PTR-ToF-MS as illustrated in Figure 3.13 (a). This is in agreement with previous studies using IR spectroscopy<sup>56</sup>, and the previous work detailed in Section 3.2.2.

The detected mixing ratios of both CI-DMPO adducts are 3-4 orders of magnitude lower than that of the reactants, which were 18, 83 and 110 ppm for  $\text{O}_3$ ,  $\beta$ -pinene and DMPO

respectively. The CI-DMPO adduct mixing ratios in general are stable over timescales of an hour or more at steady state (Figure 3.13), and are well reproduced, with a typical variation of  $\pm 25\%$  observed over multiple repeats. This error is illustrated as a lightly shaded confidence bar in Figure 3.13.

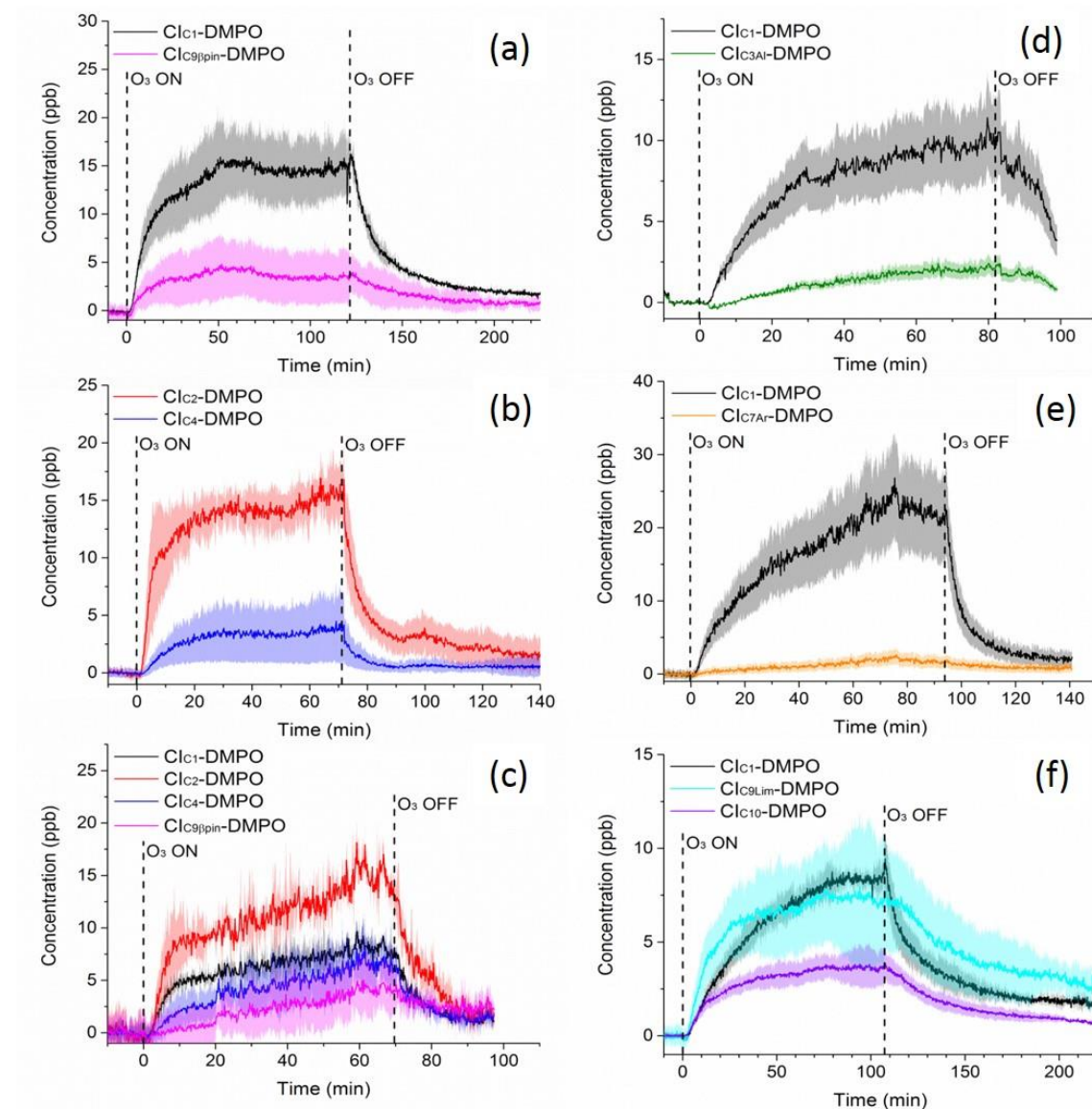


**Figure 3.13** - Time-series of CIs formed from the ozonolysis of (a)  $\beta$ -pinene, (b) cis-2-hexene, (c) a mixture of  $\beta$ -pinene and cis-2-hexene, (d) methacrolein, (e) styrene and (f) for the limonene ozonolysis, the isomers C<sub>10</sub>Al and C<sub>10</sub>K have identical masses and therefore cannot be resolved using this technique, and are given in one time trace (C<sub>10</sub>). Shading represents the variability observed over 3 repeats of each experiment, with the solid line representing the average concentration of CI-DMPO adduct observed.

The slow initial increase in CI-DMPO mixing ratio is again likely due to the warming up period of the UV lamp, where it takes typically 20-30 minutes to reach a steady state

---

mixing ratio of O<sub>3</sub>, therefore altering the gas phase chemistry during this period. Upon switching off the UV lamp, and ceasing the production of O<sub>3</sub>, there is typically a slow decay in the signal associated with the CI-DMPO adducts. This is likely due to memory effects in the system, as the fairly low volatile CI-DMPO adduct can adsorb on to the walls of the reaction system (this can be directly observed by physically looking at the PTFE tubing), and there is in most cases some CI-DMPO adduct adsorbed in the inlet of and throughout the PTR-ToF-MS.

Similarly, in the case of ozonolysis of cis-2-hexene, the two predicted CI-DMPO adducts were detected, with the elemental formula C<sub>10</sub>H<sub>20</sub>NO<sub>3</sub><sup>+</sup> ( $m/z = 202.1438$ ) and C<sub>8</sub>H<sub>16</sub>NO<sub>3</sub><sup>+</sup> ( $m/z = 174.1125$ ) (Figure 3.13 (b)). An additional experiment with these species was performed, where both β-pinene and cis-2-hexene were introduced into the reaction vessel.

All four expected CI-DMPO adducts were detected in this experiment (Figure 3.13 (c)), and reach a relatively stable concentration at steady state, as well as demonstrating good repeatability. This thesis represents, to the author's knowledge, the first time in which detection of CIs from multiple VOC precursors has been successfully achieved, again demonstrating the capabilities of this technique to probe the fate of multiple CIs in complex organic mixtures. Observed steady-state mixing ratios of the cis-2-hexene CI-DMPO adducts are higher than that of β-pinene, which is likely due to the fact that cis-2-hexene has a higher steady state mixing ratio (153 ppm) compared to that of β-pinene (96 ppm) in this experiment. Furthermore, this study has been expanded to look at VOCs with different physical and chemical properties. Methacrolein, which is a first-generation oxidation product of the ozonolysis of isoprene, underwent ozonolysis in the flow tube reaction vessel. The predicted CI-DMPO adducts, CI<sub>C1</sub>-DMPO and CI<sub>C3Al</sub>-DMPO, were both observed in this experiment (Figure 3.13 (d)). This was also the case for styrene, an aromatic anthropogenic VOC. The predicted adducts, CI<sub>C1</sub>-DMPO and CI<sub>C7Ar</sub>-DMPO were both detected using PTR-ToF-MS (Figure 3.13 (e)). These results show that this technique is capable of characterising CIs generated from species with varying volatilities, as well as anthropogenic and biogenic VOC precursors.

Figure 3.13 (f) illustrates the experiment where limonene was introduced into the flow tube and ozonolysed. Limonene can generate four different CIs (Figure 3.10) *via* the attack of O<sub>3</sub> across the endocyclic or exocyclic double bonds of limonene. The endocyclic bond liberates two CI isomers, CI<sub>C10K</sub> and CI<sub>C10Al</sub> depending on the decomposition of the

primary ozonide initially formed. This technique cannot distinguish between the  $\text{CI}_{\text{C10K}}\text{-DMPO}$  and  $\text{CI}_{\text{C10Al}}\text{-DMPO}$  adducts given that they have the same mass, so they are represented as one trace ( $\text{CI}_{\text{C10}}\text{-DMPO}$ ). The literature suggest that the reaction of ozone with limonene predominately proceeds *via* attack at the endocyclic bond compared to the exocyclic bond (95:5).<sup>178</sup> Figure 3.13 (f) shows that the  $\text{C}_1\text{-DMPO}$  and  $\text{C}_{9\text{lim}}\text{-DMPO}$  adducts are both observed at higher mixing ratios than that of the  $\text{C}_{10}\text{-DMPO}$ . In this experiment,  $\text{O}_3$  is in excess (18 ppm compared to 6 ppm limonene) which would promote more reaction across the exocyclic bond, therefore liberating more  $\text{C}_1$  and  $\text{C}_{9\text{Lim}}$  CIs that can be subsequently scavenged by DMPO. There may also be a variability in the trapping efficiency associated with the different CIs that lead to the observed mixing ratios of the various CI-DMPO adducts. The DFT calculations in Appendix 9.1.4 suggest that there is a strong dependence on the number of carbons in the backbone of each CI that alters the energetics of the reaction, and the smallest  $\text{CIC}_1$  is generally observed in the highest mixing ratio in each experiment. This result highlights the need for more research into the kinetics and reactivity of differing CIs with DMPO, so that the quantitative capability of the technique can be improved.

The  $\text{C}_{10\text{Lim}}\text{-DMPO}$  may also form a lower volatility adduct, which may be more readily lost *via* surface adsorption than the other adducts, again affecting quantification. There was no evidence of second generation CIs, formed from the ozonolysis of first generation oxidation product from ozonolysis of limonene. It is likely that these species would have a sufficiently low volatility to be lost from the gas phase into the particle phase, or that the adduct formed would have a sufficiently low volatility to be lost *via* surface adsorption. Furthermore, the short estimated reaction time ( $\sim 3$  s) may well not be long enough to allow substantial production of second-generation CIs.

Due to the large concentrations of precursors used in this study, the PTR-ToF-MS detector is saturated and therefore the estimated concentrations of the VOC precursors may be underestimated with respect to their actual concentrations in the flow tube, further complicating any absolute quantification. Several other aspects of the experimental set-up need to be investigated further in order to improve the quantification accuracy of CIs.

The fragmentation patterns of the CI-DMPO adducts in the PTR-ToF-MS is currently unknown, and this affects the ability to accurately quantify the adducts. When investigating larger CIs, loss of the large CI-DMPO adducts to the wall may lead to an underestimation of the CI steady state concentration, and therefore wall losses in the

---

system should be properly characterised for these species. There is also a substantial yield of SOA generated from these ozonolysis regimes, which increases the surface area onto which the CI-DMPO adducts can be lost. The kinetics of the reaction between all of the CIs studied in this work and DMPO are still entirely unclear, and this will need to be fully investigated. One way to probe the kinetics of the CI-DMPO with smaller CIs would be to utilise the gem-diodoalkane route to generating CIs. This is a “cleaner” chemical system, where the yield of CIs is much better defined and can be used to provide useful kinetic data<sup>46</sup>. Using this precursor, the chemical kinetics of small CIs with DMPO could be determined.

Despite this, this study represents the first time in which CIs have been detected from the ozonolysis of methacrolein, limonene, styrene and cis-2-hexene. It also represents the first time in which CIs from two different VOC precursors have been simultaneously characterised in a complex organic mixture. These results demonstrate the potential of this technique to probe the fate of multiple CIs, and indeed other reactive intermediate species, in complex atmospherically relevant organic mixtures.

### **3.3.4 Comparison between Experimental Results and MCM modelling**

To compare our experimental results and test the quantification capability of the technique in our experimental conditions, experimental results have been compared with MCM model simulations. The complexity of the entire ozonolysis reaction scheme is vast, and a plethora of compounds produced in this system can react with CIs, including the carbonyl compound produced in a 1:1 ratio during the first steps of the reaction. Whilst not a fully explicit chemical mechanism, the MCM can help in understanding the complexity of the system and evaluate the amount of both excited and stabilised CIs available at the outlet of the flow tube (3 seconds reaction time) in the experiments performed. The results of the AtChem/MCM modelling simulating the experiment of ozonolysis of the VOC mixture containing  $\beta$ -pinene and cis-2-hexene are reported in Figure 3.14. The results show the decay of  $\beta$ -pinene, cis-2-hexene and ozone with a time resolution of one second (Figure 7a) in which it can be seen that after a three seconds reaction time in the flow tube, concentrations of  $\beta$ -pinene and cis-2-hexene are still very high as ozone is not in excess and its concentration in turns rapidly decreases. It can also be seen in Figure 3.14 (c) that excited CIs decompose quickly in the flow tube and their mixing ratio *s* in our steady-state reaction system is lower than the detection limits ( $\sim 30$

ppt). Conversely, detectable amounts in the ppb range of SCIs are still present at the end of the flow tube (Figure 3.14 (d)) and can therefore be detected by our technique.

The results of the AtChem/MCM modelling for all other VOCs are reported in the Appendix 2, showing the time-series of VOCs and ozone consumption, and excited and stabilised CIs production. In general, the results of the AtChem/MCM model show that the ozonolysis reaction is very fast in our experimental conditions and the excited CIs decompose quickly in the flow tube so that their mixing ratio s (mostly below ppb levels) are estimated to be far below detection limits at the mixing point with DMPO (after 3 seconds reaction time) for all experiments. On the contrary, detectable amounts in the ppb range of SCIs are still present at the end of the flow tube and they can therefore be trapped by the DMPO. Our results show that the method used here is suitable for detection of SCIs in laboratory experiments. Further studies are needed to investigate the possibility of detecting excited CIs.

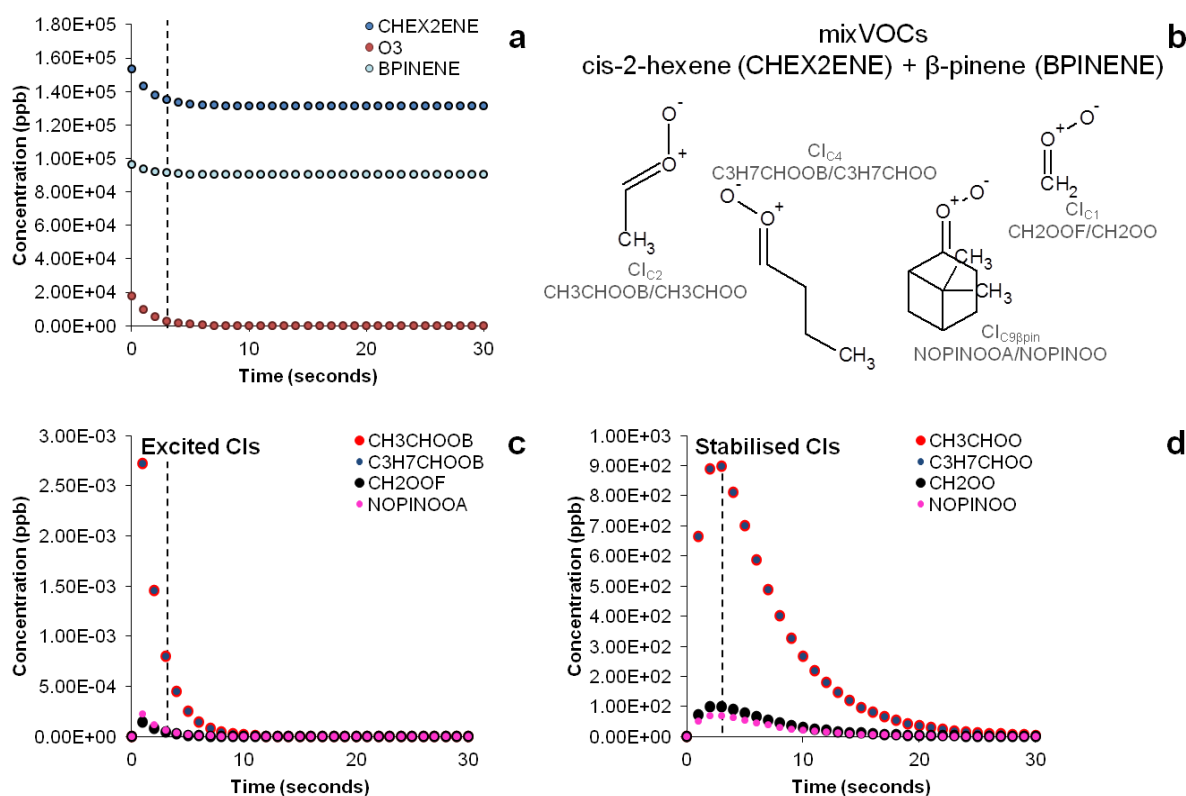


**Figure 3.14** - Time evolution of precursors (a), structures and acronyms of CIs (b) and time evolution of excited CIs (c) and stabilised CIs (d) in the ozonolysis of a VOC mixture of  $\beta$ -pinene and cis-2-hexene determined by the MCM model simulating our experimental conditions. Dashed vertical bars indicate reaction time (3 seconds) in our steady-state flow tube experiments during which ozone reacts with the olefinic precursors producing CIs before they are mixed with the DMPO.

The comparison between the theoretically expected mixing ratio of SCIs and experimental measurements of CI-DMPO adducts is reported in Table 3.1. Results show that measured mixing ratios of CI-DMPO adducts are at least one order of magnitude lower than the modelled mixing ratios of SCIs from the AtChem/MCM model.

**Table 3.1-** Initial and steady state mixing ratios of VOCs in our experiments and comparison between experimental measurement and expected mixing ratio of CIs from MCM modelling for all VOCs examined in this study and the VOC mixture.

VOCs	Measured [VOC] <sub>0</sub> (ppm) <sup>a</sup>	Measured [VOC] <sub>ss</sub> (ppm) <sup>b</sup>	CIs-DMPO	Measure d [CIs- DMPO] <sub>s</sub> s (ppb) <sup>c</sup>	Measured ratios [CIs- DMPO]:[ VOC] <sub>0</sub>	Measured fraction (%) of CIs- DMPO <sup>c</sup>	Modell ed [SCIs] (ppb)	Model led fraction (%) of SCIs
β-pinene	83	65±2	CI <sub>C1</sub> -DMPO	14.8±3.6	2·10 <sup>-04</sup>	79.6±33.5	250	59.1
			CI <sub>C9βpin</sub> -DMPO	3.8±2.8	5·10 <sup>-05</sup>	20.4±16.6	173	40.9
cis-2-hexene	120	24±1	CI <sub>C2</sub> -DMPO	14.5±1.9	1·10 <sup>-04</sup>	80.6±22.7	875	50
			CI <sub>C4</sub> -DMPO	3.5±2.6	3·10 <sup>-05</sup>	19.4±15.2	875	50
mixVOCs:								
β-pinene	96	55±13	CI <sub>C1</sub> -DMPO	6.8±1.1	7·10 <sup>-05</sup>	24.3±7.8	101	5.1
			CI <sub>C9βpin</sub> -DMPO	2.6±2.4	3·10 <sup>-05</sup>	9.3±9.0	69	3.5
cis-2-hexene	153	88±6	CI <sub>C2</sub> -DMPO	11.8±1.6	8·10 <sup>-05</sup>	42.1±13.1	897	45.7
			CI <sub>C4</sub> -DMPO	4.9±2.2	3·10 <sup>-05</sup>	17.5±9.3	897	45.7
methacrolein	838	369±419	CI <sub>C1</sub> -DMPO	8.7±1.3	1·10 <sup>-05</sup>	84.5±19.4	334	93.8
			CI <sub>C3Al</sub> -DMPO	1.6±0.5	2·10 <sup>-06</sup>	15.5±5.6	22	6.2
limonene	6.3	1.4±0.3	CI <sub>C1</sub> -DMPO	7.8±0.6	1·10 <sup>-03</sup>	42.2±10.1	0.5	0.3
			CI <sub>C9Lim</sub> -DMPO	7.2±2.8	1·10 <sup>-03</sup>	38.9±17.5	0	0
			CI <sub>C10K/C10Al</sub> -DMPO	3.5±0.8	6·10 <sup>-04</sup>	18.9±6.1	169 <sup>d</sup>	99.7
styrene	78	8±3	CI <sub>C1</sub> -DMPO	18.6±5.2	2·10 <sup>-04</sup>	93.5±38.4	191	50
			CI <sub>C7Ar</sub> -DMPO	1.3±0.8	2·10 <sup>-05</sup>	6.5±4.5	191	50

<sup>a</sup> Concentration measured in dilution experiments. <sup>b</sup> Experimental uncertainty expressed as standard deviation between 2-3 repeated experiments. Larger uncertainties affect the most volatile VOCs for difficulties in maintaining a constant gas phase concentration in our experimental set-up. <sup>c</sup> Experimental uncertainty expressed as standard deviation between 2-3 repeated experiments. It does not take into account systematic errors due to unknown fragmentation pattern. <sup>d</sup> Referred to SCI<sub>C10K</sub>.

This may be explained with wall losses in the systems, which were not estimated. Efficiency of the spin trapping reaction should be good as ozone was generally the limiting reagent, to minimise reaction with DMPO, and DMPO was at least four orders of magnitude in excess with respect to the CIs. Nevertheless, reaction kinetics of SCIs with DMPO are unknown and this could partly explain the discrepancy between experimental measurements and modelling results. The discrepancy is larger for the



CI<sub>C9βpin</sub> for which the reaction with DMPO has a larger energy barrier decreasing the adduct formation rate (Figure 3.13).

In addition, the fragmentation pattern of CI-DMPO adducts in the PTR-ToF-MS is unknown which can lead to an underestimation of adduct mixing ratio. Additionally, the MCM is not a fully explicit mechanism and, for example, does not include self-reaction of SCIs, potentially overestimating SCI mixing ratios especially in the experimental conditions used here where mixing ratios of precursors were very high.

The measured ratios of CIs produced from the different precursors do not match particularly well with the theoretically calculated distribution from the AtChem/MCM model. For example, for the ozonolysis of β-pinene, the MCM model predicts a distribution of 59% of SCI<sub>C1</sub> and 41% of SCI<sub>C9βpin</sub> while the experimentally measured distribution is 80% of CI<sub>C1</sub>-DMPO and 20% of CI<sub>C9βpin</sub>-DMPO. This large discrepancy can be explained by considering the stability of the CI-DMPO adducts. The results of the DFT calculations show that the CI<sub>C1</sub>-DMPO is more stable than the CI<sub>C9βpin</sub>-DMPO. In addition, larger CIs, like CI<sub>C9βpin</sub> and CI<sub>C7Ar</sub>, were generally measured at lower mixing ratios than expected from the modelling, which might be because of the low volatility of these large CIs resulting potentially in wall losses. However, the temperature of the line after the DMPO mixing point was kept at 85°C to minimise condensation on the walls. Volatility-related artefacts could help explaining why there is a better match between measurements and modelling results for smaller CIs compared to the large β-pinene CI<sub>C9βpin</sub> and styrene CI<sub>C7Ar</sub>. In future studies, experimental strategies to improve quantification could aim to account for both stability of the CI-DMPO adducts, as adducts with lower stability tends to be more underestimated, and their volatility because some of the adducts have rather high molecular weights, and partitioning into the condensed phase may be non-negligible.

### 3.4 Conclusions and Future Outlook

The work in this chapter has focussed on the development of a novel, cost-effective laboratory based method that is uniquely capable of characterising multiple CIs in complex, atmospherically relevant chemical systems. The reactivity of the CI with the spin trap DMPO was investigated. A combination of analytical techniques including HPLC-ESI-HRMS, EPR, and NMR, supported by DFT theoretical calculations, suggest that the CI efficiently reacts with the DMPO, to generate a relatively stable non-radical

---

adduct comprising of a 6-membered heterocycle. The reaction mechanism was postulated to proceed *via* a 1,3-dipolar cycloaddition of the CI across the nitron functionality of the spin trap. Using a flow tube set-up, CIs in the gas phase generated from a model VOC system ( $\alpha$ -pinene + O<sub>3</sub>) were trapped using DMPO, and the subsequent adduct was measured on-line with PTR-ToF-MS. The 1:1 adduct CI-DMPO, with the elemental formula C<sub>16</sub>H<sub>28</sub>NO<sub>4</sub><sup>+</sup> was detected by PTR-ToF-MS at  $m/z$  298.20, representing the first time that CIs generated from  $\alpha$ -pinene ozonolysis have been characterised. The limit of detection of this technique was calculated to be 0.03 ppb ( $\sigma_{bl}$  method), with a typical repeatability of  $\pm 0.05$  ppb for  $\alpha$ -pinene CIs observed through multiple repeats.

This technique was then applied to simultaneously characterise multiple CIs generated from a variety of VOC precursors. CIs were characterised from the ozonolysis of  $\beta$ -pinene, limonene, styrene, methacrolein and cis-2-hexene, as well as chemical system containing both  $\beta$ -pinene and cis-2-hexene. All predicted CI-DMPO adducts were observed during the experiments, representing for the first time the characterisation of CIs from methacrolein, limonene, styrene and cis-2-hexene. It also represents the first time in which CIs from two different VOC precursors have been simultaneously characterised in a complex organic mixture. DFT calculations and MCM simulations helped to validate both the CI-DMPO stability and reactivity, as well as to validate the mixing ratios of CI-DMPO adducts detected. There was some agreement between the MCM modelling and experimental results, although some discrepancies still remain, indicating that there are still several aspects of the flow tube set-up that need to be optimised further to improve the quantitative power of this technique.

As the reaction kinetics of the CI-DMPO reaction are at present unknown, this should be extensively investigated in future studies. Alternatively, the application of another molecule capable of scavenging CIs to form a known, stable adduct could be applied in this method. For example, Horie *et al.*<sup>179</sup> showed that the CI reacts rapidly with hexafluoroacetone (CF<sub>3</sub>COCF<sub>3</sub>), using Fourier-transform infrared (FTIR) measurements. The production of one particular product from the reaction was measured and assigned it to 3,3-di(trifluoro-methyl)-1,2,4-trioxilane, resulting from the addition of CH<sub>2</sub>OO (formaldehyde oxide) to hexafluoroacetone as shown in Figure 3.15. Direct kinetic measurements were recently conducted by Taatjes *et al.*<sup>40</sup> which found the rate coefficient between CH<sub>2</sub>OO and hexafluoroacetone to be  $k = (3.0 \pm 0.3) \times 10^{-11}$  cm<sup>3</sup> molecule<sup>-1</sup>. This was approximately two orders of magnitude faster than the rates of

CH<sub>2</sub>OO with other organics (CH<sub>2</sub>OO + acetaldehyde  $k = (9.5 \pm 0.7) \times 10^{-13} \text{ cm}^3 \text{ molecule}^{-1} \text{ s}^{-1}$  and CH<sub>2</sub>OO + acetone  $k = (2.3 \pm 0.3) \times 10^{-13} \text{ cm}^3 \text{ molecule}^{-1} \text{ s}^{-1}$ ). This rapid rate of reaction, as well as the fact that hexafluoroacetone should be less reactive to ozone than DMPO, could well allow the scavenging of CIs *in situ*, which would be a substantial improvement on the current technique.

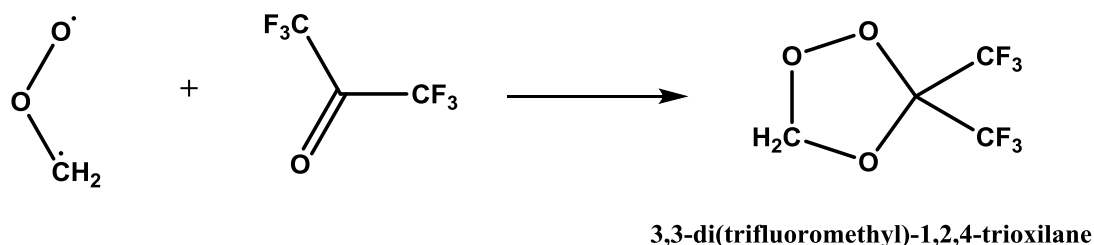


Figure 3.15 – Reaction scheme showing the addition of the simplest CI CH<sub>2</sub>OO to hexafluoroacetone.

Similarly, a study by Chantyal Pun et al.<sup>180</sup> studied the kinetics of reaction of CH<sub>2</sub>OO and (CH<sub>3</sub>)<sub>2</sub>COO with trifluoroacetic acid (CF<sub>3</sub>COOH). The rates of reaction were found to be  $k = (3.4 \pm 0.3) \times 10^{-10} \text{ cm}^3 \text{ molecule}^{-1} \text{ s}^{-1}$  and  $k = (6.1 \pm 0.2) \times 10^{-10} \text{ cm}^3 \text{ molecule}^{-1} \text{ s}^{-1}$  for CH<sub>2</sub>OO and (CH<sub>3</sub>)<sub>2</sub>COO respectively. These rates approach (or exceed) expected gas-kinetic limits predicted by collision rates<sup>181</sup>, which suggest that a long-range interaction enhances the rate of reaction on account of the permanent dipoles of the two species. This efficient rate of reaction could allow very effective scavenging of CIs *in situ* in our experimental set-up, although the products of this reaction and their ionisation efficiency in the PTR-ToF-MS would need to be determined. The volatility of the CI adducts with hexafluoroacetic acid or trifluoroacetic acid may form lower-volatility compounds, perhaps reducing the loss of CI adducts via wall adsorption. Investigating the potential of other CI scavengers, the stable adducts of which could be detected by PTR-ToF-MS, could lead to improved quantification accuracy, although at present a more suitable scavenger than DMPO is unknown.

According to a recent study, ambient SCI mixing ratio *s* in Hyytiala, Finland in the summer of 2010 was approximately  $5 \times 10^4 \text{ molecules cm}^{-3}$  with an order of magnitude uncertainty.<sup>143</sup> This is several orders of magnitude below the detection limits of our technique, and indeed, at such low ambient mixing ratio *s*, CIs prove incredibly difficult to measure in the field. Substantial technical, chemical and experimental enhancements would have to be made if there is any hope of one day applying this technique to atmospherically relevant CI mixing ratio *s*.

---

Despite this, the method has demonstrated great potential for characterising CIs in extremely complex organic systems. Understanding the fate of CIs in such systems is of crucial importance for understanding the intermediate steps of several key tropospheric processes. This technique is uniquely capable of simultaneously characterising multiple CIs in complex chemical systems, which could prove crucial in determining the role of CIs in various key tropospheric oxidation processes.

# 4 NOVEL METHOD TO DETECT CRIEGGEE INTERMEDIATES IN THE PARTICLE PHASE

---

This manuscript is based on a paper currently being drafted by Steven J. Campbell

## **Author Contributions**

Steven J. Campbell designed and performed the experiments, analysed the data and wrote the manuscript. Chiara Giorio and Markus Kalberer assisted with data interpretation.

## 4.1 Introduction

The oxidation of biogenic and anthropogenic volatile organic compounds (VOCs) by  $\cdot\text{OH}$ ,  $\text{NO}_3$  and  $\text{O}_3$  is a crucial process in defining the reactivity and composition of the lower atmosphere.<sup>143</sup> One important reaction in the troposphere is the oxidation of alkenes by ozone, which contributes to photochemical smog and global climate change.<sup>182</sup> This reaction generates a plethora of oxidised compounds including carbonyls, carboxylic acids and OH radicals, as well as contributing to the formation of secondary organic aerosol (SOA). The reaction of alkenes with  $\text{O}_3$  proceeds through a generally accepted mechanism, first proposed by Rudolf Criegee.<sup>35</sup> The initial step of the Criegee mechanism proceeds *via* the 1-3 cycloaddition of ozone across the olefin double bond, to form a primary ozonide, which promptly decomposes to form a carbonyl and the so-called Criegee intermediate, a biradical/zwitterionic species (Figure 4.1). CIs in the condensed phase can undergo further rearrangement, but this is not the case in the gas phase.<sup>183,184</sup>

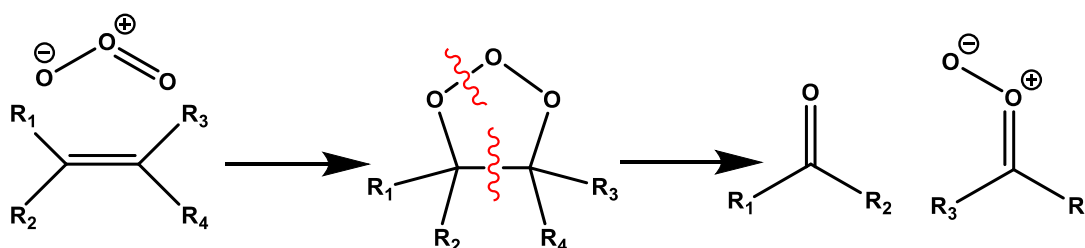


**Figure 4.1** – Reaction mechanism for the ozonolysis of alkenes postulated by Rudolf Criegee.<sup>35</sup> Ozone adds across the olefinic compound *via* a 1-3 cycloaddition, to produce a primary ozonide which promptly decomposes to form a carbonyl compound and the so-called Criegee Intermediate (CI).

The CI that is initially produced in the gas phase usually forms with internal excitation, and this excited state species can either undergo rapid unimolecular decomposition or collisional quenching to form the stabilised Criegee Intermediate (SCI).<sup>28,185</sup> The chemistry of CIs represents one of the largest uncertainties in tropospheric chemistry, playing a crucial role in determining the oxidative capacity of the atmosphere. CIs participate in bimolecular reactions with other organic species,  $\text{H}_2\text{O}$ ,  $\text{SO}_2$ ,  $\text{NO}_x$  and a variety of other trace gases.<sup>144,148,181</sup> The importance of extremely low-volatile organic compounds (ELVOCs), species which irreversibly condense into the particle phase, has recently become clear as they could well constitute a crucial link between early aerosol formation and cloud condensation nuclei formation.<sup>25,26</sup> The suggested mechanism for the formation of ELVOCs proceeds through the ozonolysis of alkenes, and therefore

through the formation of CIs, followed by an auto-oxidation mechanism *via* the vinylhydroperoxide CI channel (Figure 1.3).<sup>25,186</sup>

Although the CI reaction mechanism has been postulated for some time, characterising CIs in the atmosphere poses an analytical challenge due to their low mixing ratio and short lifetime. It is only recently that our understanding of the CIs has rapidly developed, in turn driving research into this intermediate species. Direct observation of CIs has been made possible due recent application of some advanced analytical techniques, including photoionisation mass spectrometry and tuneable photoionisation mass spectrometry.<sup>46,187</sup> These techniques have been used to study the kinetics of an array of simple CIs<sup>44</sup>, and have also brought to light the conformer dependent reactivity of *syn* and *anti* CIs, made possible by the difference in their photoionisation energies<sup>45</sup>. The first direct detection of formaldehyde oxide, the simplest CI comprising of a C<sub>1</sub> backbone, was reported only as recently as 2008, despite an exhaustive collection of previous theoretical<sup>48,151,188,189</sup> and indirect evidence<sup>143,190–192</sup>. Furthermore, a study by Welz *et al.*<sup>46</sup> in 2012 showed that CIs could be produced *via* the photolysis of *gem* di-iodoalkanes in the presence of air. This led to substantial advancements in understanding the kinetics of CIs with trace gases such as SO<sub>2</sub>, H<sub>2</sub>O and the H<sub>2</sub>O dimer.<sup>45,46,193,194</sup> This method of CI generation led to advancements regarding our understanding of CIs contribution to OH radical production *via* unimolecular decomposition,<sup>195–197</sup> developing new measurement methods<sup>55,56,198</sup> and improving our theoretical understanding of CIs<sup>199–203</sup>. The fate of volatile CIs in the gas phase has been the focus of much research in recent years. However, the fate of lower volatility CIs, which could potentially partition into the particle phase, is poorly understood.

The mechanisms of heterogeneous oxidation and organic reaction mechanisms in atmospheric aerosol are at present poorly characterised. Bulk phase reactions in aerosol occur in a complicated chemical system, with several variables influencing the particle chemistry and product distribution.<sup>14</sup> Characterising reactive intermediates and therefore investigating reaction pathways in the condensed phase proves challenging in practice due to the inherent complexity associated with bulk phase environments.<sup>128</sup> Several studies have attempted to quantify reactive uptake of OH to particles,<sup>204,205</sup> as well as the lifetimes and concentrations of marker compounds, such as pinonaldehyde, with respect to heterogeneous oxidation<sup>206,207</sup>. Studies have also shown that reactive uptake of O<sub>3</sub> into particles containing alkenes results in a rich chemistry, initiated by condensed phase

ozonolysis.<sup>206,208,209</sup> The CI plays a potentially crucial role in determining the reaction pathways and product distributions in such heterogeneous reactions, also contributing to the formation of oligomers in organic aerosol.<sup>208,210</sup> However, at present there is extremely limited evidence describing the role of the CI in defining organic aerosol composition, therefore emphasising the need to develop a method capable of characterising and quantifying CIs in the particle phase.

Recently, a novel method to characterise and quantify CIs in the gas phase by trapping CIs with spin trap molecules was developed (Chapter 3).<sup>169,177</sup> CIs generated from the ozonolysis of  $\alpha$ -pinene were scavenged by the spin trap DMPO, forming a stable adduct which is subsequently analysed using proton transfer reaction mass spectrometry (PTR-MS).<sup>169</sup> An extensive analytical study was conducted to elucidate the adduct structure and reaction mechanism between the CI and DMPO; it was found that CIs form a 6-membered non-radical adduct with DMPO. CIs in the gas phase were characterised, and their respective CI-DMPO adducts were measured on-line in the gas phase using PTR-ToF-MS. A follow up study utilised this method to capture and simultaneously quantify the adducts formed from multiple CIs generated from the ozonolysis of multiple biogenic and anthropogenic VOC precursors such as limonene, methacrolein, *cis*-2-hexene and styrene.<sup>177</sup> These studies represent a novel cost-effective method capable of characterising several different CIs simultaneously in complex organic mixtures.

In the work presented here, the focus is on CIs generated from the ozonolysis of  $\beta$ -caryophyllene, a highly reactive sesquiterpene with a high SOA yield. This reaction generates three CIs with different carbon backbones, the C<sub>1</sub>, C<sub>14</sub> and C<sub>15</sub> CI, as illustrated in Figure 4.2.

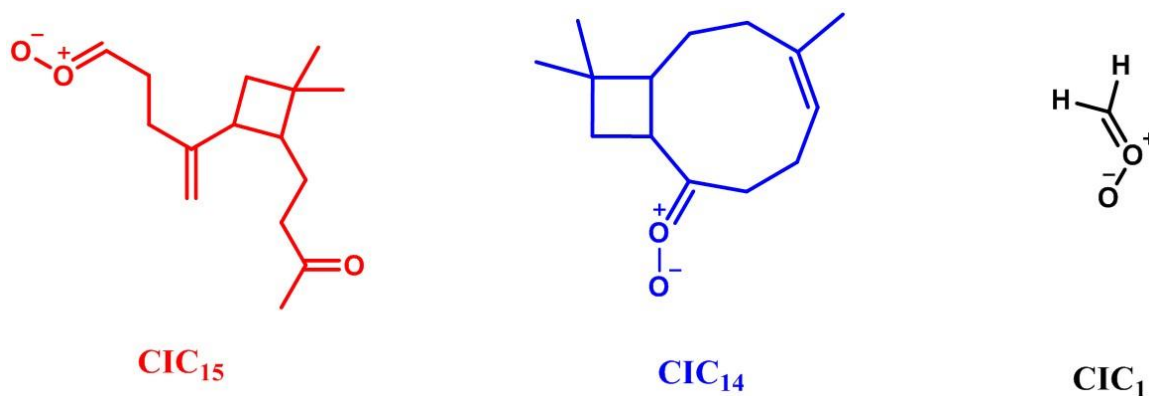


**Figure 4.2** – Structures of the three CIs formed from the ozonolysis of  $\beta$ -caryophyllene.



CIs in the gas phase were quantified by stabilisation with spin traps, and on-line analysis using PTR-MS as described previously.<sup>169,177</sup> Using this technique, it was evident that gas phase analysis of CIs alone was not sufficient to fully characterise the fate of CIs in this reaction system. The larger CIs will have a substantially lower volatility than smaller CIs, and could well condense into the particle phase. The aforementioned set-up designed to capture and characterise CIs in the gas phase was further developed to facilitate the detection of CIs in the particle phase. Preliminary tests were conducted on this method using SOA generated from  $\alpha$ -pinene ozonolysis, given the extensive study of its CI chemistry in Chapter 3. The work in this chapter demonstrates that this technique is uniquely capable of detecting multiple CIs in the particle phase. Further experiments demonstrated that the concentration of CI-spin trap adducts changed as a function of SOA mass in the reaction system; these results allowed us to derive a simple kinetic analysis, to gain insight into the gas phase loss and heterogeneous uptake of low-volatility CIs into secondary organic aerosol.

## 4.2 Methodology

### 4.2.1 Reagents

For the bulk phase, gas phase and particle phase experiments  $\alpha$ -pinene and *trans*-(-)- $\beta$ -caryophyllene ( $\geq 99\%$ , Sigma-Aldrich) were reacted with ozone produced by a UV lamp (Peak emission 185/254 nm, Appleton Woods®). The spin trap *N*-*tert*-butyl- $\alpha$ -phenylnitron (PBN) ( $\geq 98\%$ , GC grade, Sigma-Aldrich) was used to capture and stabilise Criegee intermediates in the bulk and particle phase analysis. The spin trap 5,5-dimethyl-pyrroline (DMPO) ( $\geq 97\%$ , GC grade, Sigma-Aldrich) was used to capture and stabilise Criegee intermediates in the gas phase. Acetonitrile ( $\geq 99.9\%$  Optima™ LC/MS grade, Fisher Chemical) was used as a solvent for bulk ozonolysis and to facilitate Criegee intermediate capture in the particle phase experiments *via* an impinger. Water with 0.1% formic acid (Optima™, LC/MS grade, Fisher Chemical) and methanol ( $\geq 99.9\%$ , Optima™ LC/MS grade, Fisher Chemical) were used as solvents for HPLC separation.

### 4.2.2 Bulk ozonolysis

For the bulk ozonolysis experiments, the olefinic precursor  $\beta$ -caryophyllene and the spin trap PBN were dissolved in 100 mL of acetonitrile contained in a conical flask at a

---

concentration of 1 mM and 2 mM respectively, as used in previous studies.<sup>159,169</sup> The resulting solution was placed in an ice bath for the duration of the ozonolysis; this is to further stabilise the CI-spin trap adduct<sup>160</sup>, as well as limiting solvent evaporation. Prior to the start of the ozonolysis reaction, the UV lamp used to generate ozone (185/254 nm, Appleton Woods®) was switched on and equilibrated for at least 20 minutes with a flow of 0.3 L/min of synthetic air (Zero grade, BOC) to achieve a steady-state mixing ratio of approximately 600 ppm ozone in air. Subsequently, ozone was bubbled through the solution at 0.3 L/min *via* a Teflon tube connected to a Pasteur pipette tip for 1 hour. The flow rate was controlled with a mass flow controller (20-2000 cm<sup>3</sup>/min MKS 1179A Mass-Flo® controller). For the duration of the reaction, the conical flask was covered completely with aluminium foil to prevent photolysis, and closed with parafilm to minimise evaporation and keep ozone concentrations in solution as close as possible to saturation.

The ozone concentration in solution was previously measured<sup>169</sup> and found to be (1.3±0.7) mM on average, measured by iodometric titration<sup>161,162</sup>. Control experiments were conducted under the same experimental conditions on the ozonolysis of only the spin trap (PBN + O<sub>3</sub>) or β-caryophyllene (β-caryophyllene + O<sub>3</sub>). All solutions were analysed with high-performance liquid chromatography electrospray ionisation high-resolution mass spectrometry (HPLC-ESI-HRMS), adhering to the procedures described in Section 4.2.5.

### Estimating the PBN-CI Trapping Efficiency in Solution

The trapping efficiency of the spin trap PBN towards the CI<sub>C15</sub>-PBN was estimated in order to improve the accuracy of quantification of CIs in the particle phase. Using the HPLC-ESIHRMS data acquired in the solution phase ozonolysis, and the PBN calibration curve (Figure 4.14) it is possible to estimate the concentration of CI-PBN adducts formed during this time. Despite the fact that solution-phase kinetics of β-caryophyllene and O<sub>3</sub> are unknown, the reaction in the gas phase is rapid, with a rate coefficient  $k = 1.2 \times 10^{-14}$  cm<sup>3</sup> molecules<sup>-1</sup> s<sup>-1</sup>,<sup>211</sup> and therefore an estimated lifetime in the gas phase of < 1s. Therefore, given the reaction time of 1 hour in the solution phase experiments, one can assume complete consumption of β-caryophyllene.

Using estimates of CI distributions from the Master Chemical Mechanism (v3.1.1), it is possible to theorise a 100% yield of the CI, and thus calculate the trapping yield of PBN

towards the CI. The MCM suggests a yield of the  $\text{CI}_{\text{C15}}$  of 87% from the reaction of  $\text{O}_3$  and  $\beta$ -caryophyllene. Although the MCM refers to gas phase chemistry only, it is the best estimate we have of the CI yield from this reaction in the solution phase. As the starting concentration of  $\beta$ -caryophyllene was 1mM, we can then estimate that the 0.87 mM of CI will be formed. Therefore, if 100% of the CI were to be trapped by PBN, we would expect to see 0.87 mM of the CI-PBN adduct at the end of the ozonolysis experiment.

Using the HPLC-ESI-HRMS and calibration curve, the detected concentration of PBN-CI from the experiment was found to be  $(0.21 \pm 0.05)$  mM observed over multiple repeats. Therefore, we can calculate the trapping efficiency (%) of PBN for the  $\text{CI}_{\text{C15}}$  as:

$$\text{Trapping Efficiency} = \frac{\text{Actual Yield}}{\text{Theoretical Yield}} \times 100 \quad (4.1)$$

Where the trapping efficiency of the PBN was found to be ~24% concerning the  $\text{CI}_{\text{C15}}$ -CI. This is a rough estimate, because gas phase yields of the  $\text{CI}_{\text{C15}}$  are employed to determine the yield of the CI from the ozonolysis of  $\beta$ -caryophyllene. The rate of degradation of the CI-PBN adducts is also currently unknown, and this should be taken into consideration for future calculations and it assumes that the mass spectrometry ionisation efficiency of the  $\text{CI}_{\text{C15}}$ -PBN is the same as for PBN alone, which was used to generate the calibration curve. This does, however, give a fair understanding of the CI-PBN chemistry, so that the concentration of CIs in SOA can be more accurately determined by monitoring the formation of the adduct CI-PBN. The trapping efficiency of PBN towards the  $\text{CI}_{\text{C15}}$  was estimated using this data, and was found to be approximately 24% in this particular set-up.

### 4.2.3 Flow tube experiments

#### Set-up for gas-phase measurements of CIs

The trapping of gas phase CIs with the spin trap DMPO, with subsequent PTR-ToF-MS analysis of the adduct CI-DMPO, was conducted using a technique which has been optimised previously<sup>169</sup>, and will be briefly described here. The ozonolysis reaction takes

place in a flow tube reactor maintained at ambient temperature ( $\sim 16^{\circ}\text{C}$ ) and pressure, and dry conditions (relative humidity  $< 2\%$ ).

The experimental set-up comprised of a 2.5 L glass flow tube in which  $\beta$ -caryophyllene or  $\alpha$ -pinene reacts with ozone, a mixing point (T-fitting) in which the spin trap is mixed with the sample flow from the flow tube, and a heated PTFE tube in which the spin trap reacts with the CI before quantification in the PTR-ToF-MS.

1 mL of  $\beta$ -caryophyllene was contained in a 25 mL pear-shaped flask, submersed in a water bath maintained at  $60^{\circ}\text{C}$  in order to promote release of the sesquiterpene into the gas phase. A  $\text{N}_2$  (oxygen-free nitrogen, BOC) carrier gas regulated *via* a 20-2000  $\text{cm}^3/\text{min}$  mass flow controller (MKS 1179A Mass-Flo® controller) was flowed over the  $\beta$ -caryophyllene at  $175 \text{ cm}^3/\text{min}$  to introduce the precursor into the flow tube in the gas phase. More details on the experimental set-up can be found in Giorio et al.<sup>169</sup>

### Set-up for particle-phase measurements of CIs

The flow tube set-up described previously was modified to facilitate the capture of CIs in the particle phase using the spin trap PBN, as illustrated in Figure 4.3.

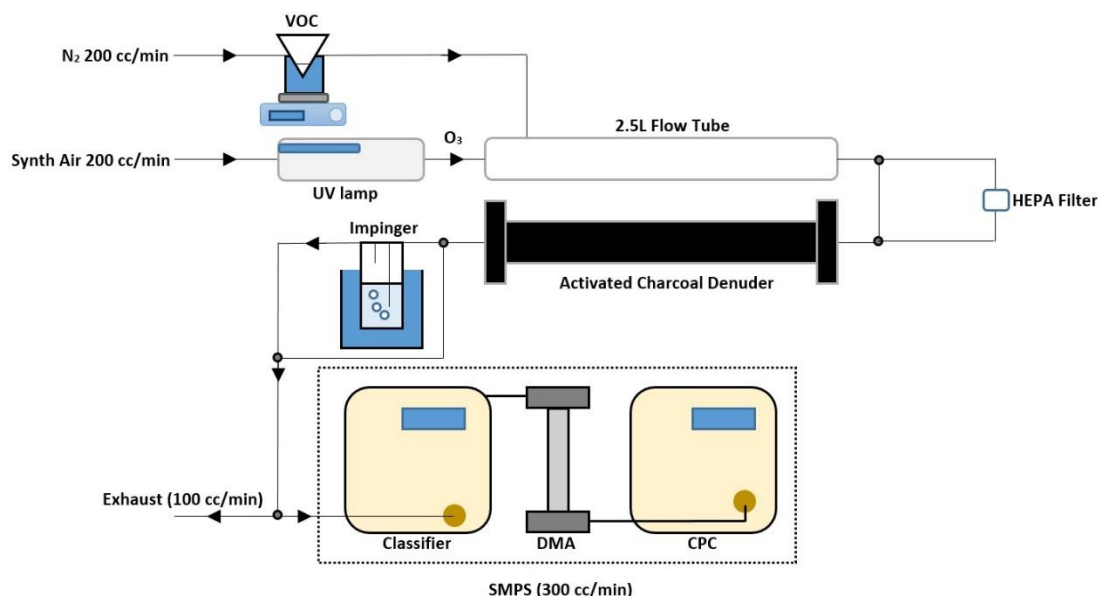


**Figure 4.3** – Diagram of the experimental set-up devised to facilitate the capture of particle phase CIs. The set-up comprises of a 2.5 L flow tube where  $\beta$ -caryophyllene reacts with ozone, an activated charcoal denuder which removes gas phase VOCs as well as  $\text{O}_3$ , an impinger containing a 5 mM solution of the spin trap PBN in acetonitrile, and an SMPS to monitor the particle mass concentration.

The ozonolysis reaction takes place in a flow tube reactor maintained at ambient temperature ( $\sim 16^{\circ}\text{C}$ ) and pressure, and under dry conditions (relative humidity approximately  $< 2\%$ ). The experimental set-up comprised a 2.5 L glass flow tube in which  $\beta$ -caryophyllene reacts with ozone, an activated charcoal denuder downstream of the flow tube to remove gas phase VOCs, an impinger, and an SMPS to monitor the particle mass concentration for the duration of the experiment. 1 mL of  $\beta$ -caryophyllene was contained in a 25 mL pear-shaped flask, submersed in a water bath maintained at  $60^{\circ}\text{C}$  in order to volatilise the sesquiterpene.

A  $\text{N}_2$  (oxygen-free nitrogen, BOC) carrier gas regulated *via* a 20-2000  $\text{cm}^3/\text{min}$  mass flow controller (MKS 1179A Mass-Flo® controller) was flowed over the  $\beta$ -caryophyllene at 200  $\text{cm}^3/\text{min}$  to introduce the VOC precursor into the flow tube in the gas phase. Ozone was produced from a UV lamp (185/254 nm, Appleton Woods®) by flowing synthetic air (Zero grade, BOC) at 200  $\text{cm}^3/\text{min}$  (20-2000  $\text{cm}^3/\text{min}$  MKS 1179A Mass-Flo® controller).

Ozone was measured using a UV photometric ozone analyser (Thermo Scientific model 49i) and particle concentration was measured using a TSI scanning mobility particle sizer (SMPS) composed of TSI 3080 electrostatic classifier (X-ray neutraliser and differential mobility analyser TSI model 3081) and a condensation particle counter (TSI model 3775). Gas phase mixing ratios of  $\beta$ -caryophyllene and ozone were measured to be 194 and 440 ppm respectively.

The ozone was mixed in the flow tube with  $\beta$ -caryophyllene; the residence time of reactants in the flow tube was calculated to be 335 seconds, with 99% of ozone completely mixed in the flow tube after approximately 12 seconds. An activated charcoal denuder was used to remove any excess ozone and substantially reduce the oxidised gas phase VOC mixing ratio before sampling the particle phase components in the impinger. The removal efficiency of the denuder with respect to ozone was measured to be  $>99.9\%$  at an  $\text{O}_3$  mixing ratio of 290 ppm in air. The particle phase CIs were captured in a 50 mL impinger containing 40 mL of a solution of PBN in acetonitrile at a concentration of 5 mM. The impinger was submersed in an acetonitrile/dry ice bath maintained at approximately  $-41^{\circ}\text{C}$  in order to improve the adduct stability, as well as to limit solvent evaporation during sampling.

---

Very high average SOA mass was generated from the reaction of  $\beta$ -caryophyllene and ozone, approximately 140 mg/m<sup>3</sup> during sampling, with a mean diameter of 297 nm. This elevated particle mass concentration was required in order to increase the subsequent concentration of particle phase CIs in the impinger to facilitate initial detection.

The SOA was sampled for two and a half hours continuously in order to pre-concentrate the CI-PBN adducts to facilitate detection. After this time, 10 mL of sample was taken from the impinger and evaporated to approximately 0.1 mL to concentrate the sample, before subsequent analysis using HPLC-ESI-HRMS, as described in Section 4.2.5.

### Collection Efficiency in the Impinger

The collection efficiency was calculated using the method described by Miljevic et.al<sup>212</sup> where the collection efficiency of the impinger ( $\eta_{\text{removal}}$ ) is described as:

$$\eta_{\text{removal}} = \left(1 - \frac{N_{\text{upstream}}}{N_{\text{downstream}}}\right) \times 100 \quad (4.2)$$

Where  $N_{\text{upstream}}$  is the particle concentration before the impinger and  $N_{\text{downstream}}$  is the particle concentration after the impinger. Using a scanning mobility particle sizer (SMPS), the average of both  $N_{\text{upstream}}$  and  $N_{\text{downstream}}$  were measured to be 445800 and 405968  $\mu\text{g m}^{-3}$  respectively. This lead to the calculation of the collection efficiency of ~9% in this particular system. There were negligible particle losses through a glass impinger containing no solvent.

Despite this low collection efficiency, compared to traditional particle collection methods (e.g. filter extraction), the impinger collection method is advantageous; filter samples have a lower time resolution, and the impacts on organic composition upon solvent extraction to the filter are at present poorly characterised. Due to the high reactivity and short lifetime of CIs, it is crucial that the SOA is sampled into the PBN solution as fast as possible to ensure the efficient scavenging of CIs by PBN.

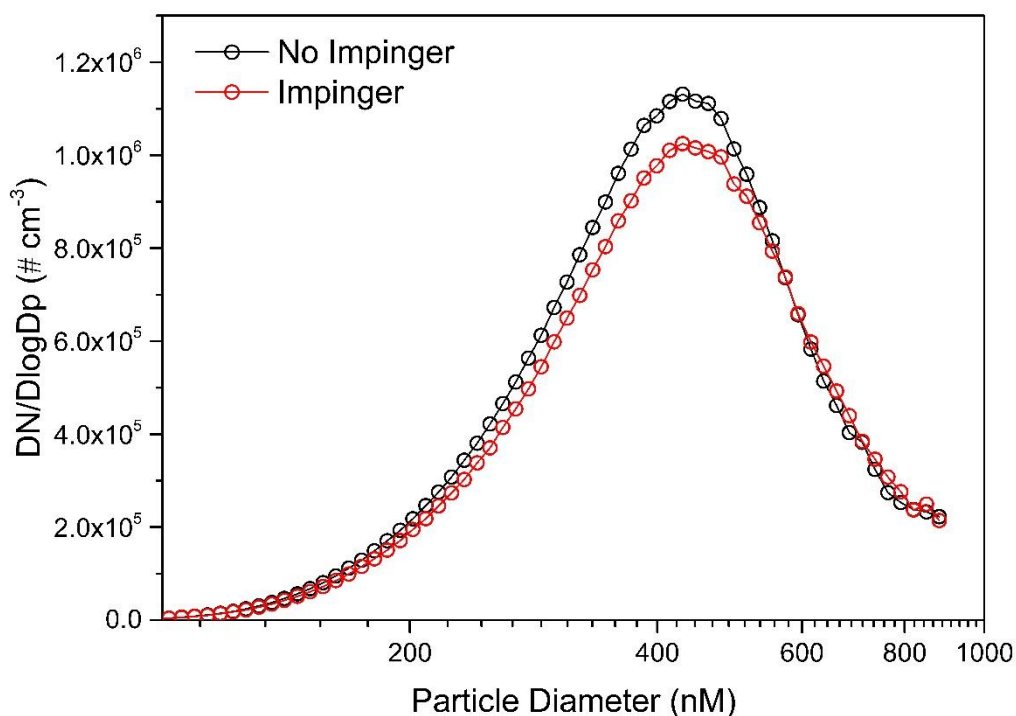


**Figure 4.4** – Plot showing number size distribution of particles with and without an impinger containing 40 mL of acetonitrile. Removal of larger particles  $> 570$  nm is very inefficient in this impinger. This is likely due to the more efficient diffusion of smaller particles from the bubble in the impinger, meaning there is a higher probability of them being captured in the solvent compared to larger particles

#### 4.2.4 PTR-ToF-MS Measurements

On-line gas phase mixing ratios of  $\beta$ -caryophyllene, DMPO and CI-DMPO adducts were measured using a proton transfer reaction time-of-flight mass spectrometer (PTR-ToF-MS 8000, Ionicon Analytik, Innsbruck, Austria) in the  $m/z$  range 10-500, with a time resolution of 10 s and a mass resolution  $m/\Delta m$  of 5000 (full width at half maximum) at the mass of protonated acetone. The source settings for the gas phase ozonolysis experiments were as follows: drift tube voltage 510 V, drift tube pressure  $\sim 2.22$  mbar and, a drift tube temperature of  $90^\circ\text{C}$ , resulting in an  $E/N$  of  $\sim 127$  Td ( $1 \text{ Td} = 10^{-17} \text{ V cm}^2$ ). The PTR-ToF-MS inlet (1 m inert peek tube ID=1 mm, OD=1.59 mm) was kept at  $100^\circ\text{C}$  and the sampling flow rate was  $100 \text{ cm}^3/\text{min}$ . Data analysis was conducted using PTR-MS Viewer 3.2 (Ionicon Analytik). Mass calibration was performed with consideration of  $\text{H}_3^{18}\text{O}^+$  ( $m/z = 21.023$ ),  $\text{NO}^+$  ( $m/z = 29.998$ ) and  $\text{C}_3\text{H}_7\text{O}^+$  ( $m/z = 59.049$ ) as references. A proton transfer rate constant of  $k = 3.1 \times 10^{-9} \text{ cm}^3 \text{ molecule}^{-1} \text{ s}^{-1}$  for  $\beta$ -caryophyllene<sup>213,214</sup> and  $k = 2.77 \times 10^{-9} \text{ cm}^3 \text{ molecule}^{-1} \text{ s}^{-1}$  for DMPO<sup>177</sup> was used for quantification. Due to

---

the elevated mixing ratios required to currently detect CIs, because of the relatively slow kinetics of the olefin ozone reaction, the  $^{12}\text{C}$  DMPO and  $\beta$ -caryophyllene signals are often in saturation during the experiments; therefore, the corresponding  $^{13}\text{C}$  isotopes were used for quantification. For  $\text{CI}_{\text{C1}}$ -DMPO,  $\text{CI}_{\text{C14}}$ -DMPO and  $\text{CI}_{\text{C15}}$ -DMPO, rates were previously estimated (Appendix 2), and rates coefficients of quantification used in this work are  $k = 2.18 \times 10^{-9} \text{ cm}^3 \text{ molecule}^{-1} \text{ s}^{-1}$ ,  $k = 3.08 \times 10^{-9} \text{ cm}^3 \text{ molecule}^{-1} \text{ s}^{-1}$  and  $k = 3.28 \times 10^{-9} \text{ cm}^3 \text{ molecule}^{-1} \text{ s}^{-1}$  respectively.

#### 4.2.5 HPLC-ESI-HRMS Analyses

The  $\beta$ -caryophyllene CI-PBN adducts were analysed with a HPLC-ESI-HRMS using an Accela system HPLC (Thermo Scientific, San Jose, USA) coupled with a LTQ Velos Orbitrap. A T3 Atlantis C18 column (3  $\mu\text{m}$ ; 2.1 $\times$ 150 mm; Waters, Milford, USA) was used for chromatographic separation with an injection volume of 50  $\mu\text{L}$ . Mobile phases were (A) water with 0.1% formic acid and (B) methanol. The separation was conducted using an elution programme as described in Giorio *et al.*<sup>169</sup>

The reaction mixtures were analysed also with direct infusion in ESI in positive ionisation mode (flow rate 5  $\mu\text{L}/\text{min}$ , spray voltage 3.0 kV, transfer capillary temperature 275 $^{\circ}\text{C}$ , Sheath flow 12 L/min, S-Lens RF Level 60%) coupled to a high-resolution mass spectrometer (LTQ Velos Orbitrap, Thermo Scientific, Bremen, Germany) with a resolution of 100 000 at  $m/z$  400, and a typical mass accuracy within  $\pm 2$  ppm. Data were acquired in full scan mode in the  $m/z$  range 150-600 and in MS/MS with a collision-induced dissociation (CID) energy of 40 (normalized collision energy). The instrument was calibrated routinely with a Pierce LTQ Velos ESI Positive Ion Calibration Solution (Thermo Scientific).

### 4.3 Results and Discussion

#### 4.3.1 Initial Method Tests: Detection of CIs in $\alpha$ -pinene SOA

Before attempting to detect the CIs generated from the ozonolysis of  $\beta$ -caryophyllene,  $\alpha$ -pinene SOA was used as a model SOA system to test the method, given its ease of use and well-defined compositional chemistry (the gas phase CI chemistry of  $\alpha$ -pinene was extensively investigated in Chapter 3). Approximately 7ppm of  $\alpha$ -pinene and 14ppm of  $\text{O}_3$  were introduced into the flow tube, using the same set-up illustrated in Figure 4.3. The  $\text{O}_3$  was flowed through a metal tube inserted into the flow tube, resulting in an estimated



reaction time between O<sub>3</sub> and  $\alpha$ -pinene of 43 seconds. These calculations are based on the assumption that a steady state, laminar flow is achieved within the flow tube.

For the initial set of experiments, the denuder was not added to the flow tube set-up, so that a gas and particle mixture was bubbled through the impinger. The impinger was attached directly to the outlet of the flow tube. The impinger contained 50 mL of a 5 mM solution of unreacted PBN (Sigma Aldrich) in acetonitrile (HPLC grade, Fisher Scientific). SMPS measurements were taken for the duration of the experiment, and showed an average particle concentration of between  $2\text{--}2.5 \times 10^3 \mu\text{g}/\text{m}^3$  was generated from the reaction of O<sub>3</sub> and  $\alpha$ -pinene. The gas/particle mixture was bubbled through the impinger for a total of 2.5 hours. Samples were extracted from the impinger after 2, 4 and 6 hours for subsequent direct infusion ESI-HRMS analysis, *i.e.* without HPLC separation.

As can be seen in Figure 4.5, the PBN ( $m/z = 178.1222$ ) and PBN dimer peaks ( $m/z = 355.2372$ ) still dominate the spectra, due to their relatively high concentrations upon direct infusion. Upon re-scaling the image around  $m/z$  350–370 (Figure 4.5 (B)), the PBN-Criegee adduct is visible. The unique elemental formula associated with the protonated CI-PBN adduct, C<sub>21</sub>H<sub>32</sub>O<sub>4</sub>N, was assigned at  $m/z = 362.2324$  with a mass drift of  $-0.373$  ppm, and observed with a relative intensity of  $8.9 \times 10^5$ , appreciably above the noise level ( $\approx 1 \times 10^2$ ). The PBN-Criegee adduct was observed in all 5 repeats, with an intensity after 6 hours of sampling varying from  $5 \times 10^4 - 8.9 \times 10^5$ , *i.e.* about 100 times above the noise level.

The same experiments were repeated with a denuder added into the flow set-up upstream of the impinger, so that gas phase organics are removed and only particle phase components should remain. Interestingly, the PBN-Criegee adduct was not observed in any of the three experiments conducted with a denuder. This potentially indicates that the Criegee radical generated from the ozonolysis of  $\alpha$ -pinene only exists in the gas phase, and does not survive long enough to partition into the particle phase in significant concentrations. This is in agreement with the results presented for  $\alpha$ -pinene ozonolysis in Chapter 3, where the CIs generated from this ozonolysis regime were indeed detected in the gas phase.

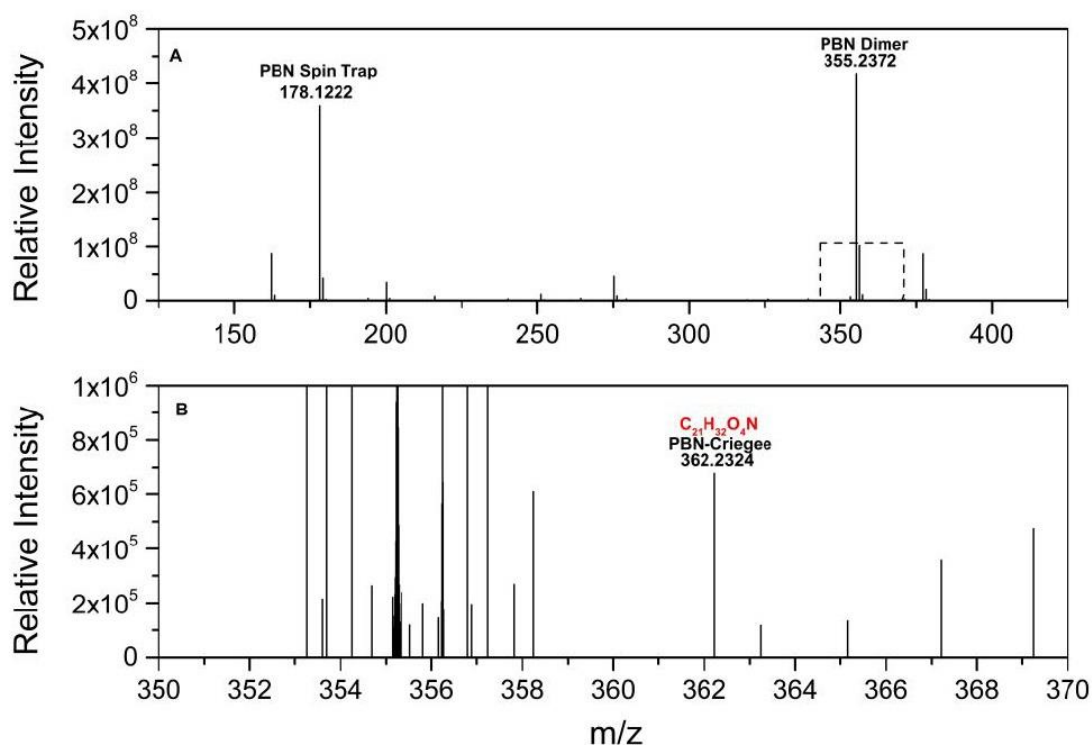


**Figure 4.5** - Positive mode UHR-MS spectrum of 5 mM PBN in acetonitrile after 6 hours sampling. The protonated Criegee intermediate was identified at  $m/z = 362.2324$ . The  $m/z$  will correspond to 1 proton more than the neutral formula.

MS/MS analysis on the PBN-Criegee ion selected (Figure 4.6(A)) and the fragments obtained (Figure 4.6(B)), with a collision energy of 40 is shown in Figure 4.6. As can be seen in (B), several fragments were observed. The fragment identified at  $m/z = 178.1228$  corresponds to the molecular formula of the spin trap PBN, strongly supporting the hypothesis that its parent ion at  $m/z = 362.2324$  is indeed the PBN-Criegee adduct. There are other fragments observed at  $m/z = 289.19$ , 306.01 and 344.19, which could not be identified.

Initial tests of the method using  $\alpha$ -pinene ozonolysis illustrate that the technique is capable of scavenging CIs, with detection off-line using direct infusion ESI-HRMS. However, these CIs were only present in the gas/particle mixture, and were not observed in the SOA components of  $\alpha$ -pinene ozonolysis alone. It is more probable that CIs generated from a lower-volatility precursor with a higher SOA yield (such as  $\beta$ -caryophyllene) would have sufficiently low volatility to efficiently partition into the condensed phase.

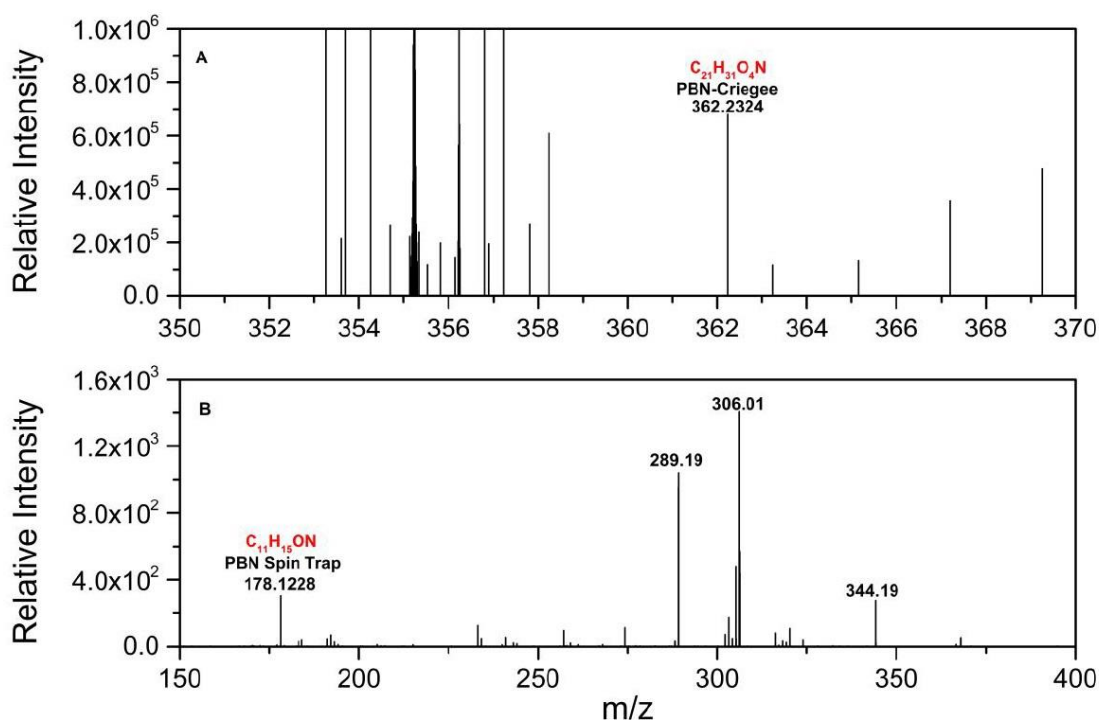


**Figure 4.6** - The PBN-Criegee adduct (A) was isolated and subjected to MS/MS analysis, to yield the spin trap PBN, as well as several unidentifiable fragments. The neutral formula is presented on the mass spectrum. The  $m/z$  will correspond to 1 proton more than the neutral formula due to the protonation occurring in the positive mode.

The following results sections will discuss the formation mechanisms of PBN-CI adducts generated from  $\beta$ -caryophyllene ozonolysis, as well as the initial characterisation of these adducts using liquid phase ozonolysis. Characterisation of gas phase CIs generated from  $\beta$ -caryophyllene ozonolysis, using the set-up described in Section 3.2.7 was also conducted. Finally, CIs present in SOA generated from  $\beta$ -caryophyllene ozonolysis were detected using the set-up described in Figure 4.3.

#### 4.3.2 Formation Mechanism of $\beta$ -caryophyllene CI-Spin Trap Adducts

Ozonolysis of  $\beta$ -caryophyllene proceeds *via* the addition of ozone across either the endocyclic or exocyclic double bond. Previous studies of the product distributions of this reaction have shown that this occurs predominantly (~99%) at the endocyclic double bond.<sup>215,216</sup> The addition of  $O_3$  across the endocyclic double bond results in the formation of an energy rich primary ozonide, which promptly decomposes to form two isomeric  $C_{15}$  CIs; these CIs have differing structures, depending on the ring opening pathway.

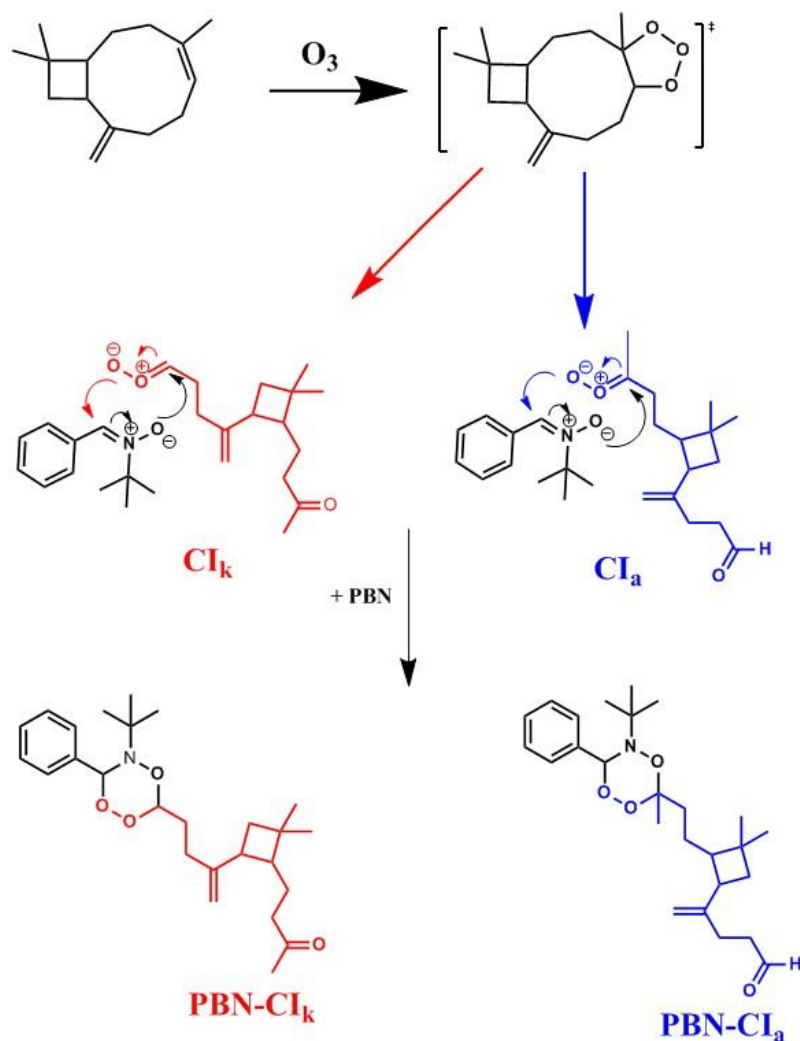


**Figure 4.7** – Proposed mechanism depicting the formation of CI<sub>k</sub> (red) and CI<sub>a</sub> (blue). The reaction proceeds *via* addition of O<sub>3</sub> across the endocyclic double bond (99% compared to 1% across the exocyclic double bond) to firstly form a primary ozonide, which promptly decomposes to form Criegee intermediates. CI<sub>k</sub> and CI<sub>a</sub> are then captured by the spin trap PBN. This reaction occurs via a 3,3-cycloaddition of the given CI to PBN, to form a non-radical adduct composing of a 6-membered ring. It is assumed the reactivity of DMPO in the gas phase will be the same as PBN due to both spin traps possessing the same functionality. In all likelihood, PBN will capture the SCI as opposed to the thermally “hot”, excited state CI. This mechanism is based on the extensive analysis conducted in Giorio et.al.<sup>169</sup>

Either a carbonyl oxide with a terminal ketone (CI<sub>k</sub>), or a carbonyl oxide with a terminal aldehyde (CI<sub>a</sub>) are formed. Although a minor product, formation of the epoxide β-caryophyllene oxide has been reported, in yields of approximately 1%.<sup>217</sup> The formation of the CI<sub>a</sub> and CI<sub>k</sub>, and subsequent formation of the 1:1 adducts CI<sub>a</sub>-PBN and CI<sub>k</sub>-PBN is illustrated in Figure 4.7. The work presented in Chapter 3<sup>169</sup> sought to fully characterise the reaction mechanism and structure of the adduct formed between Criegee intermediates, generated from the ozonolysis of α-pinene, and the spin trap PBN. A

combination of analysis with electron paramagnetic resonance (EPR) spectroscopy, nuclear magnetic resonance (NMR) spectroscopy, ESI-HRMS analyses and density functional theory (DFT) calculations convincingly showed that a non-radical, 6-membered ring is formed from the reaction of the CI with PBN.<sup>169</sup> DFT calculations suggest that the isomer  $\text{CI}_k$  would form a more stable adduct, and would proceed through a lower energy barrier than that of  $\text{CI}_a$ . This suggests that the reaction between  $\text{CI}_k$  and DMPO would form the dominant adduct, but at present it is unclear as to the isomer dependant scavenging of the CI by DMPO. The structures postulated in this study assume that the CIs generated from the ozonolysis of  $\beta$ -caryophyllene react in a similar manner to the  $\alpha$ -pinene CIs previously studied<sup>169,177</sup>.

### 4.3.3 Characterisation of $\beta$ -caryophyllene CI Adducts using HPLC-ESI-HRMS

The acetonitrile solution containing  $\beta$ -caryophyllene was ozonolysed for 1 hour in the presence of the spin trap PBN (as described in Section 4.2.2). HPLC-ESI-HRMS analyses shows the formation of the 1:1 adduct between the  $\text{CI}_{\text{C15}}$  Criegee intermediate and the spin trap PBN, at  $m/z = 430.2954$  with the elemental formula  $(\text{C}_{26}\text{H}_{39}\text{NO}_4)\text{H}^+$  and a retention time of 33.76 minutes (Figure 4.8). As both  $\text{CI}_a$  and  $\text{CI}_k$  are isomeric, and therefore have the same  $m/z$  and elemental formulae, both species could contribute to the peak assigned to  $\text{CI}_{\text{C15}}$ ; analysis using mass spectrometry alone cannot resolve these two structures.

Another peak at  $m/z = 432.2740$  was detected, and assigned the elemental formula  $(\text{C}_{25}\text{H}_{37}\text{NO}_5)\text{H}^+$  with a retention time of 36.94 minutes (Figure 4.8). This peak ( $\text{CI}_{\text{C14B}}$ -PBN) was attributed to the scavenging of the CI formed from secondary ozonolysis of  $\beta$ -caryophyllene aldehyde (BCAL) by PBN. BCAL itself is formed in a yield of approximately 21% from the initial endocyclic attack of ozone on  $\beta$ -caryophyllene and subsequent bimolecular reaction of the  $\text{CI}_{\text{C15}}$  with trace gasses or organics.<sup>218</sup> Therefore, it is likely that this will undergo ozonolysis given the excess of ozone in the system to generate the corresponding  $\text{CI}_{\text{C14B}}$ -PBN adduct when captured in the impinger. The mass spectra obtained of both  $\text{CI}_{\text{C15}}$ -PBN and  $\text{CI}_{\text{C14B}}$ -PBN using HPLC-ESI-HRMS are shown in Figure 4.8 (b) and (c). The relatively high intensity of the signal associated with these two adducts is indicative of an efficient trapping of CIs in solution by PBN, as well as demonstrating that the CI-PBN adduct is sufficiently stable to be analysed offline.

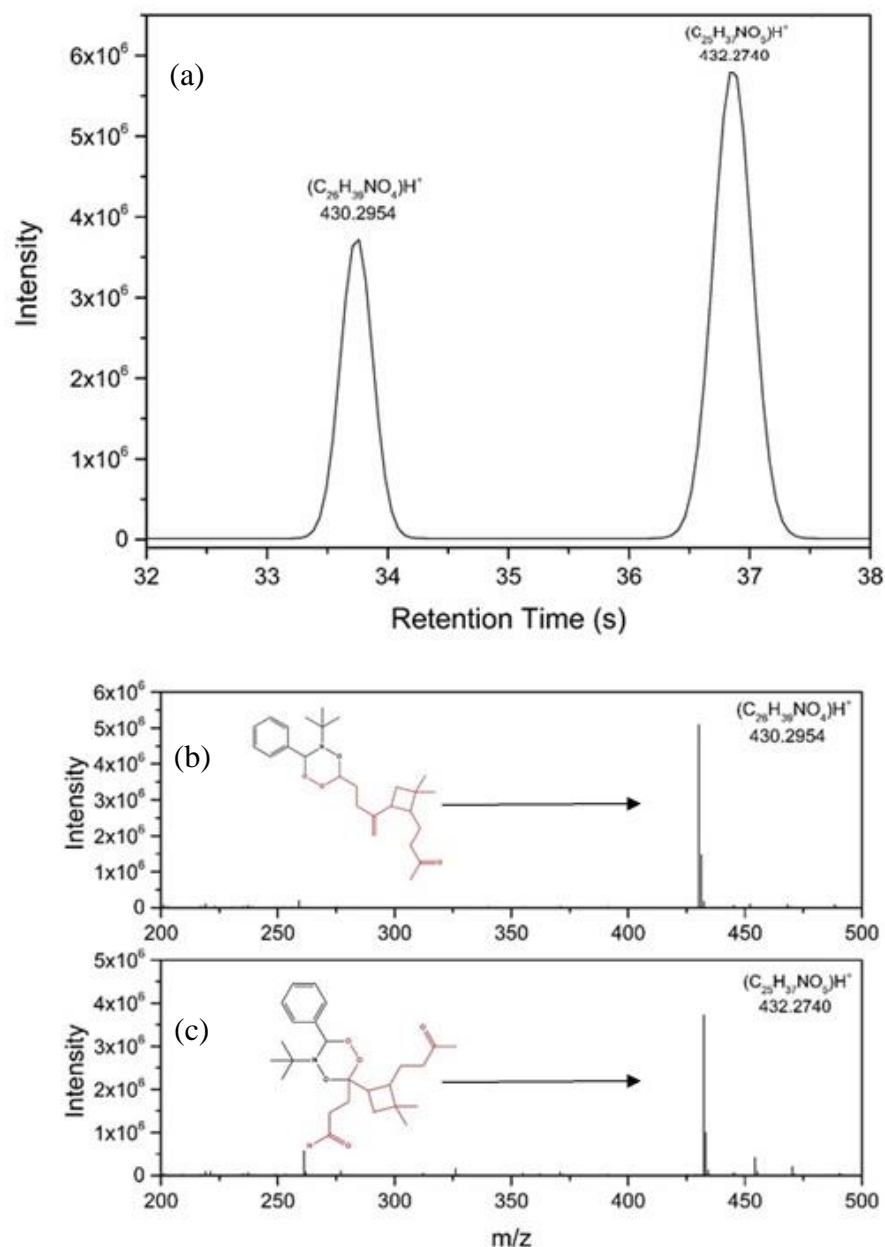


**Figure 4.8** – Characterisation of spin trap adducts using HPLC-ESI-HRMS. (a) Fitted HPLC peaks associated with the spin trap adducts  $(C_{26}H_{39}NO_4)H^+$  and  $(C_{25}H_{37}NO_5)H^+$  at a retention time of 33.76 and 36.94 minutes respectively, (b) mass spectrum where  $CI_{15}$ -PBN is detected at  $m/z$  430.2954 ( $(C_{26}H_{39}NO_4)H^+$ ) and (c) illustrates the detection of  $CI_{14B}$ -PBN at  $m/z$  432.2740 ( $(C_{25}H_{37}NO_5)H^+$ ).

MS/MS analysis was also conducted on both  $CI_{15}$ -PBN (Figure 4.9) and  $CI_{14B}$ -PBN. A fragment corresponding to the spin trap PBN at  $m/z$  178.1223 ( $C_{11}H_{15}ON)H^+$  was detected when MS/MS was conducted on both  $CI_{15}$ -PBN and  $CI_{14B}$ -PBN, with an intensity of approximately 5100, appreciably above the noise level. The presence of the PBN fragment in the MS/MS analysis, coupled with extensive characterisation in our previous

study<sup>169,177</sup> further implies that these CIs are indeed being trapped by PBN to form a stable adduct.

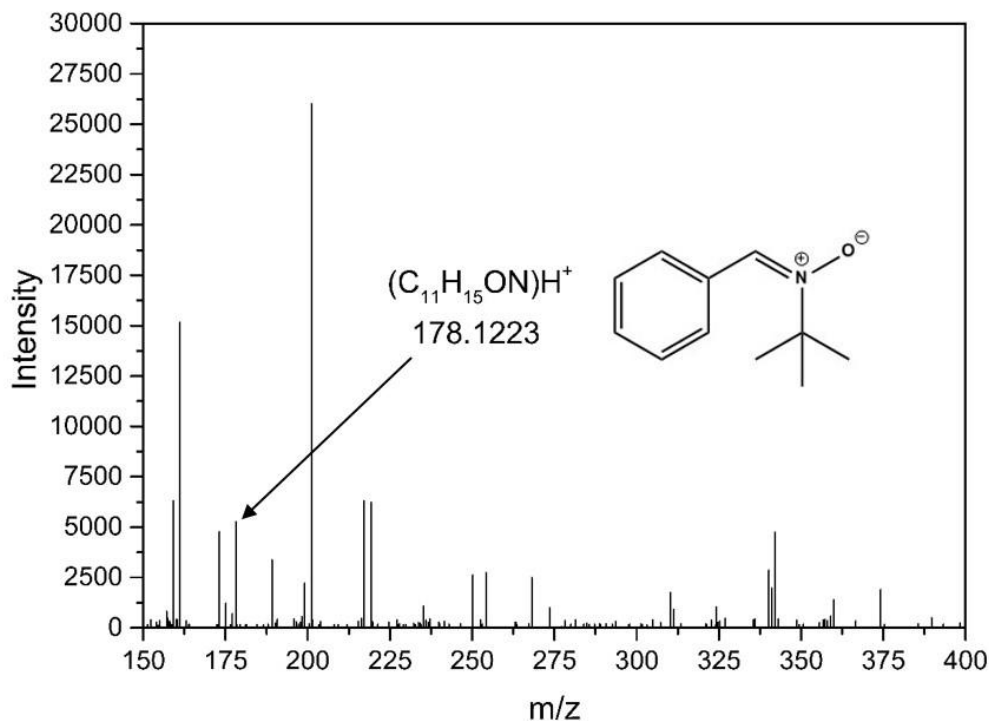


**Figure 4.9** – Mass spectrum of the MS/MS analysis of CI<sub>C15</sub>-PBN adduct. A fragment corresponding to the spin trap PBN at  $m/z = 178.1223$  was detected. This implies that the spin trap is contained within the structure of the signal assigned to the CI<sub>C15</sub>-PBN adduct, complementing the assignment.

#### 4.3.4 Quantification of $\beta$ -caryophyllene CI-DMPO Adducts in the Gas Phase

Using the set-up described in Section 3.2.7 for gas phase CI characterisation, the adducts formed between the spin trap DMPO and gas-phase  $\beta$ -caryophyllene CIs with the elemental formulae CI<sub>C1</sub>-DMPO (C<sub>7</sub>H<sub>13</sub>NO<sub>3</sub>)H<sup>+</sup> ( $m/z = 280.096$ ), CI<sub>C14</sub>-DMPO (C<sub>20</sub>H<sub>33</sub>NO<sub>4</sub>)H<sup>+</sup> ( $m/z = 352.240$ ) and CI<sub>C15</sub>-DMPO (C<sub>21</sub>H<sub>35</sub>NO<sub>4</sub>)H<sup>+</sup> ( $m/z = 366.264$ ) were detected by PTR-ToF-MS using the optimised experimental set-up described previously (Figure 3.1). This is consistent with results discussed in Chapter 3, where a variety of CIs have been detected using the same technique, where the reaction mechanism, adduct structure and adduct stability were probed using a variety of analytical techniques and theoretical calculations.<sup>169,177</sup> The observed concentrations of the CI-DMPO adducts are detected in the low ppb concentration range, approximately 3 - 4 orders of magnitude

---

lower than the initial concentration of the reactants  $\beta$ -caryophyllene and ozone, which were measured to be 220 and 290 ppm respectively. The detected concentrations of the CI-DMPO adducts are relatively stable over time once reaching steady state, with a typical variation of  $\pm 10\%$  on average as observed in multiple repeats. The slow initial rise in the concentration of the CI-DMPO adducts is likely due to the warm up time of the UV lamp of approximately 30 minutes, in which the ozone concentration exponentially increases before reaching a steady-state concentration. After the ozone lamp is switched off, the observed concentration of the CI-DMPO adducts decreases slowly towards zero. This slow decrease is likely due to memory effects of adsorbed CI-DMPO adducts on the walls of the reaction system, and potentially in the inlet of the PTR-ToF-MS.

Most notably, the detected concentration of the  $\text{CI}_{\text{C1}}$ -DMPO is substantially higher than that of the  $\text{CI}_{\text{C14}}$ -DMPO and  $\text{CI}_{\text{C15}}$ -DMPO adducts, with a steady-state concentration of 14.8 ppb. This is again consistent with the results presented in Section 3.3.3<sup>177</sup>, in which the  $\text{CI}_{\text{C1}}$ -DMPO adduct had the largest observed concentration in a variety of chemical systems where there was more than one CI formed from the initial ozonolysis. DFT calculations suggested that the  $\text{CI}_{\text{C1}}$  reaction with DMPO occurs *via* a barrierless reaction, likely contributing to more efficient scavenging of the  $\text{C}_1$  CI by DMPO. In addition, larger adducts formed between large CIs and DMPO will likely have a relatively low volatility, and will more readily condense onto the walls of the reaction vessel, and potentially adsorb onto the surface of SOA formed from the ozonolysis reaction.

The  $\text{CI}_{\text{C15}}$ -DMPO adduct should be the dominant product in this reaction scheme, as approximately 99% of the reaction occurs across the endocyclic bond of  $\beta$ -caryophyllene<sup>211,216</sup>. Figure 4.10 shows that the detected concentrations of both the  $\text{CI}_{\text{C15}}$ -DMPO and  $\text{CI}_{\text{C14}}$ -DMPO initially rise to a maximum of 0.61 and 0.44 ppb respectively when the ozone lamp initially is turned on, before promptly decreasing to zero for the remainder of the experiment. The observed low concentration of the  $\text{CI}_{\text{C14}}$ -DMPO and  $\text{CI}_{\text{C15}}$ -DMPO that the adducts formed between DMPO and the large  $\text{C}_{14}$  and  $\text{C}_{15}$  CIs would be substantially lost to the walls or particle surface due to their relatively low volatility.

Furthermore, the CIs themselves could also have a sufficiently low volatility to partition into SOA formed from the ozonolysis reaction, or adsorb onto the walls. These observations indicate that the large gas phase CIs rapidly partition into the condensed



phase themselves, therefore not persisting in a high enough concentration in the gas phase to be detected. These results indicate that characterisation of CIs in the gas phase using this technique does not fully describe the fate of CIs generated from the ozonolysis of  $\beta$ -caryophyllene, and the development of further techniques is required to probe the fate of larger CIs in the condensed phase.

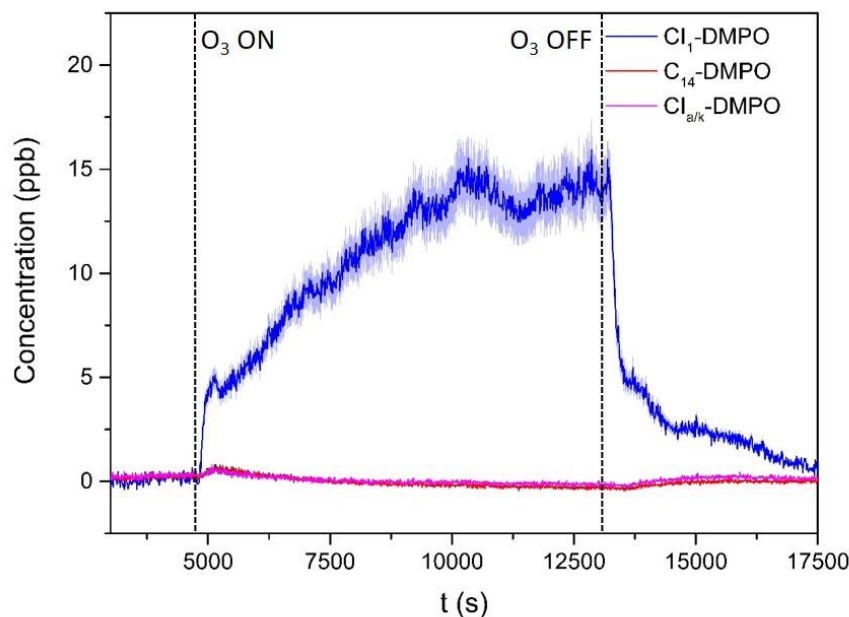


**Figure 4.10**– Time trace of  $\text{CI}_{\text{C1}}\text{-DMPO}$  ( $\text{C}_7\text{H}_{13}\text{NO}_3$ ) $\text{H}^+$ ,  $\text{CI}_{\text{C14}}\text{-DMPO}$  ( $\text{C}_{20}\text{H}_{33}\text{NO}_4$ ) $\text{H}^+$  and  $\text{CI}_{\text{C15}}\text{-DMPO}$  ( $\text{C}_{21}\text{H}_{35}\text{NO}_4$ ) $\text{H}^+$  in the gas phase generated in the flow tube set up and quantified with PTRMS. The observed concentration of  $\text{CI}_{\text{C1}}\text{-DMPO}$  is considerably higher than the other larger CI-DMPO adducts. This is likely due to the more efficient trapping of the smaller CI by the spin trap DMPO, as well as loss of the larger CIs and potentially their corresponding adducts into the particle phase.

#### 4.3.5 Detection of CIs in SOA generated from $\beta$ -caryophyllene Ozonolysis

The set-up described in described in Figure 4.3 was configured and designed to facilitate the detection of CIs in the particle phase. HPLC-ESI-HRMS analysis shows the formation of a 1:1 adduct between the spin trap PBN and the  $\text{CI}_{\text{C15}}$  and  $\text{CI}_{\text{C14B}}$  Criegee intermediates at  $m/z = 430.2954$  ( $\text{C}_{26}\text{H}_{39}\text{NO}_4$ ) $\text{H}^+$  and  $m/z = 432.2740$  ( $\text{C}_{25}\text{H}_{37}\text{NO}_5$ ) $\text{H}^+$  respectively upon sampling  $\beta$ -caryophyllene SOA into the impinger containing PBN, as shown in (Figure 4.11). These CIs were also detected in the bulk phase experiments described in Section 4.3.3. The adduct corresponding to  $\text{CI}_{\text{C1}}\text{-PBN}$  generated from the ozonolysis of the

exocyclic double bond in  $\beta$ -caryophyllene, was not detected, as it is likely too volatile to partition into the condensed phase.

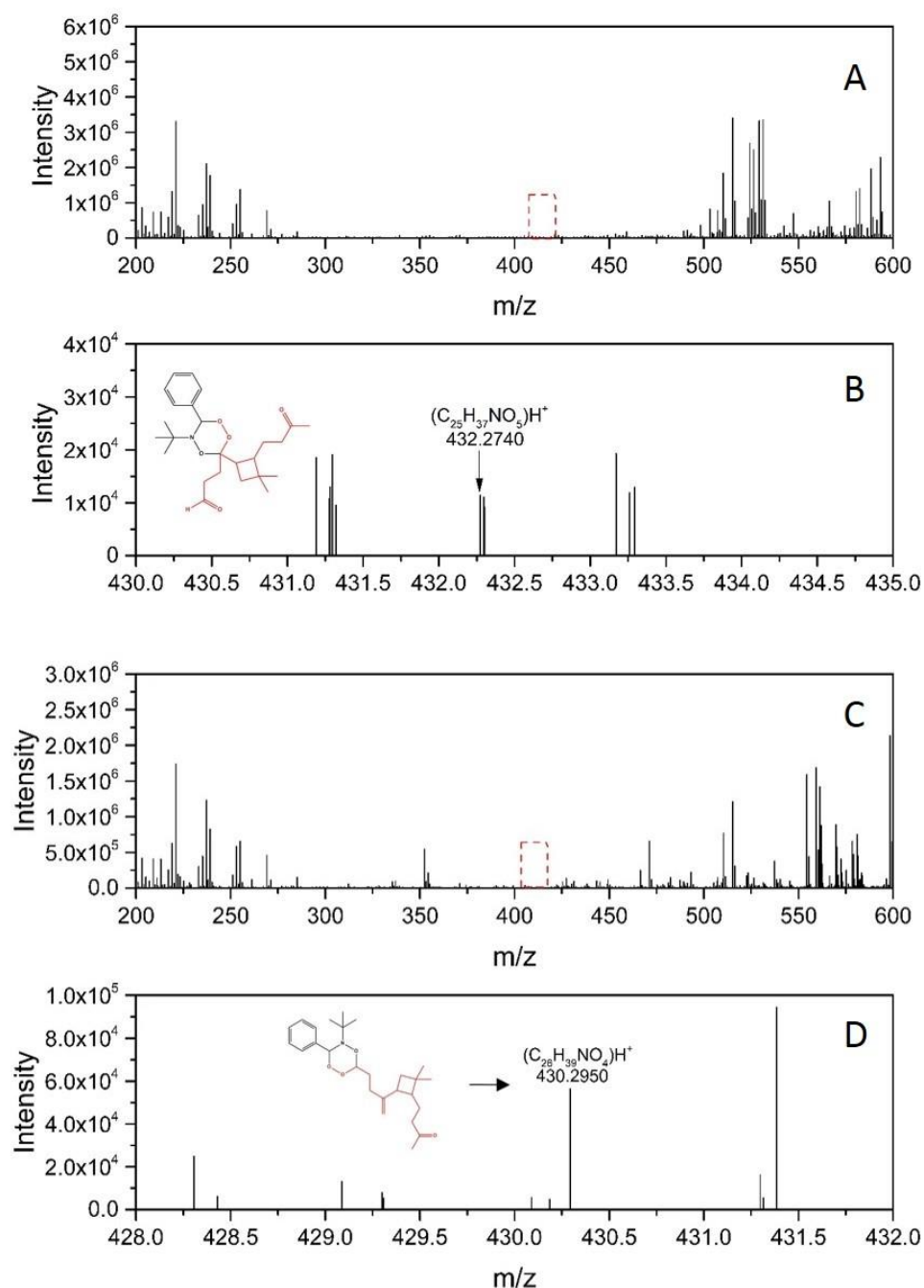


**Figure 4.11-** HPLC-ESI-HRMS analysis of  $ClC_{15}$  CI-PBN in particle phase (c) processed spectrum and (d) zoom on the peak at  $m/z = 430.2950$   $(C_{26}H_{39}NO_4)H^+$  (retention time = 36.9 minutes). (c) and (d) – HPLC-ESI-HRMS analysis of the acetonitrile-PBN-SOA solution sampled from the impinger, showing a peak assigned to  $ClC_{14}B$ -PBN adduct at  $m/z = 432.2740$   $(C_{25}H_{37}NO_5)H^+$  (retention time = 31.1 minutes). The detection of this peak is indicative of secondary ozonolysis occurring in the system, either in the gas phase or *via* heterogeneous reactive uptake of  $\beta$ -caryophyllenealdehyde and ozone into the particle.

The detection of the  $\text{CI}_{\text{C15}}$  in the particle phase potentially indicates that the CI has a sufficiently low volatility to condense into the particle phase, and partitions into the particle at a rate that is at least comparable to gas phase loss. It is at present unclear whether the CIs detected in the condensed phase are formed in the gas phase, and then partition into the aerosol, or are formed from a fraction of  $\beta$ -caryophyllene that immediately condenses into the particle phase, and then undergoes heterogeneous reaction with  $\text{O}_3$ .

Furthermore, the fact that the  $\text{CI}_{\text{C14B}}$ -PBN adduct is observed is indicative of secondary oxidation occurring in the reaction system. The  $\text{C}_{14\text{B}}$  CI was previously assigned to the product corresponding to secondary ozonolysis of BCAL (see Section 4.3.2), a product of the endocyclic ozonolysis of  $\beta$ -caryophyllene. Given the fact that ozone was in excess in this experiment, with  $[\text{O}_3] = 440 \text{ ppm}$  and  $[\beta\text{-caryophyllene}] = 184 \text{ ppm}$ , it is therefore likely that secondary oxidation of BCAL could occur in this system. It is unclear as to whether the  $\text{C}_{14\text{B}}$  CI is formed in the gas phase, and then condenses into the particle phase, or whether heterogeneous oxidation of BCAL is occurring in the SOA. A study by Jaoui *et.al.*<sup>219</sup>, found that the total yield of BCAL from the ozonolysis of  $\beta$ -caryophyllene was 17%, with 6.5% and 10.8% detected in the gas phase and aerosol phase respectively. If the same were true in this case, then both homogenous and heterogeneous formation of the  $\text{C}_{14\text{B}}$  CI could contribute to the overall detected concentration of the adduct  $\text{CI}_{\text{C14B}}$ -PBN.

In order to gain further perspective of the gas phase chemistry occurring, and qualitatively describe gas vs particle losses during the reaction of  $\text{O}_3$  with  $\beta$ -caryophyllene, a simplified kinetic model was developed using Mathematica (v9.0, Wolfram). The mechanistic information was taken from the Master Chemical Mechanism, MCM v3.2, *via* website <http://mcm.leeds.ac.uk/MCM><sup>218</sup>. Although not entirely explicit, this model provides an estimate of the concentration of products formed in the gas phase in this reaction, and does not consider loss *via* partitioning of low volatile species into the particle phase or particle phase reactions. The model outputs obtained are presented in Figure 4.12, and the Mathematica model is presented in Appendix 3.

The model estimates that the  $\text{C}_{15}$  SCI and  $\text{C}_{15}$   $\text{CI}^*$  are formed with an initial maximum concentration of approximately  $1.2 \times 10^{15} \text{ molecules cm}^{-3}$  and  $1.6 \times 10^{10} \text{ molecules cm}^{-3}$  respectively. Both species promptly decompose, with the SCI and  $\text{CI}^*$  decaying to zero within 0.1 and 0.075 s respectively. It is unclear as to whether this technique scavenges

the SCI or CI\*, but due to the elevated concentrations of the SCI (5 orders of magnitude greater than CI\*), and marginally longer lifetime, it is likely that the SCI substantially if not entirely contributes to the CIs detected in the condensed phase, which is consistent with previous results presented in Chapter 3<sup>169,177</sup>.

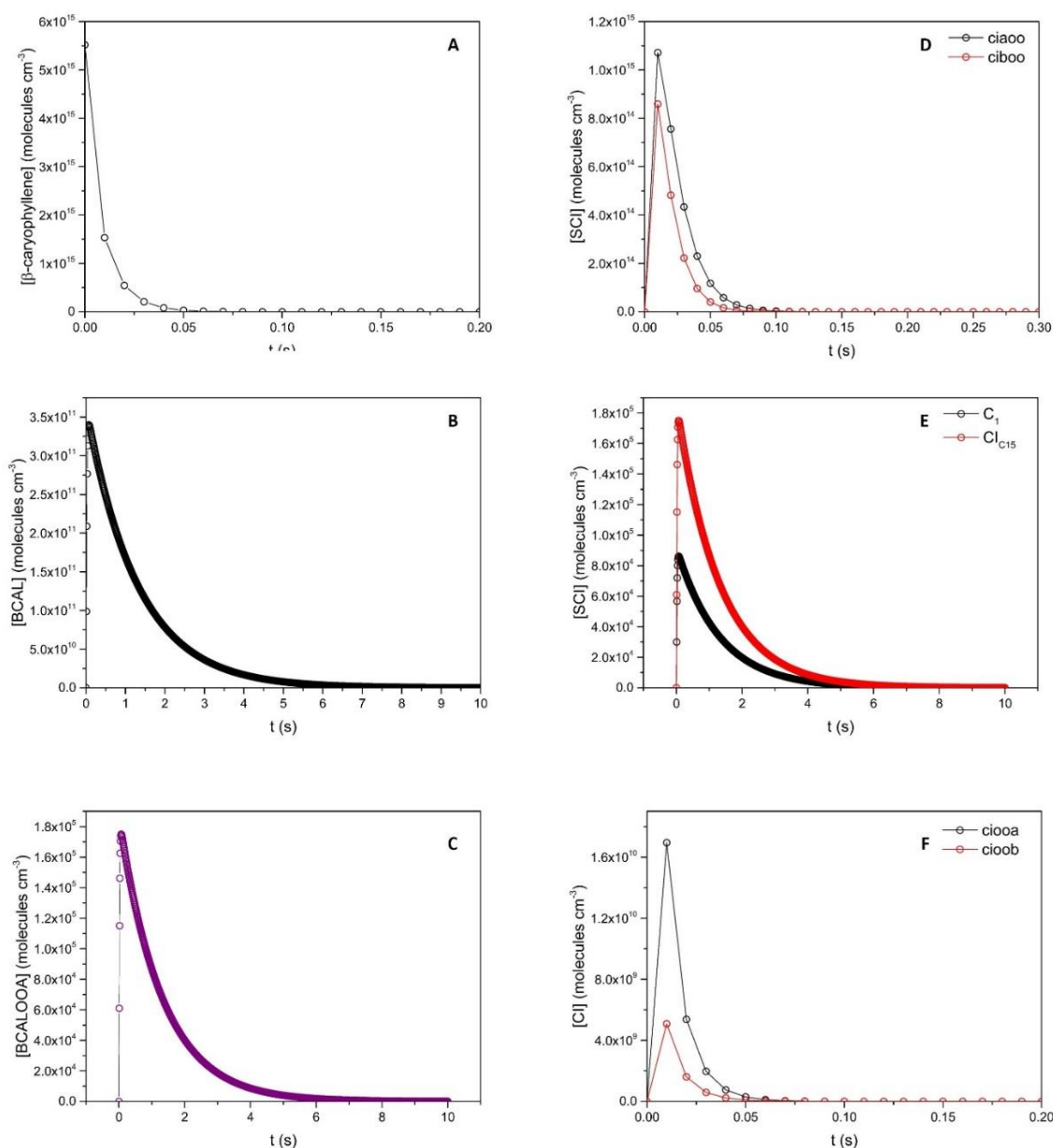


**Figure 4.12** – MCM modelling of the ozonolysis of  $\beta$ -caryophyllene depicting (a) decay of  $\beta$ -caryophyllene, (b) formation of  $\beta$ -caryophyllenealdehyde (BCAL), (c) formation of the  $CI_{C14}$  (BCALOOA), (d) formation of both isomers of  $CI_{C15}$  (ciao and ciboo), constituting the total detectable concentration of  $CI_{C15}$ , (e) comparison between the two stabilised CIs formed from ozonolysis of the exo-bond of  $\beta$ -caryophyllene ( $CI_{C1}$  and  $CI_{C14}$ ) and (f) comparison between the  $CI^*$  formed from the reaction. Initial reactant conditions were 194 ppm  $\beta$ -caryophyllene and 440 ppm  $O_3$ .

The model estimates that BCAL is formed with a maximum concentration of  $3.4 \times 10^{11}$  molecules  $\text{cm}^{-3}$ , before being entirely consumed by the excess  $\text{O}_3$  within 8 seconds, liberating both the  $\text{C}_1$  and  $\text{C}_{14\text{B}}$  CIs. The elongated lifetime of BCAL in the gas phase may allow a substantial fraction of BCAL to condense into the particle phase given the relatively low volatility of the compound; however, it is currently unclear as to the extent of heterogeneous or homogeneous loss of BCAL.

Therefore, it is currently unknown as to the extent of heterogeneous or homogenous oxidation of BCAL to yield the  $\text{C}_{14}$  CI. Given the fact that  $\beta$ -caryophyllene has a relatively low vapour pressure,  $p^\circ = 0.18 \pm 0.03 \text{ mmHg}^{220}$ , and the SOA mass generated is so large in this system it is likely a substantial fraction of BCAL itself will partition into the condensed phase. The partitioning coefficient  $K_p$  ( $\text{m}^3 \text{ug}^{-1}$ ) was estimated for BCAL using the following equation from Ziemann and Atkinson:.

$$K_p = \frac{R \cdot T}{M \cdot \gamma \cdot P} \quad (4.3)$$

Where  $R$  is the gas constant ( $8.314 \text{ J K}^{-1} \text{ mol}^{-1}$ ),  $T$  temperature (298K),  $M$  the molecular mass of the partitioning species in question ( $\mu\text{g m}^{-3}$ ),  $\gamma$  the activity coefficient and  $P$  the vapour pressure (Pa) of the organic in question. Using the information presented in Table 1.1, the vapour pressure of BCAL was estimated by assuming the multiplicative drop in vapour pressure associated with the addition of an aldehyde and ketone group to  $\beta$ -caryophyllene and  $K_p$  for BCAL was then calculated to be  $K_p = 72.8$ , substantially greater than that of  $\beta$ -caryophyllene where  $K_p = 0.42$ . This indicates a substantial fraction of BCAL will partition into the condensed phase, upon formation from the ozonolysis of  $\beta$ -caryophyllene.

There could also be a non-negligible concentration of  $\beta$ -caryophyllene lost to the particle phase given its relatively low volatility. As  $\text{O}_3$  is in excess, this could lead to the heterogeneous formation of CIs in the SOA. To the author's knowledge, this represents the first time that CIs have been detected in organic aerosol, and represents a potential new methodology to characterise radicals in the condensed phase. The experiment also suggests that CIs in the particle phase have a sufficiently long lifetime to be captured in

the impinger. The total reaction time from the entrance of the flow tube to the impinger is approximately 358 seconds, and the gas phase reaction between  $\beta$ -caryophyllene and  $O_3$  is estimated to have reached completion in  $<1$  s; this therefore indicates that the CIs have a lifetime in the order of at least many minutes in the particle phase. The technique has illustrated that it is possible to pre-concentrate CI-PBN adducts to facilitate detection, at least from a qualitative perspective.

#### 4.3.6 Quantification of $\beta$ -caryophyllene CIs in SOA using HPLC-ESI-HRMS

In order to determine the quantitative potential of this method, a series of experiments were designed to investigate the HPLC-ESI-HRMS response of the  $CI_{C15}$  as a function of SOA mass. The SOA mass concentration was lowered by reducing the concentration of  $O_3$  in the system, and therefore reducing the extent of oxidised species capable of contributing to SOA mass, as illustrated in Table 1.

**Table 1** – Parametric response of SOA Mass and SOA surface area as a function of  $O_3$  concentration

$[\beta\text{-caryophyllene}]$ (ppm)	$[O_3]$ (ppm)	SOA Mass ( $\text{mg m}^{-3}$ )	SOA Surface Area ( $\text{cm}^2/\text{cm}^3$ )
184	414	140	$1.62 \times 10^{-2}$
184	118	35	$5.5 \times 10^{-3}$
184	6	10	$1.3 \times 10^{-3}$

Using the same experimental procedure as described in Section 4.2.3, HPLC-ESI-HRMS analysis was undertaken for each of the chemical regimes listed in Table 1. For each SOA mass loading, the peak corresponding to the  $CI_{C15}$ -PBN adduct was detected at  $m/z = 430.2954$  ( $C_{26}H_{39}NO_4$ ) $H^+$ . In order to assess the quantitative response of the technique, the HPLC peak associated with the  $CI_{C15}$ -PBN adduct was plotted as a function of mass, as illustrated in Figure 4.13.

Increasing the SOA mass generated in the flow tube, and therefore a larger mass concentration of SOA sampled in the impinger, resulted in a larger peak area corresponding to the  $m/z = 430.2950$  peak. In this plot, X-error represents the variability of the SOA mass observed over multiple repeats, and Y-error represents the standard deviation of the peak area observed over four repeats. This indicates that the concentration of the  $CI_{C15}$ -PBN adduct concentration, and presumably the concentration of  $CI_{C15}$ , increases with increasing SOA mass.

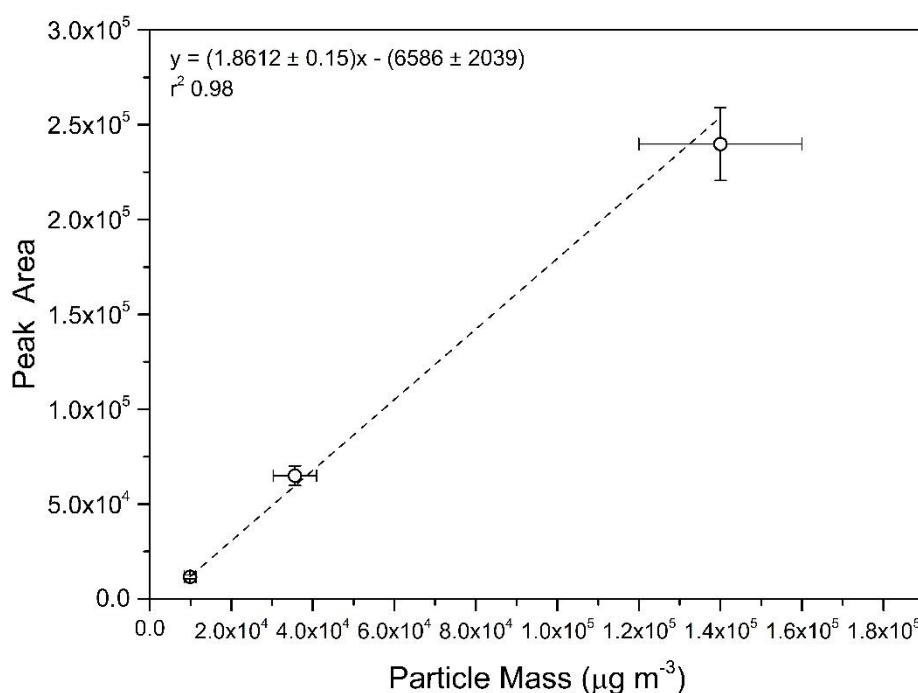


**Figure 4.13** – HPLC Peak area response as a function of SOA mass in the flow tube. An increase in the SOA mass generated in the flow tube system results in a larger peak area measured with HPLC-MS associated with the  $\text{CI}_{\text{C15}}$ -PBN adduct, implying that the CI concentration in the particle also increases as a function of mass.

Because no commercially viable standard for  $\text{CI}_{\text{C15}}$ -PBN adduct is available, and given the complex steps required to synthesise this compound, the spin trap PBN was chosen as a surrogate standard for quantification. Although not structurally identical to  $\text{CI}_{\text{C15}}$ -PBN, it allows an approximation of the concentration dependence of the peak area. A PBN calibration curve was plotted using a variety of known PBN concentrations with the peak area determined using HPLC-ESI-HRMS (Figure 4.14). Using this calibration curve, the concentration of the  $\text{CI}_{\text{C15}}$  per unit mass of SOA was estimated to be  $4.5 \pm 0.7$  ng/ $\mu\text{g}$  SOA, correcting for both the collection efficiency of the impinger and trapping efficiency of the PBN towards the CI as discussed in Section 4.3.3.

This mass could constitute about  $\sim 0.5$  % of the total mass of SOA in this oxidation regime. Given the large concentration of precursors, as well as the large SOA yield from  $\beta$ -caryophyllene ozonolysis, it is not entirely unlikely that a substantial amount of CI either could partition into the condensed phase, or be formed by heterogeneous oxidation of alkenes present in the SOA. However, given the lack of literature data available, it is difficult to contextualise this number.

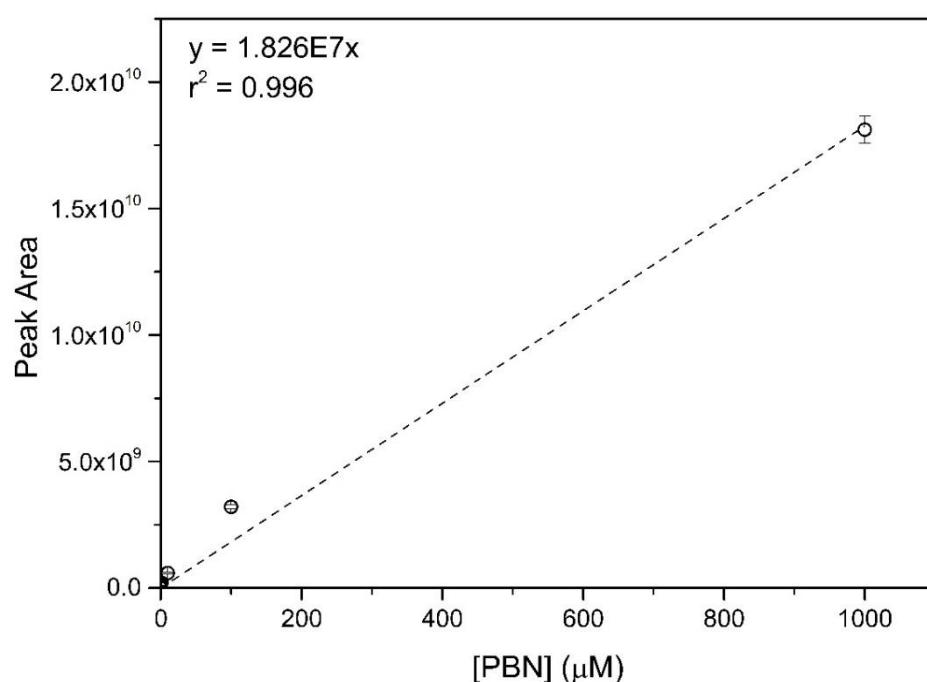


**Figure 4.14** –Calibration curve illustrating the response of the peak area obtained from HPLC-ESI-HRMS analysis as a function of [PBN] concentration.

## 4.4 Chapter Summary

This chapter presented the detection of multiple Criegee intermediates generated from the ozonolysis of  $\beta$ -caryophyllene in the particle phase. Initial gas phase analysis of CIs in this oxidation regime using our previously optimised technique detected the adduct corresponding to the  $\text{CI}_{\text{C1}}$ -DMPO adduct, but was not sufficient to fully characterise larger CIs, indicating that larger CIs may be directly lost to the particle phase. A novel technique was developed to facilitate the detection of CIs in the particle phase by stabilisation with spin traps and off-line analysis using HPLC-ESI-HRMS. The PBN adducts  $\text{CI}_{\text{C15}}$ -PBN and  $\text{CI}_{\text{C14B}}$ -PBN were detected, indicating the presence of large, low-volatile CIs in the SOA. At present, it is not entirely clear whether the CIs detected were formed from heterogeneous uptake of CIs from the gas phase, or *via* heterogeneous oxidation of  $\beta$ -caryophyllene already present in the condensed phase. An investigation into the concentration of CI at different SOA mass loadings illustrated a correlation between the peak area associated with the  $\text{CI}_{\text{C15}}$ -PBN and the mass concentration. Using PBN as a surrogate standard, the concentration of CIs in the particle phase was estimated to be  $4.5 \pm 0.7 \text{ ng}/\mu\text{g SOA}$ . Although this remains an approximation with several



uncertainties, it does illustrate the quantitative potential of this technique. At present, the trapping efficiency of the PBN is an estimate based on liquid phase ozonolysis, and would need to be properly investigated to improve quantification. A suitable standard for HPLC calibration is also required, highlighting the need to synthesise a  $\text{Cl}_{\text{C15}}$ -PBN standard. As well as this, the collection efficiency is low, estimated to be ~9%. This could be substantially improved by developing the impinger. A fritted impinger would break the airflow into many more, smaller bubbles in solution, therefore improving the likelihood of particles diffusing to the bubble surface and dissolving in solution.

The work presented in this chapter has demonstrated that this technique is uniquely capable of characterising CIs in the particle phase, and has shown some potential regarding the quantification of CIs. Large uncertainty remains regarding the role of particle-bound radicals in both SOA ageing processes as well as health-relevant toxicological impacts. There remain large uncertainties associated with the reaction mechanisms, pathways and product distributions regarding bulk phase reactions in SOA. Substantial optimisations and further development of the method are required to study the role of particle bound CIs at atmospherically relevant concentrations of SOA. However, this technique could potentially allow one to characterise the role of reactive intermediates in this process, which in turn could elucidate the reaction mechanisms and pathways that lead to observed product distributions.

---

# 5 QUANTIFICATION OF ORGANIC RADICALS IN SECONDARY ORGANIC AEROSOL

---

This Manuscript will be submitted to a journal post-submission.

## **Author Contributions**

Steven J Campbell designed and conducted the experiments and wrote the manuscript.

---

## 5.1 Introduction

Secondary organic aerosol (SOA) constitutes a substantial fraction of ambient fine particulate matter.<sup>3</sup> The formation of SOA in the atmosphere occurs *via* gas-to-particle conversion mechanisms, often initiated by the gas phase oxidation of VOCs.<sup>12,221</sup> Recently, it has been shown that extremely low volatile organic compounds contribute significantly to SOA growth.<sup>24,25,186</sup> The chemical composition and evolution of SOA in the atmosphere represents one of the largest uncertainties in our current understanding of air quality and public health.<sup>29</sup> Despite vast research, the exact toxicological mechanisms relating to adverse human health effects upon exposure to particulate matter are poorly understood.<sup>62</sup> However, studies suggest that particle bound reactive oxygen species (ROS) are a major contributor to observed health effects associated with PM.<sup>62,222,223</sup>

ROS is an umbrella term, which encompasses a large range of species including peroxides, oxidised organics, organic radicals and transition metal induced formation of peroxides and radicals.<sup>62</sup> Several chemical assays are available, all of which are sensitive to certain ROS species in aerosol.<sup>83,85,86,90,224</sup> However, the role of radicals in both the formation and ageing of aerosol, as well as their contribution to the health-relevant properties of ambient aerosol, at present remains highly uncertain. Studies have sought to understand the role of uptake of radicals such as OH into organic aerosol<sup>225–228</sup>, but there is essentially no literature available regarding the quantitative or qualitative understanding of particle-bound organic radicals in SOA.

Recently, a study by Miljevic *et al.*<sup>229</sup> introduced the profluorescent spin trap BPEA (extensively described in Section 1.3.5), which has been shown to be capable of quantifying particle-bound radicals in aerosol generated from the combustion of biomaterial and fuel. Further studies have applied this probe to quantify particle-bound radical concentrations in cigarette smoke<sup>97</sup>, smoke generated from combustion of diesel<sup>96</sup> and aerosol generated from biomass burning<sup>75</sup>.

The work in this chapter discusses the adaptation of the BPEA/DMSO assay and its application to the study of particle-bound radicals in SOA. Initial proof-of-concept experiments determining whether the assay was sensitive to radicals present in  $\alpha$ -pinene SOA were performed. Furthermore, the assays suitability to study the rate of loss of radicals in secondary organic aerosol was assessed. Radical concentrations were also

estimated SOA generated from the ozonolysis of  $\alpha$ -pinene,  $\beta$ -caryophyllene and limonene to probe the assays response to different SOA typically formed in the atmosphere.

## 5.2 Methodology

### 5.2.1 Reagents

All reagents and solvents were acquired from Sigma-Aldrich unless otherwise stated. DMSO ( $\geq 99.9\%$ , anhydrous) was used for the impinger solvent, and methanol (HPLC grade, Fisher Scientific) for the HPLC-ESI analysis. The spin trap BPEA was shipped by the Ristovski group (Queensland University of Technology, Brisbane, Australia), synthesised for the first time by Fairfull-Smith *et al.*<sup>122</sup> The VOCs used as precursors for SOA were  $\alpha$ -pinene (98% (+/-)- $\alpha$ -pinene), limonene ( $\geq 98\%$ ) and *trans*- $\beta$ -caryophyllene ( $\geq 99\%$ ), which were reacted with ozone produced by a UV lamp (185/254 nm, Appleton Woods®).

### 5.2.2 Flow tube Set-up

The flow tube set-up here was described in detail in Chapter 4 (Section 4.2.3), and will briefly be discussed here, with the schematic of the flow tube displayed in Figure 4.3.

The ozonolysis reaction takes place in a flow tube reactor maintained at ambient temperature ( $\sim 16^\circ\text{C}$ ) and pressure, and dry conditions (relative humidity approximately  $< 2\%$ ). The experimental set-up comprised a 2.5 L glass flow tube in which a VOC reacts with ozone, an activated charcoal denuder downstream of the flow tube to remove gas phase VOCs, an impinger, and an SMPS to monitor the particle mass concentration for the duration of the experiment. A HEPA filter (HEPA cap in-line, Whatman, 90406AA) can be added in-line to remove particles and perform gas-phase blank measurements.

The VOC precursor was contained in a 25 mL pear-shaped flask, and  $\text{N}_2$  (oxygen-free nitrogen, BOC) carrier gas regulated *via* a 20-2000  $\text{cm}^3/\text{min}$  mass flow controller (MKS 1179A Mass-Flo® controller) was flowed over the VOC at 200  $\text{cm}^3/\text{min}$  to introduce the VOC precursor into the flow tube in the gas phase. Ozone was produced by a UV lamp (185/254 nm, Appleton Woods®) by flowing synthetic air (Zero grade, BOC) at 200  $\text{cm}^3/\text{min}$  (20-2000  $\text{cm}^3/\text{min}$  MKS 1179A Mass-Flo® controller).

Ozone was measured using a UV photometric ozone analyser (Thermo Scientific model 49i) and particle concentration was measured using a TSI scanning mobility particle sizer (SMPS) composed of TSI 3080 electrostatic classifier (X-ray neutraliser and differential mobility analyser TSI model 3081) and a condensation particle counter (TSI model 3775). Gas phase concentrations of  $\beta$ -caryophyllene,  $\alpha$ -pinene and limonene were measured to be 194, 158 and 135 ppm respectively. The collection efficiency of DMSO concerning the collection of SOA was estimated to be  $\sim 9\%$  for 40 mL of DMSO in this impinger, using the same calculation method previously described in Section 4.2.3. An impinger is advantageous despite low collection efficiency, as it allows the direct scavenging of radicals in SOA, improving the time resolution compared to classical aerosol collection methods such as filter sampling.

### 5.2.3 Fluorescence Measurements

Fluorescence measurements of BPEA were conducted in a modified cuvette holder (Ocean Optics model CUV) illustrated in Figure 5.1. The BPEA was excited at 430 nm by an LED (Roithner APG2C1-435 435 nm, 380 mW at 350 mA) connected to an optical fibre (Ocean optics 00S-003948-07) that was subsequently coupled to an aspheric lens (Thorlabs, type C230TMD-A) to focus the light from the optical fibre into the cuvette holder. The same lens and optical fibre are then connected to a UV spectrometer (Ocean Optics UV2000+).

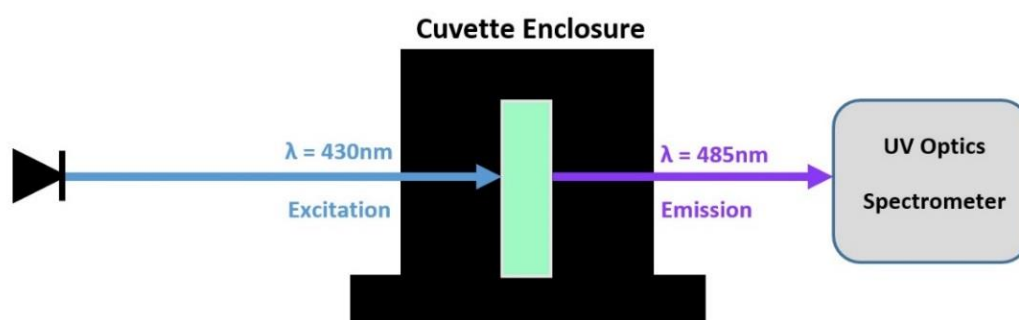


**Figure 5.1** – Cuvette enclosure used for fluorescent measurements. A sample of BPEA exposed to SOA is placed in the cuvette and excited at 430 nm. The fluorescent response at 485 nm is monitored using a UV spectrometer, which can then be used to quantify radical components of SOA.

To quantify the fluorescence response at the detector, a 10 nm peak integration window was used, from 480 – 490 nm, 5 nm either side of the peak maximum at 485 nm. A representative spectrum of BPEA-R, showing a typical fluorescence peak, is given in Figure 5.2.

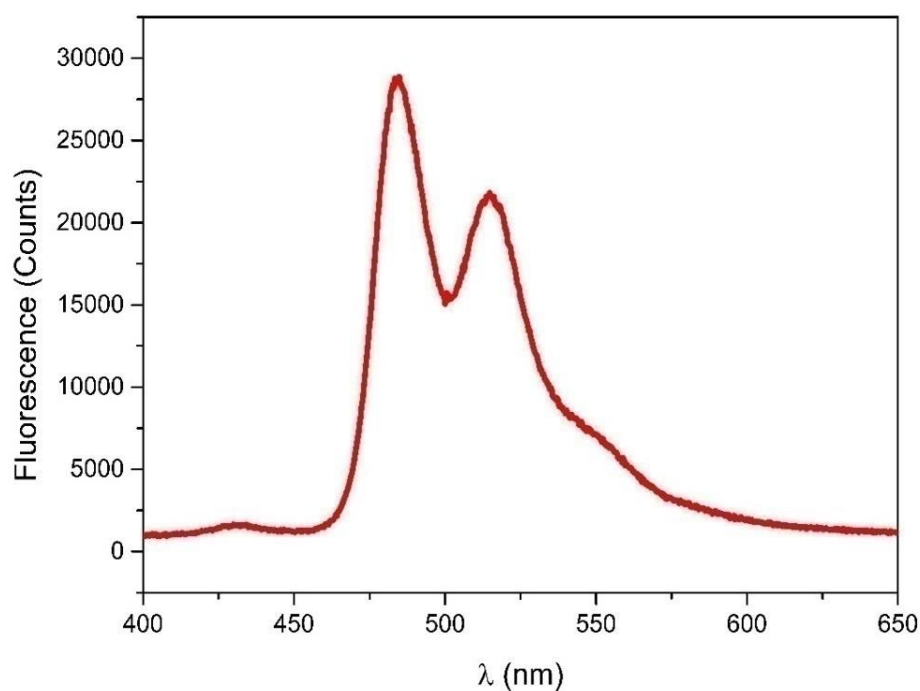


**Figure 5.2** – Spectra of the fluorescent compound BPEA-R. Two characteristic peaks at 485 nm and 510 nm are observed, consistent with previous results<sup>97</sup>.

## 5.3 Results and Discussion

### 5.3.1 ESI-HRMS Characterisation of BPEA fluorescent products

As was discussed in Section 1.3.5, the spin trap BPEA has shown considerable promise in the detection of particle bound radicals. Stevanovic *et al.*<sup>97</sup> recently proposed that the main product responsible for the fluorescent response of the BPEA in DMSO was formed by BPEA scavenging sulfoxyl radicals, which are themselves generated by reaction of DMSO with particle-bound radicals present in the aerosol. The sulfoxyl radical can subsequently undergo rearrangement to form other fluorescent products (Figure 1.17). Sonication of DMSO is well known to produce  $\cdot\text{S}(=\text{O})\text{-CH}_3$  and  $\cdot\text{CH}_3$ <sup>127</sup>, which can be scavenged by the BPEA spin trap. This method of generating radicals in a DMSO solution

was chosen to conduct preliminary ESI-HRMS measurements, to confirm that BPEA can indeed scavenge these radicals in solution to generate the products responsible for the observed fluorescent response, as proposed in the mechanism in Figure 1.17.

For the sonication experiments, solutions of 50  $\mu\text{M}$  BPEA in DMSO were subjected to sonication for 60 minutes. These experiments were conducted to provide a preliminary qualitative understanding of the products formed when BPEA scavenges radicals generated from the sonication of DMSO. Sonication was conducted in an ultrasonic bath (Grant, Cambridge) containing room temperature HPLC water, with a sonication frequency between 30-45 kHz. Sonication works by propagation of ultrasonic sound waves through a liquid medium, which in turn generates voids and cavities in solution. The bubbles may contain gas, solvent or any other volatile substance present in solution. The bubbles can grow until they reach an unstable size, at which point they violently collapse, generating local temperatures and pressures as high as 5000 K and 500 atm respectively.<sup>230</sup> These localised high temperature cavities essentially act as mini combustion chambers, where pyrolysis of volatile solvent molecules can occur, which can generate radical species.<sup>231</sup>

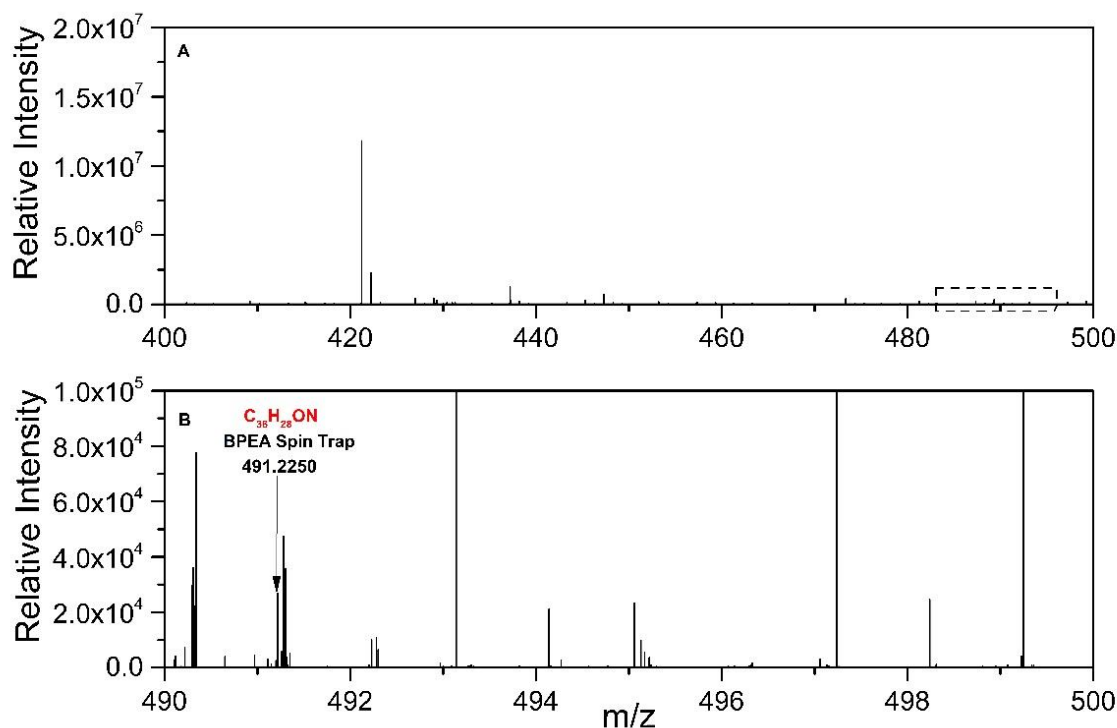


**Figure 5.3** - Positive mode UHR-MS spectrum of unreacted 50  $\mu\text{M}$  BPEA in DMSO without sonication (A) and re-scaled image to identify the protonated spin trap BPEA- $\text{H}^+$  at  $m/z = 491.2250$  (B).



The positive mode direct infusion ESI-HRMS spectra of unreacted BPEA in DMSO with no sonication can be seen in Figure 5.3 (A), and further enhanced to identify the peak corresponding to the protonated [BPEA] $\text{H}^+$  spin trap at  $m/z = 491.2250$  (Figure 5.3(B)). The relatively low intensity infers poor ionisation of BPEA in DMSO *via* direct infusion ESI-HRMS, given the relatively high concentrations of BPEA (50  $\mu\text{M}$ ) infused. Sonication of 15 mL of 50  $\mu\text{M}$  BPEA in DMSO was performed for 60 minutes, and samples were subsequently analysed using direct infusion ESI-HRMS. The peaks  $m/z = 554.2524$  and  $m/z = 476.2381$  were assigned to the products BPEA-S(O) $_2$ CH $_3$  and BPEA-H respectively, the mass spectra of which are given in Figure 5.4 and Figure 5.5.

The BPEA-H and BPEA-sulfoxyl radical adducts were previously identified as two of the main products causing fluorescence in the study by Stevanovic *et al.*<sup>97</sup> The mass spectrometry identification of these products when sonicating BPEA in DMSO suggests that a fluorescent response should be observed when sonicating BPEA in DMSO, with an increase over time, as the concentration of radicals scavenged by the BPEA should increase during the sonication process, as more methyl and sulfoxyl radicals are generated in solution. It also evidences the fact that BPEA is capable of scavenging these radicals, which are the proposed products resulting from the scavenging of radicals from SOA into solution, which subsequently leads to the fragmentation of DMSO, illustrated in the reaction mechanism given in Figure 1.17

Although the BPEA-H and BPEA-sulfoxyl radical adducts were structurally identified using NMR and IR previously<sup>97</sup>, the mechanism proposed in Figure 1.17 for the formation of these molecules is at present only theorised, and it is difficult to determine the exact mechanism that leads to the formation of these products after the initial reaction with BPEA and  $\cdot\text{S}(=\text{O})\text{CH}_3$ .

However, it is assumed for the purposes of this study that the proposed mechanism (Figure 1.17) holds true. We assume particle-bound radicals sampled in the impinger can react with DMSO to produce sulfoxyl and methyl radicals, which can be subsequently scavenged by BPEA, resulting in a fluorescent response. Assuming a 1:1 ratio between BPEA-R (fluorescent product) formed, and either direct scavenging of particle-bound radicals upon sampling, or scavenging of sulfoxyl radicals formed *via* reaction of DMSO with the particle bound radicals themselves, allows one to estimate the radical concentration present in SOA.

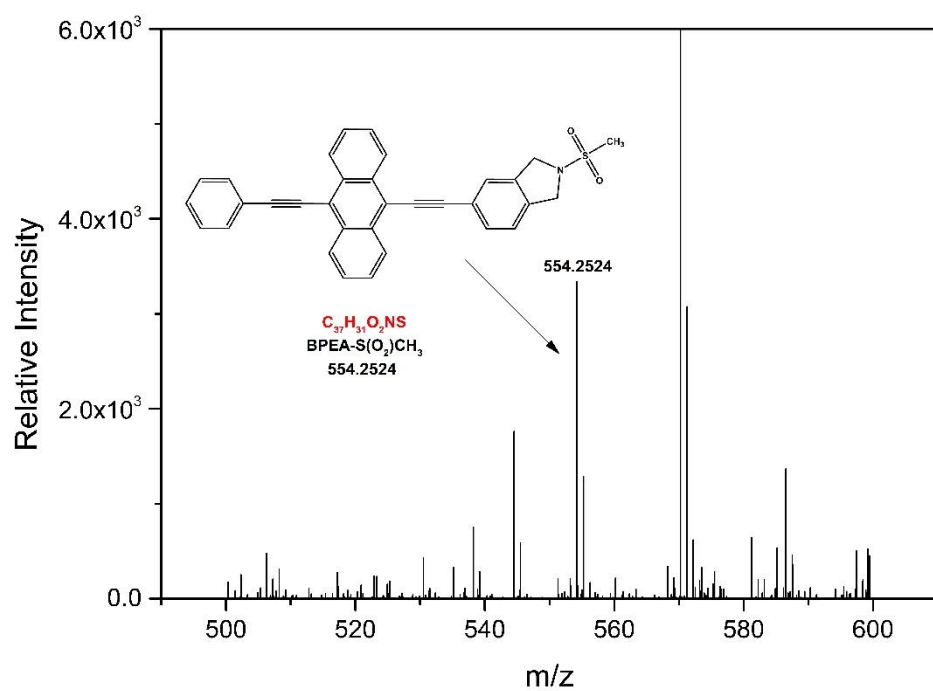


**Figure 5.4** - Positive mode UHR-MS spectra for the sonication of BPEA in DMSO after 60 minutes, with the protonated BPEA-Sulfoxyl radical adduct identified at  $m/z = 554.2524$ .

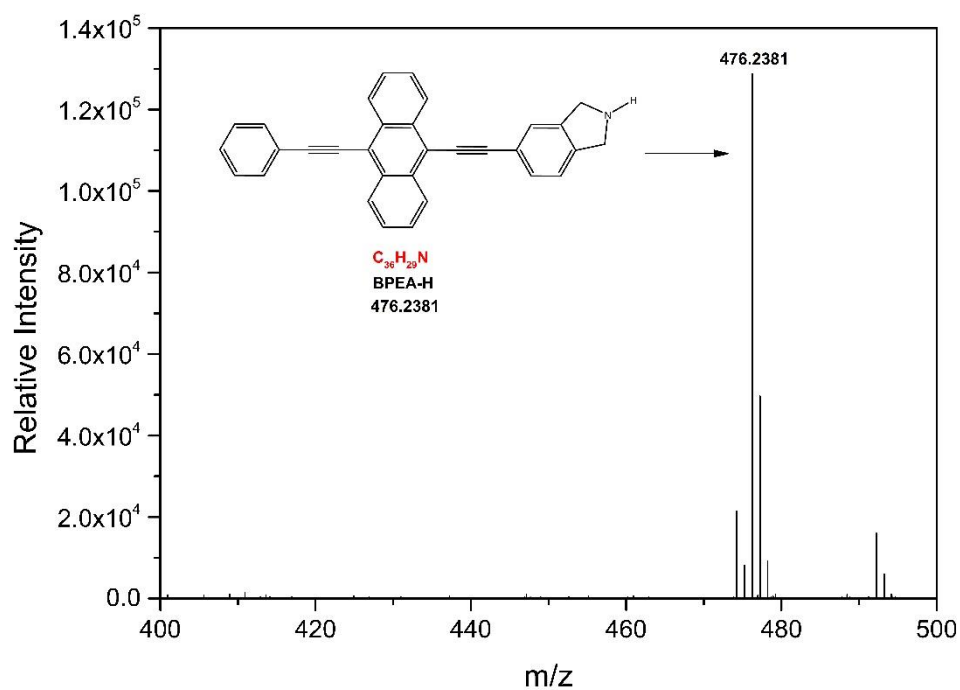


**Figure 5.5** - Positive mode UHR-MS spectra for the sonication of BPEA in DMSO after 60 minutes, with the protonated BPEA-H adduct identified at  $m/z = 476.2381$ .

### 5.3.2 Characterisation of the Fluorescent Set-up

The aforementioned sonication of BPEA in DMSO experiments were also used to determine the peak intensity response associated with the formation of the BPEA-R fluorescent product, where R is a radical species scavenged by the spin trap, therefore quenching the unpaired electron and activating the fluorophore.

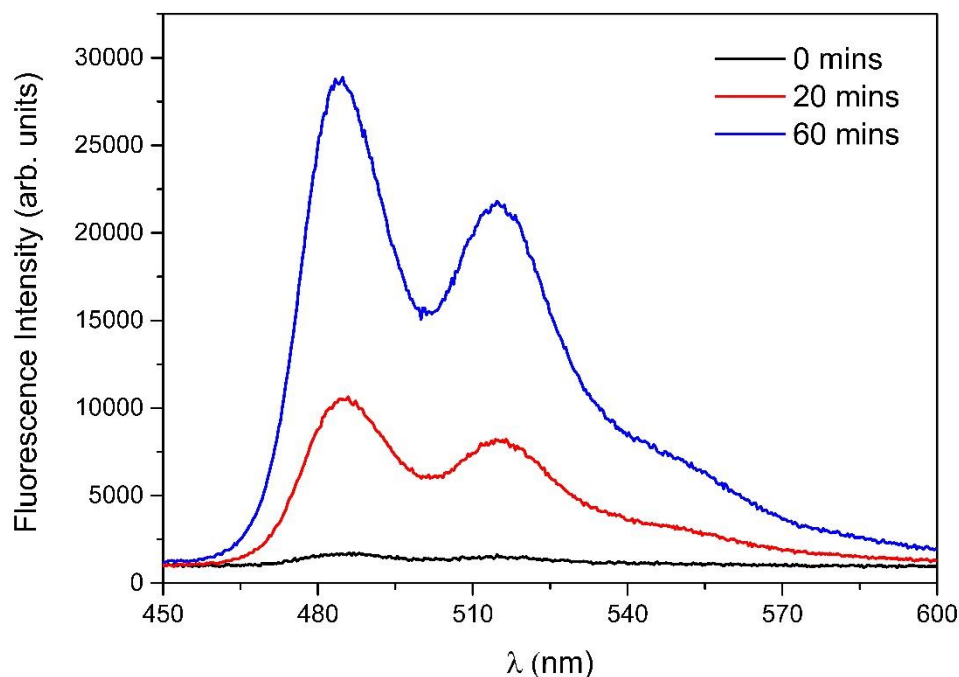


**Figure 5.6** – Fluorescent spectra of 50  $\mu\text{M}$  BPEA after 0, 20 and 60 minutes of sonication in DMSO. The fluorescent response from the assay increases upon exposure to radicals generated from the sonication of DMSO, with two dominant peaks at 485 nm and 510 nm.

Using the fluorescent set-up described in Section 5.2.3, a preliminary test involving samples of sonicated BPEA in DMSO were taken after 0, 20 and 60 minutes of sonication, the fluorescent spectra of which are illustrated in Figure 5.6. The peaks observed at  $\lambda = 485$  nm and 510 nm, characteristic of the fluorescent product BPEA-R, increase over time during the 60 minute sonication period. There is a clear increase in the concentration of the fluorescent product observed (therefore increase in BPEA-R concentration), given the steady increase of the peak area in this experiment. This is due to the scavenging of more radical species over time, therefore quenching the unpaired electron on the nitroxide group (upon formation of BPEA-R) and activating the fluorophore. Further to this, the

LED and spectrometer stability over time was determined, the results of which are illustrated in Figure 5.7.

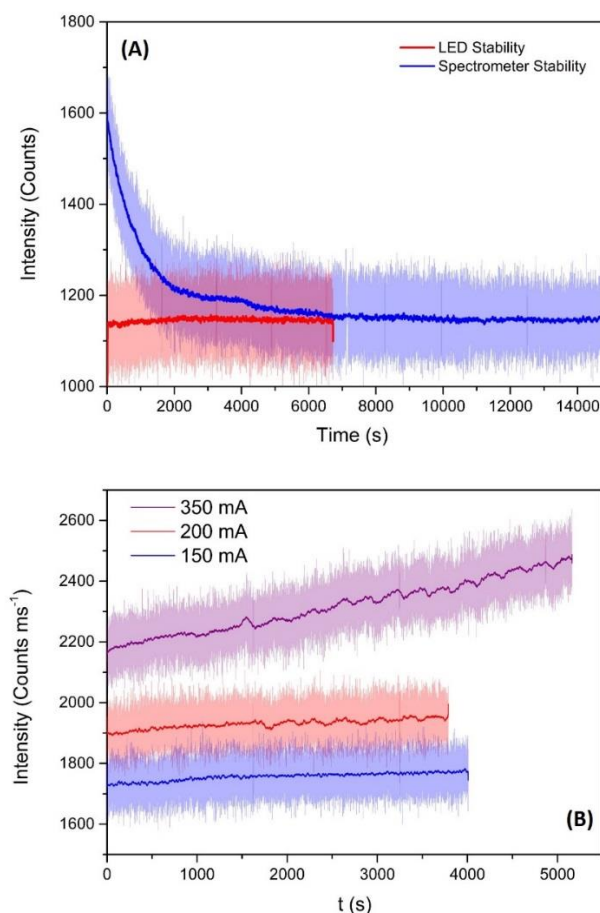


**Figure 5.7** – (A) Spectrometer background stability (blue) upon switching on, with the LED stabilised over 2 hours, and LED stability (red) upon switching on the LED and the spectrometer stabilised for 3 hours. (B) Increase in intensity of BPEA-R overtime as a function of the current passed through the LED. Larger currents, which increase the LED output, result in a significant drift in fluorescent signal of BPEA-R. Shading represents the raw signal variability. The solid line represents the 200 average smoothed signal.

Regarding Figure 5.8 (A), this shows the time it takes for the background signal to stabilise upon switching on the spectrometer (blue) and LED (red). The LED output is relatively stable upon switching on, with the background signal stabilising after 1 hour. However, the background of the spectrometer drifts over  $\sim 2$  hours before background stabilisation. Therefore, before fluorescent measurements are taken, the LED and spectrometer are switched on and left to stabilise for approximately 2 hours to ensure the background signal of the LED/spectrometer is as stable as possible.

The background can be easily corrected for in the data treatment, but drifts in the background signal may result in loss of sensitivity towards BPEA-R. Both the LED output and the spectrometer background vary as a function of temperature, so lab temperatures were kept constant for all experiments to minimise any background drift. Figure 5.8 (B) shows the stability of fluorescent background signal when a cuvette of unreacted BPEA is exposed to different power outputs of the LED, which is changed by altering the current through the LED. At larger currents through the LED, there is an observed increase in the 485 nm fluorescent response of unreacted BPEA. A background fluorescent response is observed due to degradation of the spin trap in solution, resulting in the quenching of the unpaired electron in the nitron functional group which leads to the activation of the fluorophore.<sup>97</sup> It is unclear as to why the fluorescent signal increases over time at larger photon intensities, but due to the observed increase in 485 nm photons at larger currents, all fluorescent experiments were conducted at 150 mA current through the LED (blue curve, Figure 5.7(B)) to minimise this effect.

### Calibration of the Fluorescent Assay

The highly fluorescent compound, BPEA-CH<sub>3</sub>, was used as a calibration standard to estimate the concentration of radicals detected by BPEA. The fluorescent response of the spin trap should be independent of the adduct (BPEA-CH<sub>3</sub>, BPEA-H, BPEA-S(O)CH<sub>3</sub>, etc...) as the structure of the fluorophore is unaltered, and it is the quenching of the unpaired electron that leads to the on/off switching of the fluorophore.

If one assumes that there is a 1:1 reaction stoichiometry between radicals from SOA sampled in the impinger and the spin trap BPEA (either *via* direct scavenging of particle-bound radicals or the reaction of particle-bound radicals with DMSO to produce sulfoxyl radicals in solution which, are scavenged by BPEA), the concentration of radical species in SOA can be estimated using BPEA-CH<sub>3</sub> as a calibration standard.

A calibration curve was generated, using the fluorescent set-up described in Section 5.2.3, over a concentration range of 1-1000 nM, as illustrated in Figure 5.8. The fluorescent response was measured using the spectrometer settings described previously, with a 10 nm signal integration. A linear fitting of the data showed a correlation coefficient of 0.999 with respect to fluorescent response as a function of BPEA-CH<sub>3</sub> concentration. The limit of detection (LOD) of this the fluorescent technique was estimated to be  $\sim 7 \pm 2$  nM BPEA-CH<sub>3</sub>, therefore meaning it is sensitive to the same concentration of radicals in

SOA. However, given the stability of the BPEA-CH<sub>3</sub> adduct one can pre-concentrate the BPEA-CH<sub>3</sub> over time and therefore the concentration of radicals per unit mass of SOA can be estimated.

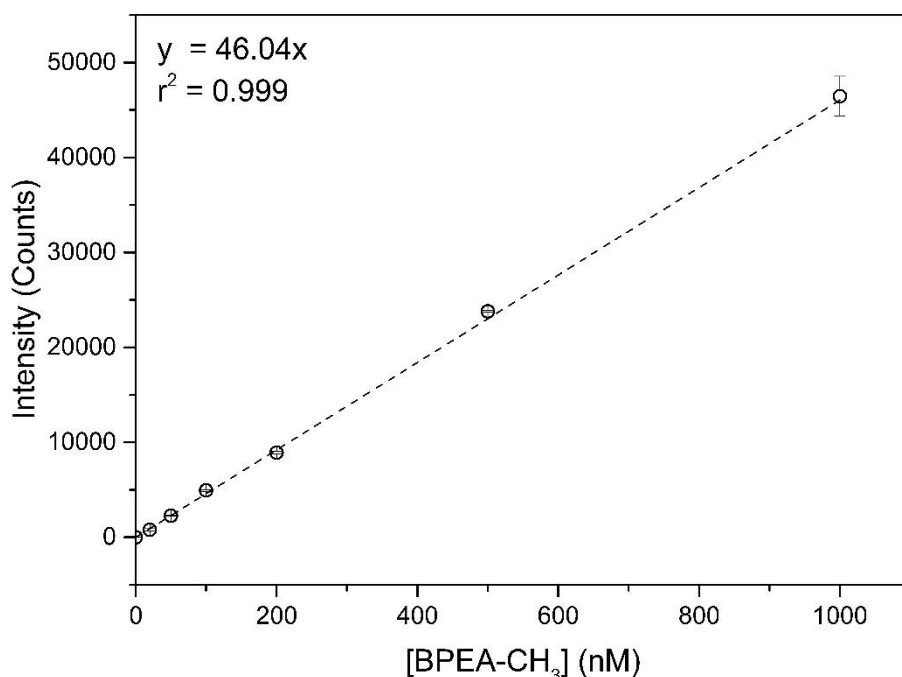


**Figure 5.8** – Calibration curve generated for varying concentrations of BPEA-CH<sub>3</sub>, with an  $r^2 = 0.999$  correlation coefficient upon linear fitting. Error bars are associated with the signal variability observed over multiple repeats. In some cases, the error bars are smaller than the data point.

### 5.3.3 Proof-of-Principle: Quantification of Radicals in SOA

In order to probe the fluorescent response of the BPEA/DMSO assay to organic aerosol,  $\alpha$ -pinene ozonolysis SOA was chosen as a model SOA system, given its ease of use and the extensive characterisation of its chemistry. SOA was generated in a flow tube and sampled in an impinger containing BPEA in DMSO, using the set-up depicted in Figure 4.3. Initially, an experiment with a high mass concentration of SOA at  $1.5 \times 10^5 \mu\text{g m}^{-3}$  was conducted as a proof-of-principle, to ascertain whether or not the BPEA/DMSO assay was sensitive to radicals bound to SOA, the results of which are displayed in Figure 5.9.

1 mL samples of the BPEA-DMSO solution are taken every 20 minutes, and the fluorescent response was measured. There is an observed linear response over time as a

function of SOA sampled into the impinger. The fluorescent compounds observed have been shown to be stable over time periods of several hours<sup>97</sup>, and therefore it can be assumed that as more SOA is sampled (and therefore more particle bound radicals are sampled) in the impinger, the concentration of fluorescent products will also accumulate, allowing a quantitative measure of radicals in the SOA captured in the impinger. A linear response is observed as more SOA is increased over time, with an  $r^2 = 0.976$  correlation. Further to this, a blank experiment was conducted by passing the SOA mixture through a HEPA filter upstream of the charcoal denuder (see Figure 4.3).

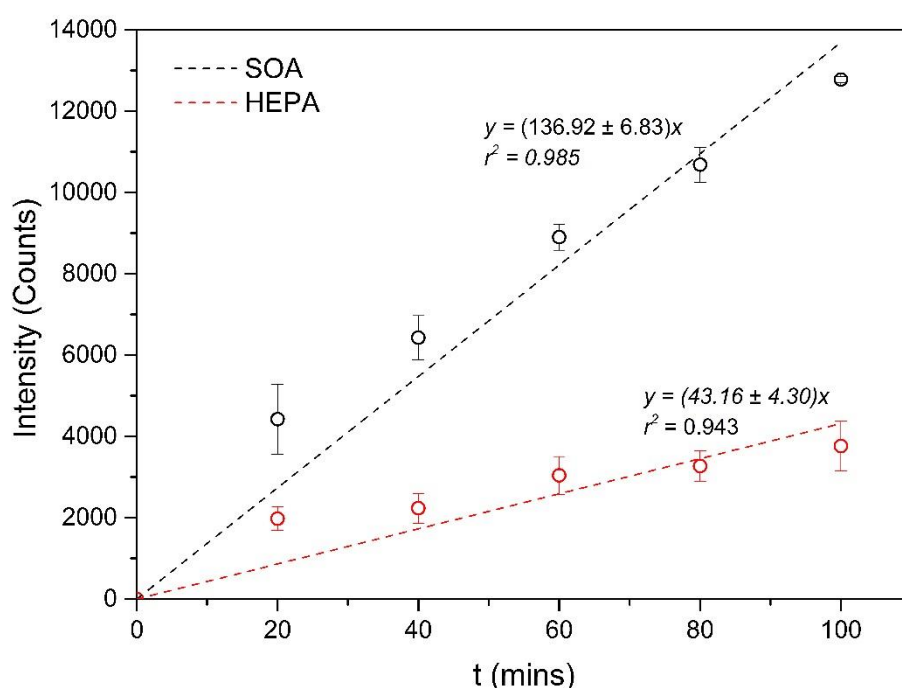


**Figure 5.9** – Initial proof-of-principle experiment where a large SOA mass concentration of  $1.5 \times 10^5 \mu\text{g m}^{-3}$  was sampled through the impinger containing BPEA and DMSO (Figure 4.3) (black), and a blank was obtained by adding a HEPA filter in-line (red). Samples of the BPEA solution are taken every 20 minutes, and the increase in fluorescence was observed over time. Error bars represent the variability observed over four repeats.

This allows the rough estimate of the signal as a response of the gas phase mixture. Despite having an activated charcoal denuder in-line, it is possible for some gas phase constituents to pass through into the impinger. The radical content due to aerosol is therefore corrected by subtracting the gas phase contribution, with the gas phase (HEPA, red) also illustrated in Figure 5.9. The spectra measured at the start of the experiment (unreacted BPEA) and after 2 hours of sampling is illustrated in Figure 5.10.

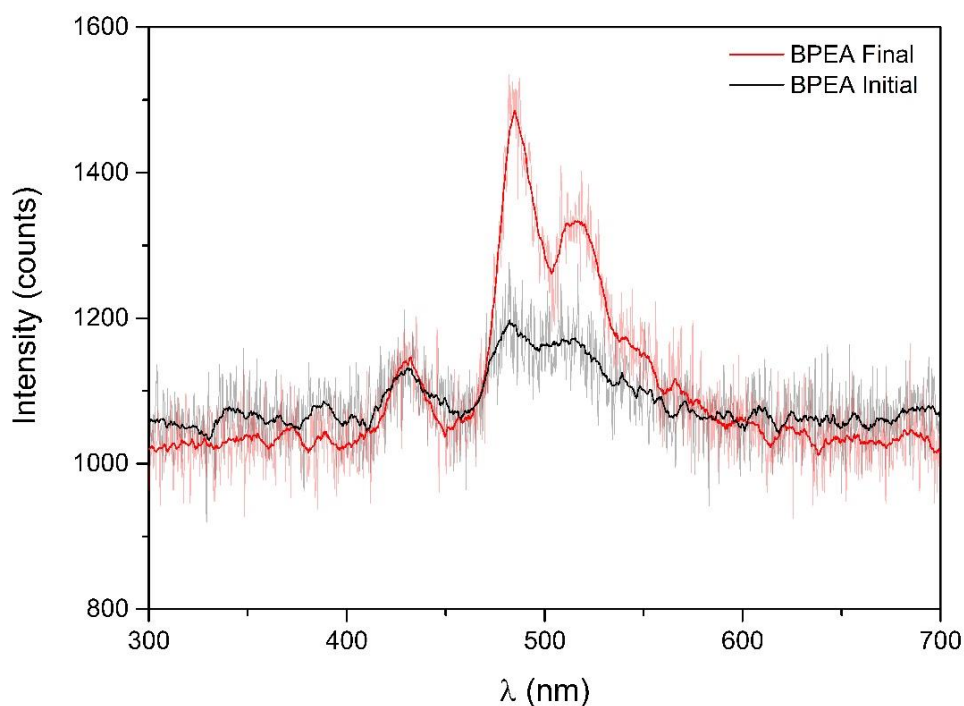


**Figure 5.10** – Smoothed spectra of unreacted BPEA solution (before sampling, black) and after two hours of sampling SOA into the BPEA/DMSO solution (red). Both characteristic peaks at 485 nm and 510 nm increase in intensity upon sampling increasing mass concentrations of SOA.

Using this data as well as the calibration curve (Figure 5.8) and the estimated collection efficiency of ~9% in the impinger, the concentration of radicals per unit mass SOA can be estimated. In this  $\alpha$ -pinene ozonolysis regime, the particle-bound radical concentration was estimated to be  $0.4 \pm 0.1$  nM/ $\mu$ g SOA, or assuming an average molar mass of  $200 \text{ g mol}^{-1}$  for  $\alpha$ -pinene SOA components,  $0.008 \pm 0.002$   $\mu$ g(radicals)/ $\mu$ g(SOA). Therefore, this measurement indicates that there is approximately 1 radical species per 800 molecules in the SOA. This is likely a lower limit estimate of the concentration of radicals; the calculation assumes that all radicals in SOA will react with DMPO, and the subsequent radicals generated here will be scavenged by the BPEA. In principle this is likely not the case.

There may also be other termination reactions occurring between organic radicals once they are introduced into the DMSO solvent, and therefore would not be scavenged by BPEA. Given the high OH yield from  $\alpha$ -pinene ozonolysis reactions as well as the high precursor concentrations used in this experiment this is a plausible value. There is no literature data for comparison of radical concentrations in SOA; however, using the same



technique, Stevanovic *et al.*<sup>75,97</sup> have used this assay to probe radical concentrations in combustion processes. The values presented here are approximately 1-2 orders of magnitude lower than the values reported in those studies. However, combustion processes are likely to generate a lot more radicals *via* pyrolysis of organic material.

These preliminary proof-of-principle experiments have demonstrated that the concentration of radicals in SOA generated from  $\alpha$ -pinene ozonolysis can be estimated. This could potentially allow one to explore other aspects of radicals in SOA, such as their rate of loss in the bulk phase as well as the radical's lifetime.

### 5.3.4 Estimating the Radical Lifetime in $\alpha$ -pinene SOA

After conducting several proof-of-concept experiments to determine whether the BPEA-DMSO assay was indeed sensitive to radicals present in SOA, a series of experiments were conceived whereby the residence time of the SOA in the flow tube after ozonolysis was altered. Therefore, one can potentially determine the loss of particle-bound radicals as a function of time.

With reference to Figure 5.11, there is a clear decrease in the fluorescent response over time as the residence time in the flow tube is increased. This is likely due to the reaction and loss of radicals in the particle phase. As the ozonolysis reaction is completed within 20 seconds, there is unlikely to be any additional formation of OH after this point, limiting the overall extent of SOA ageing and therefore an increase in the concentration of particle-bound radicals. Ozone is indeed in excess in the flow tube, but assuming that all of the  $\alpha$ -pinene is reacted in this initial 20 seconds, there should be limited secondary chemistry occurring with respect to heterogeneous oxidation by ozone. Therefore, we assume that the decrease in the fluorescent signal is observed as a function of residence time in the flow tube can be interpreted as reactive loss of radicals in SOA.

As is the case for the proof-of-concept SOA experiments described in the previous section,  $\alpha$ -pinene ozonolysis was used as a model SOA system. The residence time of the SOA in the flow tube was altered by adding additional reaction volumes to the 2.5 L flow tube set-up depicted in Figure 4.3. The SOA was then sampled in the impinger for a series of residence times varying between 27-500 s, as illustrated in Figure 5.11. Before this, an MCM modelling run was conducted at the concentrations of  $\alpha$ -pinene and ozone in this experimental set up (i.e. 340 ppm O<sub>3</sub> 158 ppm  $\alpha$ -pinene), to estimate a reaction time

between  $\alpha$ -pinene and ozone of roughly 20 seconds in the flow tube before the  $\alpha$ -pinene is entirely consumed by the excess  $O_3$ .

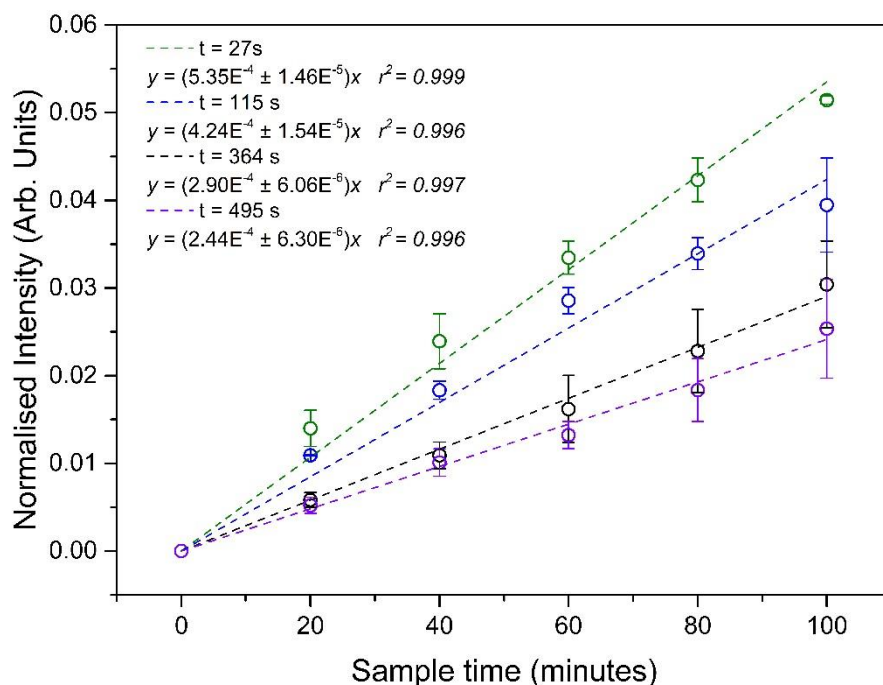


**Figure 5.11** – Fluorescence response of the BPEA assay as a function of residence time of SOA in the flow tube normalised for particle mass and corrected for gas phase contributions. A decrease in the fluorescent response upon sampling is observed when increasing the residence time of the SOA in the flow tube.

By taking the average normalised increase in intensity obtained from Figure 5.11 (normalised with respect to SOA mass) against the residence time, an exponential decay was observed as depicted in Figure 5.12, indicating a (pseudo) first order decay of radicals in SOA. It should be noted that the exponential has a non-zero intercept; if the plot were only monitoring the decay of radicals in SOA, one would expect the radical concentration to decay to zero over time. This could be due to some radical components having a much longer lifetime than that of the extent of the increase in residence time in the flow tube (*i.e.*  $\sim 10\text{min}$ ). As well as this, it could potentially indicate that there is another process that leads to the production of radicals over time, which has not been considered, complicating quantification. It could also be the result of the sensitivity of the BPEA-DMSO assay to another organic component in the SOA, which is non-radical, which would not be accounted for in blank experiments. This interaction could lead to

the production of fluorescent BPEA-adducts that could further complicate quantification.

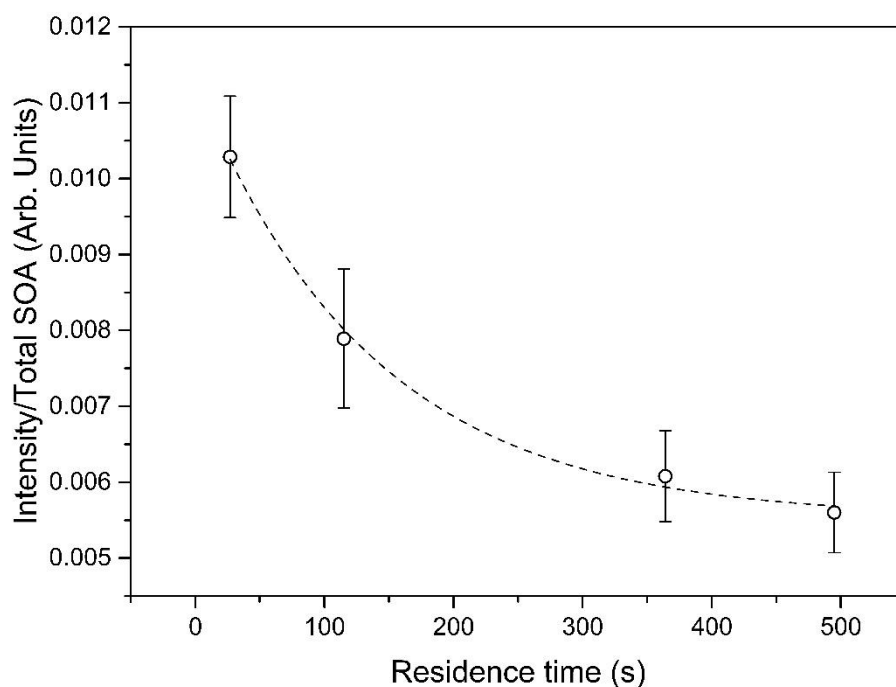


**Figure 5.12** – Plot showing the average signal increase per sampling period (intensity/SOA) as a function of residence time per experiment, with an exponential decay fitting and an  $r^2$  of 0.994. Error bars represent variability in the normalised intensity observer over multiple repeats.

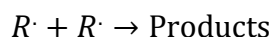
Despite this, a rough estimate of the rate of decay of radicals in SOA, as well as an average lifetime can be extracted from the fit. The data shown in Figure 5.13 suggest that the radical loss rate coefficient in freshly generated SOA particles is  $k = 7.3 \pm 1.7 \times 10^{-3} \text{ s}^{-1}$  on average, which therefore leads to an average radical lifetime in this SOA regime of approximately  $137 \pm 31 \text{ s}$ . To the author's knowledge, this is the first time that organic radicals have been quantified in SOA, and the first estimate of their particle phase loss rate as well as average lifetime in SOA particles; there are no available literature values for loss rates or concentrations of organic radicals in SOA available at present for comparison.

More experimental work is required to reduce background interferences that complicate quantification of the radical component, but this work may well offer a laboratory based method to probe the role of radicals in SOA processes, concerning their effect on SOA ageing, heterogeneous production of radicals, as well as their potential implications for health related studies. These problems still represent a considerable uncertainty concerning SOA formation, composition and ageing mechanisms.

---

## Application of 2<sup>nd</sup> Order Kinetics to Radical Decay

The previous calculation estimates the rate coefficient associated with the decay of radicals in the condensed phase by assuming pseudo first order kinetics. Given the high concentration of reactants in this system, there could be substantial loss of radical species through reaction with other radicals, which can be approximated as:



The rate of loss of radical species  $R\cdot$  can then be expressed as:

$$\frac{d[R\cdot]}{d\tau} = -2k[R\cdot]^2$$

Which when integrated leads to the integrated rate law:

$$\frac{1}{[R\cdot]} = \frac{1}{[R\cdot]_0} + k\tau$$

Thus, a plot of  $1/[R\cdot]$  vs.  $\tau$  should yield a straight line, with a slope of  $k$ . A plot of  $1/[R\cdot]$  vs  $\tau$  is given in Figure 5.13. A straight line is obtained, with an  $r^2$  correlation coefficient of 0.949. An estimate of the rate coefficient can be obtained from the linear fit, where  $k = (0.167 \pm 0.022) \text{ nM}^{-1} \text{ s}^{-1}$ . It is currently unclear whether the loss of radicals in this system can be considered by applying pseudo-first order kinetics or second order kinetics. Given that the pseudo-first order and second order fits have similar  $r^2$  correlations, 0.994 and 0.949 respectively, it is difficult to resolve from the given data which of the two best describes the loss of radicals in the SOA.

Given the fact that it is statistically problematic to resolve these two kinetic assumptions, it is most likely that radical loss in the system will be due to both second order loss given the high concentration of radical species, as well as the pseudo-first order loss *via* reaction of the radical species with a host of organic molecules contained within the aerosol bulk. A more in-depth analysis is required to probe the extent of these two processes, and to elucidate the radical loss processes that lead to the observed lifetime of the radical species.

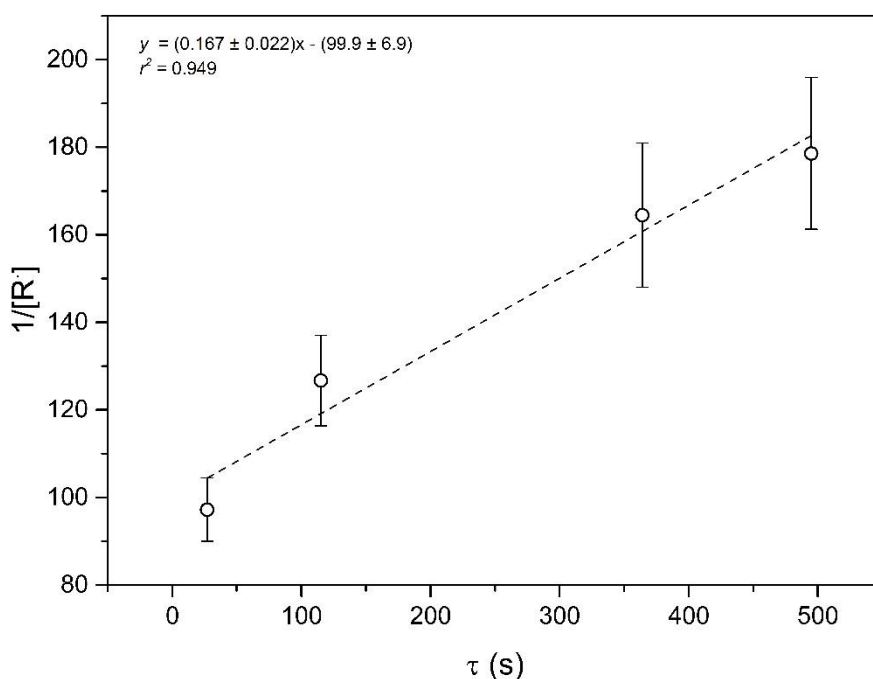
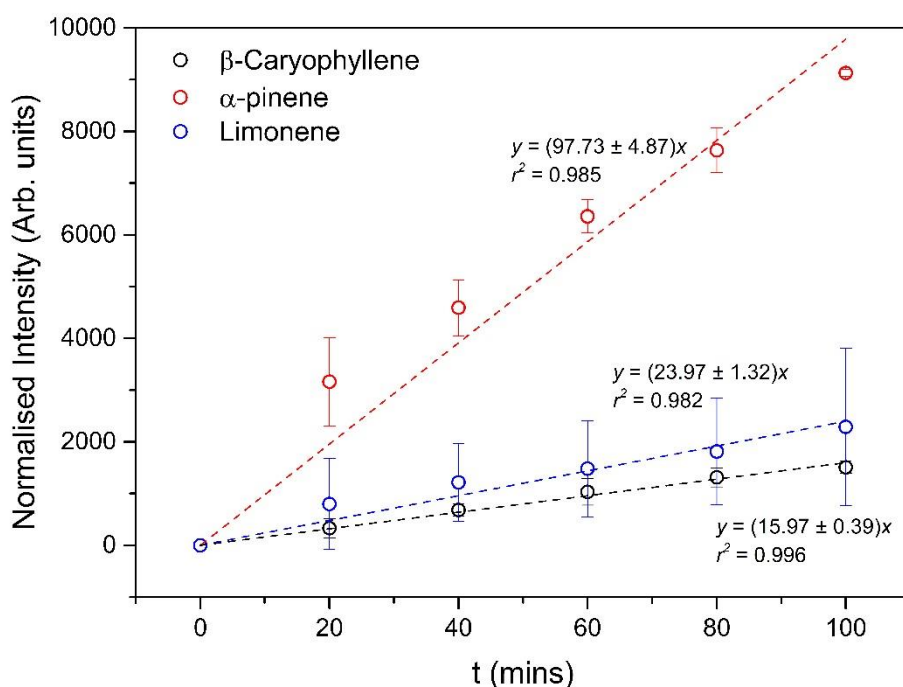


Figure 5.13 – Plot of  $1/[R\cdot]$  vs  $\tau$ , describing the second order loss of radical species in the condensed phase. A linear fit yields an  $r^2$  correlation coefficient of 0.949, and an estimate of the rate coefficient  $k = (0.167 \pm 0.022) \text{ nM}^{-1} \text{ s}^{-1}$ .

### 5.3.5 Radical Concentrations in SOA formed from different VOCs

The radical concentrations in SOA generated from a variety of VOCs was investigated, to expand on the proof-of-principle study on  $\alpha$ -pinene as described in Section 5.3.2.  $\alpha$ -pinene, limonene and  $\beta$ -caryophyllene were the VOC precursors chosen for comparison. Using the flow tube set-up and fluorescent cuvette apparatus described previously, the fluorescent response of the assay over time was measured for SOA generated from the ozonolysis of each precursor, the results of which are illustrated in Figure 5.14.

The data has been normalised to account for varying SOA mass concentrations generated from the different VOC precursors, and corrected for gas phase (i.e. background) contributions to the fluorescent signal. VOC precursor concentrations were measured to be 194, 158 and 135 ppm for  $\beta$ -caryophyllene,  $\alpha$ -pinene and limonene respectively, and the  $\text{O}_3$  concentration was 340 ppm for each of the VOC experiments.



**Figure 5.14** – Increase in the fluorescent response upon sampling SOA generated from the ozonolysis of limonene,  $\beta$ -caryophyllene and  $\alpha$ -pinene, respectively. The intensity was normalised to SOA mass to account for slight differing SOA masses generated from the ozonolysis reaction. A larger increase in the fluorescent signal is observed for  $\alpha$ -pinene than either limonene or  $\beta$ -caryophyllene. Error bars represent variability observed over four repeats.

It is evident that fluorescent response over time upon sampling  $\alpha$ -pinene SOA is substantially larger than that of both  $\beta$ -caryophyllene and limonene SOA regimes. The radical concentration per unit mass of SOA for the three VOC oxidation regimes was calculated, using the aforementioned method of calculation accounting for collection efficiency and mass concentration. The concentrations of radicals for each SOA oxidation regime are presented in Figure 5.15.

One likely explanation for the evidently higher concentration of radicals present in  $\alpha$ -pinene SOA is the higher  $\cdot\text{OH}$  yield associated with this ozonolysis oxidation scheme compared to that of  $\beta$ -caryophyllene and limonene.<sup>1</sup> Yields reported in the literature are  $0.83 \pm 0.23$ <sup>172</sup>,  $0.28 \pm 0.08$ <sup>232</sup> and  $0.14 \pm 2.3$ <sup>211</sup> for  $\alpha$ -pinene, limonene and  $\beta$ -caryophyllene respectively. A greater  $\cdot\text{OH}$  yield in the  $\alpha$ -pinene ozonolysis system could therefore lead to more heterogeneous uptake of  $\cdot\text{OH}$ , which can react on the particle surface to yield a larger concentration of organic radicals in the SOA. The  $\cdot\text{OH}$  uptake to  $\alpha$ -pinene SOA has been extensively studied before<sup>225,226,233</sup>, altering the chemical

composition of SOA as well as increasing the SOA mass concentration and volatility upon ageing.<sup>228</sup>

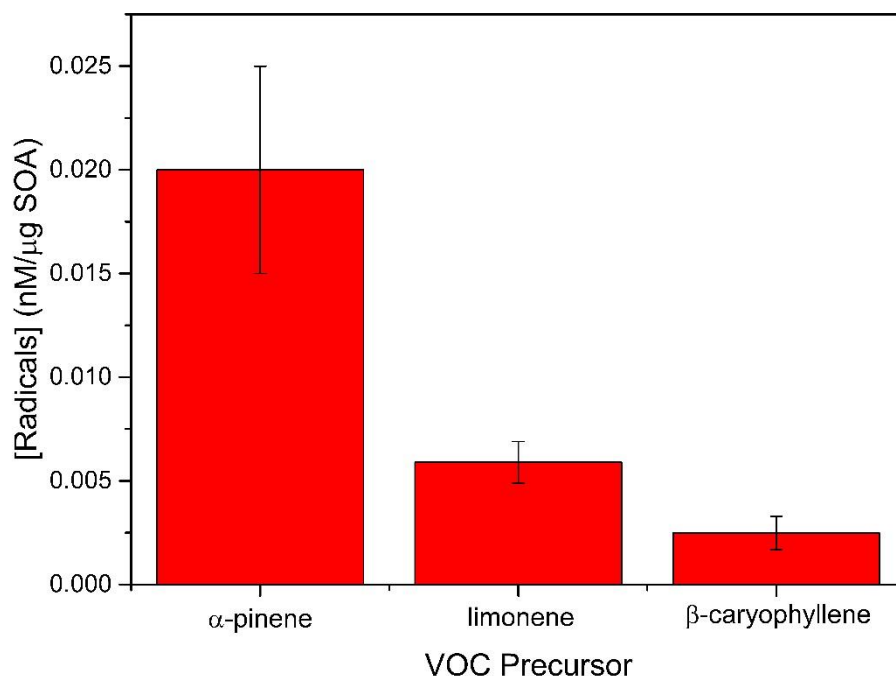


**Figure 5.15** – Concentration of radicals calculated per unit mass of SOA (nM/μg SOA), corrected for differing mass concentrations in the flow tube as well as the collection efficiency of the impinger. Error bars are the observed deviation of fluorescent signal per 20-minute sample step.

A model run using the Master Chemical Mechanism (MCM v3.3.1) was conducted to determine the approximate OH concentrations generated from these reactions at the experimental precursor concentrations mentioned previously. The OH concentrations over time during the experiment are given in Figure 5.16. The initial OH concentration from  $\alpha$ -pinene ozonolysis is a factor of 2 greater than that of  $\beta$ -caryophyllene, with a larger OH production for the first 8 seconds of the reaction.

The increased OH concentration could well lead to an increase in the extent of heterogeneous OH oxidation of  $\alpha$ -pinene SOA compared to that of the  $\beta$ -caryophyllene and limonene SOA. Therefore, one would expect greater extent of radicals in the SOA for  $\alpha$ -pinene given that OH radicals can readily abstract hydrogen atoms from a plethora of organic compounds, or add across unsaturated C=C bonds to form carbon-centred radical species. However, it is currently unclear as to what is causing the increase in fluorescent signal associated with  $\alpha$ -pinene SOA.

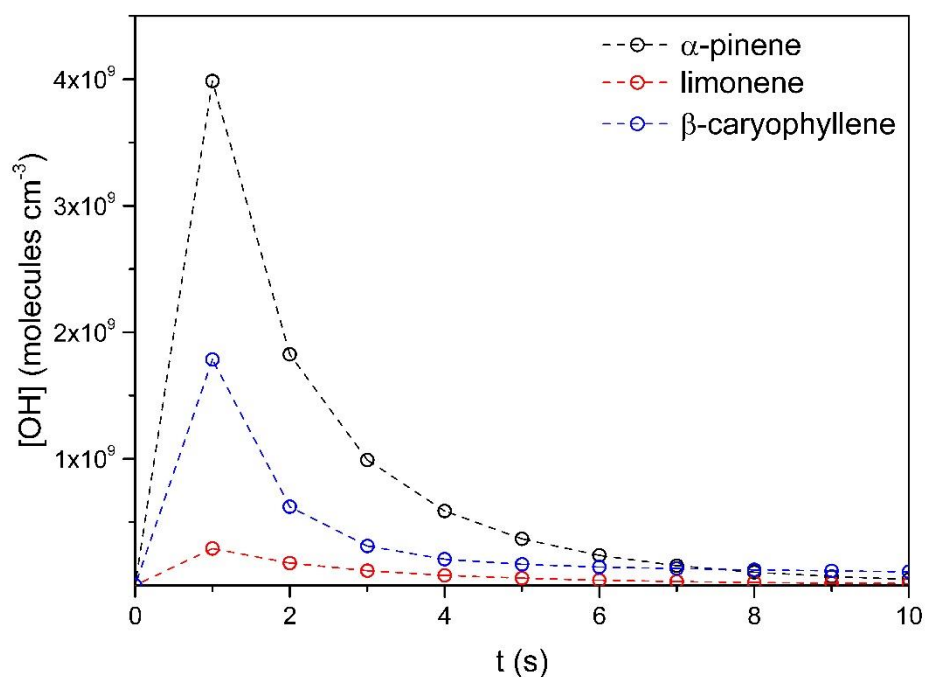


Figure 5.16 – OH concentrations from the ozonolysis of VOC precursors, modelled using the MCM v3.1.1.

There could be other products formed in large quantities in the  $\alpha$ -pinene  $O_3$  system that lead to the production of BPEA-R (*i.e.* fluorescent product), although limited literature data is available to estimate the extent of this effect. More detailed studies would need to be conducted to probe this effect. One could age the SOA before introducing known quantities of OH radicals into a flow tube and monitor the fluorescent response as a function of OH concentration, therefore indicating whether OH variability can account for the observations. Recently, a study by Shiraiwa *et al.*<sup>233</sup> showed that the ageing of organic aerosol by reactive species could be limited by bulk-phase diffusivity, which in turn reduces the extent of oxidation in the particle by species such as OH radicals. It is assumed the viscosity of SOA used in this study likely follows the trend  $\beta$ -caryophyllene > Limonene >  $\alpha$ -pinene, given the fact that the general volatility of the oxidised products formed from ozonolysis follows the trend  $\alpha$ -pinene > limonene >  $\beta$ -caryophyllene. A combination of both the diffusion-limited kinetics upon reactive uptake of OH, as well as the increased OH yield from the  $\alpha$ -pinene reaction could lead to the observation of a larger radical concentration in  $\alpha$ -pinene SOA compared to both limonene and  $\beta$ -caryophyllene SOA. One could design experiments where increasing concentrations of OH can be introduced to SOA generated from ozonolysis to monitor the extent of the increase in particle-bound radical concentration in the SOA as a function of OH concentration; this



would allow the investigation into the effect of OH concentration on the results presented in Figure 5.14.

## 5.4 Chapter Summary

The work presented in this chapter has discussed the application of the profluorescent nitroxide probe BPEA to the detection of particle-bound radicals formed from the ozonolysis of a series of VOC precursors. The methodology of the assay was based on those presented in studies by Stevanovic *et al.*<sup>97,124</sup> where they applied the BPEA/DMSO to combustion generated PM. The fluorescent set-up was initially optimised with respect to the LED and the spectrometer, and a calibration curve was produced using the fluorescent calibration standard BPEA-CH<sub>3</sub>. Initial tests to determine the product responsible for observed fluorescence was undertaken using ESI-HRMS by sonicating the spin trap BPEA in DMSO. It was found that the BPEA-H and BPEA-S(O)<sub>2</sub>CH<sub>3</sub> were the two main products resulting in a fluorescent response, in agreement with previous results<sup>97</sup>. A series of proof-of-concept experiments were designed to determine whether the BPEA assay was sensitive to particle-bound radicals in SOA formed from the ozonolysis of  $\alpha$ -pinene. A linear response in the fluorescent signal (and therefore BPEA-R production) was observed as the concentration of SOA sampled in the impinger increased over time, with an  $r^2 = 0.976$  correlation. Using this data as well as the calibration curve (Figure 5.8) and the estimated collection efficiency of ~9% in the impinger, the concentration of radicals per unit mass SOA was estimated to be  $0.4 \pm 0.1$  nM/ $\mu$ g SOA, or assuming a molar mass of  $200 \text{ g mol}^{-1}$  for average  $\alpha$ -pinene SOA components,  $0.008 \pm 0.002$   $\mu$ g radicals/ $\mu$ g SOA. Therefore, this measurement indicates that there is approximately 1 radical per 800 molecules in the SOA. This represents, to the authors knowledge, the first concentration estimate of particle-bound radical species present in  $\alpha$ -pinene SOA.

Further to this, experiments altering the residence time of the SOA in the flow tube were conducted to probe the rate of decay of radicals in  $\alpha$ -pinene SOA. An exponential fit of the data produced a curve with a non-zero background, contrary to what one would expect if it were purely the radical decay that was being monitored. This implies that the assay is sensitive to another component of the SOA being sampled, or there is another process resulting in the fluorescent signal that has not been accounted for at present. It could also be the result of a longer-lived radical component in the SOA, which results in a fluorescent response, but decays at a much slower rate. This technique is not capable of

---

distinguishing the specific radical species responsible for the observed fluorescent response. Despite this, the loss of radical species in this system was estimated to be  $k = (7.3 \pm 1.7) \times 10^{-3} \text{ s}^{-1}$  on average, which therefore leads to an average radical lifetime in this SOA regime of approximately  $(137 \pm 3) \text{ s}$ . This represents the first estimate of the rate of loss of radicals in SOA.

A final set of experiments compared SOA generated from the ozonolysis of  $\beta$ -caryophyllene,  $\alpha$ -pinene and limonene.  $\alpha$ -pinene was found to have the highest radical concentration as detected by fluorescence, with an average concentration 4 times greater than that of limonene per unit mass of SOA. This was explained by considering the higher OH yield from  $\alpha$ -pinene SOA, as well as higher viscosity of the SOA compared to the other systems. A higher OH yield would lead to an increase in the extent of heterogeneous oxidation by OH (thereby generating more radicals in the particle), as well as the fact that a lower viscosity SOA may allow a faster diffusion of OH, potentially enhancing the kinetics of OH chemistry in the particle phase. These experiments have demonstrated that the spin trap BPEA is capable of quantifying radicals in SOA generated from the ozonolysis of a variety of VOC precursors. The relative stability of the BPEA-R radical adduct allows the pre-concentration of the adduct, and therefore improves sensitivity towards lower concentrations of radicals by sampling them over time. This allows the radical concentration per unit mass of SOA to be calculated for each regime. However, the SOA mass loadings in these experiments are  $\sim 2$ -4 orders of magnitude greater than that found in ambient SOA. More experiments are required to determine the sensitivity of this technique to much lower mass concentrations that are more representative of atmospheric chemistry. If the BPEA/DMSO assay is indeed sensitive in this range, the assay could be applied to probe various atmospheric processes that are believed to introduce radicals into the particle phase (heterogeneous oxidation, Fenton chemistry, photochemistry, etc...). Radical chemistry in organic aerosol represents a large area of uncertainty; further development of this technique could result in a valuable assay that in principle could be applied to probe various chemical processes involved in the initial formation, as well as ageing, of SOA.

# 6 DEVELOPMENT OF AN ON-LINE CHEMICAL ASSAY TO MEASURE PARTICLE- BOUND ROS

---

## **Author Contributions**

Steven J Campbell designed the experiments in this Chapter and wrote the manuscript. The initial prototype of the on-line instrument was designed by Daniel Leinhardt, and fully optimised by Steven J Campbell with the help of Battist Uttinger.

---

## 6.1 Introduction

The negative effects of air pollution on human health has been subject to a number of epidemiological studies which consistently link respiratory and cardiovascular diseases to exposure to particulate matter (PM).<sup>60,64–66,234</sup> It is currently estimated that up to 0.3 million premature deaths per year in Europe and 2.1 million deaths worldwide are the result of exposure to particles with an aerodynamic diameter less than 2.5  $\mu\text{m}$  (PM<sub>2.5</sub>).<sup>235</sup> However, the identification of the particle properties responsible for these health effects, such as their physical properties (size, surface, mass, number density, surface morphology, charge, *etc*), physicochemical characteristics (hygroscopicity, acidity, lipophilicity, bioavailability *etc*), and chemical composition (metals, biogenic and anthropogenic organic and inorganic compounds *etc*) remains a challenge.<sup>62</sup> Toxicological studies suggest that some of the observed adverse health effects derive from the occurrence of reactive oxygen species (ROS) in cells, added directly through inhalation of PM<sup>236</sup> or stimulated by bio-transformation of particle components *in vivo*<sup>62</sup>. Particle-phase ROS originate from a number of sources; these include a wide range of chemical species such as transition metals (iron, nickel and copper), a range of organic compounds including polyaromatic hydrocarbons (PAHs), quinones, peroxides and radicals.<sup>62</sup> Verma *et al.*<sup>237</sup> identified biomass burning, vehicular emissions and oxidation processes in the atmosphere, that lead to the formation of secondary organic aerosol (SOA), as major sources of particle-bound ROS.

In order to protect the body against these oxidising species, lung cells generate antioxidants such as glutathione (GSH), uric acid (UA) and ascorbic acid (AA) which are present in the respiratory tract lining fluid (RTLFL); these anti-oxidants act as the first line of defence against oxidising components of PM<sub>2.5</sub>.<sup>61,238</sup> When these antioxidants are depleted (defined as oxidative stress), a number of cellular responses are induced which can lead to inflammatory responses, cell proliferation, DNA damage and even cell death.

Traditional methods for the measurement of ROS concentrations in ambient particles are based on the off-line analysis of filter extracts sampled over time, typically for several hours to days.<sup>239,240</sup> In one of these assays, particle-bound ROS oxidise a reagent called horseradish peroxidase (HRP), which in turn reacts with a dye to form a highly fluorescent product, which can be detected by spectrofluorimetry with excitation at 470 nm and emission at 520 nm. In another common assay, ROS oxidise dithiothreitol (DTT) to suppress its reaction with dithiobisnitrobenzoic acid (DTNB) to form 2-nitro-5-

thiobenzoic acid (TNB) which can be quantified by absorptivity measurements and compared to a control measurement without ROS.<sup>224,241</sup>

Another approach, utilising a more physiologically relevant assay, was developed in which a synthetic RTLF is exposed to filter extracts. The reduction in the concentration of the antioxidants can then be considered as an indicator of the potential of the adverse health effect and of inducing oxidative stress by the sampled air.<sup>77,98,242</sup>

The time delay between sampling and analysis in these off-line methods, which might be hours to days, may result in an underestimation of the ROS concentrations or adverse health effects as some of the more reactive species might be converted to more stable compounds before analysis. In addition, the effect on composition caused by the filter extraction (typically using ethanol or methanol) remains uncertain.<sup>243</sup>

In order to address these problems resulting from the off-line analysis, Venkatachari et al.<sup>244</sup> developed an on-line technique based on the reaction of HRP with 2',7'-dichlorofluorescein (DFCH) to form the fluorescent product DCF that is then detected by fluorescent spectroscopy, and related to the initial concentration of ROS. Fuller et al.<sup>90</sup> have adapted this approach to demonstrate that a significant amount of oxidizing species which contribute to ROS are not accounted for in the off-line analyses of particles produced by the ozonolysis of oleic acid. Wragg et al.<sup>85</sup> have also recently adopted this assay to develop a prototype field instrument capable of measuring particle-bound ROS on-line, demonstrating the instrument's sensitivity to a range of organic peroxides, as well as SOA generated from the ozonolysis of both  $\alpha$ -pinene and limonene.

In this work, a new on-line method to measure the oxidation of ascorbic acid in synthetic RTLF was developed, thus combining the advantages of the on-line measurement with the more physiologically relevant assay. In this Chapter, the method was calibrated against a series of metals in the solution phase. Furthermore, the applicability of this method to the oxidation of ascorbic acid by SOA particles generated from the ozonolysis of  $\alpha$ -pinene in a flow tube is demonstrated. The assay's response to particles containing a mixture of SOA and iron sulphate was also investigated, illustrating an enhancement of the oxidation of ascorbic acid when organic SOA and iron are sampled simultaneously, compared to SOA and iron sulphate particles separately.

---

## 6.2 Methodology

### 6.2.1 Reagents

The chemicals and gases were obtained from Sigma unless otherwise indicated and used without further purification: ascorbic acid ( $\geq 99.0\%$ ), glutathione ( $\geq 98.0\%$ ), uric acid ( $\geq 99.0\%$ ), chelex<sup>TM</sup> 100 sodium form, 0.1M HCl solution, 0.1M NaOH solution, CuSO<sub>4</sub> ( $\geq 99.0\%$ ), FeSO<sub>4</sub> ( $\geq 99\%$ ), Fe<sub>2</sub>(SO<sub>4</sub>)<sub>3</sub> ( $\geq 98\%$ ), *o*-phenylenediamine ( $\geq 99.5\%$ ),  $\alpha$ -pinene (98%), zero grade air (BOC), N<sub>2</sub> gas (BOC). H<sub>2</sub>O used for the RTL solution was obtained from a Milli-Q high purity water unit (resistivity  $< 18 \text{ M } \Omega \text{ cm}^{-1}$ ).

### 6.2.2 Development of an Ascorbic Acid Chemical Assay

In order to quantify the oxidation of ascorbic acid by particle-phase ROS, the on-line instrument introduced by Fuller *et al.*<sup>90</sup> and further developed by Wragg *et al.*<sup>85</sup> was modified to facilitate the ascorbic acid based assay. The detection is based on the quantification of the oxidised form of ascorbic acid, dehydroascorbic acid (DHA).

In solution, ascorbic acid (AA) can readily lose a proton to form the ascorbate anion (HAsc<sup>-</sup>) which can then subsequently lose an electron (*via* oxidation) to produce the ascorbyl radical (HAsc<sup>•</sup>). HAsc<sup>•</sup> can undergo a disproportionation reaction to form the first stable oxidation product of ascorbic acid, DHA.<sup>245,246</sup> Furthermore, ascorbic acid can be converted directly to the ascorbate radical (Asc<sup>•-</sup>) *via* reaction with superoxide (O<sub>2</sub><sup>-</sup>) or hydroperoxyl (HO<sub>2</sub>) radicals.<sup>245</sup> A schematic summarising the chemistry of ascorbic acid is given in Figure 6.1.

As illustrated in Figure 6.2, under acidic conditions, DHA can react *o*-phenylenediamine (OPDA) to form the product 3-(1,2-dihydroxyethyl)fluoro[3,4-b]quinoxaline-1-one (DFQ)<sup>247</sup>, a highly fluorescent compound which can be detected by fluorescence spectroscopy. Due to the 1:1 reaction stoichiometry between DHA and OPDA, monitoring the change in concentration of DFQ can be used to quantify the extent of oxidation of ascorbic acid, and the concentration of the oxidising species.

Since DHA is susceptible to further reactions, a fraction of the DHA might be hydrolysed to 2,3-diketogulonic acid (DKG) or further oxidation products before reaction with OPDA.<sup>245</sup>

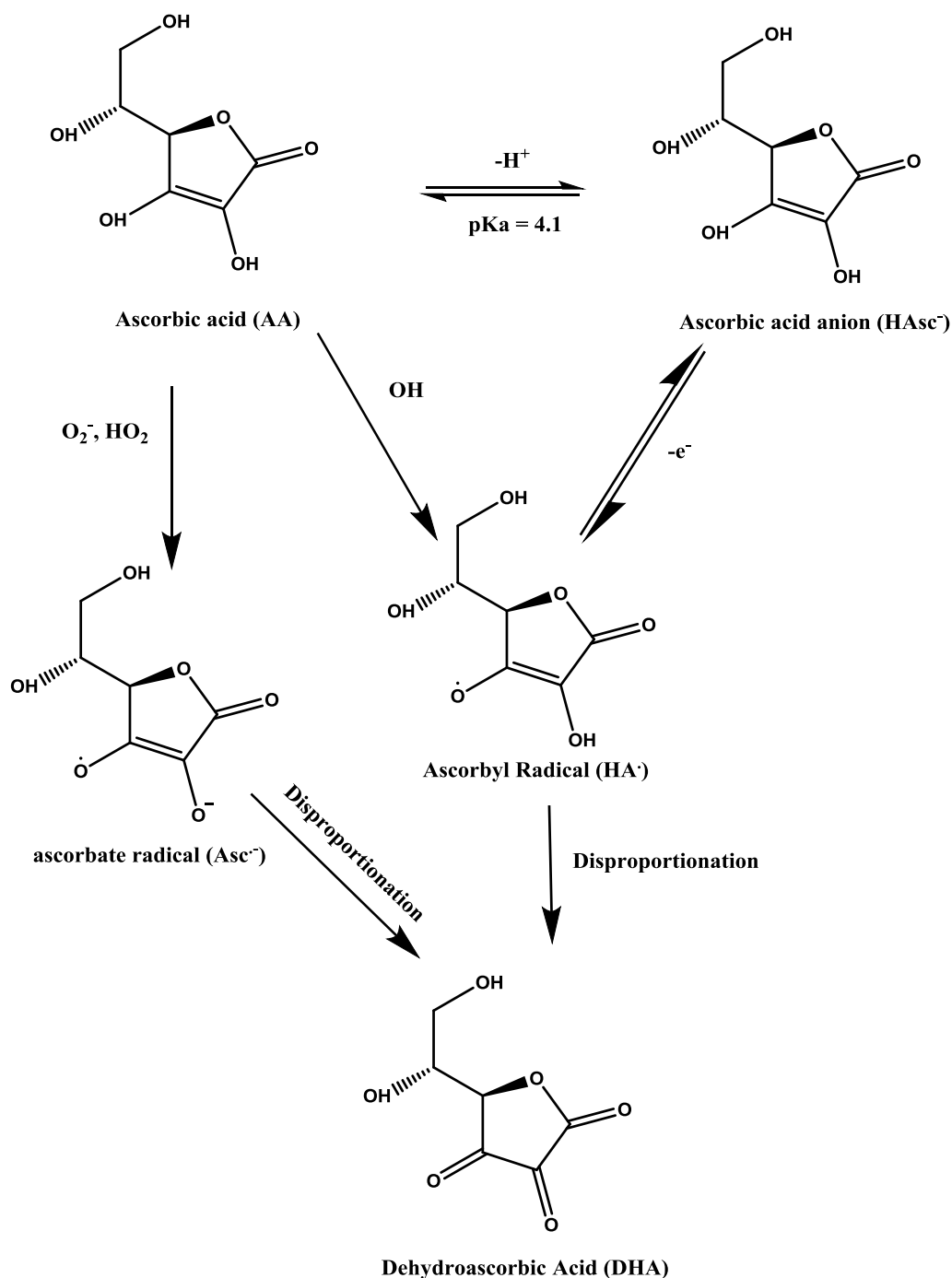


**Figure 6.1** – Schematic illustrating a brief overview of ascorbic acid chemistry in solution.

In solution, Ascorbic acid (AA) can readily lose a proton to form the ascorbate anion (HAsc<sup>-</sup>) which can then subsequently lose an electron (*via* oxidation) to produce the ascorbyl radical (HA $\cdot$ ). HA $\cdot$  can undergo a disproportionation reaction to form the first stable oxidation product of ascorbic acid, (DHA).<sup>245,246</sup> Furthermore, ascorbic acid can be converted directly to the ascorbate radical (Asc $\cdot^-$ ) via reaction with superoxide ( $O_2^{\cdot-}$ ) or hydroperoxyl ( $HO_2$ ) radicals.<sup>245</sup>

However, the influence of these reactions is small because: (i) the other antioxidants (AA, GSH and UA) are present in much higher concentrations than DHA, therefore making further oxidation of DHA unlikely and (ii) further oxidation products might retain the two carbonyl groups which can undergo reaction with OPDA, resulting in a fluorescent response, although this may be at a different excitation/emission wavelength due to changes in the fluorophore structure.

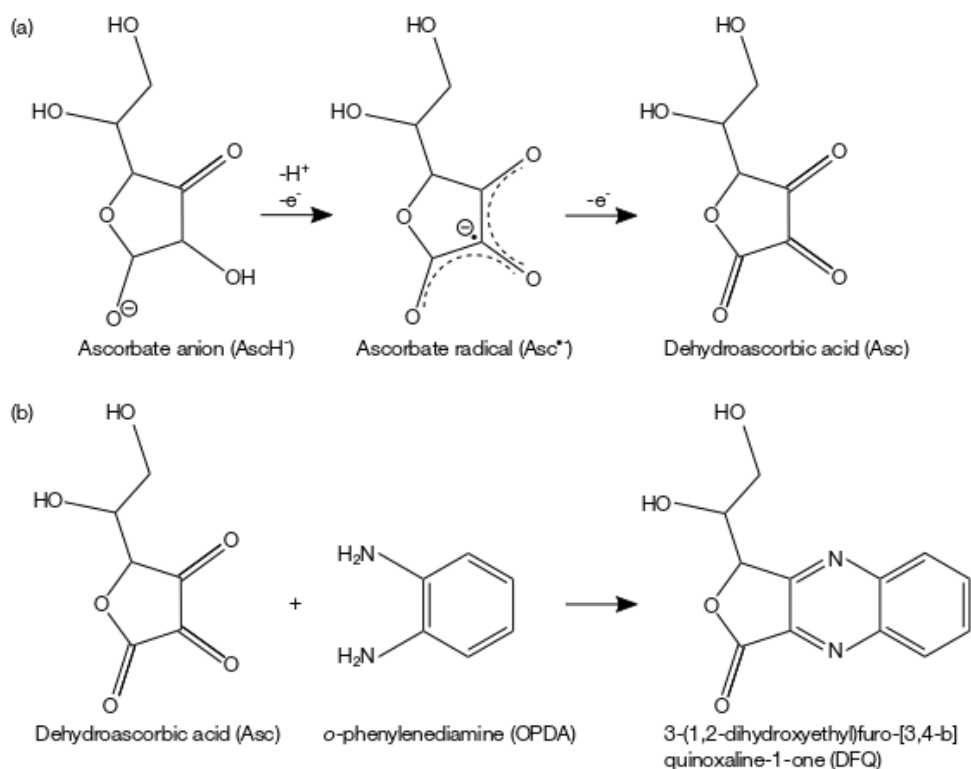


**Figure 6.2** – (a) Oxidation of ascorbic acid (AA) to dehydroascorbic acid (DHA) via the semi-dehydroascorbic acid free radical (SDHA). SDHA is very reactive and either converts promptly to form DHA. (b) DHA then reacts with a dye o-phenylenediamine (OPDA) to form the highly fluorescent compound DFQ.

## Chemical Preparation

The depletion of ascorbic acid was measured in a synthetic respiratory tract lining fluid (RTLFL) composed of ascorbic acid, glutathione and uric acid at physiologically relevant concentrations of 200  $\mu$ M. The synthetic RTLFL was prepared as described in Godri *et al.*<sup>242</sup> in Chelex-resin treated water. The Chelex resin treatment was necessary to eliminate the presence of trace concentrations of transition metals in already pure Millipore water (resistivity  $\geq 18.2$  M  $\Omega$  cm), and was carried out by mixing 3 g of Chelex per 100 ml of solution for 24 hours (with constant stirring) before vacuum filtration in a Sartorius



vacuum filtration unit, using a Whatman cellulose nitrate filter with 4.7 cm diameter and 0.45  $\mu\text{m}$  pore size. This process is necessary to ensure the background concentrations of transition metals are as low as possible, as their presence can cause the formation of DHA *via* ROS production or direct oxidation of ascorbic acid, and therefore complicate quantification. All preparation of the RTLF was conducted in sterilised plastic bottles and containers to minimise contamination from trace metals and biological material. RTLF solution was made fresh daily to ensure the background DHA concentration, formed from AA degradation in solution, was minimised, therefore keeping the background signal as low and stable as possible. The dye OPDA was dissolved in 500 mL of 0.1 M HCl at a concentration of 46 mM. To minimise contamination from metals, HCl solution was also treated with Chelex-resin in the same way described for MillQ H<sub>2</sub>O. All OPDA solutions were also kept in sterile plastic bottles to minimise contamination from transition metals. All transition metal solutions, as well as the DHA solution, used for calibration of the technique were all prepared in Millipore water treated with Chelex resin overnight.

### 6.2.3 Experimental set-up

#### Calibration of the On-line Assay

In order to characterise the assays response to certain species, a prototype on-line method was developed, based in principle on the design by Fuller *et al.*<sup>90</sup> (Figure 6.3). Initial calibrations of the assays' response as a function of DHA concentration was probed, followed by experiments designed to investigate the assays response to transition metals such as Copper (II), Iron (II) and Iron (III).

A solenoid diaphragm-metering pump (KNF, type FMM 20) delivers a flow of 0.8 mL/min of RTLF, which is mixed with either DHA, Cu- or Fe-salts, also delivered by a diaphragm-metering pump at 0.8 mL/min. The initial mixture is then passed into a reaction coil with a residence time of 20 minutes, which is housed in a small metal box filled with ethylene glycol held at  $37\text{ }^{\circ}\text{C} \pm 2\text{ }^{\circ}\text{C}$  by two 15 W enclosure heating elements (DBK Enclosures) to mimic physiological conditions. After 20 minutes reaction time in the heated bath, the reaction mixture is then mixed with a 46 mM solution of OPDA in 0.1M HCl, with acidic conditions required to ensure efficient reaction between DHA and OPDA.<sup>242</sup> OPDA is introduced into the reaction system using a diaphragm-metering pump at 0.8 mL/min. This resulting mixture is then passed through a reaction coil for 10

minutes at room temperature, where the highly fluorescent compound DFQ<sup>247</sup> is formed between the reaction of DHA and OPDA (Figure 6.2).

DFQ is excited at 365 nm with a high power UV LED (Roithner Lasertechnik, type UVLED-365-330-SMD) in a cuvette holder (OceanOptics, type CUV-ALL-UV) which was modified into a flow through system, allowing continuous on-line fluorescence measurements of DFQ. The emission spectrum of DFQ shows a peak around 430 nm and was measured with a femtowatt photoreceiver which saturates at 2.5 Volts (Thorlabs, type PDF10A) using a cyan fluorescent protein excitation filter (Thorlabs, type MF434-17) to block light outside the emission window and an aspheric lens (Thorlabs, type C230TMD-A) to focus the light on the active area of the photoreceiver. Stainless steel optical fibres (Thorlabs, M93L01) were used for light coupling between the LED, flow cell cuvette and the photoreceiver.

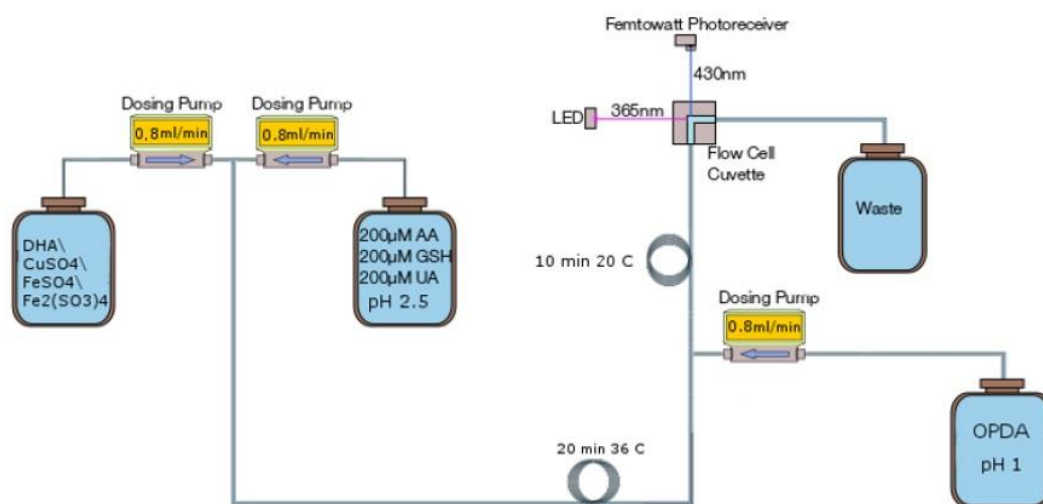


**Figure 6.3** – Schematic of the simple set-up used to calibrate the on-line ascorbic acid assay. Calibrants such as DHA/Cu/Fe(II)/Fe(III) salts are introduced into the reaction system and mixed with RTLf using diaphragm metering pumps, with a flow rate of 0.8 mL/min for each respectively. This mixture is flowed through a temperature-controlled bath at 37 °C to allow the oxidation of ascorbic acid to occur at physiologically relevant conditions. The resulting reaction mixture is then mixed with a 46 mM solution of OPDA where the highly fluorescent product DFQ is formed between the reaction of DHA and OPDA. The concentration of DFQ is then monitored using fluorescent spectroscopy, serving as a proxy for the extent of ascorbic acid oxidation.

### On-line Measurement of Particle Bound ROS

A prototype on-line instrument, based on the designs of Fuller<sup>90</sup> and Wragg<sup>85</sup>, was constructed to house the ascorbic acid assay as opposed to the DCFH assay used in the

mentioned studies. The full characterisation and considerations with respect to the design of the instrument are detailed in full in these studies, and will be discussed in brief here. A schematic of the ascorbic acid based on-line instrument is presented in Figure 6.4.

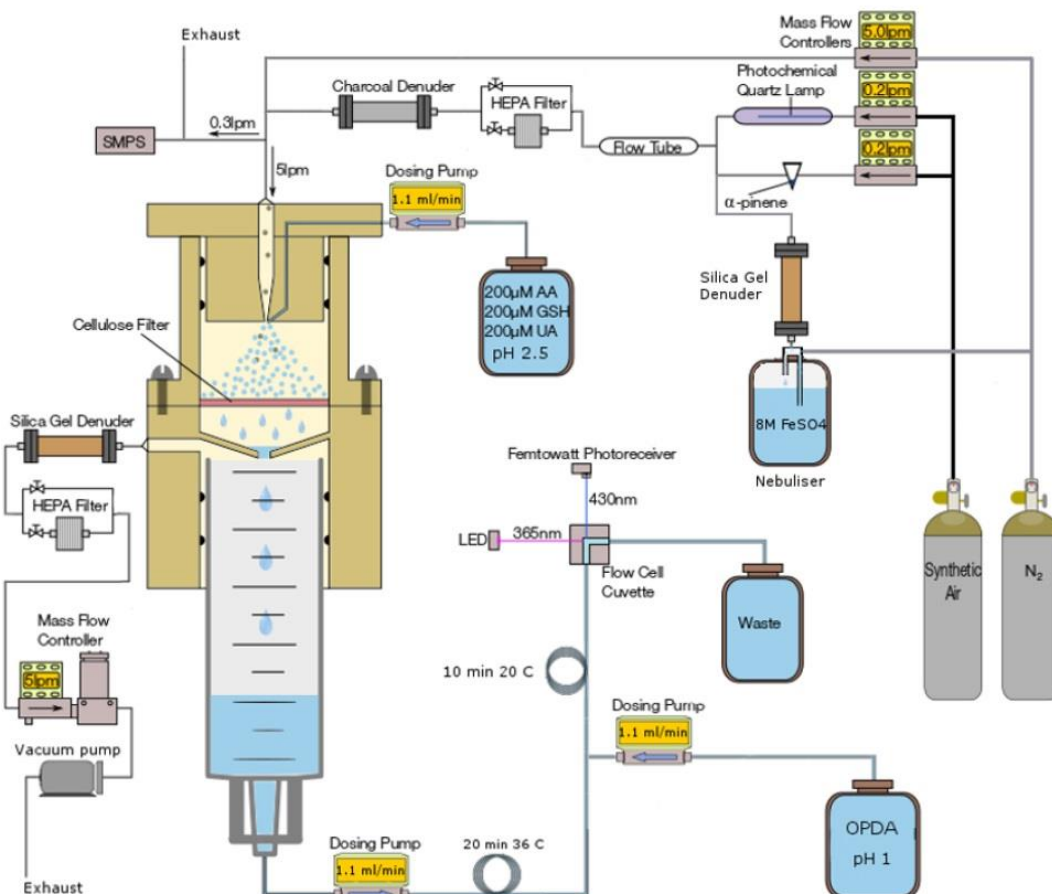


**Figure 6.4** – Schematic of the on-line ascorbic acid assay. Particles are drawn into the aerosol collector at 5 L/min, where the inlet airflow is met by a spray of RTLF. The particles are collected onto a wetted filter and extracted into the RTLF solution. The resulting reaction mixture is then pumped from the collection syringe through a reaction coil for 20 minutes, with the reaction bath maintained at 37 °C to replicate physiologically relevant conditions. Oxidising species present in the SOA may react with the ascorbic acid to produce DHA, the resulting mixture of which is then added to OPDA in 0.1M HCl. Under these acidic conditions, the DHA reacts with OPDA to form the highly fluorescent product DFQ, which can act as a proxy for oxidised ascorbic acid and therefore the concentration of oxidising species present in the aerosol. DFQ is measured by fluorescent spectroscopy. This instrument is based on the design presented in full by Wragg *et al.*<sup>85</sup>

A solenoid diaphragm metering pump (KNF, type FMM 20) delivers a flow of 1.1 ml/min of RTLF into an aerosol collector through which an air flow of 5 L/min is maintained by a combination of a vacuum pump (Rietschle Thomas, type VTE 3) and a mass flow controller (Alicat Scientific, type MCR-50slpm). A silica gel denuder is also connected

---

to dry the air prior to entering the mass flow controller. The design of the aerosol collector is described in detail by Takeuchi *et al.*<sup>248</sup> and will only be briefly discussed here. Supplying the RTLF through a PEEK tubing to the nozzle of the collector creates a spray that wets the surface of a Whatman grade 1 cellulose filter with a diameter of 2.5 cm. This cellulose filter is supported by a PEEK mesh in order to avoid wet burst. The particle collection efficiency at a gas flow rate of 5 L/min was investigated and indicates that 75% of particles with a diameter > 50 nm and 90% of particles with a diameter >80nm diameter are collected and extracted into in the RTLF.

The particle/RTLF mixture accumulates in the bottom part of a 20 ml plastic syringe from where it is pumped into a reaction coil by a second solenoid diaphragm-metering pump at a flow rate of 1.1 mL/min. The pulsations of both metering pumps in use are reduced by using a flexible Tygon R3607 tubing followed by a 0.005 ft inner diameter PEEK tubing (Upchurch Scientific) at the outlet of the pumps. The reaction coil with a residence time of 20 minutes is housed in a small metal box filled with ethylene glycol held at  $37^{\circ}\text{C} \pm 2^{\circ}\text{C}$  by two 15 W heating elements (DBK Enclosures) in order to impose physiologically relevant conditions for the reaction of ascorbic acid with reactive species extracted in the aerosol collector. Exposure of ascorbic acid to even higher temperatures is not recommended due to the increased likelihood of denaturation of ascorbic acid.<sup>249</sup>

After passing through the reaction coil, a solution containing 46 mM *o*-phenylenediamine (OPDA) in 0.1 M HCl is added to the particle/RTLF mixture by a diaphragm-metering pump at a flow rate of 1.1 mL/min. Under the acidic conditions set by the addition of the 0.1 M HCl solution, OPDA reacts with oxidised ascorbic acid (DHA) for 10 minutes in a second reaction coil at room temperature to form the highly fluorescent product 3-(1,2-dihydroxyethyl)-fluoro-[3,4-b]quinoxaline-1-one (DFQ).<sup>247</sup> The DFQ is excited by the same LED optical set-up as described earlier for instrument calibration. The photoreceiver outputs a voltage as a function of the amount of photons received at the detector, therefore it is capable of monitoring the amount of photons emitted from the excited fluorophore in this assay. Stainless steel optical fibres (Thorlabs, M93L01) were used for light coupling between the LED, flow cell cuvette and the photoreceiver.

For experiments that sampled SOA into the on-line assay, the aerosol collector was connected to a set-up generating high concentrations of SOA particles, which were formed through ozonolysis of  $\alpha$ -pinene as shown in Figure 6.4. In this arrangement, O<sub>3</sub> is formed *via* photolysis of oxygen in a flow of 0.2 L/min of zero grade air passed through

a Pen-Ray photochemical quartz lamp (UVP, peak emissions at 185 nm, 254 nm) while  $\alpha$ -pinene was evaporated by passing 0.2 L/min of  $N_2$ -gas over a 0.5 mL reservoir of  $\alpha$ -pinene in a pear shaped flask.

The two gas flows were then combined to form SOA in a glass flow tube. After removal of  $O_3$  and VOCs by an activated charcoal denuder, the flow is then diluted from 0.4 L/min to 5 L/min, and the SOA then enters the aerosol collector. For background experiments, particles are removed with a HEPA filter (Whatman, type HEPA-CAP 75). Particle number and mass concentrations were measured simultaneously using a Scanning Mobility Particle Sizer (SMPS) with an input flow rate of 0.3 l/min. Final experiments were conducted by mixing  $\alpha$ -pinene SOA with particles of  $Fe_2SO_4$ . The  $Fe_2SO_4$  was introduced into the flow tube by nebulising an 8 mM solution of  $Fe_2SO_4$  by applying two bar pressure using  $N_2$ .

## 6.3 Results and Discussion

This section will present the results from initial calibrations of the on-line ascorbic acid assay. The fluorescent response as a function of DHA concentration was initially investigated, to ensure there is an appropriate fluorescent response upon increasing the concentration of DHA. Furthermore, the response of RTLFB to increasing concentrations of transition metal salts, including  $CuSO_4$ ,  $Fe(II)SO_4$  and  $Fe(III)_2(SO_4)_3$  which serve as surrogates for sources of transition metals one might expect to find in ambient particulate matter, will be discussed.

The assays sensitivity to organic aerosol was also studied, to probe the assays suitability for incorporation into a portable on-line instrument capable of monitoring concentrations of organic aerosol at atmospherically relevant concentrations. Finally, the effect of adding  $Fe(III)_2(SO_4)_3$  to organic aerosol particles before analysis using the on-line ascorbic acid assay was probed, demonstrating enhanced ascorbic acid oxidation when both the iron salts and organic components of SOA are present in the reaction mixture.

### 6.3.1 Calibration of the On-line Ascorbic Acid Assay

A series of calibration tests were conducted in order to probe the signal stability and initial response of the on-line ascorbic acid based assay. In order for this on-line assay to provide quantitative information regarding the oxidation of ascorbic acid, it is crucial that the chemistry between DHA and OPDA is investigated. As described previously in Figure

6.2, DHA reacts with OPDA to produce the highly fluorescent compound DFQ, the concentration of which can be monitored by fluorescence spectroscopy. Therefore, the fluorescent compound DFQ can be used to monitor the extent of oxidation of ascorbic acid. However, it is important to understand the efficacy of DFQ production, and therefore fluorescent response, as a function of DHA concentration.

Figure 6.5 illustrates one such test, which was conducted using the experimental set-up described in Figure 6.3, and chemical method presented in Section 6.2.2. Varying concentrations of DHA were introduced into the on-line ascorbic acid assay set-up, by switching the vial introducing the reactants into the system.

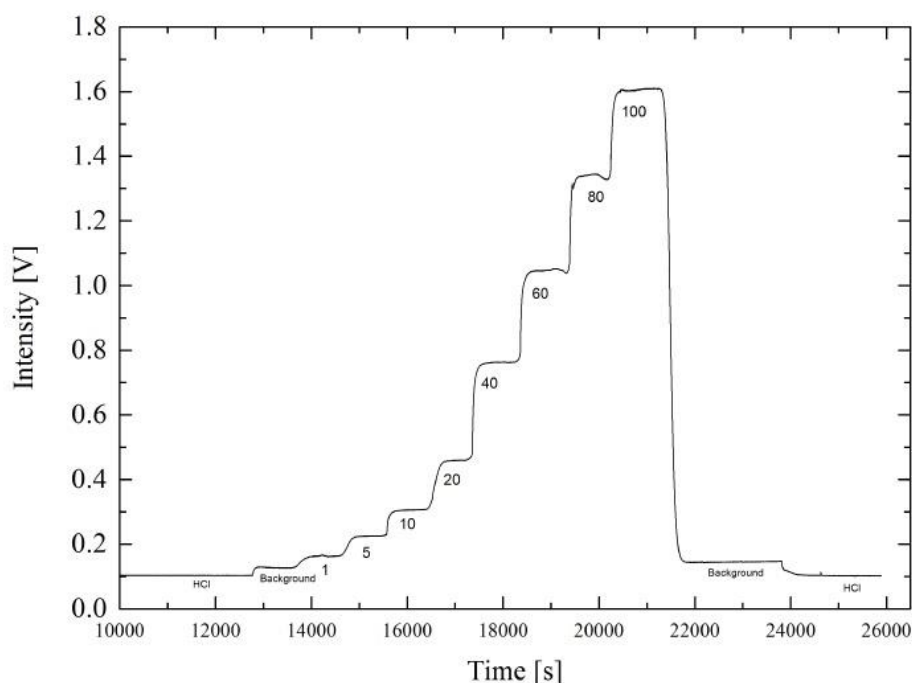


**Figure 6.5** – Response of the on-line ascorbic acid assay as a function of DHA concentration, numbers at each plateau representing the DHA concentration ( $\mu\text{M}$ ). Increasing the concentration of DHA introduced into the on-line system results in a higher voltage at the photoreceiver, demonstrating that the fluorescent product DFQ also increased as a function of DHA concentration, as expected. The assay exhibits good signal stability with each respective DHA concentration as well as the background signals associates with HCl and RTLF.

As can be seen in Figure 6.5, there is a response in the voltage at the photoreceiver as a function of DHA concentration. Therefore, it can be assumed that increasing DHA results in an increasing concentration of DFQ *via* reaction of DHA with OPDA. The signal associated with each concentration of DHA, as well as the HCl and RTLF background

signals, is relatively stable over sampling times of approximately 30 minutes for each DHA concentration.

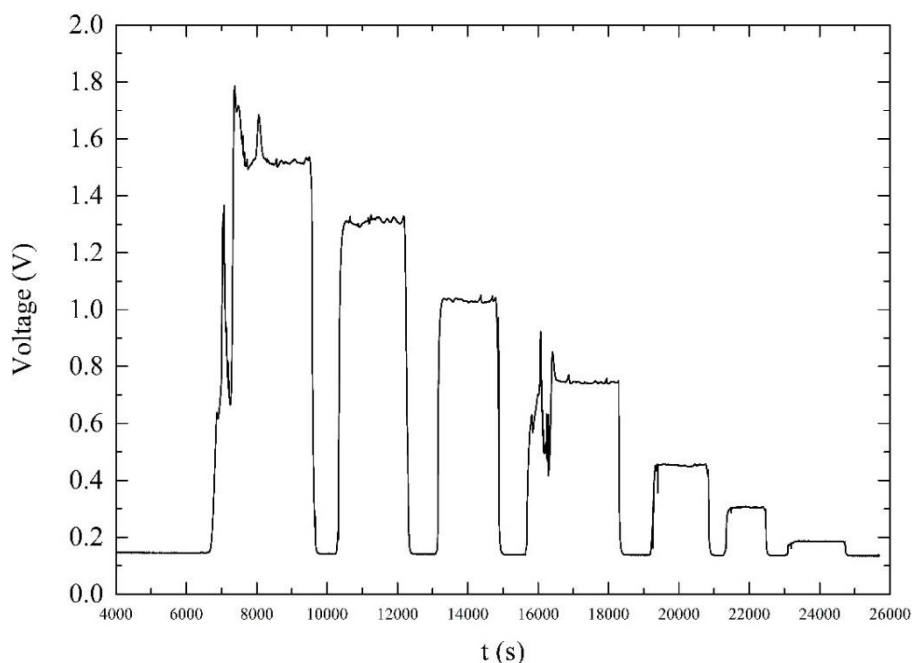


**Figure 6.6** – Investigation into the background stability when introducing differing concentrations of DHA, by flushing RTLF into the system intermittently. There is sharp drop in voltage and therefore fluorescent signal when DHA is no longer present in the system, and only RTLF and OPDA are present. There is no obvious increase in the background after each DHA experiment, implying that flushing with RTLF would be sufficient to clean the system daily to negate the effect of memory effects in the system.

A background signal is observed when introducing HCl (0.1 V) and RTLF (0.15 V). Upon addition of RTLF into the system, the background increases by approximately 0.05V compared to that of HCl and OPDA. This is likely due to degraded ascorbic acid in solution, which is known to steadily oxidise and form DHA, resulting in the formation of DFQ *via* OPDA, therefore promoting a fluorescent response at the detector and contributing to the background signal. This is evidenced when considering the background reading of RTLF taken after several DHA readings, whereby the background is approximately 0.03 V higher than the initial RTLF background at the start of the experiment, over a time-period of approximately 3 hours. This could be due to memory effects of residual DHA, or DFQ in the system or due to the degradation of ascorbic acid in RTLF solution during the course of the experiment before introduction to the on-line assay. The background drift after several DHA samples is illustrated in Figure 6.6.

There is sharp drop in voltage and therefore fluorescent signal, when DHA is no longer present in the system, and only RTLF and OPDA are flowing through the fluorescent detection unit. There is no obvious increase in the background after each DHA experiment, implying that flushing with RTLF or HCl would be sufficient to clean the system daily to negate the effect of memory effects in the system. Therefore, it is likely that constant background readings would need to be taken if this assay was applied on-line over considerable timescales (~ many hours, days), so that any drifts in the background signal can be corrected.

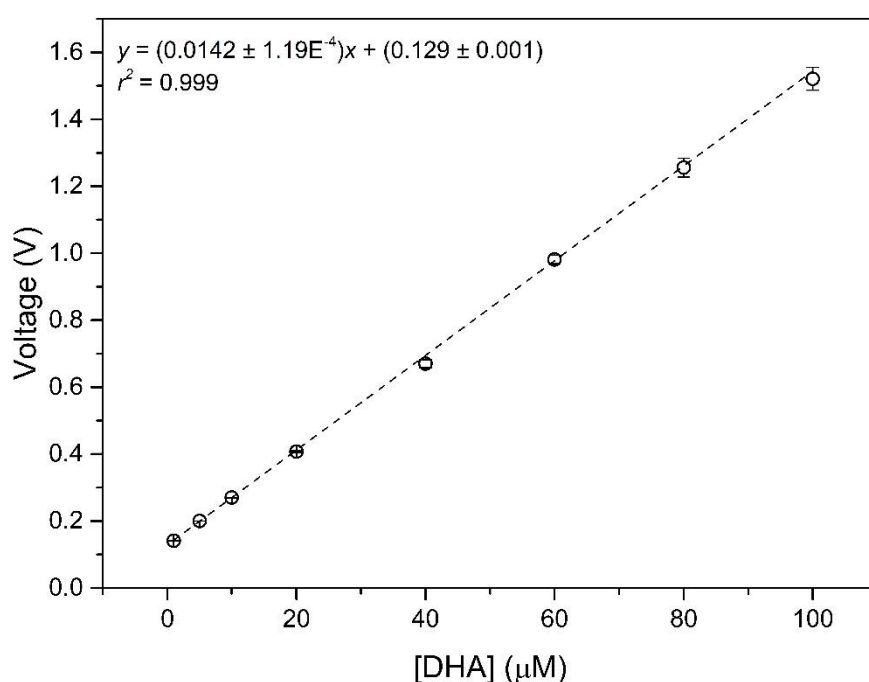


**Figure 6.7** – Calibration of the on-line assay as a function of DHA concentration. A linear response in voltage as a function of DHA concentration implies efficient production of the fluorescent product DFQ *via* reaction of DHA with OPDA. Error bars show standard error observed over multiple calibration repeats, with the variability of the voltage detected from lower concentrations of DHA so low that the error bars are contained within the data point. A linear fit of the calibration data showed an  $r^2$  correlation coefficient of 0.999, implying an excellent quantitative response of the technique as a function of DHA concentration.

A calibration curve, monitoring the voltage change as a function of DHA concentration, was then obtained using the experimental set-up described in Figure 6.3. The calibration curve, with standard error observed over multiple repeats, is presented in Figure 6.7. This calibration curve is generated by taking the average signal per unit concentration from multiple experiments such as those illustrated in Figure 6.5 and Figure 6.6.



The voltage output, and therefore amount of photons detected by the photoreceiver, exhibits a linear response as a function of DHA concentration. The linear fit of the calibration curve shows an  $r^2$  correlation coefficient of 0.999. This linear response in voltage as a function of DHA concentration demonstrates that the fluorescent response in the detection cell is also linear with respect to DHA. This further implies that the reaction between DHA and OPDA, producing the fluorescent product DFQ, is extremely efficient across all concentrations of DHA probed in this study. Therefore, from the perspective of the formation of DFQ, this assay can confidently predict the extent of oxidation of ascorbic acid in RTLF *via* the monitoring of DFQ concentrations. However, the linear increase of signal as a function of DHA concentration does not fully probe the instruments response as a function of ascorbic acid oxidation, and this needs to be investigated further to probe the instruments capability of quantifying the extent of ascorbic acid oxidation by atmospherically relevant particle components. The limit of detection with respect to DHA was calculated to be  $0.17 \pm 0.02 \mu\text{M}$ , by considering the variability of the photoreceiver signal over time.

### 6.3.2 Calibration of the On-line Ascorbic Acid Assay with Metal Salts

As discussed in Section 1.3.2, transition metals are widely regarded to induce oxidative stress in the lung either by directly oxidising ascorbic acid, or participating in catalytic redox chemistry which produces ROS in the lung, leading to toxicological responses.<sup>62</sup> Copper and iron are two commonly found transition metals in ambient aerosol, and have implications on both aerosol composition and health relevant effects of aerosol.<sup>62,250–253</sup> The transition metal salts copper (II) sulfate ( $\text{CuSO}_4$ ), iron (II) sulfate ( $\text{FeSO}_4$ ) and iron (III) sulfate ( $\text{Fe}_2(\text{SO}_4)_3$ ) were used as surrogate compounds to mimic transition metals in aerosol. Using the set-up described in Figure 6.3, the solutions of these metal salts were introduced into the reaction system. This experiment aimed to probe the fluorescent response of the assay as a function of increasing transition metal concentration.

#### Calibration of the On-line Assay with $\text{CuSO}_4$

Initial tests on the signal stability, as well as response of the instrument to increasing concentrations of  $\text{CuSO}_4$  was investigated by introducing two different concentrations of  $\text{CuSO}_4$  into the on-line experimental set-up depicted in Figure 6.3. The raw data showing the background signal with only RTLF + OPDA flowing through the reaction system, and  $10 \mu\text{M}$  and  $5 \mu\text{M}$  of  $\text{CuSO}_4$  is shown in Figure 6.8. There is an increase in voltage at the

photoreceiver of 0.16 V upon the addition of 10  $\mu\text{M}$  of  $\text{CuSO}_4$  and 0.1 V for 5  $\mu\text{M}$   $\text{CuSO}_4$ , with a relatively stable signal attained for each concentration over the sampling time of approximately one hour.

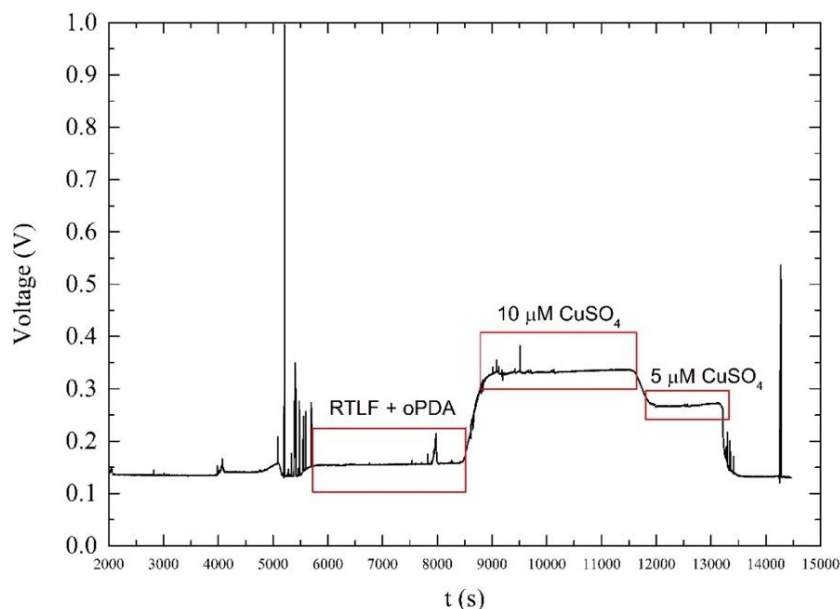


**Figure 6.8** – Initial test of the assays response to differing concentrations of  $\text{CuSO}_4$ . The signal associated with the background (RTL F + OPDA), 10  $\mu\text{M}$  and 5  $\mu\text{M}$   $\text{CuSO}_4$  is relatively stable over sampling time of approximately one hour. There is an obvious increase when copper is introduced into the system, either with the copper initiating oxidation of ascorbic acid directly or *via* production of ROS in an aqueous environment. There are intermittent spikes in signal over the duration of the experiment, likely due to bubbles in the system introduced when changing the vial containing the solution to be introduced into the instrument.

This implies that the copper is initiating the oxidation of ascorbic acid in solution; the signal stability implies that the chemistry is well regulated in this on-line flow through the reaction system, where the ascorbic acid is oxidised to the same extent by the same concentration of Cu (II), leading to a constant production of DFQ *via* the reaction of DHA and OPDA. There are intermittent spikes in voltage observed during the course of the experiment, and indeed this has been observed in other experiments. It is at present not entirely clear what causes these sudden spikes, but it is likely bubbles in the system introduced when changing the vial of reactant, which then pass through the fluorescence detection system, potentially causing this interference. It could also be particles of dirt accumulated over multiple experiments that are dislodged and pass through the detection

system. The relatively short timescale of these spikes means that they can be easily corrected and accounted for an on-line experiment in the data analysis.

Subsequently, a calibration curve was generated whereby several concentrations of  $\text{CuSO}_4$  were introduced to the on-line assay, as depicted in Figure 6.9. It should be noted that further optimisations to the chemical preparation were conducted before obtaining this calibration curve, so the Cu (II) response is larger than that depicted in Figure 6.8 (*e.g.* improvement of chelexing method, improving the detection cell and optimisation of pH).

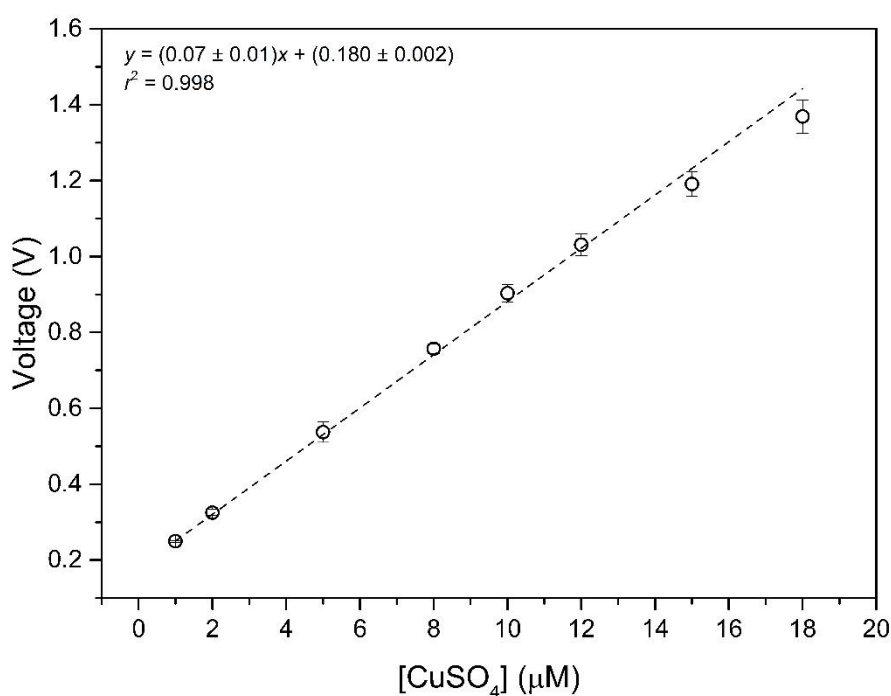


**Figure 6.9** - Calibration curve generated from increasing concentrations of  $\text{CuSO}_4$ . A linear increase in the voltage is observed, with an  $r^2 = 0.989$  correlation coefficient. Error bars for each concentration indicate the variability in signal observed over multiple repeats, in some cases the error is so low that the error bars are contained within the diameter of the data point.

A linear response in the voltage at the photoreceiver was observed over a concentration range of 1 – 18  $\mu\text{M}$  of  $\text{CuSO}_4$ , with an  $r^2 = 0.989$  correlation coefficient, and a voltage response of 0.2 – 1.4V across this concentration range. Error bars in the plot represent the standard deviation of the voltage at each concentration, as observed over multiple repeats; in some cases, the error associated with each measurement is smaller than the diameter of the data point, indicating a high degree of repeatability across multiple experiments. A

limit of detection (LOD) considering three times the standard deviation of the signal over multiple repeats was estimated to be  $0.035 \pm 0.004 \mu\text{M Cu (II)}$

**Table 6.1** – Summary of the reactions likely occurring between Cu and ascorbic acid in aqueous acidic solution. This is not an explicit summary, but captures the key reactions that likely lead to DHA production in the on-line assay. Reactions (1-6) describe primary Cu reactions, 7-16 Cu and anti-oxidant reactions and 17-23 ROS reactions occurring in the system. Rates are expressed as  $\text{M}^{-1} \text{s}^{-1}$ . References are given in the table for each class of reactions.

Reaction Number	Reaction	Rate (k) ( $\text{M}^{-1} \text{s}^{-1}$ )
<i>Primary Cu Reactions</i> <sup>254</sup>		
1	$\text{Cu(I)} + \text{O}_2 \rightarrow \text{Cu(II)} + \text{O}_2^-$	$4.9 \times 10^3$
2	$\text{Cu(I)} + \text{O}_2^- + 2\text{H}^+ \rightarrow \text{Cu(II)} + \text{H}_2\text{O}_2$	.975
3	$\text{Cu(I)} + \text{H}_2\text{O}_2 \rightarrow \text{Cu(II)} + \cdot\text{OH} + \text{OH}^-$	200.4
4	$\text{Cu(II)} + \text{O}_2^- \rightarrow \text{Cu(I)} + \text{O}_2$	55
5	$\text{Cu(II)} + \text{H}_2\text{O}_2 \rightarrow \text{Cu(I)} + \text{O}_2^- + 2\text{H}^+$	$2 \times 10^{-3}$
6	$\text{Cu(III)} + \text{Cu(I)} \rightarrow 2\text{Cu(II)}$	$2 \times 10^3$
<i>Anti-oxidant Reactions</i> <sup>255</sup>		
7	$2\text{Asc}^- + \text{H}^+ \rightleftharpoons \text{HAsc}^- + \text{DHA}$	$1.4 \times 10^6$
8	$\text{Cu(II)} + \text{HAsc}^- \rightarrow \text{Cu(I)} + \text{H}^+ + \text{DHA}$	$1 \times 10^9$
9	$\text{Cu(II)} + \text{HAsc}^- \rightarrow \text{Cu(I)} + \text{Asc}^-$	$2 \times 10^6$
10	$\text{Cu(II)} + \text{HAsc}^- \rightarrow [\text{Cu(HAsc)}]^+$	$2.22 \times 10^2$
11	$[\text{Cu(HAsc)}]^+ \rightarrow \text{Cu(II)} + \text{HAsc}^-$	$2 \times 10^{-2} \text{s}^{-1}$
12	$[\text{Cu(HAsc)}]^+ + \text{HAsc}^- \rightarrow \text{Cu(I)} + \text{AA} + \text{DHA}$	$1 \times 10^9$
13	$\text{HAsc}^- + \text{OH}^- \rightarrow \text{Asc}^- + \text{H}_2\text{O}$	$1.1 \times 10^{10}$
14	$\text{HAsc}^- + \text{Asc}^- \rightarrow \text{Asc}^- + \text{HAsc}^-$	$2 \times 10^5$
15	$\text{HAsc}^- + \text{O}_2^- \rightarrow \text{Asc}^- + \text{HO}_2$	$2.7 \times 10^5$
16	$\text{HAsc}^- + \text{HO}_2 \rightarrow \text{Asc}^- + \text{H}_2\text{O}_2$	$2.7 \times 10^5$
<i>ROS Reactions</i> <sup>256</sup>		
17	$\text{H}_2\text{O}_2 + \text{OH}^- \rightarrow \text{H}_2\text{O} + \text{HO}_2$	$2.7 \times 10^7$
18	$\text{H}_2\text{O}_2 + \text{HO}_2 \rightarrow \text{H}_2\text{O} + \text{O}_2 + \text{OH}^-$	3.1
19	$\text{OH}^- + \text{OH}^- \rightarrow \text{H}_2\text{O}_2$	$5.5 \times 10^9$
20	$\text{OH}^- + \text{HO}_2 \rightarrow \text{H}_2\text{O} + \text{O}_2$	$6.6 \times 10^9$
21	$\text{OH}^- + \text{O}_2^- \rightarrow \text{HO}^- + \text{O}_2$	$1.01 \times 10^{10}$
22	$\text{HO}_2 + \text{O}_2^- \rightarrow \text{H}_2\text{O}_2 + \text{O}_2$	$9.7 \times 10^7$
23	$\text{HO}_2 + \text{HO}_2 \rightarrow \text{H}_2\text{O}_2 + \text{O}_2$	$8.3 \times 10^5$

The chemistry initiating the oxidation of ascorbic acid in this chemical system is complex; it involves direct reaction of Cu (II) with ascorbic acid, as well as the aqueous phase redox chemistry producing ROS (Table 6.1) which will subsequently oxidise ascorbic acid, producing DHA.<sup>254</sup> A summary of the chemistry occurring between Cu (II) and ascorbic acid in aqueous solution is presented in Table 6.1.

It is evident that there is substantial DHA production from the Cu chemistry occurring in the assay. 18  $\mu\text{M}$  of Cu (II) generates a voltage response of 1.4 V, corresponding to approximately 90  $\mu\text{M}$  of DHA, according to the DHA calibration curve in Figure 6.7.

Considering the chemistry in Table 6.1, there is evidence to suggest efficient direct conversion of the ascorbate radicals ( $\text{HAsc}^\cdot$ ) to DHA *via* reaction with Cu (II) (reaction 8), at a rate approximately 3 orders of magnitude faster than the  $\text{Asc}^\cdot$  disproportionation reaction to produce DHA (reaction 7).

There is also re-cycling of Cu (I) to Cu (II) *via* reaction 1-3, the re-generation of which can increase the formation of DHA, as well as forming superoxide radicals which themselves can initiate the oxidation of ascorbic acid, leading to the production of DHA. The catalytic action of direct oxidation of ascorbic acid by Cu(II), as well as the direct production of DHA by Cu (II) (reaction 8), likely explains the efficient formation of DHA in the on-line assay. Given the complexity of the chemistry, kinetic modelling studies need to be conducted to fully grasp the production mechanisms of DHA in the system with respect to Cu.

### **Calibration of the On-line assay with Fe (II) and Fe (III)**

Further to the study involving  $\text{Cu(II)SO}_4$ , calibration curves were generated for both  $\text{Fe(II)SO}_4$  and  $\text{Fe(III)}_2\text{SO}_4$  using the experimental set-up illustrated in Figure 6.3. Varying concentrations of both Fe(II) and Fe(III) were introduced into the system, and the voltage response as a function of increasing concentrations of Fe(II) and Fe(III) are presented in Figure 6.10 and Figure 6.11 respectively.

Considering Figure 6.10, a linear response in fluorescent signal is attained as a function of Fe (III) concentrations, with a voltage response of 0.2 – 0.8V between the concentrations of 1-18  $\mu\text{M}$ . The assay is much less sensitive to Fe (II) compared to Fe (III); the response across the concentration range of 1-18  $\mu\text{M}$  was approximately 0.05V, with a concentration of around 200  $\mu\text{M}$  required to promote a voltage response of 1 V at the photoreceiver (Figure 6.11). There is an order-of-magnitude difference in the detector response of Fe(II) compared to Fe(III), implying that the oxidation of ascorbic acid is much more efficient when Fe (III) ions are present. The limit of detection, calculated in the same manner as described for the Cu(II), was estimated to be  $0.13 \pm 0.019 \mu\text{M Fe(III)}$  and  $8.57 \pm 0.95 \mu\text{M Fe(II)}$ , indicating that the assay has an order of magnitude greater sensitivity towards Fe(III) than Fe(II).

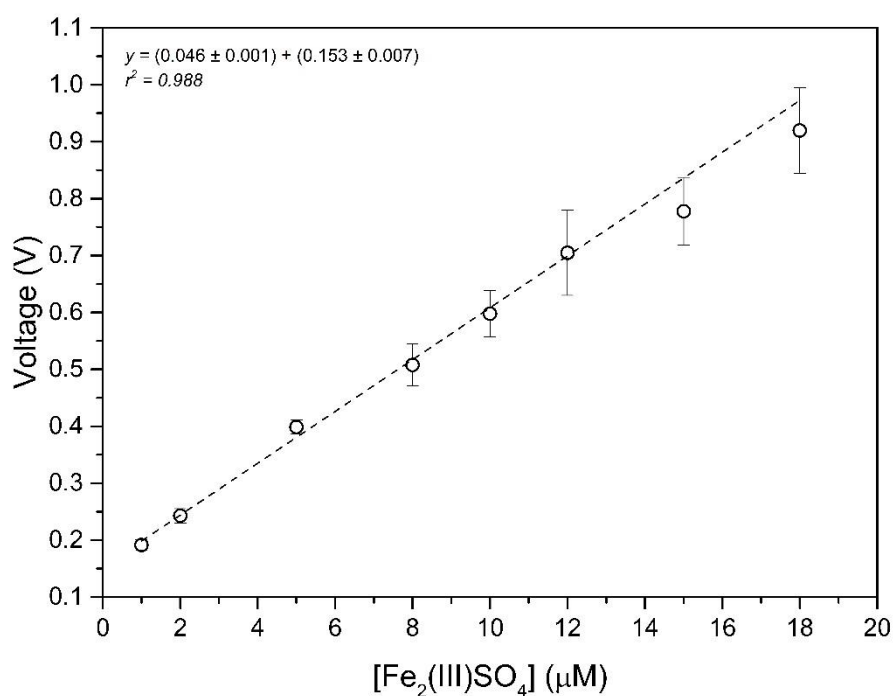


**Figure 6.10** – Calibration curve generated for  $\text{Fe(III)}_2(\text{SO}_4)_2$  in the concentration range of 1 – 18  $\mu\text{M}$ , inducing a response of 0.2 – 0.95 V at the photodetector, with a linear  $r^2 = 0.976$  correlation coefficient. Error bars indicate standard variability observed over four repeats.

It should be noted that the concentration of iron ions in solution will be a factor of two higher for Fe(III) as opposed to Fe (II), given the fact that two iron atoms are introduced for  $\text{Fe(III)}_2\text{SO}_4$  compared to one for  $\text{Fe(II)SO}_4$ . Therefore, in the Fe(III) system, there is more iron to initiate redox chemistry that will affect the extent of oxidation of ascorbic acid. A simplified summary of iron and ascorbic acid chemistry in this regime is presented in Table 6.2. The table summarises some of the key reactions occurring between Fe (II), Fe (III), ascorbic acid and ROS commonly produced in aqueous Fe chemistry. This is a complex chemical system, with several interrelating processes, as well as the cycling between Fe (II) and Fe (III).

As illustrated in Table 6.2, Fe (III) is capable at converting ascorbate ( $\text{HAsc}^-$ ) into ascorbate radicals ( $\text{Asc}^\cdot$ ) (reaction 10) at an appreciable rate. Ascorbate radicals then undergo a disproportionation reaction to produce DHA (reaction 11). Fe (II) does not participate in the direct oxidation of ascorbic acid, and this may have some effect on the observed sensitivity towards Fe (III) and Fe (II), as a larger concentration of DHA will in turn produce more DFQ, increasing the fluorescent response at the photo receiver.

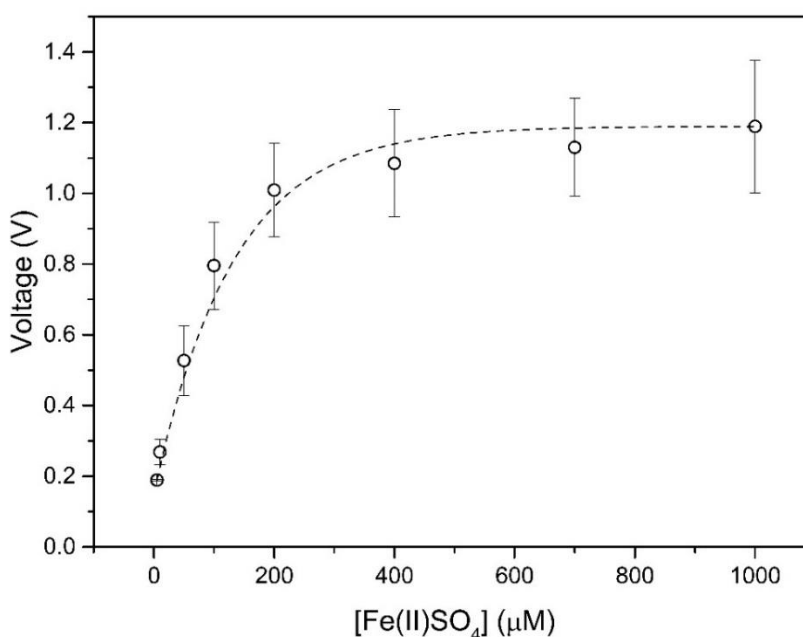


**Figure 6.11** – Calibration curve for Fe(II)SO<sub>4</sub>. The response in the assay was far less than that of Fe(III), this calibration was conducted over the concentration range of 0-1000 μM, although the voltage response as a function of Fe(II) concentration plateaus between 200-400 μM at 1.1 V. Error bars represent the standard variation of the voltage as observed in multiple repeats.

The other main route to the production of Asc<sup>•−</sup> would be through Fe(II) + O<sub>2</sub> chemistry which produces the superoxide radical. This in turn produces H<sub>2</sub>O<sub>2</sub>, which *via* Fenton chemistry (Fe (II) + H<sub>2</sub>O<sub>2</sub>) can produce •OH radicals which rapidly oxidise HAsc<sup>•−</sup> to Asc<sup>•−</sup> (reaction 11). As Fe (III) enhances the production of Asc<sup>•−</sup> Fe (II) is subsequently generated, which in turn can participate in the aforementioned reactions to produce ROS, which re-generates Fe (III), which can directly participate in HAsc<sup>•−</sup> oxidation. This recycling of Fe (III) may lead to much more efficient oxidation of Ascorbic acid when more Fe (III) is present initially.

Due to the complexity of the chemistry at play here, it is difficult to determine the main mechanisms that dictate the sensitivity between Fe (II) and Fe (III). At present, a model is being developed by collaborators, which may provide insight into the mechanisms governing our observation. There is evidently a kinetic effect associated with increasing Fe (II) concentrations introduced into the assay above 200-300 μM, as the production of DFQ does not increase above this concentration of Fe (II), as evidenced by the plateau in the voltage at the photoreceiver. The processes resulting in this profile are at present

unclear, but the ongoing modelling of the chemistry in these two Fe oxidation regimes will allow better understanding of these two calibration experiments.

**Table 6.2** – Summary of the reactions likely affecting the oxidation of ascorbate, and therefore DHA production, in the on-line assay. There are primary reactions of Fe (II) and Fe (III), anti-oxidant reactions and ROS reactions. Rates are given as  $\text{M}^{-1} \text{s}^{-1}$ . References are given for Fe (II)/Fe (III) reactions for each individual reaction, and for the other reactions the reference is given for each class of reactions.

Reaction Number	Reaction	Rate (k) ( $\text{M}^{-1} \text{s}^{-1}$ )
<u><i>Fe(II)/Fe(III) Reactions</i></u>		
<b>1</b> <sup>257</sup>	$\text{Fe(II)} + \text{O}_2 \rightarrow \text{Fe(III)} + \text{O}_2^-$	$4.9 \times 10^3$
<b>2</b> <sup>258</sup>	$\text{Fe(II)} + \text{O}_2^- + 2\text{H}^+ \rightarrow \text{Fe(III)} + \text{H}_2\text{O}_2$	.975
<b>3</b> <sup>259</sup>	$\text{Fe(II)} + \text{H}_2\text{O}_2 \rightarrow \text{Fe(III)} + \text{OH} + \text{OH}^-$	200.4
<b>4</b> <sup>264</sup>	$\text{Fe(III)} + \text{H}_2\text{O}_2 \rightarrow \text{Fe(II)} + \text{HO}_2 + \text{H}^+$	55
<b>5</b> <sup>264</sup>	$\text{Fe(III)} + \text{HO}_2 \rightarrow \text{Fe(II)} + \text{O}_2 + \text{H}^+$	$2 \times 10^{-3}$
<b>6</b> <sup>264</sup>	$\text{Fe(II)} + \text{HO}_2 \rightarrow \text{Fe(III)} + \text{HO}_2^-$	$2 \times 10^3$
<b>7</b> <sup>264</sup>	$\text{Fe(II)} + \text{OH} \rightarrow \text{Fe(III)} + \text{OH}^-$	$1.2 \times 10^6$
<b>8</b> <sup>260</sup>	$\text{O}_2^- + \text{H}_2\text{O}_2 \rightarrow \text{OH}^- + \text{OH} + \text{O}_2$	$2 \times 10^3$
<u><i>Anti-oxidant Reactions</i></u> <sup>255</sup>		
<b>9</b>	$2\text{Asc}^- + \text{H}^+ \rightleftharpoons \text{HAsc}^- + \text{DHA}$	$1.4 \times 10^6$
<b>10</b>	$\text{Fe(III)} + \text{HAsc}^- \rightarrow \text{Fe(II)} + \text{H}^+ + \text{Asc}^-$	$10^2$
<b>11</b>	$\text{HAsc}^- + \text{OH} \rightarrow \text{Asc}^- + \text{H}_2\text{O}$	$1.1 \times 10^{10}$
<b>12</b>	$\text{HAsc}^- + \text{Asc}^- \rightarrow \text{Asc}^- + \text{HAsc}^-$	$2 \times 10^5$
<b>13</b>	$\text{HAsc}^- + \text{O}_2^- \rightarrow \text{Asc}^- + \text{HO}_2$	$2.7 \times 10^5$
<b>14</b>	$\text{HAsc}^- + \text{HO}_2 \rightarrow \text{Asc}^- + \text{H}_2\text{O}_2$	$2.7 \times 10^5$
<u><i>ROS Reactions</i></u> <sup>256</sup>		
<b>15</b>	$\text{H}_2\text{O}_2 + \text{OH} \rightarrow \text{H}_2\text{O} + \text{HO}_2$	$2.7 \times 10^7$
<b>16</b>	$\text{H}_2\text{O}_2 + \text{HO}_2 \rightarrow \text{H}_2\text{O} + \text{O}_2 + \text{OH}$	3.1
<b>17</b>	$\text{OH} + \text{OH} \rightarrow \text{H}_2\text{O}_2$	$5.5 \times 10^9$
<b>18</b>	$\text{OH} + \text{HO}_2 \rightarrow \text{H}_2\text{O} + \text{O}_2$	$6.6 \times 10^9$
<b>19</b>	$\text{OH} + \text{O}_2^- \rightarrow \text{HO}^- + \text{O}_2$	$1.01 \times 10^{10}$
<b>20</b>	$\text{HO}_2 + \text{O}_2^- \rightarrow \text{H}_2\text{O}_2 + \text{O}_2$	$9.7 \times 10^7$
<b>21</b>	$\text{HO}_2 + \text{HO}_2 \rightarrow \text{H}_2\text{O}_2 + \text{O}_2$	$8.3 \times 10^5$

### 6.3.3 Assessment of Sensitivity towards Secondary Organic Aerosol

Following the calibrations conducted with DHA and a series of transition metal salts, the experimental set-up was developed further, following the design of Wragg *et al.*<sup>85</sup>. The ascorbic acid/OPDA assay was incorporated into an on-line prototype instrument capable of sampling aerosol particles, as illustrated in Figure 6.4. This instrument is capable of sampling aerosol on-line, by impacting the aerosol onto a filter wetted with RTLF. The resulting reaction mixture is then flowed through a reaction bath, mixed with the dye OPDA that reacts with DHA to produce the fluorescent product DFQ, allowing the detection of oxidised ascorbic acid. SOA generated from the ozonolysis of  $\alpha$ -pinene in a flow tube was used as a model aerosol system, with a range of highly oxidised compounds



including peroxides and peracids formed in this oxidation regime<sup>261</sup>. One such experiment is displayed in Figure 6.12, displaying the response of the assay as well as the mass concentration of SOA measured by an SMPS.

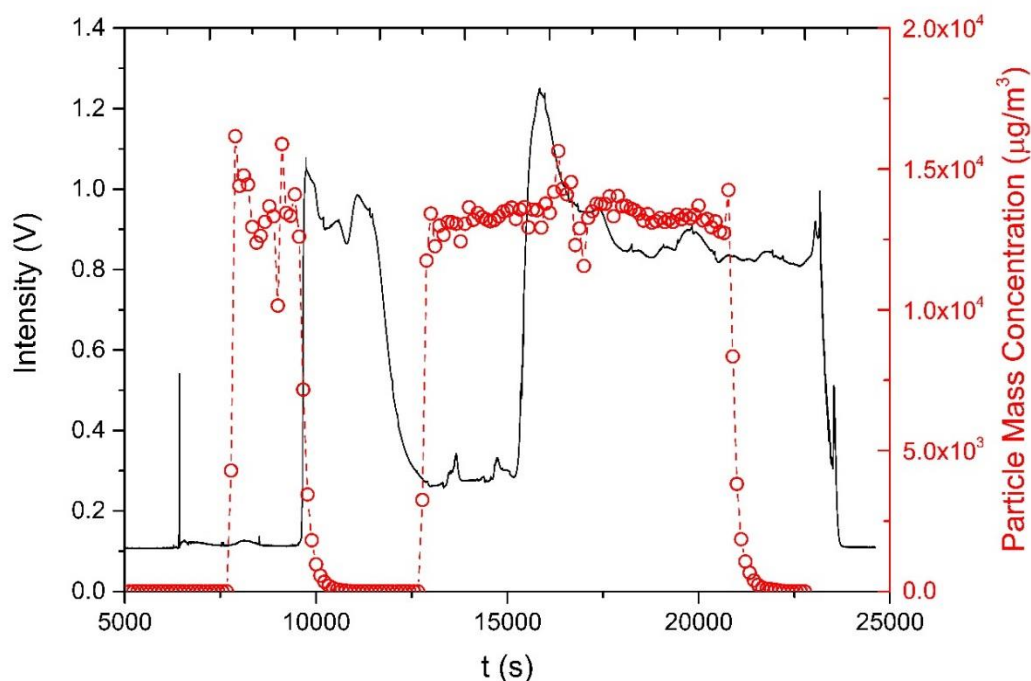


**Figure 6.12** – Sampling SOA into the on-line instrument, with the black line tracing the signal over time (V), and red dots representing the SOA mass measured by an SMPS. There is a lag in signal of approximately half an hour after the introduction of SOA, as this is the time it takes for the initially sampled SOA to be pumped through both reaction baths into the fluorescent detection cell.

The first introduction of SOA into the system at 7500 s does not result in an immediate response in the instrument; it should be noted that it takes 30 minutes for the reaction mixture to travel through both reaction baths and into the fluorescent detection cell. There is a sudden response in the instrument 1800 s after the introduction of SOA, with a SOA mass of  $1.3 \times 10^4 \mu\text{g m}^{-3}$  resulting in a response of 0.955 V on average, illustrating the high time resolution of the instrument. The stabilised response in intensity once the SOA reaction mixture enters the flow cell (after passing through the various reaction coils) is approximately 1300 s.

This corresponds well with the time taken for the SOA mass to stabilise in the flow tube ( $\sim 1500$  s). The variability in the signal from 10000-12000 s, upon introduction of SOA into the reaction system, is typically greater than that observed in previous calibration

---

tests. This is likely due to small changes in the SOA mass concentration in the flow tube, which varies across the experiment, with small fluctuations in SOA mass concentration often correlating with variance in the voltage at the photoreceiver. There are two spikes in SOA mass at 8000 s and 9200 s, which results in two sudden increases in the voltage approximately 1800 s after the SOA mass increase. The second experiment, starting at 12500 s with the introduction of the same mass of SOA, results in an average signal of 0.88 V.

A similar experiment was conducted at lower mass, the SMPS data and voltage response is illustrated in Figure 6.13. The introduction of a large concentration of SOA, with a maximum concentration of  $9800 \mu\text{g m}^{-3}$  at 12500 s into the assay results in a substantial response, to a maximum of 0.82 V. There is an additional spike observed to 1.1 V when the SOA mass is suddenly reduced. It is unclear what caused this anomaly at present, but more work is required to improve the signal stability when sampling organic aerosol.

After this spike to 1.1 V, the signal promptly returns to background once the SOA mass concentration is reduced to zero. A lower SOA mass concentration was introduced at 16000 s, at a more modest average concentration of  $1070 \mu\text{g m}^{-3}$ . There is a lower response in the signal at this lower concentration, with an average signal of 0.25 V, approximately 0.04 V above the background signal. As the background signal drifts over time, it is important to take regular blank readings so that the signal can be corrected appropriately. This would be particularly important for autonomous measurements during smog chamber experiments or ambient measurements.

The data from a series of SOA experiments, inclusive of those illustrated in Figure 6.12 and Figure 6.13, with various SOA mass concentrations is displayed in Figure 6.14. There is a clear response in the voltage at the photoreceiver as a function of SOA mass, with an  $r^2 = 0.951$  correlation coefficient. This indicates that the extent of ascorbic acid oxidation also increases linearly as a function of SOA mass. There is more deviation from linearity in these results compared to the DHA or metal salt calibrations, which is likely due to small fluctuations in SOA mass which is more difficult to control, or slight changes in reaction conditions which could lead to a compositional difference in the SOA.

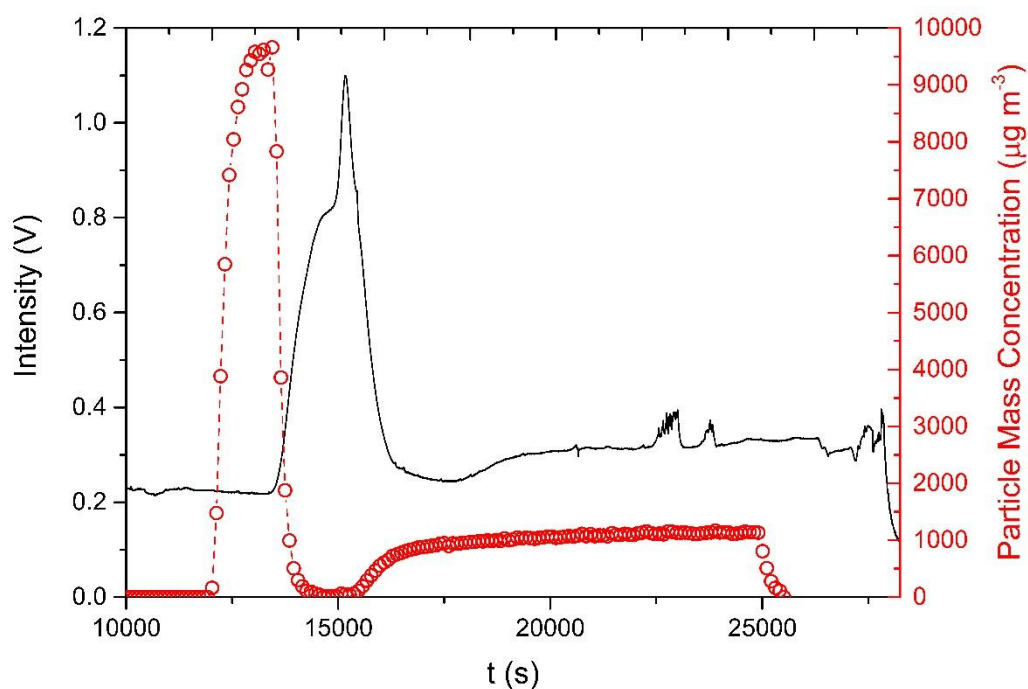


**Figure 6.13** - Sampling of SOA into the on-line assay. Initially, a large spike in SOA mass results in an increase in the fluorescent signal. A more continuous steady-state concentration of SOA at 16000 s results in an increase in the voltage, which is relatively stable over the sampling time of 10000 s. There are small fluctuations in the signal at 22600 s and 23100 s, although their origin is currently unclear.

The LOD of this assay with regards to SOA is approximately  $41.2 \pm 6.9 \mu\text{g m}^{-3}$  by considering three times the background signal stability at the photoreceiver observed over 10 repeats. Compared to results obtained by Wragg *et al.*<sup>85</sup> using the DCFH/HRP assay (limit of detection  $\sim 5\text{-}10 \mu\text{g m}^{-3}$  SOA), the ascorbic acid assay is at present approximately 10 times less sensitive than that technique, although the ascorbic acid based assay would potentially be capable of measuring ambient concentrations of aerosol in polluted urban environments

However, the absolute background signal associated with RTLF is highly variable at present on a per-experiment basis. There are several factors that could affect background levels and stability: Ascorbic acid is known to degrade in aqueous media, which could lead to DHA and therefore an increase in the background signal. As demonstrated in Section 6.3.2, the assay is particularly sensitive to transition metals; although every precaution is taken to minimise contaminants from metals in RTLF, this contamination could well vary on a per-experiment basis, therefore influencing the background signal of the assay.

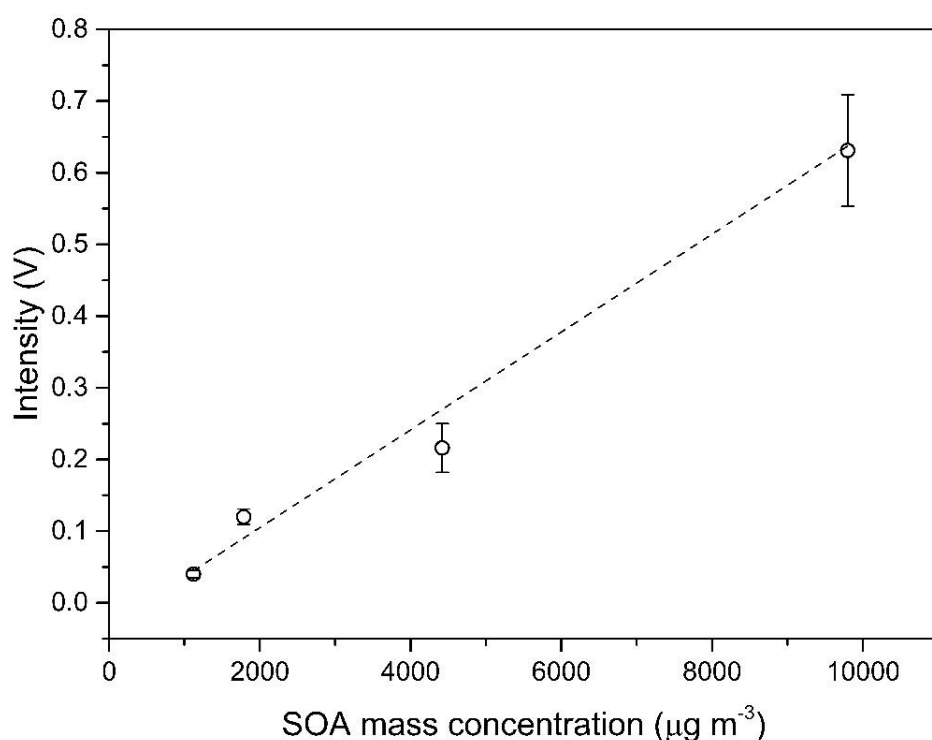


**Figure 6.14** – Plots showing the voltage response of the photoreceiver as a function of SOA mass concentration, with an  $r^2 = 0.951$  correlation coefficient. An increase in the SOA mass sampled results in an increase in the Voltage at the photoreceiver. Error bars represent the variation in signal as a function of SOA mass concentration as observed over multiple repeats.

Temperature or pH differences between experiments could well affect the production of DHA in RTLF, therefore affecting the background signal. Further work is required to fully characterise these effects, and to make the necessary physical and chemical alterations to the on-line assay to ensure that the sensitivity, stability and reproducibility of the technique is improved.

### Summary of Assay Sensitivity towards Fe, Cu and SOA

The values obtained for limits of detection towards Cu (II), Fe (II), Fe (III) and SOA are presented in both  $\mu\text{M}$  and converted  $\mu\text{g m}^{-3}$  mass concentrations, as illustrated in Table 6.3. The limits of detection (LODs) previously expressed in  $\mu\text{M}$  were converted to estimate particle mass concentration  $\mu\text{g m}^{-3}$  to aid with comparison to ambient studies, and estimate the assays current capability to detect these species at atmospherically relevant concentrations. Table 6.3 illustrates that the assay is particularly sensitive to Cu

(II) and Fe (III), which both have an LOD ~1-2 orders of magnitude greater than that of SOA and Fe (II) respectively.

The Cu (II) LOD is approximately an order of magnitude greater, in terms of mass concentration, compared to Cu concentrations observed in the ambient observations at various UK, and European locations ( $\sim 0.001$ - $0.009 \mu\text{g m}^{-3}$ ).<sup>262,263,264</sup> However, concentrations measured in polluted environments (Beijing) have been detected in the range  $0.06 - 4 \mu\text{g m}^{-3}$ , which this assay would be capable of quantifying.<sup>262</sup> Fe concentrations have been observed in the UK and Europe in the range of  $0.01$ - $0.1 \mu\text{g m}^{-3}$ <sup>263,264</sup>, and as high as  $1.12$ - $4.18 \mu\text{g m}^{-3}$  in polluted urban environments.<sup>262</sup> The results of the calibration experiments also demonstrate that the assay would be capable of measuring  $\text{PM}_{2.5}$  in polluted urban environments given the organic LOD of  $41.2 \mu\text{g m}^{-3}$ , although at present it may not be sensitive enough for ambient measurements in less polluted environments. These results indicate that with further optimisation, this assay may well be capable of detecting particle bound ROS in polluted urban environments.

**Table 6.3** – Summary of the limits of detection (LOD) calculated for Cu (II), Fe (II), Fe (III) and SOA. Values are expressed both  $\mu\text{M}$  and  $\mu\text{g m}^{-3}$  to aid with comparison to ambient observations.

Chemical Component	LOD ( $\mu\text{M}$ )	LOD ( $\mu\text{g m}^{-3}$ )
DHA	$0.17 \pm 0.02$	-----
Cu(II)	$0.035 \pm 0.004$	$0.44 \pm 0.06$
Fe(II)	$8.57 \pm 0.9$	$95.6 \pm 11$
Fe(III)	$0.13 \pm 0.01$	$1.26 \pm 0.2$
SOA	-----	$41.2 \pm 6.9$

However, concerning urban ambient aerosol, there is a rich and complex condensed phase chemistry, which often includes a mixture of organics and transition metals such as copper and iron which can undergo secondary chemistry in the condensed phase. As has been demonstrated, the assay has differing sensitivities to different chemical components; therefore, individual metal or SOA experiments may not be an entirely representative model system for probing the assays potential for measuring ambient aerosol, and further experiments are required to investigate sensitivity for metal + SOA mixtures.

#### 6.3.4 Investigating the Assay Response to an Iron Sulphate – SOA mixture

Further to the investigation of the sensitivity of the assay to varying concentrations of SOA, a second set of experiments were conducted to probe the response of the assay to a

mixture of SOA and Fe(III) using the experimental set-up described in Figure 6.4. This involved the aforementioned experimental set-up for SOA measurements, with the addition of a nebuliser containing a 8  $\mu\text{M}$  solution of  $\text{Fe(III)}_2(\text{SO}_4)_3$  in Chelexed MilliQ water.

The nebuliser was optimised to introduce a constant aerosol concentration of  $220 \pm 32 \mu\text{g m}^{-3}$  into the flow tube, which was mixed with varying concentrations of  $\text{O}_3$  (resulting in varying SOA concentrations) in the flow tube before being sampled into the assay. SMPS particle number distributions for SOA, Fe (III) and SOA + Fe (III) are shown in Figure 6.15. The scans evidence that the SOA generated from  $\alpha$ -pinene ozonolysis and  $\text{Fe(III)}_2(\text{SO}_4)_3$  particles introduced into the flow tube *via* the nebuliser form internally mixed particles, as one mode is observed for the mixture.

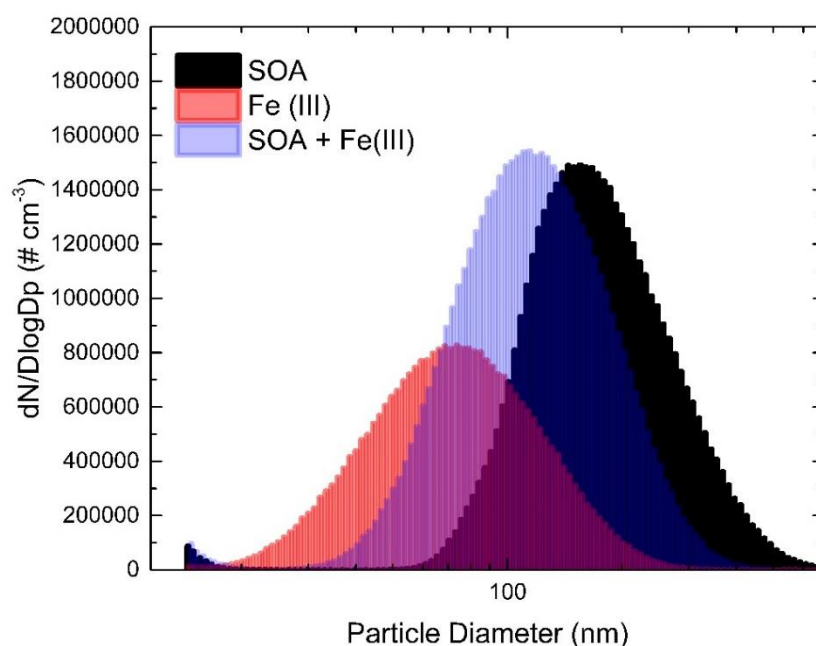


**Figure 6.15** – SMPS scans showing the average particle number distributions for SOA (black), Fe(III) (red) and SOA + Fe(III) (blue). The single mode observed upon mixing SOA and Fe(III) implies that there is heterogeneous condensation of organic SOA onto the iron particles, and/or that the iron particles coagulate with SOA particles.

The SMPS data tracing the Fe(III) and SOA particle mass concentration over time as well as the voltage response at the photoreceiver are presented in Figure 6.16.

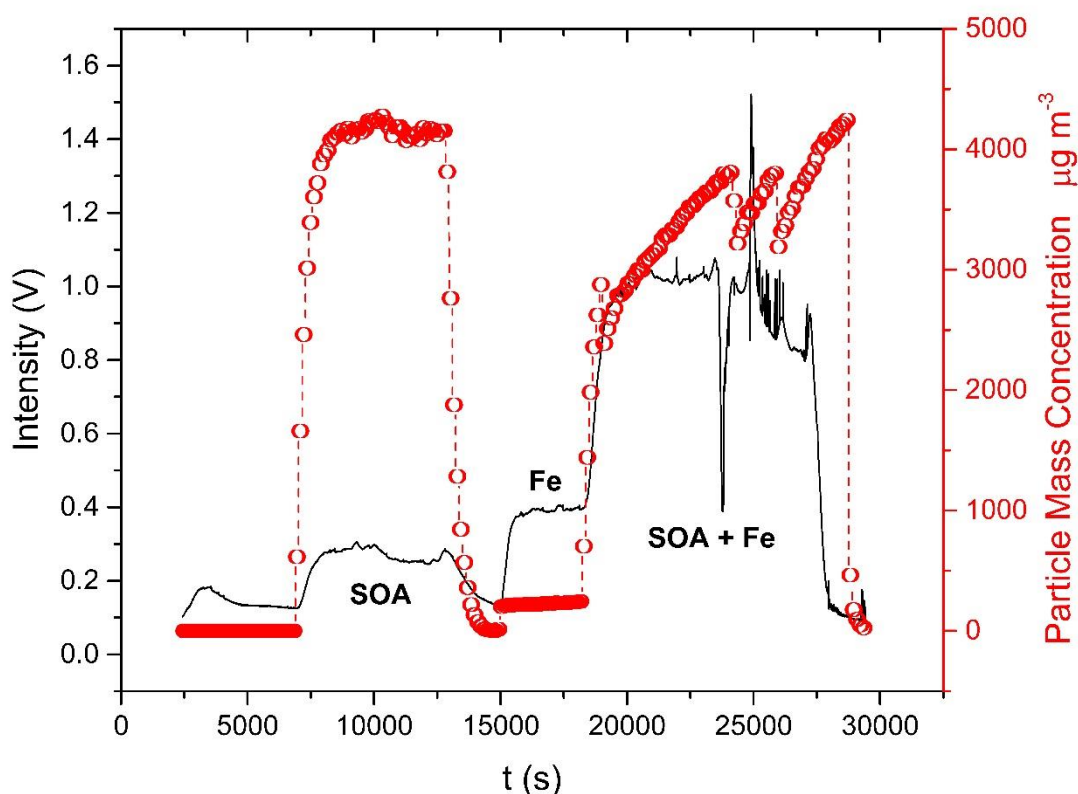


**Figure 6.16** – Raw data showing the average particle mass in the flow tube, as well as the voltage response over time. After taking a background reading, SOA was sampled into assay initially. SOA production was turned off, and Fe was nebulised into the assay. Further to this, an experiment was conducted where Fe +SOA were introduced into the flow tube together. It should be noted that the SMPS data has been corrected to account for the 30-minute lag time between SOA sampling and fluorescent detection. As can be seen, there is an apparent synergistic effect of mixing SOA + Fe (III), as the signal associated with this result is greater than the combined signal of the individual experiments involving SOA and Fe (III).

It should be noted that in this figure, the SMPS scans have been corrected for time so that the SOA signals overlay the corresponding voltage response. Firstly, pure SOA was introduced into the assay at 7500 s a mass concentration of  $4125 \mu\text{g m}^{-3}$ , resulting in a voltage of approximately 0.29 V, appreciably above the background. Following this, SOA production was turned off and  $220 \mu\text{g m}^{-3}$   $\text{Fe(III)}_2(\text{SO}_4)_3$  was nebulised into the flow tube at 15000 s, resulting in a response of 0.4 V at the photoreceiver. Finally, SOA was generated whilst the same amount of  $\text{Fe(III)}_2(\text{SO}_4)_3$  (*i.e.*  $220 \mu\text{g m}^{-3}$ ) was simultaneously nebulised into the flow tube.

There is a clear enhancement of the extent of ascorbic acid oxidation when the SOA and Fe (III) are analysed together, evidenced by the increased fluorescent response. The SOA

and Fe (III) individual fluorescent responses total 0.69 V, whereas the SOA + Fe (III) experiment has an average signal of 1.15 V. Using the calibration curve displayed in Figure 6.7, this is the equivalent to the production of 58  $\mu\text{M}$  and 91  $\mu\text{M}$  DHA respectively, resulting in an approximately 50% increased oxidation of ascorbic acid when the Fe (III) is mixed with organics from SOA. The enhancement of ascorbic oxidation could be the result of the production of superoxide and therefore hydrogen peroxide and  $\cdot\text{OH}$  radicals *via* Fenton-like chemistry, which could further oxidise SOA components to produce more oxidising species such as organic peroxides and peracids. This process would require some reduction of Fe (III) to Fe (II) to initiate this chemistry, which can occur *via* direct reaction of Fe (III) with ascorbate to produce ascorbate radicals and Fe (II).

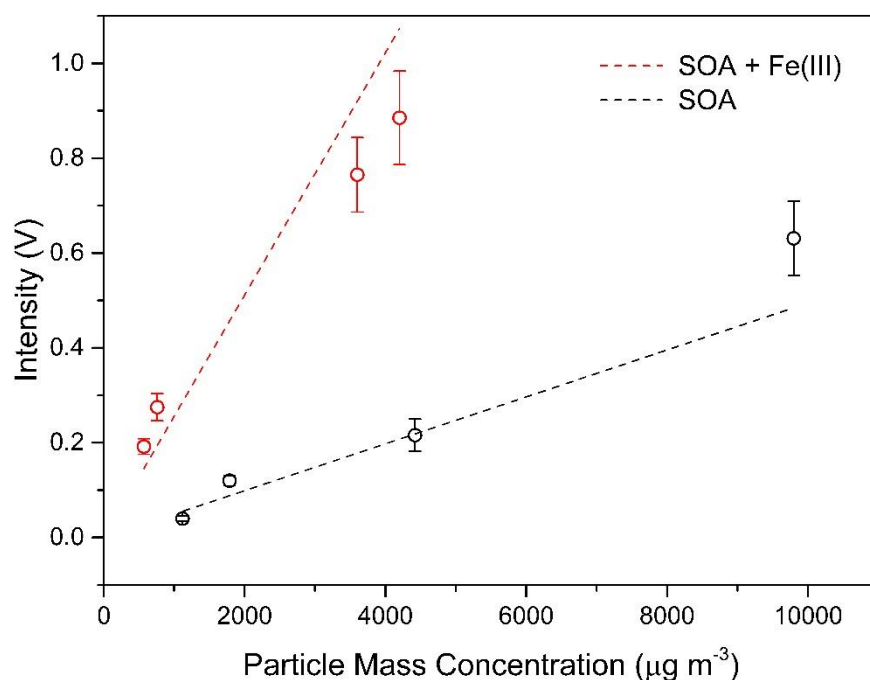


**Figure 6.17** – Comparison between the intensity (V) observed for SOA alone and SOA + Fe (III) mixed in the flow tube. The Fe (III) concentration is kept relatively constant, between 200-220  $\mu\text{g m}^{-3}$  for each experiment, so the SOA + Fe (III) data represents additional SOA mass concentration formed in the flow tube. There is a clear enhancement of the oxidation of ascorbate by adding Fe (III) to the SOA in the flow tube, although at present it is unclear as to the origin of this effect. Error bars represent variability observed over multiple repeats.

Furthermore, studies have shown that complex organic mixtures found in ambient aerosol can chelate Fe(II), enhancing the production of superoxide and subsequently  $\text{H}_2\text{O}_2$  and  $\cdot\text{OH}$  radicals.<sup>257,265,266</sup> As Fe(III) will be converted to Fe(II) *via* reaction with ascorbate,



this will produce Fe(II) which could be chelated by organics in SOA, producing more ROS which will result in greater ascorbate oxidation. The enhancement of the fluorescent signal as a function of SOA mass and SOA + Fe (III) mass is displayed in Figure 6.17.

The Fe(III)<sub>2</sub>(SO<sub>4</sub>)<sub>3</sub> mass in each Fe(III) + SOA experiment (red) is kept relatively constant in each experiment, with the concentration varying between 200-240  $\mu\text{g m}^{-3}$  in each case. There is a clear and distinct enhancement of ascorbate oxidation when adding Fe (III) to the SOA, as well as an increasing fluorescent response as more SOA mass is added to the Fe (III) in the flow tube. At present, it is not entirely clear where this effect comes from, and as is the case for the calibrations as well as the experiments sampling only SOA, modelling studies could improve our understanding of this complex chemical system. At present, collaborators are developing a model constrained by the data described in this thesis, in a bid to further understand the chemistry occurring in the ascorbic acid assay.

## 6.4 Chapter Summary

This chapter has presented the development of a new ascorbic acid based chemical assay which has been incorporated into a prototype on-line instrument, based on a design published in Fuller *et al.*<sup>90</sup> and Wragg *et al.*<sup>85</sup> The chemistry associated with the ascorbic acid assay was extensively investigated, and a simplified on-line flow through experimental set-up was designed to calibrate the prototype instrument. Initial calibrations with dehydroascorbic acid (DHA) showed a linear response in the fluorescent signal as a function of DHA concentration, with DHA forming the fluorescent product DFQ via reaction with the dye OPDA. The LOD for DHA was calculated to be  $0.17 \pm 0.02 \mu\text{M}$ .

Furthermore, the instruments sensitivity to Cu (II), Fe (II) and Fe (III) was probed. The assay was particularly sensitive to Cu(II), with an appreciable fluorescent response over a concentration range of 1-18  $\mu\text{M}$ , with 18  $\mu\text{M}$  of Cu(II) resulting in the production of approximately 90  $\mu\text{M}$  DHA, illustrating efficient ascorbate oxidation. The assay was substantially more sensitive to Fe (III) than Fe (II); the exact origin of this difference is at present unclear, although it is likely that direct oxidation of ascorbate anions to ascorbate radicals by Fe (III) leads to the efficient production of DHA, leading to a large concentration of DHA being formed. The LODs were calculated for Cu (II), Fe (II) and Fe (III) to be  $0.44 \pm 0.06$ ,  $95.6 \pm 11$  and  $0.68 \pm 0.102 \mu\text{g m}^{-3}$  respectively, indicating that the assay is ~2 orders of magnitude more sensitive to Cu (II) and Fe (III) compared to

---

Fe(II). Comparison of these values to concentrations of Cu and Fe observed in ambient studies show that at present, the instrument might be capable of detecting ROS generated from particle-bound Cu and Fe in extremely polluted environments.

The on-line instrument was then further developed to allow the sampling of aerosol particles. SOA generated from the ozonolysis of  $\alpha$ -pinene was used as a model system to probe the assays response. The LOD of the instrument with respect to SOA was estimated to be  $41.2 \pm 6.9 \text{ ug m}^{-3}$  SOA. This detection limit is approximately an order of magnitude less sensitive to organic ROS than the OPROSI developed by Wragg *et al.*<sup>85</sup>, although given this assays substantially larger sensitivity to Fe and Cu compared to the OPROSI, it may well be suitable for studies of particle bound ROS in urban polluted environments.

Furthermore, a brief study was conducted to investigate the effect of adding Fe(III) to SOA in the flow tube before analysis using the ascorbic acid assay. It was found that Fe (III) mixed with SOA substantially enhances the oxidation of ascorbate in the system, as the fluorescent response of mixing both Fe (III) and SOA is about 50% greater than that of the individually sampled experiments. This could be due to the chelation of organics to Fe (II) after conversion of Fe (III) to Fe (II) *via* reaction with ascorbate. The chelation of organics to Fe (II) could substantially increase the production of ROS *via* Fenton like chemistry, therefore increasing the extent of ascorbate oxidation to form DHA. At present, the mechanisms of this observation are unclear, and further experiments are required in order to probe the chemistry at play here.

The sets of experiments discussed in this chapter have sought to characterise the efficacy of the instrument, probing the instruments suitability to quantify particle-bound ROS in aerosol generated in the laboratory on-line, as well as potential future deployment in the field. The chemical preparation required to have suitable reagents is already at present extensive. Greater care could be taken to avoid contamination by metals, although the water used is already of the highest purity. Therefore, in terms of developing an on-line instrument, some physical developments could be made to improve sensitivity even further.

The ascorbic acid/OPDA assay with subsequent fluorescent detection has shown promise concerning the quantification of particle bound ROS. As opposed to a Teflon coil submersed in a bath, one could replace this with a microfluidic flow chamber. This would allow the sampling of lower volumes of liquid in the reaction bath, which would allow

more stringent control of temperature. Although experiments have not been conducted in this study, small temperature changes in the reaction bath could affect the background signal as well as the sensitivity of ascorbate towards oxidants, therefore resulting in a less stable signal. The mixing can also be stringently controlled in such microfluidic flow cells, perhaps allowing for more efficient and reproducible mixing in the flow cell, reducing the instability of the fluorescent signal. A microfluidic cell based on the DTT assay has recently been developed to probe the oxidative potential of organics, although this is still in development.<sup>87</sup>

Further to this, a series of electrochemical sensors have been developed for application to food chemistry, where these devices have been extensively applied to monitor the degradation of ascorbic acid.<sup>267–269</sup> These electrochemical sensors monitor the concentration of ascorbic acid, which could still be used as a proxy for oxidative potential of organics by tracing the decrease in concentration of ascorbic acid upon exposure to ROS. It is unclear whether these sensors would improve the sensitivity of the technique, but in terms of instrument development, it would negate the need for OPDA at all, reducing size as well as the chemical complexity of the assay, which may in turn improve the signal reproducibility. However, the current assay has showed promise concerning the probing of health-relevant chemical components bound to aerosol. The prototype assay has been shown that even at its early stage of development, could in principle detect ROS in ambient aerosol in polluted urban environments such as Beijing, although further optimisation is required for studies in less polluted urban environments.

---

# 7 CONCLUSIONS AND FUTURE WORK

## 7.1 Introduction

This thesis set out to develop four analytical techniques capable of characterising both atmospherically relevant reactive intermediates (such as Criegee intermediates and particle-bound organic radicals) and health-relevant reactive oxygen species. The research conducted in this thesis was broadly motivated based on the following:

- Despite vast amounts of research, large uncertainties remain regarding the chemistry of Criegee intermediates in the gas phase. Several methods have recently been developed which have drastically improved our understanding of CIs in the atmosphere. However, most available techniques currently struggle to simultaneously detect multiple Criegee intermediates produced in complex ozonolysis regimes.
- There is limited literature data describing the fate of low-volatility, atmospherically relevant CIs generated from the ozonolysis VOCs. Therefore, large uncertainties remain regarding the effect of particle-bound CIs on organic aerosol composition and ageing, motivating the need to develop a method of characterising particle-bound CIs.
- The role of particle-bound radical species in aerosol composition, aerosol ageing and their effect on the oxidative potential (and therefore health relevant toxicological effects) of aerosol is at present poorly characterised. A novel method capable of quantifying particle-bound radicals would help to bridge current knowledge gaps.
- There are multiple assays currently being utilised to detect reactive oxygen species in ambient aerosol, which are believed to contribute significantly to observed adverse human health effects upon uptake of particles into the lung. The development of an on-line chemical assay, utilising a physiologically relevant anti-oxidant as a reagent (ascorbic acid) may lead to the development of an

instrument that is selective to species that are likely to induce a toxicological effect upon uptake into the lung.

## 7.2 Summary of Research Findings

Extensive conclusions and key research findings are presented at the end of each respective results chapter. The next four sections in this results chapter will briefly summarise the key findings of Chapters 3-6, and aim to bind them in the wider context of this thesis.

### 7.2.1 Online Quantification of Criegee Intermediates in the Gas Phase

The work in this chapter focussed on the development of a novel, cost-effective laboratory based technique that is uniquely capable of characterising multiple CIs in complex, atmospherically relevant chemical systems. The reactivity and reaction products of CIs with the spin trap DMPO was investigated. A combination of analytical techniques including HPLC-ESI-HRMS, EPR, and NMR, supported by DFT theoretical calculations, suggest that the CI efficiently reacts with the DMPO, to generate a relatively stable non-radical adduct comprising of a 6-membered heterocycle. The reaction mechanism was postulated to proceed *via* a 1,3-dipolar cycloaddition of the CI across the nitron functionality of the spin trap. Using a flow tube set-up, CIs in the gas phase generated from a model VOC system ( $\alpha$ -pinene + O<sub>3</sub>) were scavenged using DMPO, and the subsequent adduct was measured on-line with PTR-ToF-MS. The 1:1 adduct CI-DMPO, with the elemental formula C<sub>16</sub>H<sub>28</sub>NO<sub>4</sub><sup>+</sup> was detected by PTR-ToF-MS at  $m/z$  298.20, representing the first time that CIs generated from  $\alpha$ -pinene ozonolysis have been characterised. The limit of detection of this technique was calculated to be 0.03 ppb, with a typical repeatability of  $\pm 0.05$  ppb for  $\alpha$ -pinene CIs observed through multiple repeats.

This technique was then applied to simultaneously characterise multiple CIs generated from a variety of VOC precursors. CIs were characterised from the ozonolysis of  $\beta$ -pinene, limonene, styrene, methacrolein and cis-2-hexene, as well as chemical system containing both  $\beta$ -pinene and cis-2-hexene. All predicted CI-DMPO adducts were observed in the experiments, representing for the first time the characterisation of CIs from methacrolein, limonene, styrene and cis-2-hexene. It also represents the first time in which four CIs from two different VOC precursors have been simultaneously characterised in a complex organic mixture.

---

The estimated concentrations of ambient CIs remains several orders of magnitude below the detection limits of this technique, and indeed, at such low ambient concentrations CIs prove incredibly difficult to measure in the field. Substantial technical, chemical and experimental enhancements would have to be made if there is any hope of one day applying this technique to atmospherically relevant CI concentrations.

Despite this, the method has demonstrated great potential for characterising CIs in extremely complex organic systems. Understanding the fate of CIs in such systems is of crucial importance for understanding the intermediate steps of several key tropospheric processes. This technique is uniquely capable of simultaneously characterising multiple CIs in complex chemical systems, which could prove crucial in determining the role of CIs in various key tropospheric oxidation processes.

### **7.2.2 Novel Method to Detect Criegee Intermediates in the Particle Phase**

This chapter presented the detection of multiple Criegee intermediates generated from the ozonolysis of  $\beta$ -caryophyllene in the particle phase. A novel technique was developed to facilitate the detection of CIs in the particle phase by stabilisation with spin traps and off-line analysis using HPLC-ESI-HRMS. The PBN adducts  $\text{CI}_{\text{C15}}$ -PBN and  $\text{CI}_{\text{C14B}}$ -PBN were detected, indicating the presence of large, low-volatile CIs in the SOA. At present, it is not entirely clear whether the CIs detected were formed from heterogeneous uptake of CIs from the gas phase, or *via* heterogeneous oxidation of  $\beta$ -caryophyllene already present in the condensed phase. An investigation into the concentration of CIs at different SOA mass loadings illustrated a correlation between the peak area associated with the  $\text{CI}_{\text{C15}}$ -PBN and the mass concentration. Using PBN as a surrogate standard, the concentration of CIs in the particle phase was estimated to be  $4.5 \pm 0.7 \text{ ng}/\mu\text{g SOA}$ . Although this remains an approximation with several uncertainties, it does illustrate the quantitative potential of this technique. At present, the trapping efficiency of the PBN is an estimate based on liquid phase ozonolysis, and would need to be properly investigated to improve quantification. A suitable standard for HPLC calibration is also required, highlighting the need to synthesise a  $\text{CI}_{\text{C15}}$ -PBN standard

This chapter has demonstrated that this technique is uniquely capable of characterising CIs in the particle phase, and has shown some potential regarding the quantification of CIs. Large uncertainty remains regarding the role of particle-bound radicals in both SOA

ageing processes as well as health-relevant toxicological impacts. There remain large uncertainties associated with the reaction mechanisms, pathways and product distributions regarding bulk phase reactions in SOA. This technique could potentially allow one to characterise the role of reactive intermediates in this process, which in turn could elucidate the reaction mechanisms and pathways that lead to observed product distributions.

### 7.2.3 Quantification of Radicals in Secondary Organic Aerosol

The work presented in this chapter discussed the application of the profluorescent nitroxide probe BPEA to the detection of particle-bound radicals formed from the ozonolysis of a series of VOC precursors.

A series of proof-of-concept experiments were designed to determine whether the BPEA assay was sensitive to particle-bound radicals in SOA formed from the ozonolysis of  $\alpha$ -pinene. A linear response in the fluorescent signal was observed as the concentration of SOA sampled in an impinger increased over time. Using this data, the concentration of radicals per unit mass  $\alpha$ -pinene SOA was estimated to be  $0.4 \pm 0.1$  nM/ $\mu$ g SOA or  $8 \pm 2$  ng(radicals)/ $\mu$ g(SOA). Therefore, this measurement indicates that there is approximately 1 radical per 800 molecules in the SOA. This represents, to authors knowledge, the first estimate of the concentration of radical species present in  $\alpha$ -pinene SOA.

Further to this, experiments altering the residence time of the SOA in the flow tube were conducted to probe the rate of decay of radicals in  $\alpha$ -pinene SOA. The rate coefficient associated with the loss of radical species in this system was estimated to be  $k = (7.3 \pm 1.7) \times 10^{-3} \text{ s}^{-1}$  on average, which therefore leads to an average radical lifetime in this SOA regime of approximately  $137 \pm 31$  s assuming 1<sup>st</sup> order kinetics. This work represents the first estimate of the rate of loss of radicals in SOA.

A final set of experiments compared SOA generated from the ozonolysis of  $\beta$ -caryophyllene,  $\alpha$ -pinene and limonene.  $\alpha$ -pinene was found to have the highest radical concentration as detected by fluorescence, with an average concentration 4 times greater than that of limonene per unit mass of SOA. This was explained by considering the higher OH yield from  $\alpha$ -pinene SOA, as well as higher viscosity of the SOA formed from  $\beta$ -caryophyllene ozonolysis compared to the other regimes. A higher OH yield would lead

---

to an increase in the extent of heterogeneous oxidation by OH (thereby generating more radicals in the particle), as well as the fact that a lower viscosity SOA may allow a faster diffusion of OH, potentially enhancing the kinetics of OH chemistry in the particle phase.

These experiments have demonstrated that the spin trap BPEA is capable of quantifying radicals in SOA generated from a variety of precursors. The SOA mass loadings in these experiments are ~2-4 orders of magnitude greater than that found in the ambient. More experiments are required to determine the sensitivity of this technique to much lower mass concentrations that are more representative of those found in the atmosphere. If the BPEA/DMSO assay is indeed sensitive in this range, the assay could be applied to probe various atmospheric processes that are believed to introduce radicals into the particle phase (heterogeneous oxidation, Fenton chemistry, particle surface photochemistry, etc). Radical chemistry in organic aerosol represents a large area of uncertainty; further development of this technique could result in a valuable assay that in principle could be applied to probe various chemical processes involved in the initial formation, as well as ageing, of SOA.

#### **7.2.4 Development of an On-line Chemical Assay to Measure Particle Bound ROS**

The work in this chapter presented the development of a new ascorbic acid based chemical assay, which has been incorporated into a prototype on-line instrument. The chemistry associated with the ascorbic acid assay was extensively investigated, and a simplified on-line flow through experimental set-up was designed to calibrate the prototype instrument. Initial calibrations with dehydroascorbic acid (DHA) showed a linear response in the fluorescent signal as a function of DHA concentration, with DHA forming the fluorescent product DFQ via reaction with the dye OPDA. The LOD for DHA was calculated to be  $0.17 \pm 0.02 \mu\text{M}$ .

Furthermore, the instruments sensitivity to Cu (II), Fe (II) and Fe (III) was probed. The assay was particularly sensitive to Cu (II), with an appreciable fluorescent response over a concentration range of 1-18  $\mu\text{M}$ , with 18  $\mu\text{M}$  of Cu (II) resulting in the production of approximately 90  $\mu\text{M}$  DHA, illustrating efficient ascorbate oxidation. The assay was substantially more sensitive to Fe (III) than Fe (II); the exact origin of this difference is at present unclear, although it is likely that direct oxidation of ascorbate anions to ascorbate radicals by Fe (III) leads to the efficient production of DHA, leading to a large



concentration of DHA being formed. The LODs were calculated for Cu (II), Fe (II) and Fe (III) to be  $0.44 \pm 0.06$ ,  $95.6 \pm 11$  and  $0.68 \pm 0.102 \mu\text{g m}^{-3}$  respectively, indicating that the assay is ~2 orders of magnitude more sensitive to Cu (II) and Fe(III) compared to Fe (II). Comparison of these values to concentrations of Cu and Fe observed in ambient studies show that at present, the instrument might be capable of detecting ROS generated from particle-bound Cu and Fe in extremely polluted environments.

The on-line instrument was then further developed to allow the sampling of aerosol particles. SOA generated from the ozonolysis of  $\alpha$ -pinene was used as a model system to probe the assays response. The LOD of the instrument with respect to SOA was estimated to be  $41.2 \pm 6.9 \mu\text{g m}^{-3}$  SOA. This detection limit is approximately an order of magnitude less sensitive to organic ROS than the OPROSI developed by Wragg *et al.*<sup>85</sup>, although given this assays substantially larger sensitivity to Fe and Cu compared to the OPROSI, it may well be suitable for studies of particle bound ROS in urban polluted environments.

Furthermore, a brief study was conducted to investigate the effect of adding Fe (III) aerosol to SOA in the flow tube before analysis using the ascorbic acid assay. It was found that Fe (III) mixed with SOA substantially enhances the oxidation of ascorbate in the system, as the fluorescent response of mixing both Fe(III) and SOA is about 50% greater than that of the individually sampled experiments.

The sets of experiments discussed in this chapter have sought to characterise the efficacy of the instrument, probing the instruments suitability to probe particle-bound ROS in aerosol generated in the laboratory online, as well as potential future deployment in the field. The chemical preparation required to have suitable reagents is already at present extensive, and every precaution is taken to ensure that the reaction mixture is as pure as possible. Therefore, in terms of developing an on-line instrument, some physical developments could be made to improve sensitivity even further. These particular recommendations for future development are discussed in detail in the next Section.

The current assay has showed promise concerning the probing of health-relevant chemical components bound to aerosol. The prototype assay has been shown that even at its early stage of development, could in principle detect ROS in ambient aerosol in polluted urban environments such as Beijing, although further optimisation is required for studies in less polluted urban environments.

---

## 7.3 Potential Implications and Future Recommendations

The work conducted in this thesis has developed and applied a series of novel chemical assays that are capable of characterising and quantifying a range of tropospherically relevant species. Chapters 3 and 4 focus on specifically characterising one intermediate species, which plays a crucial role in gas phase ozonolysis of VOCs in the troposphere, Criegee intermediates. The aim of Chapters 5 and 6, however, was to develop methods which cannot necessarily qualitatively describe any one species, but can quantify a wide range of species in aerosol that have impacts on both organic aerosol composition and ageing, as well as potential implications regarding adverse health effects of particulate matter.

It is important to approach such problems from both a specific and general perspective; understanding fundamental processes, inclusive of the role of the Criegee intermediate, will develop our understanding of the complex reaction mechanisms that lead to observed organic product distribution and composition in aerosol. However, it is also of great importance to quantitatively describe species that have a potentially large impact on aerosol composition and therefore also health effects.

The methods developed in this thesis have sought to probe complex chemical environments and measure specific species or groups of species that are of atmospheric relevance. The methods are all in relative infancy in terms of development; large gas phase precursor and aerosol concentrations were used in proof-of-principle experiments, and more work is required to optimise these methods to operate at atmospherically relevant concentrations. However, these methods represent potentially important steps in developing our understanding in the role of radicals and ROS in both aerosol composition and human health. The conclusions in previous Chapters have given a detailed overview of potential optimisations for these methods, and a brief set of recommendations for further development will be given here.

### Chapter 3: Online Quantification of Criegee Intermediates in the Gas Phase

This method has been shown to be uniquely capable of simultaneously characterising multiple CIs generated from the ozonolysis of a range of biogenic and anthropogenic VOCs, although given the slow reaction kinetics of ozone-olefin reactions, at present large precursor concentrations are required to facilitate detection. The reaction kinetics of DMPO and a range of CIs (all with differing sizes) is poorly characterised, and will need

to be investigated to improve the quantitative capabilities of this method. The detection limit of this method is still several orders of magnitude above ambient concentrations of CIs, although most methods of CI detection struggle at such low concentrations.

- One potential improvement would be the synthesis or identification of a CI scavenger that is unreactive towards ozone, meaning it can be added *in situ*. This is likely problematic given the zwitterionic character of  $O_3$ , it shares similar reaction characteristics with the CI. As mentioned in Section 3.4, studies have shown rapid reaction kinetics between the CI and trifluoroacetic acid close to the gas-collision limit, implying efficient scavenging of the CI. The PTR-ToF-MS should be capable of detecting the adduct formed from this reaction, and the fact that the kinetics are known is advantageous, although several physical and chemical optimisations (reaction time, reaction temperature, etc..) would need to be performed to probe the suitability of this scavenger.
- The current method is, at present, uniquely capable of detecting multiple CIs. If one could ascertain the rate of reaction even between simple CIs and DMPO that would substantially aid our current ability to quantify CIs in the gas phase. Utilising the gem-diodoalkanes precursor route to CIs, with its well-defined chemistry, would potentially allow the accurate determination of the rate of reaction between small CIs and DMPO, further improving our understanding of this method. This kinetic study could be supported by further DFT calculations, to estimate the rate coefficient associated with the reaction of a range of CIs with the spin trap DMPO.

#### Chapter 4: Novel Method to Measure Criegee Intermediates in the Particle Phase

The method developed in this section represented the first detection of CIs in the particle phase. Large uncertainty remains regarding the fate of low-volatility CIs in the particle phase, formed either from heterogeneous oxidation of alkenes in SOA, or CIs that have a low enough volatility to partition into the condensed phase before loss in the gas phase. This method has been shown to be capable of characterising multiple CIs in the condensed phase. Some recommended optimisations:

- Improvement of the impinger to improve collection efficiency. The addition of a fritted impinger with the right porosity grade, which creates many smaller bubbles in solution, would improve the collection efficiency of SOA by increasing the

---

probability of particles diffusing out of the bubble. This would improve detection limits by potentially a factor of 3-5 and thus the detection of CIs at lower SOA mass concentrations. However, particle losses in the frit, as well as memory effects associated with the deposition of organics in the frit, would need to be fully characterised.

- In order to improve the quantitative capabilities of this technique, a more representative standard should be synthesised for HPLC-ESI-HRMS quantification of the CI-PBN adducts. This would more accurately represent the concentration response of the CI-PBN as a function of peak area. This may prove challenging in practice, given the stability of CI-PBN adducts (on the order of days).
- Further tests should be undertaken concerning the observed peak area response as a function of SOA mass concentrations. With reference to **Figure 4.13**, the collection of more mass-dependant CI concentration data may be sufficient to constrain a simple kinetic model that could allow insight into the rate of loss of CIs in the condensed phase, as well as probing the heterogeneous vs. homogenous loss of CIs in the  $\beta$ -caryophyllene ozonolysis regime.

## **Chapter 5: Novel Method to Quantify Radicals in Organic Aerosol**

This Chapter developed a method that was applied, for the first time, to quantify radicals in SOA generated from a variety of VOC precursors. Initial proof-of-principle experiments at high SOA mass concentrations highlighted that this technique was indeed capable of detecting organic radicals formed from the ozonolysis of VOCs. There remains large uncertainty concerning the role of particle-bound radicals in defining organic aerosol composition, ageing mechanisms and the toxicological impact of PM. This motivates further development and application of this technique to improve detection:

- As previously mentioned, a fritted impinger would improve the collection efficiency of SOA in the impinger, and therefore improve the sensitivity of this technique
- A series of proof-of-principle experiments were conducted at high SOA mass concentrations. Further experiments should be conducted to probe the sensitivity of this technique over a range of SOA masses, to estimate a detection limit for this technique. Efforts should be made to determine whether this method can detect radicals at atmospherically relevant SOA mass concentrations.

- The currently optimised method is capable of investigating the effect of heterogeneous OH chemistry on the increase in radical loading of organic aerosol. By comparing SOA generated from ozonolysis vs. SOA generated from ozonolysis which is subsequently exposed to known concentrations of OH, gaining insight into the formation of particle-bound radical concentrations initiated by OH chemistry
- In principle, given the stability of the BPEA adducts in DMSO and fluorometric methods of detection, this assay could be applied to an on-line prototype instrument, similar in design to that described in Chapter 6. This would require extensive optimisation and further development, but may allow sufficient time resolution to probe the formation or decay rates of particle-bound radicals in smog chamber or flow tube studies.

## **Chapter 6: Development of an On-line Chemical Assay to Measure Particle-bound ROS**

The ascorbic acid based on-line assay has shown considerable promise concerning the detection of metals and organics in ambient aerosol, even at this early stage of development. The key steps for future development of this assay are as follows:

- With the current AA/OPDA assay, improve the daily variation of the RTLF background signal. Taking regular background readings can easily correct for this, but a drifting background on a daily basis may affect the sensitivity of the assay.
- Further investigation into the individual and combined effect of Fe, Cu and other metals and SOA, by increasing RH in the flow tube and monitoring the increase in ascorbic acid oxidation.
- Investigation into miniaturising the assay. There is potential to use microfluidic chambers instead of Teflon tubing as a reaction bath. This would be advantageous when thinking of designing a low-cost portable instrument, but may prove challenging in terms of introducing the aerosol into the reaction solution, given the current gas and liquid flow rates required for particle collection.
- The addition of a microfluidic cell could potentially allow the addition of an electrochemical sensor capable of measuring the concentration of AA directly. A range of materials have been developed that can monitor the loss of ascorbic acid over time, and may well constitute a substantial physical optimisation of the current technique. However, it is at present unclear as to whether this would

---

improve the sensitivity of the instrument. It would, however, certainly improve its ease-of-use, as OPDA would no longer be required to monitor ascorbic acid concentration. This simpler method of measuring ascorbic acid concentrations may improve the performance of the instrument.

## **7.4 Closing Remarks**

Despite recent advancements in our understanding of atmospheric science, with particular reference to the formation, ageing and health effects of organic aerosol, many knowledge gaps remain. Aerosol particles have far-reaching consequences for both air quality and climate change. Understanding the fundamental chemical processes that determine aerosol composition is crucial to determine the extent to which aerosol affects the atmosphere, both in terms of their climate and adverse human health effects.

Novel techniques capable of measuring reactive intermediates, whose reactions affect aerosol composition as well as their physiologically relevant properties, are essential to tackle the open questions remaining in this field. Laboratory based development of such techniques, the sole focus of this thesis, is pivotal in order to establish the operational viability of the techniques in question; they represent the first step in terms of translating these techniques into ambient studies in the field.

# 8 REFERENCES

- 1 J. H. Seinfeld and S. N. Pandis, *Atmospheric Chemistry and Physics: From Air Pollution to Climate Change SECOND EDITION*, 2006.
- 2 O. Boucher, D. Randall, P. Artaxo, C. Bretherton, G. Feingold, P. Forster, V.-M. V.-M. Kerminen, Y. Kondo, H. Liao, U. Lohmann, P. Rasch, S. K. Satheesh, S. Sherwood, B. Stevens, X. Y. Zhang and X. Y. Zhan, *IPCC Climate Change 2013: The Physical Science Basis. Contribution of Working Group I to the Fifth Assessment Report of the Intergovernmental Panel on Climate Change*, 2013.
- 3 J. L. Jimenez, M. R. Canagaratna, N. M. Donahue, a. S. H. Prevot, Q. Zhang, J. H. Kroll, P. F. DeCarlo, J. D. Allan, H. Coe, N. L. Ng, a. C. Aiken, K. S. Docherty, I. M. Ulbrich, A. P. Grieshop, a. L. Robinson, J. Duplissy, J. D. Smith, K. R. Wilson, V. a. Lanz, C. Hueglin, Y. L. Sun, J. Tian, A. Laaksonen, T. Raatikainen, J. Rautiainen, P. Vaattovaara, M. Ehn, M. Kulmala, J. M. Tomlinson, D. R. Collins, M. J. Cubison, J. Dunlea, J. A. Huffman, T. B. Onasch, M. R. Alfarra, P. I. Williams, K. Bower, Y. Kondo, J. Schneider, F. Drewnick, S. Borrmann, S. Weimer, K. Demerjian, D. Salcedo, L. Cottrell, R. Griffin, A. Takami, T. Miyoshi, S. Hatakeyama, A. Shimono, J. Y. Sun, Y. M. Zhang, K. Dzepina, J. R. Kimmel, D. Sueper, J. T. Jayne, S. C. Herndon, a. M. Trimborn, L. R. Williams, E. C. Wood, A. M. Middlebrook, C. E. Kolb, U. Baltensperger and D. R. Worsnop, *Science* (80-. ), 2009, **326**, 1525–1529.
- 4 D. M. Murphy, D. J. Cziczo, K. D. Froyd, P. K. Hudson, B. M. Matthew, A. M. Middlebrook, R. E. Peltier, A. Sullivan, D. S. Thomson and R. J. Weber, *J. Geophys. Res. Atmos.*, 2006, **111**, 1–15.
- 5 Q. Zhang, J. L. Jimenez, M. R. Canagaratna, J. D. Allan, H. Coe, I. Ulbrich, M. R. Alfarra, A. Takami, A. M. Middlebrook, Y. L. Sun, K. Dzepina, E. Dunlea, K. Docherty, P. F. DeCarlo, D. Salcedo, T. Onasch, J. T. Jayne, T. Miyoshi, A. Shimono, S. Hatakeyama, N. Takegawa, Y. Kondo, J. Schneider, F. Drewnick, S. Borrmann, S. Weimer, K. Demerjian, P. Williams, K. Bower, R. Bahreini, L.

- 
- Cottrell, R. J. Griffin, J. Rautiainen, J. Y. Sun, Y. M. Zhang and D. R. Worsnop, *Geophys. Res. Lett.*, 2007, **34**, 1–6.
- 6 A. H. Goldstein and I. E. Galbally, *Environ. Sci. Technol.*, 2007, **41**, 1514–1521.
- 7 J. J. Schauer, W. F. Rogge, L. M. Hildemann, M. A. Mazurek, G. R. Cass and B. R. T. Simoneit, *Atmos. Environ.*, 1996, **30**, 3837–3855.
- 8 W. F. Rogge, G. R. Cass, L. M. Hildemann, M. A. Mazurek and B. R. T. Simoneit, *Environ. Sci. Technol.*, 1991, **25**, 1112–1125.
- 9 J. A. de Gouw, A. M. Middlebrook, C. Warneke, P. D. Goldan, W. C. Kuster, J. M. Roberts, F. C. Fehsenfeld, D. R. Worsnop, M. R. Canagaratna, A. A. P. Pszenny, W. C. Keene, M. Marchewka, S. B. Bertman and T. S. Bates, *J. Geophys. Res. D Atmos.*, 2005, **110**, 1–22.
- 10 J. H. Murillo, J. F. Rojas Marin, S. R. Roman, V. H. Beita Guerrero, D. S. Arias, A. C. Ramos, B. C. Gonzalez and D. G. Baumgardner, *Atmos. Pollut. Res.*, 2013, **4**, 53–63.
- 11 W. Dechapanya, M. Russel and D. T. Allen, *Aerosol Sci. Technol.*, 2004, **38**, 60–67.
- 12 M. Hallquist, J. C. Wenger, U. Baltensperger, Y. Rudich, D. Simpson, M. Claeys, J. Dommen, N. M. Donahue, C. George, a. H. Goldstein, J. F. Hamilton, H. Herrmann, T. Hoffmann, Y. Iinuma, M. Jang, M. E. Jenkin, J. L. Jimenez, a. Kiendler-Scharr, W. Maenhaut, G. McFiggans, T. F. Mentel, a. Monod, a. S. H. Prévôt, J. H. Seinfeld, J. D. Surratt, R. Szmigielski and J. Wildt, *Atmos. Chem. Phys.*, 2009, **9**, 5155–5236.
- 13 J. F. Pankow and W. E. Asher, *Atmos. Chem. Phys.*, 2008, **8**, 2773–2796.
- 14 J. H. Kroll and J. H. Seinfeld, *Atmos. Environ.*, 2008, **42**, 3593–3624.
- 15 J. F. Pankow, *Atmos. Environ.*, 2007, **41**, 75–79.
- 16 J. R. Odum, T. Hoffmann, F. Bowman, D. Collins, R. C. Flagan and J. H. Seinfeld, *Environ. Sci. Technol.*, 1996, **30**, 2580–2585.



- 
- 17 J. H. Seinfeld and J. F. Pankow, *Annu. Rev. Phys. Chem.*, 2003, **54**, 121–140.
- 18 J. F. Pankow, *Atmos. Environ.*, 2003, **37**, 3323–3333.
- 19 M. Kalberer, D. Paulsen, M. Sax, M. Steinbacher, J. Dommen, A. S. H. Prevot, R. Fisseha, E. Weingartner, V. Frankevich, R. Zenobi and U. Baltensperger, *Science* (80-. ), 2004, **303**, 1659–1662.
- 20 M. Kalberer, M. Sax and V. Samburova, *Environ. Sci. Technol.*, 2006, **40**, 5917–5922.
- 21 W. A. Hall and M. V. Johnston, *Aerosol Sci. Technol.*, 2011, **45**, 37–45.
- 22 K. J. Heaton, R. L. Sleighter, P. G. Hatcher, W. A. Hall IV and M. V. Johnston, *Environ. Sci. Technol.*, 2009, **43**, 7797–7802.
- 23 K. J. Heaton, M. A. Dreyfus, S. Wang and M. V Johnston, *Environ. Sci. Technol.*, 2007, **41**, 6129–36.
- 24 T. Jokinen, T. Berndt, R. Makkonen, V.-M. Kerminen, H. Junninen, P. Paasonen, F. Stratmann, H. Herrmann, A. B. Guenther, D. R. Worsnop, M. Kulmala, M. Ehn and M. Sipilä, *Proc. Natl. Acad. Sci.*, 2015, **112**, 7123–7128.
- 25 M. Ehn, J. A. Thornton, E. Kleist, M. Sipilä, H. Junninen, I. Pullinen, M. Springer, F. Rubach, R. Tillmann, B. Lee, F. Lopez-Hilfiker, S. Andres, I.-H. Acir, M. Rissanen, T. Jokinen, S. Schobesberger, J. Kangasluoma, J. Kontkanen, T. Nieminen, T. Kurtén, L. B. Nielsen, S. Jørgensen, H. G. Kjaergaard, M. Canagaratna, M. D. Maso, T. Berndt, T. Petäjä, A. Wahner, V.-M. Kerminen, M. Kulmala, D. R. Worsnop, J. Wildt and T. F. Mentel, *Nature*, 2014, **506**, 476–479.
- 26 J. Tröstl, W. K. Chuang, H. Gordon, M. Heinritzi, C. Yan, U. Molteni, L. Ahlm, C. Frege, F. Bianchi, R. Wagner, M. Simon, K. Lehtipalo, C. Williamson, J. S. Craven, J. Duplissy, A. Adamov, J. Almeida, A.-K. Bernhammer, M. Breitenlechner, S. Brilke, A. Dias, S. Ehrhart, R. C. Flagan, A. Franchin, C. Fuchs, R. Guida, M. Gysel, A. Hansel, C. R. Hoyle, T. Jokinen, H. Junninen, J. Kangasluoma, H. Keskinen, J. Kim, M. Krapf, A. Kürten, A. Laaksonen, M. Lawler, M. Leiminger, S. Mathot, O. Möhler, T. Nieminen, A. Onnela, T. Petäjä, F. M. Piel, P. Miettinen, M. P. Rissanen, L. Rondo, N. Sarnela, S. Schobesberger,

- 
- K. Sengupta, M. Sipilä, J. N. Smith, G. Steiner, A. Tomè, A. Virtanen, A. C. Wagner, E. Weingartner, D. Wimmer, P. M. Winkler, P. Ye, K. S. Carslaw, J. Curtius, J. Dommen, J. Kirkby, M. Kulmala, I. Riipinen, D. R. Worsnop, N. M. Donahue and U. Baltensperger, *Nature*, 2016, **533**, 527–531.
- 27 M. Ehn, E. Kleist, H. Junninen, T. Petäjä, G. Lönn, S. Schobesberger, M. Dal Maso, A. Trimborn, M. Kulmala, D. R. Worsnop, A. Wahner, J. Wildt and T. F. Mentel, *Atmos. Chem. Phys.*, 2012, **12**, 5113–5127.
- 28 L. Vereecken and J. S. Francisco, *Chem. Soc. Rev.*, 2012, **41**, 6217–6708.
- 29 M. Kanakidou, J. H. Seinfeld, S. N. Pandis, I. Barnes, F. J. Dentener, M. C. Facchini, R. Van Dingenen, B. Ervens, A. Nenes, C. J. Nielsen, E. Swietlicki, J. P. Putaud, Y. Balkanski, S. Fuzzi, J. Horth, G. K. Moortgat, R. Winterhalter, C. E. L. Myhre, K. Tsigaridis, E. Vignati, E. G. Stephanou and J. Wilson, *Atmos. Chem. Phys.*, 2005, **5**, 1053–1123.
- 30 P. J. Ziemann and R. Atkinson, *Chem. Soc. Rev.*, 2012, **41**, 6582.
- 31 A. Miyoshi, S. Hatakeyama and N. Washida, *J. Geophys. Res.*, 1994, **99**, 18779.
- 32 B. Bonn, R. von Kuhlmann and M. G. Lawrence, *Geophys. Res. Lett.*, 2004, **31**, 1–4.
- 33 D. Johnson, M. E. Jenkin, K. Wirtz and M. Martin-Reviejo, *Environ. Chem.*, 2005, **2**, 35–48.
- 34 M. Camredon, B. Aumont, J. Lee-Taylor and S. Madronich, *Atmos. Chem. Phys.*, 2007, **7**, 5599–5610.
- 35 R. Criegee, *Angew. Chem, Int. Ed. Engl.*, 1975, **14**, 745–752.
- 36 M. Olzmann, E. Kraka, D. Cremer, R. Gutbrod and S. Andersson, *J. Phys. Chem. A*, 1997, **101**, 9421–9429.
- 37 G. Vayner, S. V. Addepalli, K. Song and W. L. Hase, *J. Chem. Phys.*, 2006, **125**.
- 38 C. A. Taatjes, G. Meloni, T. M. Selby, A. J. D. L. Osborn, C. J. Percival, D. E. Shallcross and A. J. Trevitt, *J. Am. Chem. Soc. Commun.*, 2008, 11883–11885.

- 39 C. Womack, M.-A. Martin-Drumel, G. B. Brown, R. W. Field and M. C. McCarthy, *Sci. Adv.*, 2015, **1**, 1–6.
- 40 C. A. Taatjes, O. Welz, A. J. Eskola, J. D. Savee, D. L. Osborn, E. P. F. Lee, J. M. Dyke, D. W. K. Mok, D. E. Shallcross and C. J. Percival, *Phys. Chem. Chem. Phys.*, 2012, **14**, 10391.
- 41 A. J. A. J. Eskola, D. Wojcik-Pastuszka, E. Ratajczak and R. S. R. S. Timonen, *Phys. Chem. Chem. Phys.*, 2006, **8**, 1416–1424.
- 42 W. L. Ting, C. H. Chang, Y. F. Lee, H. Matsui, Y. P. Lee and J. J. M. Lin, *J. Chem. Phys.*, 2014, **141**.
- 43 J. G. Calvert and W. R. Stockwell, *Environ. Sci. Technol.*, 1984, **17**, 428–443.
- 44 C. A. Taatjes, D. E. Shallcross and C. J. Percival, *Phys. Chem. Chem. Phys.*, 2014, **16**, 1704.
- 45 C. A. Taatjes, O. Welz, A. J. Eskola, J. D. Savee, A. M. Scheer, D. E. Shallcross, B. Rotavera, E. P. F. Lee, J. M. Dyke, D. K. W. Mok, D. L. Osborn and C. J. Percival, *Science (80-. )*, 2013, **340**, 177–180.
- 46 O. Welz, J. D. Savee, D. L. Osborn, S. S. Vasu, C. J. Percival, D. E. Shallcross and C. a. Taatjes, *Science (80-. )*, 2012, **335**, 204–207.
- 47 M. T. Nguyen, T. L. Nguyen, V. T. Ngan and H. M. T. Nguyen, *Chem. Phys. Lett.*, 2007, **448**, 183–188.
- 48 D. Cremer, J. Gauss, E. Kraka, J. F. Stanton and R. J. Bartlett, *Chem. Phys. Lett.*, 1993, **209**, 547–556.
- 49 K. E. Leather, M. R. McGillen, M. C. Cooke, S. R. Utembe, A. T. Archibald, M. E. Jenkin, R. G. Derwent, D. E. Shallcross and C. J. Percival, *Atmos. Chem. Phys.*, 2012, **12**, 469–479.
- 50 L. Sheps, B. Rotavera, A. J. Eskola, D. L. Osborn, C. A. Taatjes, K. Au, D. E. Shallcross, M. A. H. Khan and C. Percival, *Phys. Chem. Chem. Phys.*, 2017, **19**, 21970–21979.

- 
- 51 Y. Ma, R. A. Porter, D. Chappell, A. T. Russell and G. Marston, *Phys. Chem. Chem. Phys.*, 2009, **11**, 4184–4197.
- 52 C. A. Taatjes, O. Welz, A. J. Eskola, J. D. Savee, A. M. Scheer, D. E. Shallcross, B. Rotavera, E. P. F. Lee, J. M. Dyke, D. K. W. Mok, D. L. Osborn and C. J. Percival, *Science (80-. )*, 2013, **340**, 177–180.
- 53 J. M. Beames, F. Liu, L. Lu and M. I. Lester, *J. Chem. Phys.*, 2013, **138**.
- 54 J. M. Beames, F. Liu, L. Lu and M. I. Lester, *J. Am. Chem. Soc.*, 2012, **134**, 20045–20048.
- 55 Y. Su, Y. Huang, H. A. Witek and Y. Lee, *Science (80-. )*, 2013, **174**, 174–177.
- 56 J. Ahrens, P. T. M. Carlsson, N. Hertl, M. Olzmann, M. Pfeifle, J. L. Wolf and T. Zeuch, *Angew. Chemie - Int. Ed.*, 2014, **53**, 715–719.
- 57 D. W. Dockery, C. A. Pope III, X. Xu, J. D. Spengler, J. H. Ware, M. E. Fay, B. G. Ferris and F. E. Speizer, *N. Engl. J. Med.*, 1993, **329**, 1753.
- 58 R. D. Brook, B. Franklin, W. Cascio, Y. Hong, G. Howard, M. Lipsett, R. Luepker, M. Mittleman, J. Samet, S. C. Smith and I. Tager, *Am. Hear. Assoc. Sci. Statement*, 2004, **109**, 2655–2671.
- 59 B. Brunekreef and S. T. Holgate, *Lancet*, 2002, **360**, 1233–1242.
- 60 J. E. Hart, X. Liao, B. Hong, R. C. Puett, J. D. Yanosky, H. Suh, M.-A. Kioumourtzoglou, D. Spiegelman and F. Laden, *Environ. Heal.*, 2015, **14**, 38.
- 61 F. J. Kelly, *Occup. Environ. Med.*, 2003, **60**, 612–616.
- 62 F. J. Kelly and J. C. Fussell, *Atmos. Environ.*, 2012, **60**, 504–526.
- 63 L. Küenzi, P. Mertes, S. Schneider, N. Jeannet, C. Menzi, J. Dommen, U. Baltensperger, A. S. H. S. H. Prévôt, M. Salathe, M. Kalberer, M. Geiser, L. Küenzi, P. Mertes, S. Schneider, N. Jeannet, C. Menzi, J. Dommen, U. Baltensperger, A. S. H. Prévôt, M. Salathe, M. Kalberer, M. Geiser, L. Küenzi, P. Mertes, S. Schneider, N. Jeannet, C. Menzi, J. Dommen, U. Baltensperger, A. S. H. S. H. Prévôt, M. Salathe, M. Kalberer and M. Geiser, *Atmos. Environ.*, 2013,

- 68**, 143–150.
- 64 F. Laden, J. Schwartz, F. E. Speizer and D. W. Dockery, *Am. J. Respir. Crit. Care Med.*, 2006, **173**, 667–672.
- 65 J. Lepeule, F. Laden, D. Dockery and J. Schwartz, *Environ. Health Perspect.*, 2012, **120**, 965–970.
- 66 R. C. Puett, J. E. Hart, J. D. Yanosky, D. Spiegelman, M. Wang, J. A. Fisher, B. Hong and F. Laden, *Environ. Health Perspect.*, 2014, **122**, 926–932.
- 67 A. A. Chew and R. Atkinson, *J. Geophys. Res.*, 1996, **101**, 649–653.
- 68 M. L. Bell and D. L. Davis, *Environ. Health Perspect.*, 2001, **109**, 389–394.
- 69 G. Oberdörster, E. Oberdörster and J. Oberdörster, *Environ. Health Perspect.*, 2005, **113**, 823–839.
- 70 M. Geiser, B. Rothen-Rutishauser, N. Kapp, S. Schürch, W. Kreyling, H. Schulz, M. Semmler, V. Im Hof, J. Heyder and P. Gehr, *Environ. Health Perspect.*, 2005, **113**, 1555–1560.
- 71 P. J. A. Borm, F. Kelly, N. Kunzli, R. P. F. Schins and K. Donaldson, *Occup. Environ. Med.*, 2006, **64**, 73–74.
- 72 K. Donaldson, V. Stone, P. J. A. Borm, L. A. Jimenez, P. S. Gilmour, R. P. F. Schins, A. M. Knaapen, I. Rahman, S. P. Faux, D. M. Brown and W. MacNee, *Free Radic. Biol. Med.*, 2003, **34**, 1369–1382.
- 73 L. A. Morio, K. A. Hooper, J. Brittingham, T. H. Li, R. E. Gordon, B. J. Turpin and D. L. Laskin, *Toxicol Appl Pharmacol*, 2001, **177**, 188–199.
- 74 W. A. Pryor and D. F. Church, *Free Radic. Bio. Med.*, 1991, **11**, 41–46.
- 75 S. Stevanovic, B. Miljevic, N. C. Surawski, K. E. Fairfull-Smith, S. E. Bottle, R. Brown and Z. D. Ristovski, *Environ. Sci. Technol.*, 2013, **47**, 7655–7662.
- 76 G. Oberdörster, *Int. Arch. Occup. Environ. Health*, 2001, **74**, 1–8.
- 77 M. Steenhof, I. Gosens, M. Strak, K. J. Godri, G. Hoek, F. R. Cassee, I. S. Mudway,

- 
- F. J. Kelly, R. M. Harrison, E. Lebret, B. Brunekreef, N. A. Janssen and R. H. Pieters, *Part. Fibre Toxicol.*, 2011, **8**, 26.
- 78 H. Tong, A. M. Arangio, P. S. J. Lakey, T. Berkemeier, F. Liu, C. J. Kampf, W. H. Brune, U. Poschl and M. Shiraiwa, *Atmos. Chem. Phys.*, 2016, **16**, 1761–1771.
- 79 A. K. Cho, C. Sioutas, A. H. Miguel, Y. Kumagai, D. A. Schmitz, M. Singh, A. Eiguren-Fernandez and J. R. Froines, *Environ. Res.*, 2005, **99**, 40–47.
- 80 L. E. King and R. J. Weber, *Atmos. Meas. Tech.*, 2013, **6**, 1647–1658.
- 81 I. S. Mudway, N. Stenfors, S. T. Duggan, H. Roxborough, H. Zielinski, S. L. Marklund, A. Blomberg, A. J. Frew, T. Sandstrom and F. J. Kelly, *Arch. Biochem. Biophys.*, 2004, **423**, 200–212.
- 82 T. M. Shi, R. P. F. Schins, A. M. Knaapen, T. Kuhlbusch, M. Pitz, J. Heinrich and P. J. A. Borm, *J. Environ. Monit.*, 2003, **5**, 550–556.
- 83 P. K. Hopke, Y. Wang, L. Sun, D. C. Chalupa and M. J. Utell, *J. Toxicol.*, 2011, **2011**.
- 84 S. Stevanovic, B. Miljevic, G. K. Eaglesham, S. E. Bottle, Z. D. Ristovski and K. E. Fairfull-Smith, *European J. Org. Chem.*, 2012, 5908–5912.
- 85 F. P. H. H. Wragg, S. J. Fuller, R. Freshwater, D. C. Green, F. J. Kelly and M. Kalberer, *Atmos. Meas. Tech.*, 2016, **9**, 4891–4900.
- 86 D. Gao, T. Fang, V. Verma, L. Zeng and R. J. Weber, *Atmos. Meas. Tech.*, 2017, **10**, 2821–2835.
- 87 Y. Sameenoi, K. Koehler, J. Shapiro, K. Boonsong, Y. Sun, J. Collett, J. Volckens and C. S. Henry, *J. Am. Chem. Soc.*, 2012, **134**, 10562–10568.
- 88 Y. Sameenoi, P. Panymeesamer, N. Supalakorn, K. Koehler, O. Chailapakul, C. S. Henry and J. Volckens, *Environ. Sci. Technol.*, 2013, **47**, 932–940.
- 89 J. G. Charrier and C. Anastasio, *Natl. Inst. Heal. Public Access*, 2013, **80**, 631–637.
- 90 S. J. Fuller, F. P. H. Wragg, J. Nutter and M. Kalberer, *Atmos. Environ.*, 2014, **92**,

- 97–103.
- 91 G. I. Berglund, G. H. Carlsson, A. T. Smith, H. Szöke, A. Henriksen and J. Hajdu, *Nature*, 2002, **417**, 463–468.
- 92 C. F. Chignell and R. H. Sik, *Free Radic. Biol. Med.*, 2003, **34**, 1029–1034.
- 93 C. P. LeBel, H. Ischiropoulos and S. C. Bondy, *Chem. Res. Toxicol.*, 1992, **5**, 227–231.
- 94 P. J. Gallimore, B. M. Mahon, F. P. H. Wragg, S. J. Fuller, C. Giorio, I. Kourtchev and M. Kalberer, *Atmos. Chem. Phys. Discuss.*, 2017, **17**, 9853–9868.
- 95 B. Miljevic, K. E. Fairfull-Smith, S. E. Bottle and Z. D. Ristovski, *Atmos. Environ.*, 2010, **44**, 2224–2230.
- 96 F. Hedayat, S. Stevanovic, A. Milic, B. Miljevic, M. N. Nabi, A. Zare, S. E. Bottle, R. J. Brown and Z. D. Ristovski, *Sci. Total Environ.*, 2016, **545–546**, 381–388.
- 97 F. Hedayat, S. Stevanovic, A. Milic, B. Miljevic, M. N. Nabi, A. Zare, S. E. Bottle, R. J. Brown and Z. D. Ristovski, *Chem. Ind. Chem. Eng. Q.*, 2012, **18**, 653–659.
- 98 K. J. Godri, D. C. Green, G. W. Fuller, M. Dall’osto, D. C. Beddows, F. J. Kelly, R. M. Harrison and I. S. Mudway, *Environ. Sci. Technol.*, 2010, **44**, 8295–8301.
- 99 N. A. H. Janssen, A. Yang, M. Strak, M. Steenhof, B. Hellack, M. E. Gerlofs-Nijland, T. Kuhlbusch, F. Kelly, R. Harrison, B. Brunekreef, G. Hoek and F. Cassee, *Sci. Total Environ.*, 2014, **472**, 572–581.
- 100 P. J. Gallimore and M. Kalberer, *Environ. Sci. Technol.*, 2013, **47**, 7324–7331.
- 101 E. G. Janzen, *Acc. Chem. Res.*, 1971, **4**, 31–40.
- 102 G. R. Buettner, *Free Radic. Bio. Med.*, 1987, **3**, 259–303.
- 103 O. M. Lardinois, K. B. Tomer, R. P. Mason and L. J. Deterding, *Biochemistry*, 2008, **47**, 10440–10448.
- 104 B. Li, N. V. Blough and P. L. Gutierrez, *Free Radic. Biol. Med.*, 2000, **29**, 548–556.

- 
- 105 E. G. Janzen, H. J. Stronks, C. M. Dubose, J. Lee Poyer and B. McCay, *Environ. Health Perspect.*, 1985, **64**, 151–170.
- 106 C. Simões, P. Domingues and M. R. M. Domingues, *Rapid Commun. Mass Spectrom.*, 2012, **26**, 931–939.
- 107 Biospin Bruker Manual:, *EPR Detection of the Superoxide Free Radical with the Nitron Spin Traps DMPO and BMPO*, .
- 108 Z.-Y. Bian, X.-Q. Guo, Y.-B. Zhao and J.-O. Du, *Anal. Sci.*, 2005, **21**, 553–9.
- 109 S. Hauck, Y. Lorat, F. Leinisch and W. E. Trommer, *Appl. Magn. Reson.*, 2009, **36**, 133–147.
- 110 M. Mojović, M. Vuletić and G. G. Bačić, *Ann. N. Y. Acad. Sci.*, 2005, **1048**, 471–475.
- 111 H. M. Swartz, N. Khan, J. Buckey, R. Comi, L. Gould, O. Grinberg, A. Hartford, H. Hopf, H. Hou, E. Hug, A. Iwasaki, P. Lesniewski, I. Salikhov and T. Walczak, *NMR Biomed.*, 2004, **17**, 335–351.
- 112 F. A. Villamena, A. Rockenbauer, J. Gallucci, M. Velayutham, C. M. Hadad and J. L. Zweier, *J. Org. Chem.*, 2004, **69**, 7994–8004.
- 113 A. Samuni, A. Carmichael, A. Russo, J. B. Mithcell and P. Riesz, *Proc. Natl. Acad. Sci.*, 1986, **83**, 7593–7597.
- 114 H. A. O. Hill and P. J. Thornalley, *Inorganica Chim. Acta*, 1982, **67**, 35–36.
- 115 Q. Guo, S. Y. Qian and R. P. Mason, *J. Am. Soc. Mass Spectrom.*, 2003, **14**, 862–871.
- 116 T. S. Shoji, L. I. Linxiang, Y. A. Be, M. O. Gata, Y. I. Shimoto, R. G. Onda, T. M. Ashino, M. M. Ochizuki, M. U. Emoto and N. M. Iyata, *Anal. Sci.*, 2007, **23**, 219–221.
- 117 E. Marchesi, C. Rota, Y. C. Fann, C. F. Chignell and R. P. Mason, *Free Radic. Biol. Med.*, 1999, **26**, 148–161.
- 118 E. Finkelstein, G. M. Rosen and E. J. Rauckman, *Arch. Biochem. Biophys.*, 1980,



- 200**, 1–16.
- 119 R. P. Mason, P. M. Hanna, M. J. Burkitt and M. B. Kadiiska, *Environ. Health Perspect.*, 1994, **102**, 33–36.
- 120 J. Pavlovic and P. K. Hopke, *J. Atmos. Chem.*, 2011, **66**, 137–155.
- 121 A. Reis, M. R. Domingues, F. M. L. Amado, A. J. V Ferrer-Correia, P. Domingues and M. Rosa, *J. Am. Soc. Mass Spectrom.*, 2003, **14**, 1250–1261.
- 122 K. E. Fairfull-Smith and S. E. Bottle, *European J. Org. Chem.*, 2008, **32**, 5391–5400.
- 123 M. M. Rahman, A. M. Pourkhesalian, M. I. Jahirul, S. Stevanovic, P. X. Pham, H. Wang, A. R. Masri, R. J. Brown and Z. D. Ristovski, *Fuel*, 2014, **134**, 201–208.
- 124 M. M. Rahman, S. Stevanovic, R. J. Brown and Z. Ristovski, *Procedia Eng.*, 2013, **56**, 381–386.
- 125 R. Green, *Int. J. Photoenergy*, 1973, **1**, 173–176.
- 126 L. . Shevdova, A. S. Tatikolov, E. Borisevich, A. P. Kokorin and V. A. Kuzmin, *Inst. Chem. Phys.*, 1982, 475–478.
- 127 T. Kondo, L. J. L. J. Kirschenbaum, H. Kim and P. Riesz, *J. Phys. Chem.*, 1993, **97**, 522–527.
- 128 B. Nozière, M. Kalberer, M. Claeys, J. Allan, B. D’Anna, S. Decesari, E. Finessi, M. Glasius, I. Grgić, J. F. Hamilton, T. Hoffmann, Y. Iinuma, M. Jaoui, A. Kahnt, C. J. Kampf, I. Kourtchev, W. Maenhaut, N. Marsden, S. Saarikoski, J. Schnelle-Kreis, J. D. Surratt, S. Szidat, R. Szmigielski and A. Wisthaler, *Chem. Rev.*, 2015, **115**, 3919–3983.
- 129 I. Kourtchev, S. Fuller, J. Aalto, T. M. Ruuskanen, M. W. McLeod, W. Maenhaut, R. Jones, M. Kulmala and M. Kalberer, *Environ. Sci. Technol.*, 2013, **47**, 4069–4079.
- 130 S. J. Gaskell, *J. Mass Spectrom.*, 1997, **32**, 677–688.
- 131 N. B. Cech and C. G. Enke, *Mass Spectrom. Rev.*, 2001, **20**, 362–387.

- 
- 132 I. Kourtchev, S. J. Fuller, C. Giorio, R. M. Healy, E. Wilson, I. O'Connor, J. C. Wenger, M. McLeod, J. Aalto, T. M. Ruuskanen, W. Maenhaut, R. Jones, D. S. Venables, J. R. Sodeau, M. Kulmala and M. Kalberer, *Atmos. Chem. Phys.*, 2014, **14**, 2155–2167.
- 133 A. Makarov, E. Denisov, O. Lange and S. Horning, *J. Am. Soc. Mass Spectrom.*, 2006, **17**, 977–982.
- 134 Q. Hu, R. J. Noll, H. Li, A. Makarov, M. Hardman and R. G. Cooks, *J. Mass Spectrom.*, 2005, **40**, 430–443.
- 135 A. Reinhardt, C. Emmenegger, B. Gerrits, C. Panse, J. Dommen, U. Baltensperger, R. Zenobi and M. Kalberer, *Anal. Chem.*, 2007, **79**, 4074–4082.
- 136 M. Graus, M. Miller and A. Hansel, *J. Am. Soc. Mass Spectrom.*, 2010, **21**, 1037–1044.
- 137 A. Hansel, A. Jordan, R. Holzinger, P. Prazeller, W. Vogel and W. Lindinger, *Int. J. Mass Spectrom. Ion Process.*, 1995, **150**, 609–619.
- 138 W. Lindinger and A. Jordan, *Chem. Soc. Rev.*, 1998, **27**, 347.
- 139 E. O. Knutson and K. T. Whitby, *J. Aerosol Sci.*, 1975, **6**, 443–451.
- 140 A. Wiedensohler, *J. Aerosol Sci.*, 1988, **19**, 387–389.
- 141 J. R. Lakowicz, *Principles of Fluorescence Spectroscopy Third Edition*, 2006.
- 142 S. J. Fuller, *Time Resolved Measurements of Organic Aerosol Composition, PhD Thesis*, 2013.
- 143 R. L. I. Mauldin, T. Berndt, M. Sipila, P. Paasonen, T. Petaja, S. Kim, T. Kurten, F. Stratmann, V.-M. Kerminen and M. Kulmala, *Nat. Res. Lett.*, 2012, **488**, 193–197.
- 144 L. Vereecken, *Science*, 2013, **340**, 154–155.
- 145 D. L. Osborn and C. A. Taatjes, *Int. Rev. Phys. Chem.*, 2015, **34**, 309–360.
- 146 J. Kalinowski, P. Heinonen, I. Kilpela and M. Ra, *J. Phys. Chem. A*, 2015, 2318–

- 2325.
- 147 E. Miliordos, K. Ruedenberg and S. S. Xantheas, *Angew. Chemie - Int. Ed.*, 2013, **52**, 5736–5739.
- 148 J. Kalinowski, P. Heinonen, I. Kilpeläinen, M. Räsänen and R. B. Gerber, *J. Phys. Chem. A*, 2015, **119**, 2318–2325.
- 149 W. Sander, *Angew. Chemie - Int. Ed.*, 2014, **53**, 362–364.
- 150 M. Boy, D. Mogensen, S. Smolander, L. Zhou, T. Nieminen, P. Paasonen, C. Plass-Dulmer, N. Sipila, T. Petaja, L. Mauldin, H. Berresheim and M. Kulmala, *Atmos. Chem. Phys.*, 2013, **13**, 3865–3879.
- 151 R. M. Harrison, J. Yin, R. M. Tilling, X. Cai, P. W. Seakins, J. R. Hopkins, D. L. Lansley, A. C. Lewis, M. C. Hunter, D. E. Heard, L. J. Carpenter, D. J. Creasey, J. D. Lee, M. J. Pilling, N. Carslaw, K. M. Emmerson, A. Redington, R. G. Derwent, D. Ryall, G. Mills and S. A. Penkett, *Sci. Total Environ.*, 2006, **360**, 5–25.
- 152 K. M. Emmerson, N. Carslaw, L. J. Carpenter, D. E. Heard, J. D. Lee and M. J. Pilling, *J. Atmos. Chem.*, 2005, **52**, 143–164.
- 153 K. M. Emmerson, N. Carslaw and M. J. Pilling, *J. Atmos. Chem.*, 2005, **52**, 165–183.
- 154 K. M. Emmerson, N. Carslaw, D. C. Carslaw, J. D. Lee, G. McFiggans, W. J. Bloss, T. Gravestock, D. E. Heard, J. Hopkins, T. Ingham, M. J. Pilling, S. C. Smith, M. Jacob and P. S. Monks, *Atmos. Chem. Phys.*, 2007, **7**, 167–181.
- 155 W. A. Pryor, D. G. Prier and D. F. Church, *J. Am. Chem. Soc.*, 1983, **105**, 2883–2888.
- 156 W. A. Pryor, D. G. Prier and D. F. Church, *Environ. Health Perspect.*, 1983, **Vol. 47**, 345–355.
- 157 W. A. Pryor, *Free Radic. Biol. Med.*, 1994, **17**, 451–465.
- 158 A. Samuni, A. J. Carmichael, A. Russo, J. B. Mitchell and P. Riesz, *Biochemistry*, 1986, **83**, 7593–7597.

- 
- 159 R. Suarez-Bertoa, F. Saliu, M. Bruschi and B. Rindone, *Tetrahedron*, 2012, **68**, 8267–8275.
- 160 K. Matsumoto, M. Nyui, M. Kamibayashi, T. Ozawa, I. Nakanishi and K. Anzai, *J. Clin. Biochem. Nutr.*, 2011, **50**, 40–46.
- 161 S. A. Gordon, A. R. Chughtai and D. M. Smith, *Am. Lab.*, 2000, **32**, 12–13.
- 162 K. Rakness, G. Gordon, B. Langlais, W. Masschelein, N. Matsumoto, Y. Richard, C. M. Robson and I. Somiya, *Ozone Sci. Eng.*, 1996, **18**, 209–229.
- 163 M. Piotto, M. Bourdonneau, K. Elbayed, J.-M. Wieruszeski and G. Lippens, *Magn. Reson. Chem.*, 2006, **44**, 943–947.
- 164 S. G. Hyberts, K. Takeuchi and G. Wagner, *J. Am. Chem. Soc.*, 2010, **132**, 2145–2147.
- 165 D. R. Duling, *J. Magn. Reson. B*, 1994, 104, 105–110.
- 166 J. Zhao and R. Zhang, *Atmos. Environ.*, 2004, **38**, 2177–2185.
- 167 M. E. Jenkin, D. E. Shallcross and J. N. Harvey, *Atmos. Environ.*, 2000, **34**, 2837–2850.
- 168 G. R. Buettner, *Free Radic. Biol. Med.*, 1987, **3**, 259–303.
- 169 C. Giorio, S. J. Campbell, M. Bruschi, F. Tampieri, A. Barbon, A. Toffoletti, A. Tapparo, C. Paijens, A. J. Wedlake, P. Grice, D. J. Howe and M. Kalberer, *J. Am. Chem. Soc.*, 2017, **139**, 3999–4008.
- 170 S. M. M. Saunders, M. E. E. Jenkin, R. G. G. Derwent, M. J. J. Pilling, S. M. M. Saunders, V. Wagner, M. J. J. Pilling, M. E. E. Jenkin, R. G. G. Derwent and M. J. J. Pilling, *Atmos. Chem. Phys.*, 2003, **3**, 161–180.
- 171 B. Chuong, J. Zhang and N. M. Donahue, *J. Am. Chem. Soc.*, 2004, **126**, 12363–12373.
- 172 A. R. Rickard, D. Johnson, C. D. McGill and G. Marston, *J. Phys. Chem. A*, 1999, **103**, 7656–7664.

- 173 S. E. Paulson, M. Chung, A. D. Sen and G. Orzechowska, *J. Geophys. Res.*, 1998, **103**, 533–539.
- 174 J. Baker, S. M. Aschmann, J. Arey and R. Atkinson, *Int. J. Chem. Kinet.*, 2002, **34**, 73–85.
- 175 W. Adam, K. Briviba, F. Duschek, D. Golsch, W. Kiefer and H. Sies, *J. Chem. Soc. Chem. Commun.*, 1995, 1831–1832.
- 176 F. Liu, Y. Fang, M. Kumar, W. H. Thompson and M. I. Lester, *Phys. Chem. Chem. Phys.*, 2015, **17**, 20490–20494.
- 177 C. Giorio, S. Campbell, M. Bruschi, A. Archibald and M. Kalberer, *Faraday Discuss.*, 2017, **19**, 10200.
- 178 IUPAC Task Group on Atmospheric Chemical Kinetic Data Evaluation – Data Sheet Ox \_ VOC20, 2013, vol. 1.
- 179 O. Horie, C. Schäfer and G. K. Moortgat, *Int. J. Chem. Kinet.*, 1999, **31**, 261–269.
- 180 R. Chhantyal-Pun, M. McGillen, J. Beames, A. Khan, C. Percival, D. Shallcross and A. Orr-Ewing, *Angew. Chemie Int. Ed.*, 2017, 9044–9047.
- 181 O. Welz, A. J. Eskola, L. Sheps, B. Rotavera, J. D. Savee, A. M. Scheer, D. L. Osborn, D. Lowe, A. Murray Booth, P. Xiao, M. A. H. Khan, C. J. Percival, D. E. Shallcross and C. A. Taatjes, *Angew. Chemie - Int. Ed.*, 2014, **53**, 4547–4550.
- 182 L. Vereecken, H. Harder and A. Novelli, *Phys. Chem. Chem. Phys.*, 2012, **14**, 14682–14695.
- 183 J. Clayden, N. Greeves, S. Warren and P. Wothers *Organic Chemistry (1st ed.)*, Oxford University Press, 2001.
- 184 O. Horie and G. K. Moortgat, *Acc. Chem. Res.*, 1998, **31**, 387–396.
- 185 G. T. Drozd and N. M. Donahue, *J. Phys. Chem. A*, 2011, **115**, 4381–4387.
- 186 T. F. Mentel, M. Springer, M. Ehn, E. Kleist, I. Pullinen, T. Kurtén, M. Rissanen, A. Wahner and J. Wildt, *Atmos. Chem. Phys.*, 2015, **15**, 6745–6765.

- 
- 187 D. Stone, M. Blitz, L. Daubney, N. U. M. Howes and P. Seakins, *Phys. Chem. Chem. Phys.*, 2014, **16**, 1139–1149.
- 188 A. B. Ryzhkov and P. A. Ariya, *Chem. Phys. Lett.*, 2003, **367**, 423–429.
- 189 A. B. Ryzhkov and P. A. Ariya, *Chem. Phys. Lett.*, 2006, **419**, 479–485.
- 190 T. Berndt, J. Voigtländer, F. Stratmann, H. Junninen, R. L. Mauldin, M. Sipilä, M. Kulmala and H. Herrmann, *Phys. Chem. Chem. Phys.*, 2014, **16**, 19130–6.
- 191 M. J. Newland, A. R. Rickard, M. S. Alam, L. Vereecken, A. Muñoz, M. Ródenas, W. J. Bloss, A. Munoz, M. Rodenas, W. J. Bloss, A. Muñoz, M. Ródenas and W. J. Bloss, *Phys. Chem. Chem. Phys.*, 2015, **17**, 4076–4088.
- 192 M. J. Newland, A. R. Rickard, L. Vereecken, A. Munoz, M. Rodenas and W. J. Bloss, *Atmos. Chem. Phys.*, 2015, **15**, 9521–9536.
- 193 R. Chhantyal-Pun, A. Davey, D. E. Shallcross, C. J. Percival and A. J. Orr-Ewing, *Phys. Chem. Chem. Phys.*, 2015, **17**, 3617–3626.
- 194 T. R. Lewis, M. A. Blitz, D. E. Heard and P. W. Seakins, *Phys Chem Chem Phys*, 2015, **17**, 4859–4863.
- 195 Y. Fang, F. Liu, V. P. Barber, S. J. Klippenstein, A. B. McCoy and M. I. Lester, *J. Chem. Phys.*, 2016, **145**.
- 196 X. Wang and J. M. Bowman, *J. Phys. Chem. Lett.*, 2016, **7**, 3359–3364.
- 197 A. Novelli, L. Vereecken, J. Lelieveld and H. Harder, *Phys. Chem. Chem. Phys.*, 2014, **16**, 19941–19951.
- 198 Z. C. J. Decker, K. Au, L. Vereecken, L. Sheps, Y.-P. Lee, J. J.-M. Lin, M. M. Coggon, L. Zhang, P. Feiner, D. O. Milller, K. M. Skog, J. C. Rivera-Rios, M. Dorris, K. F. Olson, A. Koss, R. J. B. Wild, S. Stephen, A. H. Goldstein, J. A. de Gouw, W. H. Brune, F. N. Keutsch, J. H. Seinfeld and P. O. Wennberg, *Phys. Chem. Chem. Phys.*, 2017, **19**, 8541–8551.
- 199 S. Kim, A. Guenther, B. Lefer, J. Flynn, R. Griffin, A. P. Rutter, L. Gong and B. K. Cevik, *Environ. Sci. Technol.*, 2015, **49**, 3383–3391.

- 
- 200 T. B. Nguyen, G. S. Tyndall, J. D. Crounse, A. P. Teng, K. H. Bates, R. H. Schwantes, M. M. Coggon, L. Zhang, P. Feiner, D. O. Miller, K. M. Skog, J. C. Rivera-Rios, M. Dorris, K. F. Olson, A. Koss, R. J. Wild, S. S. Brown, A. H. Goldstein, J. A. de Gouw, W. H. Brune, F. N. Keutsch, J. H. Seinfeld and P. O. Wennberg, *Phys. Chem. Chem. Phys.*, 2016, **18**, 10241–10254.
- 201 J. M. Anglada, J. González and M. Torrent-Sucarrat, *Phys. Chem. Chem. Phys.*, 2011, **13**, 13034–13045.
- 202 J. M. Anglada and A. Solé, *Phys. Chem. Chem. Phys.*, 2016, **18**, 17698–17712.
- 203 L. Vereecken, A. R. Rickard, M. J. Newland and W. J. Bloss, *Phys. Chem. Chem. Phys.*, 2015, **17**, 23847–23858.
- 204 Y. Rudich, N. M. N. M. Donahue and T. F. T. F. Mentel, *Annu Rev Phys Chem*, 2007, **58**, 321–352.
- 205 J. Liggio and S. M. Li, *J. Geophys. Res. Atmos.*, 2006, **111**, 1–12.
- 206 A. L. A. L. Robinson, N. M. N. M. Donahue, M. K. M. K. Shrivastava, E. A. E. A. Weitkamp, A. M. A. M. Sage, A. P. A. P. Grieshop, T. E. T. E. Lane, J. R. J. R. Pierce and S. N. S. N. Pandis, *Science (80-. )*, 2007, **315**, 1259–1262.
- 207 R. Zhao, E. L. Mungall, A. K. Y. Lee, D. Aljawhary and J. P. D. Abbatt, *Atmos. Chem. Phys.*, 2014, **14**, 9695–9705.
- 208 J. Zahardis and G. A. Petrucci, *Atmos. Chem. Phys. Discuss.*, 2006, **6**, 11093–11179.
- 209 J. Lee, V. Carrascón, P. Gallimore, S. Fuller, A. Björkegren, D. Spring, F. Pope and M. Kalberer, *Phys. Chem. Chem. Phys.*, 2012, **14**, 8023–31.
- 210 Y. Sakamoto, S. Inomata and J. Hirokawa, *J. Phys. Chem. A*, 2013, **117**, 12912–12921.
- 211 R. Winterhalter, F. Herrmann, B. Kanawati, T. L. Nguyen, J. Peeters, L. Vereecken and G. K. Moortgat, *Phys. Chem. Chem. Phys.*, 2009, **11**, 4152.
- 212 B. Miljevic, R. L. Modini, S. E. Bottle and Z. D. Ristovski, *Atmos. Environ.*, 2009,

- 213 F. Dhooghe, C. Amelynck, N. Schoon, E. Debie, P. Bultinck and F. Vanhaecke, *Int. J. Mass Spectrom.*, 2008, **272**, 137–148.
- 214 S. Kim, T. Karl, D. Helmig, R. Daly, R. Rasmussen and A. Guenther, *Atmos. Meas. Tech.*, 2009, **2**, 99–112.
- 215 R. Winterhalter, F. Herrmann, B. Kanawati and L. Nguyen, 2009, 4152–4172.
- 216 D. Grosjean, E. L. Williams, E. Grosjean, J. M. Andino and J. H. Seinfeld, *Environ. Sci. Technol.*, 1993, **27**, 2754–2758.
- 217 A. Calogirou, B. R. Larsen and D. Kotzias, *Atmos. Environ.*, 1999, **33**, 1423–1439.
- 218 M. E. Jenkin, K. P. Wyche, C. J. Evans, T. Carr, P. S. Monks, M. R. Alfarra, M. H. Barley and G. B. Mcfiggans, 2012, 5275–5308.
- 219 M. Jaoui, S. Leungsakul and R. M. Kamens, *J. Atmos. Chem.*, 2003, **45**, 261–287.
- 220 K. Hartonen, J. Parshintsev, V. P. Vilja, H. Tiala, S. Knuuti, C. K. Lai and M. L. Riekkola, *Atmos. Environ.*, 2013, **81**, 330–338.
- 221 N. M. Donahue, K. M. Henry, T. F. Mentel, A. Kiendler-Scharr, C. Spindler, B. Bohn, T. Brauers, H. P. Dorn, H. Fuchs, R. Tillmann, A. Wahner, H. Saathoff, K.-H. Naumann, O. Mohler, T. Leisner, L. Muller, M.-C. Reinnig, T. Hoffmann, K. Salo, M. Hallquist, M. Frosch, M. Bilde, T. Tritscher, P. Barmet, A. P. Praplan, P. F. DeCarlo, J. Dommen, A. S. H. Prevot and U. Baltensperger, *Proc. Natl. Acad. Sci.*, 2012, **109**, 13503–13508.
- 222 M. Sorensen, H. Autrup, P. Moller, O. Hertel, S. S. Jensen, P. Vinzents, L. E. Knudsen and S. Loft, *Mutat. Res. Mutat. Res.*, 2003, **544**, 255–271.
- 223 R. W. Atkinson, H. R. Anderson, J. Sunyer, J. Ayres, M. Baccini, J. M. Vonk, A. Boumghar, F. Forastiere, B. Forsberg, G. Touloumi, J. Schwartz and K. Katsouyanni, *Am. J. Respir. Crit. Care Med.*, 2001, **164**, 1860–1866.
- 224 J. G. Charrier and C. Anastasio, *Atmos. Chem. Phys.*, 2012, **12**, 9321–9333.
- 225 T. Nah, S. H. Kessler, K. E. Daumit, J. H. Kroll, S. R. Leone and K. R. Wilson, *J.*



- Phys. Chem. A*, 2014, **118**, 4106–4119.
- 226 J. D. Smith, J. H. Kroll, C. D. Cappa, D. L. Che, C. L. Liu, M. Ahmed, S. R. Leone, D. R. Worsnop and K. R. Wilson, *Atmos. Chem. Phys.*, 2009, **9**, 3209–3222.
- 227 K. M. Henry and N. M. Donahue, *J. Phys. Chem. A*, 2012, **116**, 5932–5940.
- 228 K. Salo, M. Hallquist, A. M. Jonsson, H. Saathoff, K. H. Naumann, C. Spindler, R. Tillmann, H. Fuchs, B. Bohn, F. Rubach, T. F. Mentel, L. Müller, M. Reinnig, T. Hoffmann and N. M. Donahue, *Atmos. Chem. Phys.*, 2011, **11**, 11055–11067.
- 229 B. Miljevic, *the Application of a Profluorescent Nitroxide Probe To Detect Reactive Oxygen Species Derived From Combustion-Generated Particulate Matter*, PhD, 2010.
- 230 K. S. Suslick, *Science (80-. )*, 1990, **247**, 1439–1445.
- 231 B. Miljevic, F. Hedayat, S. Stevanovic, K. E. Fairfull-Smith, S. E. Bottle and Z. D. Ristovski, *Aerosol Sci. Technol.*, 2014, **48**, 1276–1284.
- 232 L. Baptista, R. Pfeifer, E. C. Da Silva and G. Arbilla, *J. Phys. Chem. A*, 2011, **115**, 10911–10919.
- 233 M. Shiraiwa, M. Ammann, T. Koop and U. Poschl, *Proc. Natl. Acad. Sci.*, 2011, **108**, 11003–11008.
- 234 N. Englert, *Toxicol. Lett.*, 2004, **149**, 235–242.
- 235 C. Andersson, R. Bergström and C. Johansson, *Atmos. Environ.*, 2009, **43**, 3614–3620.
- 236 J. G. Ayres, P. Borm, F. R. Cassee, V. Castranova, K. Donaldson, A. Ghio, R. M. Harrison, R. Hider, F. Kelly, I. M. Kooter, F. Marano, R. L. Maynard, I. Mudway, A. Nel, C. Sioutas, S. Smith, A. Baeza-Squiban, A. Cho, S. Duggan and J. Froines, *Inhal. Toxicol.*, 2008, **20**, 75–99.
- 237 V. Verma, T. Fang, H. Guo, L. King, J. T. Bates, R. E. Peltier, E. Edgerton, A. G. Russell and R. J. Weber, *Atmos. Chem. Phys.*, 2014, **14**, 12915–12930.
- 238 B. Halliwell, *Plant Physiol.*, 2006, **141**, 312–322.

- 
- 239 P. Venkatachari, P. K. Hopke, B. D. Grover and D. J. Eatough, *J. Atmos. Chem.*, 2005, **50**, 49–58.
- 240 A. S. Hasson and S. E. Paulson, *J. Aerosol Sci.*, 2003, **34**, 459–468.
- 241 Y. Kumagai, S. Koide, K. Taguchi, A. Endo, Y. Nakai, T. Yoshikawa and N. Shimojo, *Chem. Res. Toxicol.*, 2002, **15**, 483–489.
- 242 K. J. Godri, R. M. Harrison, T. Evans, T. Baker, C. Dunster, I. S. Mudway and F. J. Kelly, *PLoS One*, 2011, **6**.
- 243 A. P. Bateman, M. L. Walser, Y. Desyaterik, J. Laskin, A. Laskin and S. A. Nizkorodov, *Environ. Sci. Technol.*, 2008, **42**, 7341–7346.
- 244 P. Venkatachari and P. K. Hopke, *J. Aerosol Sci.*, 2008, **39**, 168–174.
- 245 J. C. Deutsch, *Anal. Biochem.*, 1998, **265**, 238–45.
- 246 H. Loertzer, S. Bauer, W. Mörke, P. Fornara and H. J. Brömme, *Transplant. Proc.*, 2006, **38**, 674–678.
- 247 G. Burini, *J. Chromatogr. A*, 2007, **1154**, 97–102.
- 248 M. Takeuchi, S. M. Rahmat Ullah, P. K. Dasgupta, D. R. Collins and A. Williams, *Anal. Chem.*, 2005, **77**, 8031–8040.
- 249 I. Oey, P. Verlinde, M. Hendrickx and A. Van Loey, *Eur. Food Res. Technol.*, 2006, **223**, 71–77.
- 250 R. L. Siefert, S. M. Webb and M. R. Hoffmann, *J. Geophys. Res.*, 1996, **101**, 441–449.
- 251 R. L. Siefert, A. M. Johansen and M. R. Hoffmann, *J. Geophys. Res.*, 1999, **104**, 3511–3526.
- 252 N. Bukowiecki, R. Gehrig, M. Hill, P. Lienemann, C. N. Zwicky, B. Buchmann, E. Weingartner and U. Baltensperger, *Atmos. Environ.*, 2007, **41**, 878–889.
- 253 S. A. Gurgueira, J. Lawrence, B. Coull, G. G. Krishna Murthy and B. González-Flecha, *Environ. Health Perspect.*, 2002, **110**, 749–755.

- 254 J. Xu and R. B. Jordan, *Inorg. Chem.*, 1990, **29**, 2933–2936.
- 255 G. R. Buettner and B. A. Jurkiewicz, *Radiat Res*, 1996, **145**, 532–541.
- 256 K. Sehested, O. L. Rasmussen and H. Fricke, *J. Phys. Chem.*, 1968, **72**, 626–631.
- 257 D. H. Gonzalez, C. K. Cala, Q. Peng and S. E. Paulson, *Environ. Sci. Technol.*, 2017, **51**, 7676–7685.
- 258 J. M. Santana-Casiano, M. González-Dávila and F. J. Millero, *Environ. Sci. Technol.*, 2005, **39**, 2073–2079.
- 259 J. De Laat and T. G. Le, *Environ. Sci. Technol.*, 2005, **39**, 1811–1818.
- 260 B. H. J. Bielski, *Philos. Trans. R. Soc. Lond. B. Biol. Sci.*, 1985, **311**, 473–482.
- 261 B. Nozière, I. Barnes and K.-H. Becker, *J. Geophys. Res. Atmos.*, 1999, **104**, 23645–23656.
- 262 Y. Sun, G. Zhuang, A. Tang, Y. Wang and Z. An, *Environ. Sci. Technol.*, 2006, **40**, 3148–3155.
- 263 V. Martins, M. C. Minguillon, T. Moreno, L. Mendes, E. Konstantions, C. Alves, E. Miguel and X. Querol, *Characterisation of Airborne Particulate Matter in Different European Subway Systems*, 2017.
- 264 P. Pant, Z. Shi, F. D. Pope and R. M. Harrison, *Aerosol Air Qual. Res.*, 2017, **17**, 117–130.
- 265 M. Fujii, A. Rose, D. Waite and T. Omura, *Environ. Sci. Technol.*, 2010, 9337–9342.
- 266 M. M. Taqui Khan and A. E. Martell, *J. Am. Chem. Soc.*, 1967, **89**, 4176–4185.
- 267 S. Pakapongpan, J. P. Mensing, D. Phokharatkul, T. Lomas and A. Tuantranont, *Electrochim. Acta*, 2014, **133**, 294–301.
- 268 J. Huang, Y. Liu, H. Hou and T. You, *Biosens. Bioelectron.*, 2008, **24**, 632–637.
- 269 J. Kulys and E. J. D’Costa, *Anal. Chim. Acta*, 1991, **243**, 173–178.

- 
- 270 R. Ahlrichs, M. Bär, M. Häser, H. Horn and C. Kölmel, *Chem. Phys. Lett.*, 1989, **162**, 165–169.
- 271 A. D. Becke, *Phys. Rev. A*, 1988, **38**, 3098–3100.
- 272 J. P. Perdew, *Phys. Rev. B*, 1986, **33**, 8822–8824.
- 273 A. D. Becke, *J. Chem. Phys.*, 1993, **98**, 5648–5652.
- 274 C. Lee, W. Yang and R. Parr, *Phys. Rev. B*, 1988, **37**, 785–789.
- 275 P. Stephens, F. Devlin, C. Chabalowski and M. Frisch, *J. Phys. Chem.*, 1994, **98**, 11623–11627.
- 276 K. Eichkorn, F. Weigend, O. Treutler and R. Ahlrichs, *Theor. Chem. Acc.*, 1997, **97**, 119–124.
- 277 A. Schäfer, C. Huber and R. Ahlrichs, *J. Chem. Phys.*, 1994, **100**, 5829.
- 278 F. Jensen, *Introduction to computational chemistry*, John Wiley & Sons, Chichester, England, 2007.
- 279 S. F. Boys and F. Bernardi, *Mol. Phys.*, 1970, **19**, 553–566.
- 280 D. Zhang and R. Zhang, *J. Chem. Phys.*, 2005, **122**.
- 281 R. S. Blake, P. S. Monks, A. M. Ellis, R. S. Blake, P. S. Monks and A. M. Ellis, *Chem. Rev.*, 2009, **109**, 861–896.
- 282 T. Su and W. J. Chesnavich, *J. Chem. Phys.*, 1982, **76**, 5183–5185.
- 283 L. Cappellin, F. Biasioli, A. Fabris, E. Schuhfried, C. Soukoulis, T. D. Märk and F. Gasperi, *Int. J. Mass Spectrom.*, 2010, **290**, 60–63.
- 284 R. Gutbrod, E. Kraka, R. N. Schindler and D. Cremer, *J. Am. Chem. Soc.*, 1997, **119**, 7330–7342.
- 285 J. M. Anglada, J. M. Boffil, S. Olivella and A. Sole, *J. Am. Chem. Soc.*, 1996, **118**, 4636–4647.



---

# 9 APPENDICES

APPENDIX 1 – EXTENSIVE NMR ANALYSIS OF CI-PBN ADDUCTS.....	227
APPENDIX 2 – DENSITY FUNCTIONAL THEORY CALCULATIONS.....	239
APPENDIX 3– MATHEMATICA MODEL FOR B-CARYOPHYLLENE MODELLING STUDY ....	247

## APPENDIX 1 – EXTENSIVE NMR ANALYSIS OF CI-PBN ADDUCTS

The NMR characterisation in this section was performed by Steven J. Campbell, and analysed by Steven J. Campbell and Chiara Giorio with the help of Duncan J. Howe and Peter Grice.

NMR characterisation of CI-PBN adduct samples shows a triplet proton centred at ~5.7 ppm and carbon at 105.35 ppm, close to the predicted chemical shift for the -CH (no.4-CI<sub>K</sub>-PBN, Table 9.1) upfield of the N-O for the CI<sub>K</sub>-PBN adduct (blue square in Figure 9.1 and **Figure 9.2**). Conversely, the most distinctive peak for the CI<sub>A</sub>-PBN adduct would be from the quaternary carbon (no.4-CI<sub>A</sub>-PBN) upfield of the N-O correlating with the protons on the terminal methyl group in the HMBC spectrum. This peak may be completely covered by the solvent signal in HMBC-NMR (Figure 9.3).

The same proton (-CH no.4-CI<sub>K</sub>-PBN upfield in the heterocycle) correlates with protons at ~1.6 ppm from the -CH<sub>2</sub> (no.13-CI<sub>K</sub>-PBN) in the COSY spectrum in Figure 9.4, matching the predicted value (Figure 9.1). Those protons (no.13-CI<sub>K</sub>-PBN) correlate with the proton from the -CH (no.14-CI<sub>K</sub>-PBN) in the cyclobutane part (Figure 9.5) and their carbon at 33 ppm (predicted at 29.6ppm) (Figure 9.5). The -CH (no.14-CI<sub>K</sub>-PBN) in the cyclobutane correlates with a carbon at 38 ppm in the HSQC spectrum, close to the predicted value of 31 ppm (Figure 9.5).

In the cyclobutane part, the proton nearest the ketone (no.16-CI<sub>K</sub>-PBN) is the most distinctive, predicted to be at 2.80 and observed at 2.88 ppm. The HSQC gives the <sup>13</sup>C be 54.8 ppm, different from the predicted value of 60.2 ppm Figure 9.6). Looking at the COSY (Figure 9.5) and HSQC (Figure 9.6) spectra, this <sup>1</sup>H at 2.88 (no.16-CI<sub>K</sub>-PBN) couples to a -CH<sub>2</sub> cross peak from 1.92 to 1.8 ppm in the <sup>1</sup>H, 24.23 ppm in the <sup>13</sup>C, close to the predicted value of 23.4 ppm (no.15-CI<sub>K</sub>-PBN).

The protons (no.21-CI<sub>K</sub>-PBN) on the terminal methyl in the ketonic functional group observed at 1.98 ppm (matching the predicted value) correlates with a carbon at 208 ppm in the HMBC spectrum, close to the predicted value of 209.5 ppm (no.20-CI<sub>K</sub>-PBN) (Figure 9.3).

From the HMBC spectrum in Figure 9.7, it appears that two different cyclobutane groups are present, suggesting that both the CI<sub>K</sub>-PBN and CI<sub>A</sub>-PBN adducts may be present. In

---

fact, an aldehyde proton (no.20- $\text{CI}_\text{A}$ -PBN) can be observed in the full  $^1\text{H}$ -NMR spectrum 9.66 ppm in **Figure 9.8**.

The methyl groups in the *t*-butyl attached to the nitrogen; there look to be three different types, one with protons at 0.91 ppm, one at 1.13 ppm and another at 1.14 ppm all correlating to carbons of very similar shifts between 27.5 and 28 ppm (Figure 9.6). The protons at 1.13 ppm and 1.14 ppm show long-range correlations (over 2 bonds) with quaternary carbons at 59.17 ppm and 59.32 ppm. The protons at 0.91 ppm correlate with a quaternary carbon at 59.62 ppm, off the predicted value of 50.4 ppm for  $\text{CI}_\text{K}$ -PBN (no.23) but close to the predicted value of 60.7 for  $\text{CI}_\text{A}$ -PBN (no.21) (Figure 9.7).

Concerning the  $\text{CI}_\text{A}$ -PBN adduct, low intensity signals in the HSQC spectrum can be associated with the  $-\text{CH}_2$  next to the aldehydic functional group (no.19- $\text{CI}_\text{A}$ -PBN, the  $-\text{CH}_2$  in the cyclobutane (no.14- $\text{CI}_\text{A}$ -PBN) and the terminal methyl attached to the quaternary carbon (no.25- $\text{CI}_\text{A}$ -PBN) in the heterocycle (Figure 9.6).

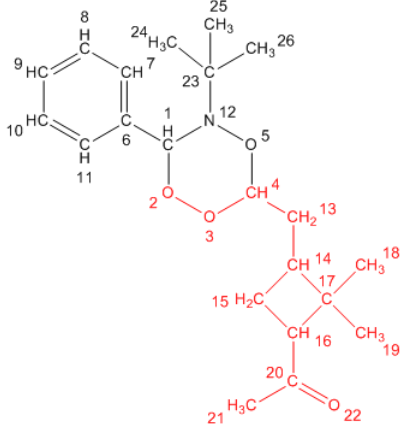
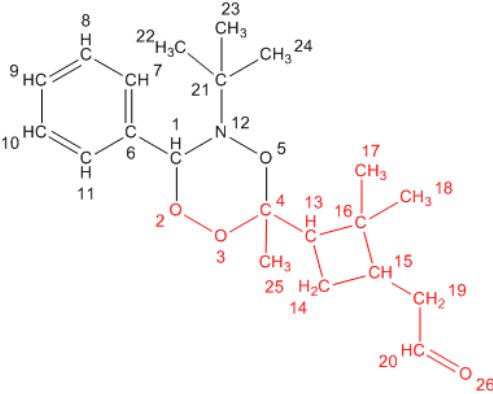
In the  $\text{CI}_\text{K}$ -PBN, the  $-\text{CH}$  group (no.1) has predicted chemical shifts of 5.64 ppm for the proton, close to the observed values at 5.77 ppm (Figure 9.1 and **Figure 9.2**) and 88.5 ppm for the carbon, which is observed at 99.15 ppm (Figure 9.7). However, there seems to be two protons (double peak in the  $^1\text{H}$ -NMR) suggesting again that the  $\text{CI}_\text{A}$ -PBN ( $-\text{CH}$  no.1) may also be present. Looking at the HMBC (**Figure 9.8**), this peak at 5.77 ppm shows a correlation over 2-bonds to a carbon at 130 ppm, close to the predicted value to be a 135.1 ppm (no.6  $\text{CI}_\text{K}$ -PBN and  $\text{CI}_\text{A}$ -PBN) (Table 9.1).

Concerning the aromatic part, aromatic protons can be observed around 7.35-7.70 ppm correlating to carbons at 128-132 ppm (Figure 9.9). There seems to be two different ortho- protons (that can be seen also in the HMBC spectrum in Figure 9.10).

In conclusion, the NMR characterisation confirms the presence of the  $\text{CI}_\text{K}$ -PBN adduct in which the CI reacts through a cycloaddition to the nitron functional group of the PBN spin trap forming a 6-atoms heterocycle. The presence of two different cyclobutane groups, 2-3 different *t*-butyl groups and low intensity signals associated with the  $\text{CI}_\text{A}$ -PBN adduct suggest that this is also present in solution although probably at lower concentration and partially broken down during the course of the NMR analysis (>12h).



**Table 9.1** - Proposed structures of the two  $\alpha$ -pinene CI-PBN adducts with predicted chemical shifts for  $^1\text{H}$ -NMR and  $^{13}\text{C}$ -NMR in DMSO and 300MHz using ChemDraw Ultra 10.0.

CI <sub>K</sub> -PBN					CI <sub>A</sub> -PBN				
									
Group No.	Predicted chemical shift		Measured chemical shift		Group No.	Predicted chemical shift		Measured chemical shift	
	$\delta$ $^1\text{H}$ -NMR (ppm)	$\delta$ $^{13}\text{C}$ -NMR (ppm)	$\delta$ $^1\text{H}$ -NMR (ppm)	$\delta$ $^{13}\text{C}$ -NMR (ppm)		$\delta$ $^1\text{H}$ -NMR (ppm)	$\delta$ $^{13}\text{C}$ -NMR (ppm)	$\delta$ $^1\text{H}$ -NMR (ppm)	$\delta$ $^{13}\text{C}$ -NMR (ppm)
1	5.64	88.5	5.77	99.15	1	6.01	101.0	5.77	99.15
2	-	-	-	-	2	-	-	-	-
3	-	-	-	-	3	-	-	-	-
4	4.96	102.9	5.7	105.35	4	-	117.9	-	*
5	-	-	-	-	5	-	-	-	-
6	-	135.1	-	130	6	-	135.1	-	130
7	7.36	127.9	7.50	130	7	7.28	127.9	7.45	131
8	7.38	128.5	7.37	129	8	7.33	128.5	7.37	129
9	7.38	127.0	7.66	130	9	7.29	127.0	7.66	130
10	7.38	128.5	7.37	129	10	7.33	128.5	7.37	129
11	7.36	127.9	7.50	130	11	7.28	127.9	7.45	131
12	-	-	-	-	12	-	-	-	-
13	1.59	29.6	~1.6	33	13	1.84	53.2	2.1-2.2	38
14	1.93	31.0	2.1-2.2	38	14	1.66/1.41	17.4	1.7	19
15	1.96/1.71	23.4	1.8-1.9	24.23	15	2.26	31.8	2.88	54.8
16	2.80	60.2	2.88	54.8	16	-	31.0	-	45
17	-	39.3	-	45	17	0.89	25.4	~0.8	~17
18	0.99	24.6	~1.30	~30	18	0.89	25.4	~0.8	~17
19	0.99	24.6	~1.30	~30	19	2.44/2.19	43.0	2.3	42
20	-	209.5	-	208	20	9.72	202.2	9.66	~199
21	1.98	30.9	1.98	30	21	-	60.7	-	59
22	-	-	-	-	22	1.22	26.4	0.9	27
23	-	50.4	-	59	23	1.22	26.4	0.9	27
24	1.27	26.4	1.15	28	24	1.22	26.4	0.9	27
25	1.27	26.4	1.15	28	25	1.27	16.1	1.45	18
26	1.27	26.4	1.15	28	26	-	-	-	-

\*Solvent interference (acetonitrile)

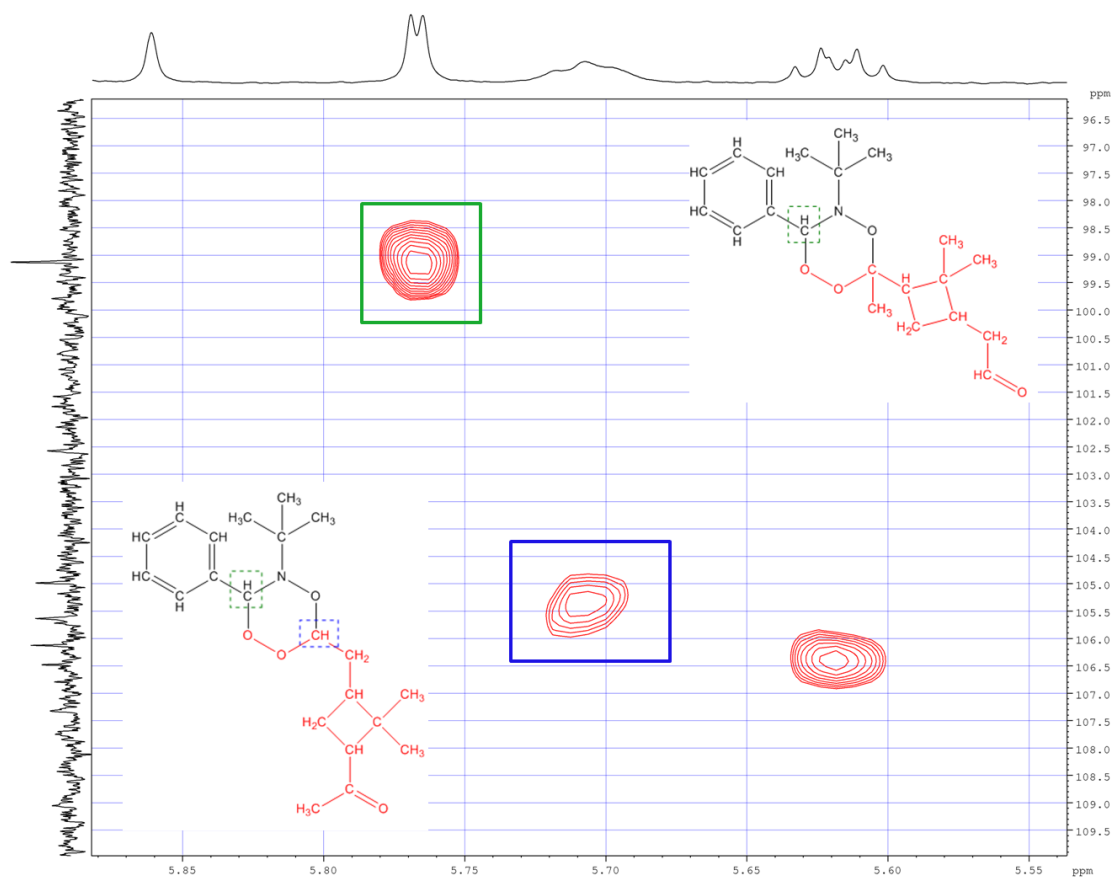


**Figure 9.1** -. Zoom of HSQC-NMR showing the short-range correlation between the  $^1\text{H}$  and  $^{13}\text{C}$  of the two  $-\text{CH}$  groups in the heterocycle. Negative phase cross-peaks are in blue and indicate  $-\text{CH}_2$  groups; positive phase cross-peaks are in red and indicate  $-\text{CH}$  and  $-\text{CH}_3$  groups.

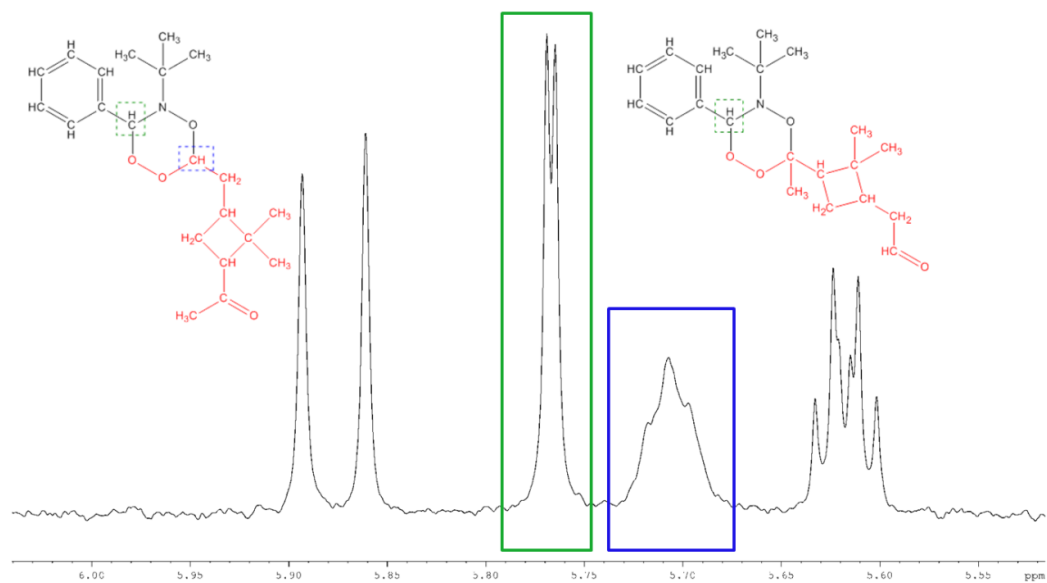


**Figure 9.2** - Zoom of  $^1\text{H}$ -NMR showing the protons of the  $-\text{CH}$  groups in the heterocycle.

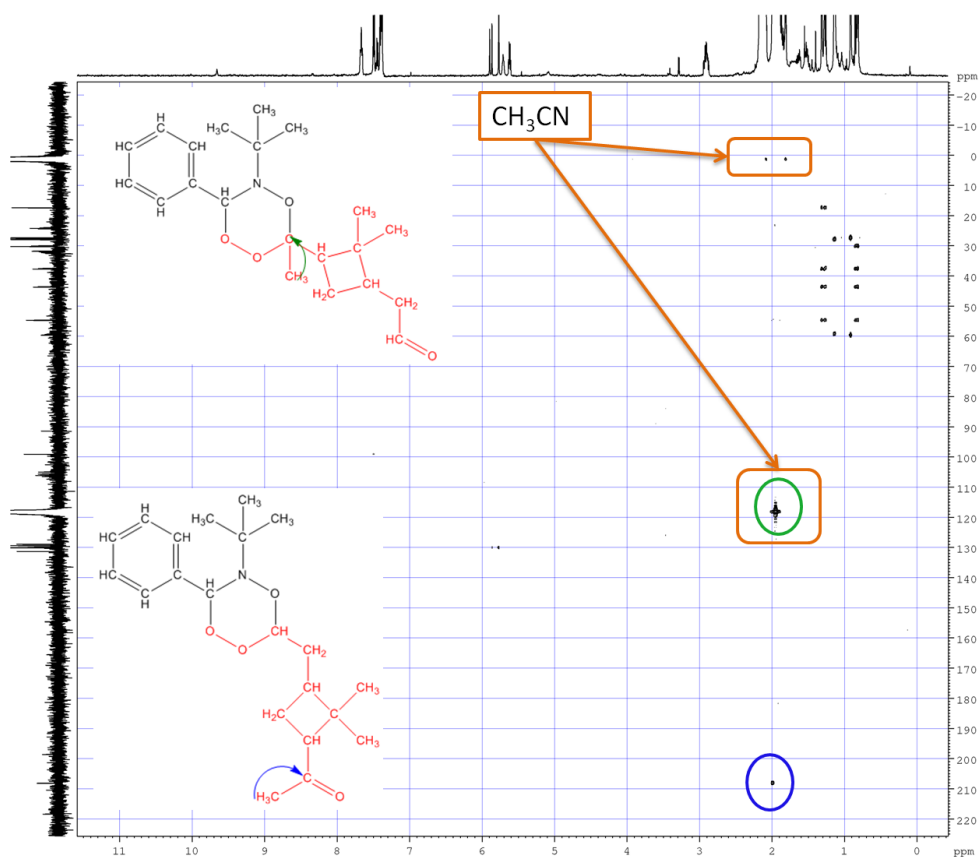


**Figure 9.3** - Full HMBC-NMR showing acetonitrile (solvent) peaks, a long range correlation (2 bonds) between the protons at the terminal methyl and the ketonic  $^{13}\text{C}$  (in blue) and where the long range correlation (2 bonds) between the protons at the terminal methyl and the quaternary  $^{13}\text{C}$  in the heterocycle (in green) should be according to the NMR predictions from ChemDraw (therefore covered by the solvent peaks).

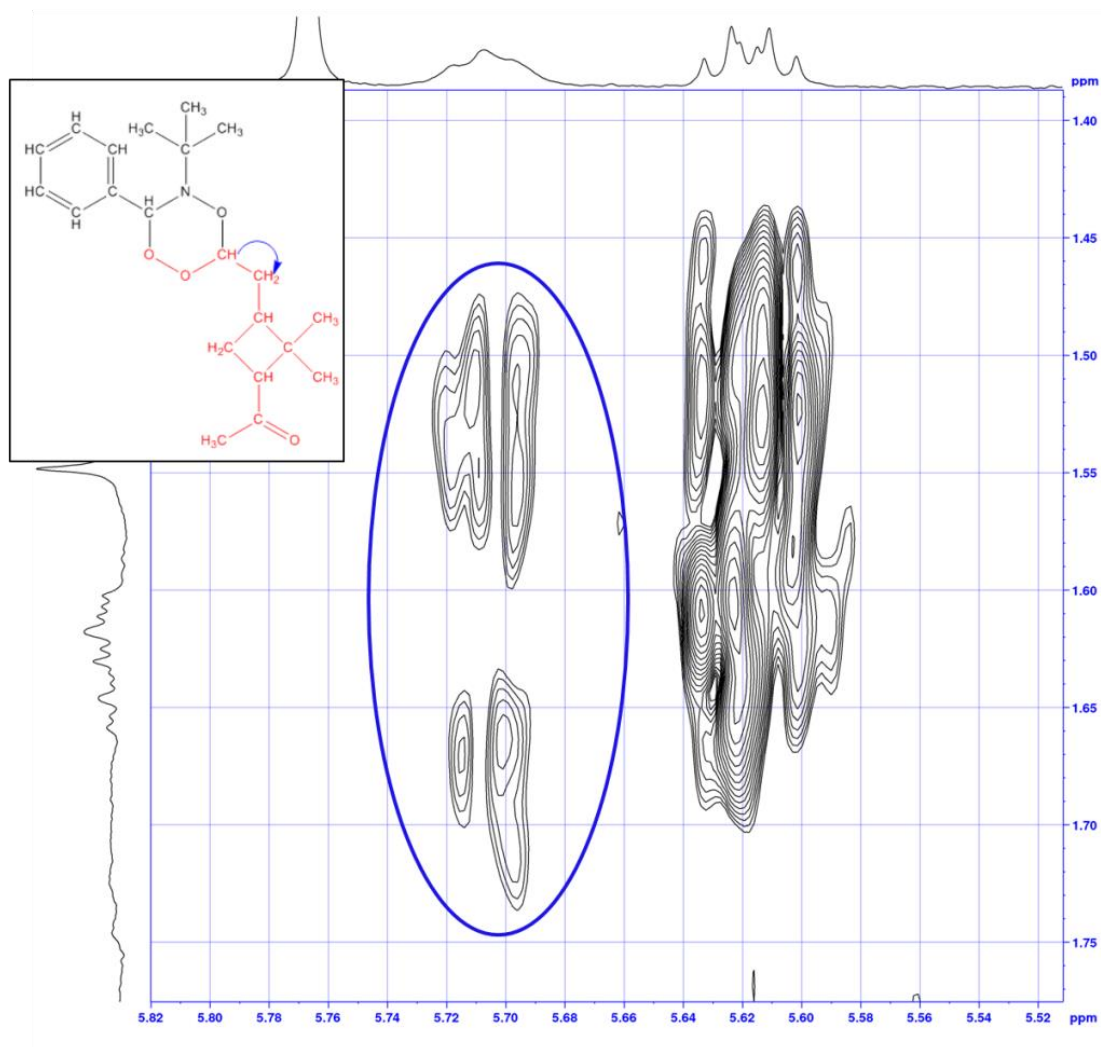


**Figure 9.4** - Zoom of COSY-NMR showing the correlation between the proton of the –CH within the heterocycle and the –CH<sub>2</sub> group bridging the heterocycle and the cyclobutane parts of the CI<sub>K</sub>-PBN

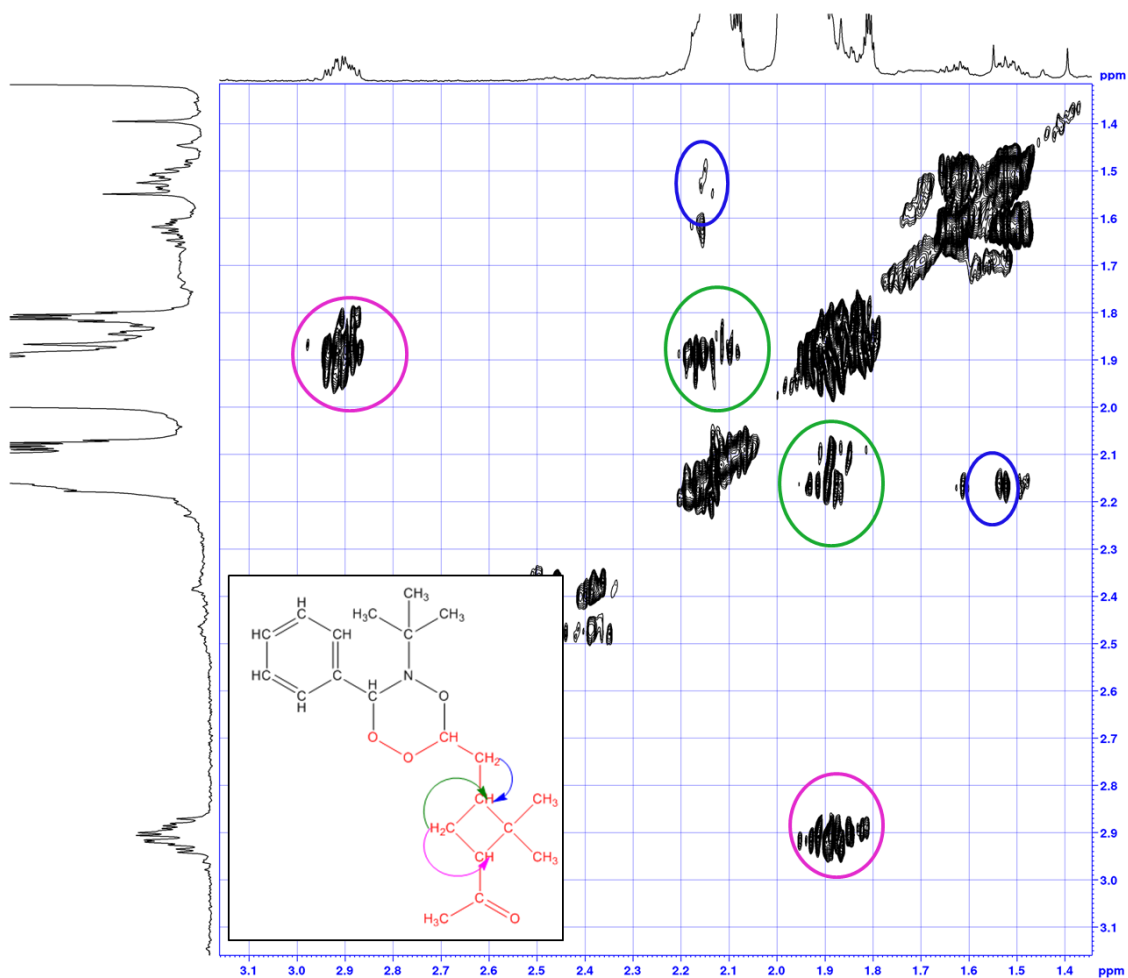


**Figure 9.5** - Zoom of COSY-NMR showing the correlations between the  $^1\text{H}$  of the  $-\text{CH}_2$  group bridging the heterocycle with cyclobutane and the  $^1\text{H}$  of the  $-\text{CH}$  within the cyclobutane (blue) and the correlation between the  $^1\text{H}$  of the  $-\text{CH}_2$  within the cyclobutane with the  $^1\text{H}$  of the two adjacent  $-\text{CH}$  groups (in green and magenta).

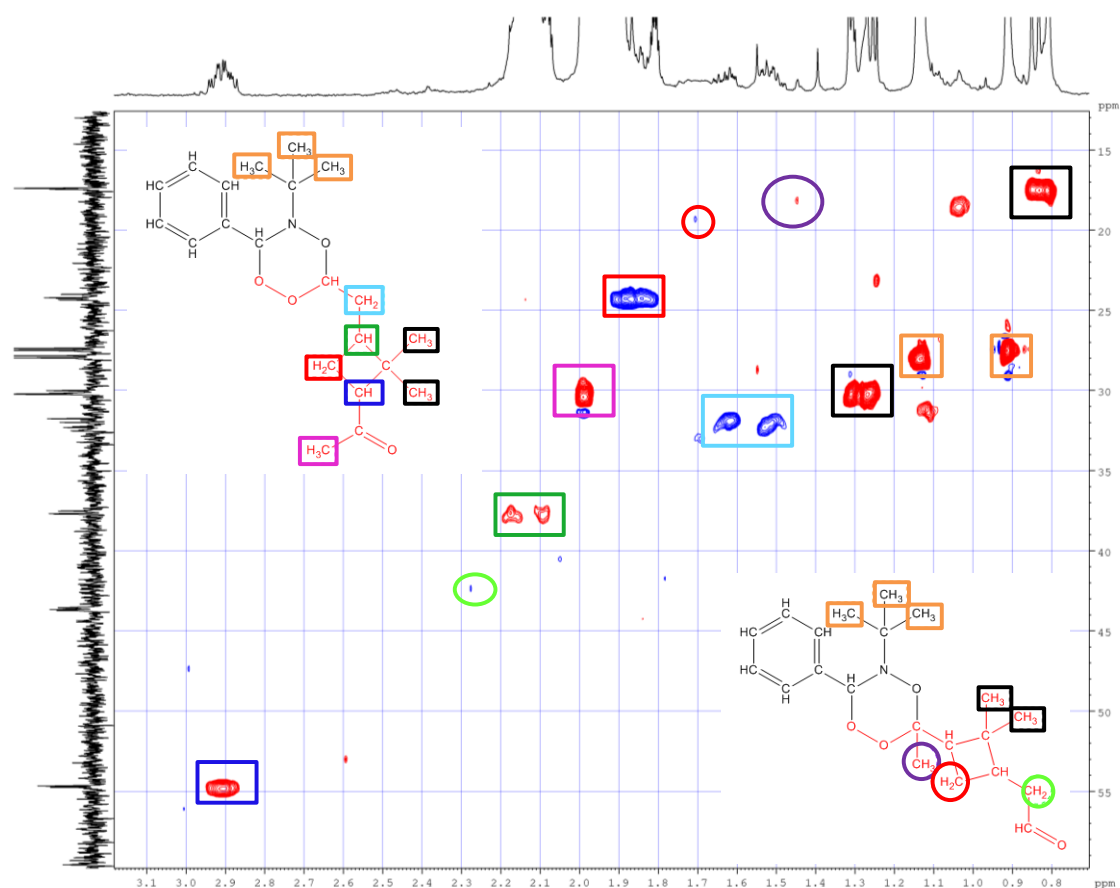


**Figure 9.6** - Zoom of HSQC-NMR showing short-range correlations between  $^1\text{H}$  and  $^{13}\text{C}$  of the groups in the red part of the molecules. The  $\text{Cl}_A\text{-PBN}$  looks at much lower intensity for some of its signals but not for others ( $-\text{CH}_3$  groups) maybe because the adduct breaks down over the course of the analysis (several hours/room temperature). Negative phase cross-peaks are in blue and indicate  $-\text{CH}_2$  groups; positive phase cross-peaks are in red and indicate  $-\text{CH}$  and  $-\text{CH}_3$  groups.

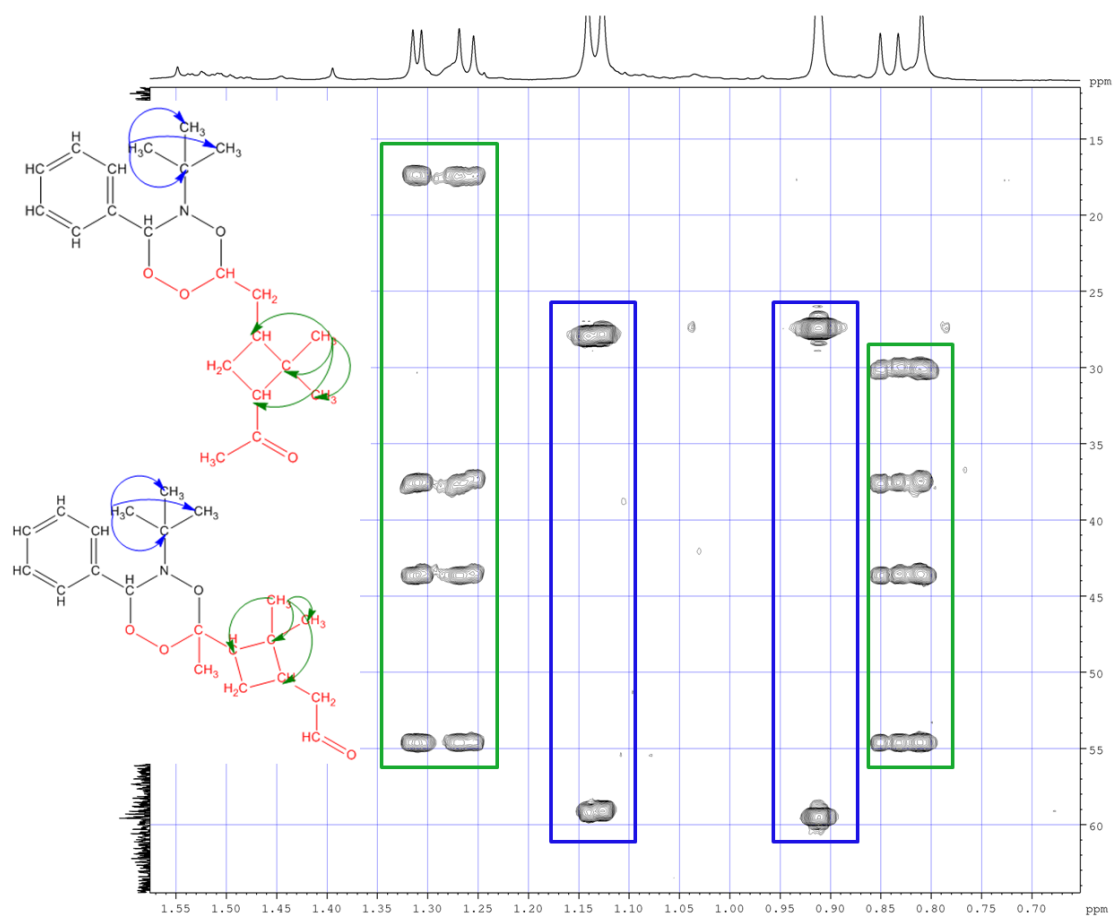


**Figure 9.7** - Zoom of HMBC-NMR showing the long range correlations (over 2-3 bonds) of the terminal methyl groups with the adjacent  $^{13}\text{C}$  in the t-butyl and cyclobutane parts of the molecules.



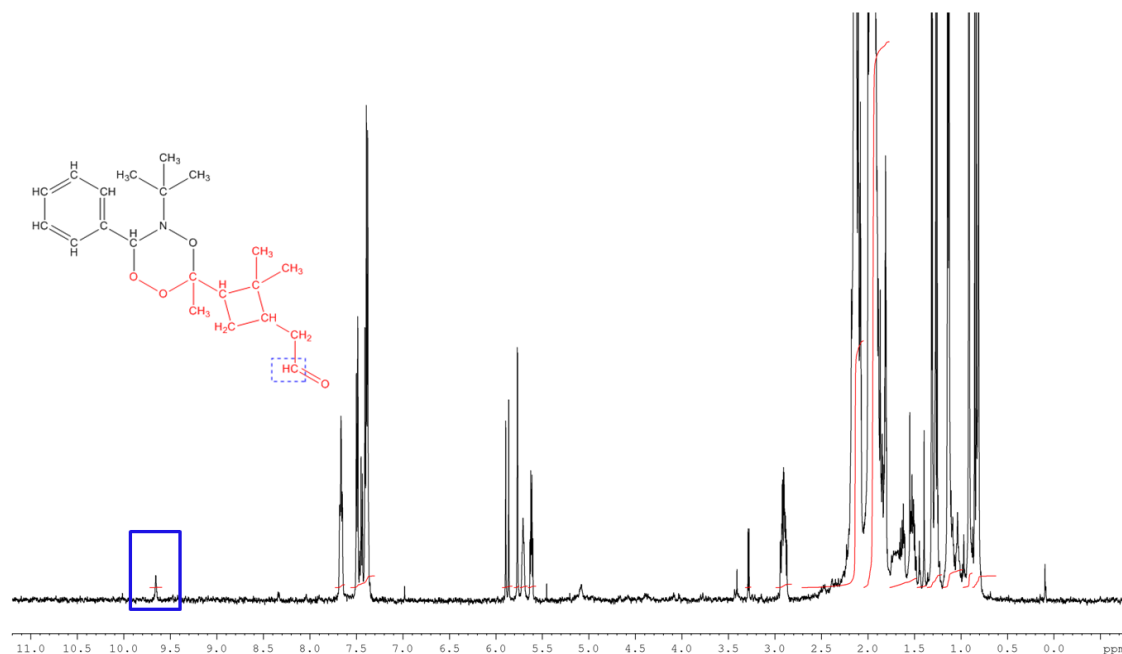


**Figure 9.8** - Full  $^1\text{H}$ -NMR spectrum showing the aldehydic proton (blue square).

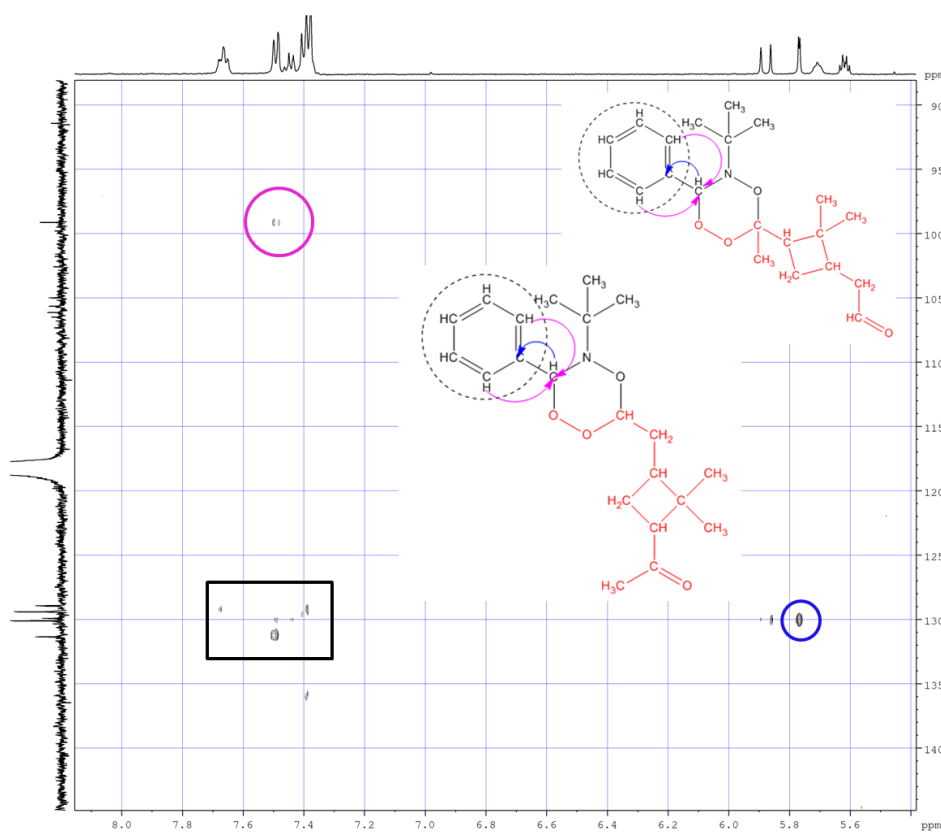


**Figure 9.9** - Zoom of HMBC-NMR showing long range correlations (over 2-3 bonds) between:  $^1\text{H}$  of the heterocycle with quaternary  $^{13}\text{C}$  of the aromatic ring (in blue), ortho  $^1\text{H}$  of the aromatic ring with  $^{13}\text{C}$  of the heterocycle (in green) and aromatic  $^1\text{H}$  with aromatic  $^{13}\text{C}$  (in black square).

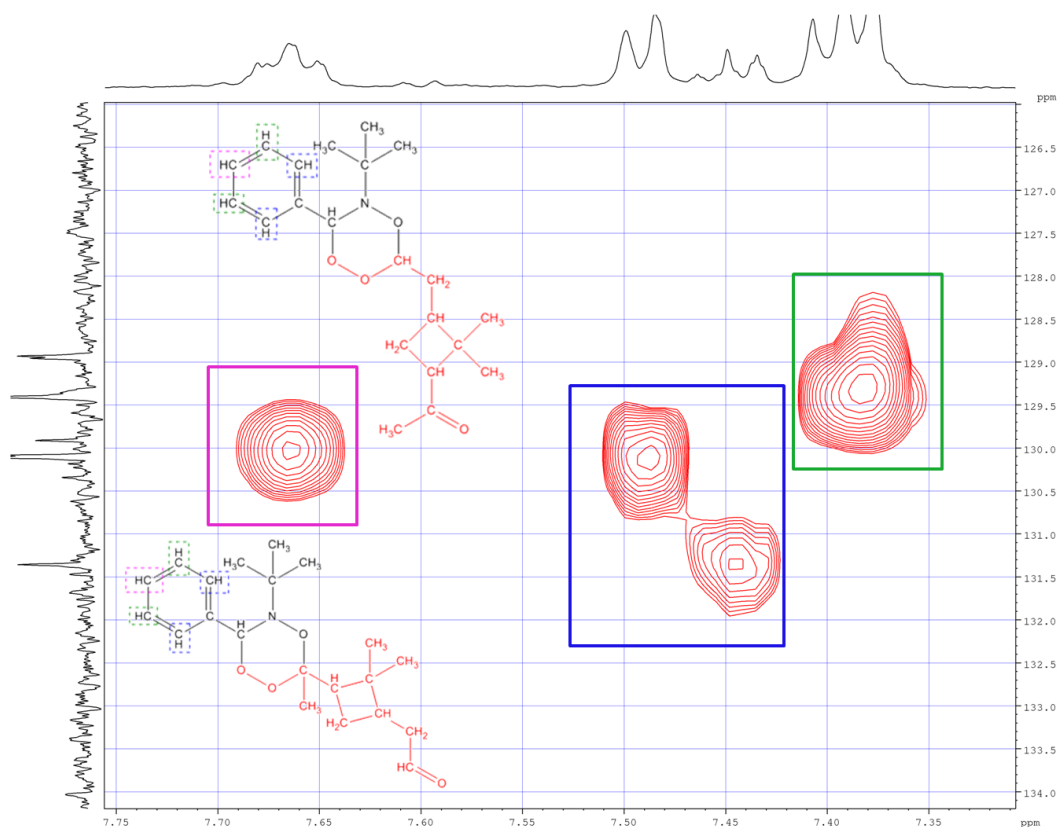


**Figure 9.10** - Zoom of HSQC-NMR showing short range correlations of aromatics protons with their  $^{13}\text{C}$ . There seems to be two different ortho  $-\text{CH}$  (inside the blue square). Negative phase cross-peaks are in blue and indicate  $-\text{CH}_2$  groups; positive phase cross-peaks are in red and indicate  $-\text{CH}$  and  $-\text{CH}_3$  groups.

## APPENDIX 2 – DENSITY FUNCTIONAL THEORY CALCULATIONS

### 9.1.1 Density Functional Theory Calculations: Optimisation

Geometry optimizations and energy calculations have been carried out in the DFT framework with the TURBOMOLE 6.4 suite of programs<sup>270</sup> by using the BP86<sup>271,272</sup> and B3LYP<sup>273–275</sup> functionals, in conjunction with a valence triple- $\xi$  basis set with polarization functions on all atoms (TZVP).<sup>276</sup> For the BP86 functional the resolution-of-the-identity (RI) technique is applied.<sup>277</sup> As the geometries and the energy differences calculated by the two functionals are very similar in the section 3.2 only the BP86 results will be discussed.

Stationary points of the energy hypersurface have been located by means of energy gradient techniques and full vibrational analysis has been carried out to further characterise each stationary point.

The optimization of transition state structures has been carried out according to a procedure based on a pseudo Newton-Raphson method. The search of the transition state structure is carried out using an eigenvector-following algorithm: the eigenvectors in the Hessian are sorted in ascending order, the first one being that associated to the negative eigenvalue. After the first step, the search is performed by choosing the critical eigenvector with a maximum overlap criterion, which is based on the dot product with the eigenvector followed at the previous step. Finally, the analytical Hessian matrix is calculated to carry out the vibrational analysis of the stationary point.

Free energy (G) values have been obtained from the electronic SCF energy considering three contributions to the total partition function (Q), namely  $q_{\text{translational}}$ ,  $q_{\text{rotational}}$ ,  $q_{\text{vibrational}}$ , under the assumption that Q may be written as the product of such terms.<sup>278</sup> In order to evaluate enthalpy and entropy contributions, the values of temperature, pressure and scaling factor for the SCF wavenumbers have been set to 298.15 K, 1 bar and 0.9914, respectively. Rotations have been treated classically and vibrational modes have been described according to the harmonic approximation. Energies of the van der Waals complexes have been corrected for the basis set superposition error using the procedure of Boys and Bernardi.<sup>279</sup>

---

### 9.1.2 DFT calculations of $\alpha$ -pinene – PBN Adducts

An extensive search of the potential energy surfaces (PES) of both CIs generated from the ozonolysis of  $\alpha$ -pinene, CI<sub>A</sub> and CI<sub>K</sub>, was conducted to identify all of the minimum energy conformations, the Gibbs free energies of the most stable conformers ( $\Delta G_s$  kcal mol<sup>-1</sup>) and for the DMPO + CI<sub>A/K</sub> reaction ( $\Delta G_r$  kcal mol<sup>-1</sup>) calculated are summarised in Table 9.2

The conformers found to have the most stable arrangement were the CI<sub>A</sub> and CI<sub>K</sub>, with the CCOO group in a near planar arrangement with a dihedral angle of 0° (CI<sub>A(0)</sub> and CI<sub>K(0)</sub> in ), which is in agreement with previous theoretical calculations<sup>28,280</sup>. CI<sub>A</sub> in this conformation is more stable than the CI<sub>K</sub> conformer by 1.5 kcal mol<sup>-1</sup>, in relative agreement to the value calculated by Zhang *et.al.*<sup>280</sup> with an energy difference of 2.6 kcal mol<sup>-1</sup> using the CCSD(T)/6-31G(d)+CF level of theory. Another relevant conformation, with the dihedral bond angle of the CCOO group 180°, was found to be less stable than that of the 0° dihedral angle by 0.2 kcal mol<sup>-1</sup> and 2 kcal mol<sup>-1</sup> for CI<sub>A</sub> and CI<sub>K</sub> respectively, with CI<sub>A(180)</sub> more stable than CI<sub>K(180)</sub> by 3.5 kcal mol<sup>-1</sup>.

The cycloaddition of the two CIs to DMPO can occur *via* attack at the nitrogen or oxygen centred group on the nitron functionality of the DMPO by the carbon centre of the CI. This cycloaddition can lead to the formation of either a 5- or 6- membered ring. A recent study of the CH<sub>2</sub>OO using IR spectroscopy<sup>55</sup>, as well as theoretical calculations<sup>48</sup> are more consistent with a zwitterionic, 1,3 dipole structural representation of the CI as opposed to being biradical in character. Therefore, the reaction between the CI and DMPO can be considered as a 1,3 dipolar cycloaddition reaction. The cycloaddition reaction of both CI<sub>A</sub> and CI<sub>K</sub> with DMPO can generate 4 stereoisomers. The ring closure leads to two stereogenic centres, one at the C atom of the CI and one at the C atom of the nitron group. These centres consist of the two RR/SS and RS/SR pairs of enantiomers.

The calculated activation free energies for the cyclisation reaction can help to distinguish the different reaction mechanisms. The lowest calculated energy barrier values were obtained by starting with the CI<sub>A180</sub> and CI<sub>K180</sub> reactants, leading to the formation of a 6-membered ring in the trans- conformation.

**Table 9.2-** Relative stabilities referred to the most stable (stereo)isomer ( $\Delta G_S$  in kcal mol<sup>-1</sup>), and  $CI_{K/A} + DMPO \rightarrow CI_{K/A}$ -DMPO Gibbs free reaction energies ( $\Delta G_r$  in kcal mol<sup>-1</sup>) calculated for all of the isomers investigated at the BP86 and B3LYP levels of theory. vdw- $CI_K$  and vdw- $CI_A$  are the pre-reactive van der Waals complexes. In the labels 5R and 6R refer to the 5- and 6-membered ring adducts, respectively and RR/RS to the absolute configuration of the two stereogenic centres generated by the addition reaction. In the case of 6-membered ring adducts, the subscript cis/trans indicates the relative orientation of the nitrogen lone pair and the hydrogen of the adjacent carbon atom. The values in parenthesis are the relative stabilities of the 5-membered ring adducts referred to their most stable stereoisomer.

Species	BP86/def-TZVP		B3LYP/def-TZVP	
	$\Delta G_S$	$\Delta G_r$	$\Delta G_S$	$\Delta G_r$
<b><math>CI_{A(0)}</math></b>	0.0	—	0.0	—
<b><math>CI_{K(0)}</math></b>	1.5	—	1.2	—
<b><math>CI_{A(180)}</math></b>	0.2	—	0.3	—
<b><math>CI_{K(180)}</math></b>	3.7	—	3.3	—
<b>VDW-<math>CI_{K(180)}</math>-DMPO</b>	—	-2.8	—	-4.9
<b>VDW-<math>CI_{A(180)}</math>-DMPO</b>	—	-1.6	—	-2.3
<b>VDW-<math>CI_{K(0)}</math>-DMPO</b>	—	-3.5	—	-5.7
<b>VDW-<math>CI_{A(0)}</math>-DMPO</b>	—	-0.6	—	-1.5
<b>TS-<math>CI_K</math>-6R-RR<sub>trans</sub></b>	—	2.3	—	0.5
<b>TS-<math>CI_A</math>-6R-RR<sub>trans</sub></b>	—	12.8	—	14.5
<b>TS-<math>CI_K</math>-6R-RR<sub>cis</sub></b>	—	7.7	—	3.9
<b>TS-<math>CI_A</math>-6R-RR<sub>cis</sub></b>	—	17.9	—	17.5
<b><math>CI_K</math>-6R-RR<sub>trans</sub></b>	0.0	-31.6	0.0	-33.3
<b><math>CI_K</math>-6R-RS<sub>trans</sub></b>	2.9	-28.7	2.8	-30.5
<b><math>CI_K</math>-6R-RR<sub>cis</sub></b>	6.6	-21.9	3.9	-27.1
<b><math>CI_K</math>-6R-RS<sub>cis</sub></b>	3.6	-24.9	1.3	-29.7
<b><math>CI_A</math>-6R-RR<sub>trans</sub></b>	9.1	-18.8	10.7	-17.8
<b><math>CI_A</math>-6R-RS<sub>trans</sub></b>	10.3	-17.7	11.3	-17.1
<b><math>CI_A</math>-6R-RR<sub>cis</sub></b>	11.2	-17.9	12.0	-18.4
<b><math>CI_A</math>-6R-RS<sub>cis</sub></b>	11.5	-17.6	10.6	-19.8
<b><math>CI_K</math>-5R-RR</b>	18.4 (0.0)	-13.2	22.7 (0.0)	-10.6
<b><math>CI_K</math>-5R-RS</b>	29.6 (11.2)	-2.0	32.9 (10.1)	-0.5
<b><math>CI_A</math>-5R-RR</b>	33.0 (14.6)	5.2	41.0 (18.3)	12.5
<b><math>CI_A</math>-5R-RS</b>	39.6(21.1)	11.7	47.5 (24.8)	19.3

The cyclisation reactions were preceded by the formation of pre-reactive van der Waals complexes between the CI and DMPO. The complexes for  $CI_{K(180)}$  (vdw- $CI_{K(180)}$ ) and  $CI_{A(180)}$  (vdw- $CI_{K(180)}$ ) are about 3 and 2 kcal mol<sup>-1</sup> more stable than the separated species

respectively. The  $\Delta G^\ddagger$  values calculated for the addition of  $\text{CI}_{\text{K}(180)}$  to DMPO was  $2.3 \text{ kcal mol}^{-1}$ , indicating this reaction is only limited by a relatively small reaction barrier.

Conversely, the  $\Delta G^\ddagger$  value calculated for the addition of  $\text{CI}_{\text{A}(180)}$  with DMPO was  $12 \text{ kcal mol}^{-1}$ . The  $\Delta G^\ddagger$  values calculated for CIs in the “0°” conformation were larger than that found for the “180°” conformation. The  $\Delta G^\ddagger$  values calculated for the formation of a 5-membered ring were substantially higher, 36 and  $49 \text{ kcal mol}^{-1}$  for both the  $\text{CI}_{\text{K}(180)}$  and  $\text{CI}_{\text{A}(180)}$  respectively. The simplified orbital diagram, depicted in Figure 9.11, can help to explain the cycloaddition mechanism between the CI and DMPO, leading to the formation of a 6-membered ring adduct.

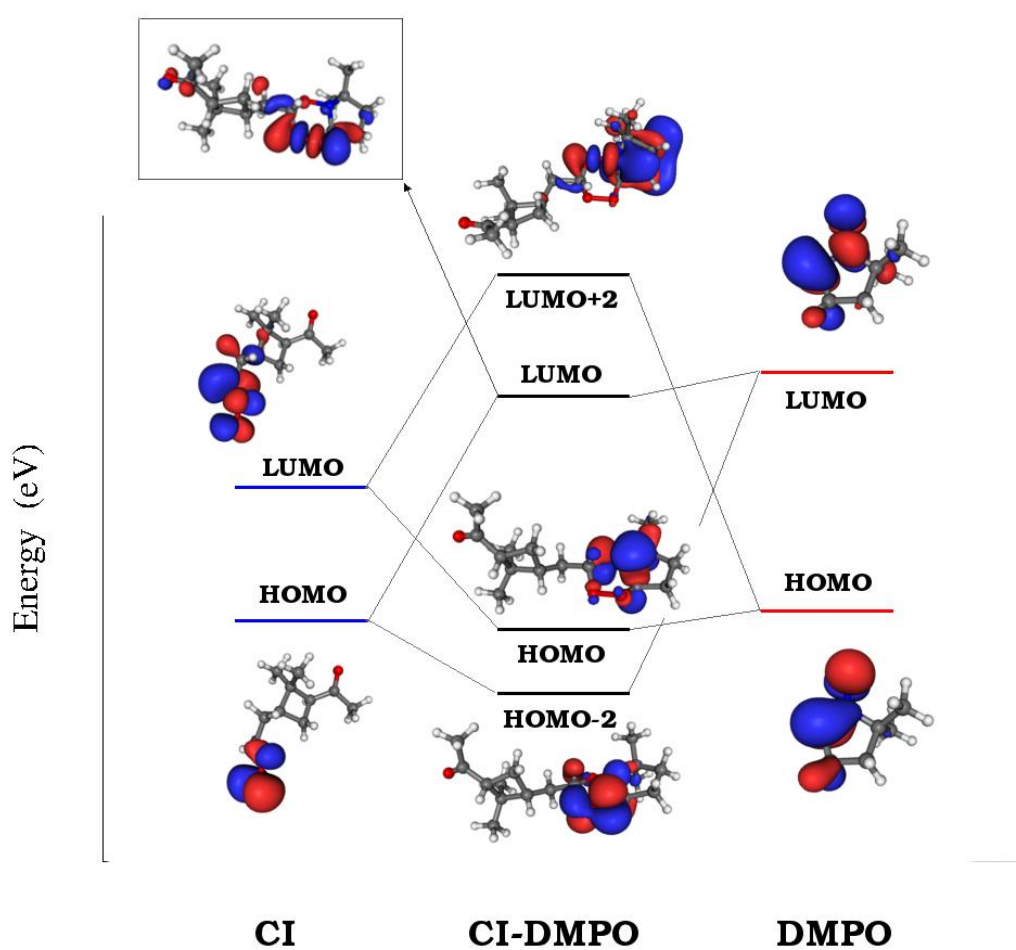


**Figure 9.11** – Simplified reaction co-ordinate profile showing the HOMO and LUMO of both  $\text{CI}_{\text{K}}$  and DMPO, forming the 1:1 adduct  $\text{CI}_{\text{K}}\text{-DMPO}$ .

The highest occupied molecular orbital (HOMO) of DMPO consists of a  $\pi$ -orbital with a C=N-O framework. There is substantial contribution to the HOMO from the oxygen atom, which can interact with the lowest unoccupied molecular orbital (LUMO) of the

CI, which is mainly localised on the carbon atom. The formation of C<sub>CI</sub>-O<sub>DMPO</sub> bond decreases the electron density on the carbon atom of the DMPO which can then interact with the HOMO of the of the CI, which is mainly localised on the terminal oxygen atom of the CI.

### 9.1.3 DFT Calculation of CI-DMPO Proton Reaction Rate Constants

**Table 9.3** - Polarizability, dipole moment, Langevin collision rate constant ( $k_L$ ), ADO collision rate constant ( $k_{ADO}$ ) and ion-polar molecule capture collisions rate constant ( $k_{cap}$ ) at 300K and 363.15K (operating drift tube temperature in our experiments).  $\alpha$  represents the (angle-averaged) polarizability of each molecule, and  $\mu_D$  is the dipole moment of the neutral molecule.

Compound	$\alpha$ ( $\text{\AA}^3$ )	$\mu_D$ (D)	T (K)	$k_L$ ( $\times 10^{-9} \text{ cm}^3 \text{ s}^{-1}$ )	$k_{ADO}$ ( $\times 10^{-9} \text{ cm}^3 \text{ s}^{-1}$ )	$k_{cap}$ ( $\times 10^{-9} \text{ cm}^3 \text{ s}^{-1}$ )
<b>DMPO</b>	12.06	4.07	300	2.02	4.34	2.77
			363.15	2.02	4.13	2.75
<b>Cl<sub>3</sub>Al (RR)-DMPO</b>	18.42	4.8	300	2.41	5.04	3.37
			363.15	2.41	4.80	3.35
<b>Cl<sub>3</sub>Al (SR)-DMPO</b>	18.49	4.84	300	2.42	5.07	3.37
			363.15	2.42	4.83	3.35
<b>C<sub>9</sub>bpin (RR)-DMPO</b>	27.55	2.144	300	2.92	3.79	3.25
			363.15	2.92	3.71	3.22
<b>C<sub>9</sub>bpin (SR)-DMPO</b>	27.38	2.073	300	2.91	3.74	3.21
			363.15	2.91	3.67	3.19
<b>Cl<sub>1</sub> (R)-DMPO</b>	14.66	2.558	300	2.18	3.44	3.01
			363.15	2.18	3.33	2.95
<b>Cl<sub>4</sub> (RR)-DMPO</b>	20.27	2.378	300	2.53	3.61	3.07
			363.15	2.53	3.51	3.03
<b>Cl<sub>4</sub> (SR)-DMPO</b>	19.96	2.283	300	2.51	3.53	3.01
			363.15	2.51	3.44	2.97
<b>Cl<sub>2</sub> (RR)-DMPO</b>	16.61	2.294	300	2.31	3.37	2.89
			363.15	2.31	3.28	2.85
<b>Cl<sub>2</sub> (SR)-DMPO</b>	16.35	2.400	300	2.29	3.43	2.94
			363.15	2.29	3.33	2.90
<b>Cl<sub>7</sub>Ar (RR)-DMPO</b>	24.67	2.339	300	2.77	3.78	3.22
			363.15	2.77	3.69	3.19
<b>Cl<sub>9</sub>lim (RR)-DMPO</b>	28.40	2.068	300	2.96	3.78	3.26
			363.15	2.96	3.71	3.24
<b>Cl<sub>10</sub>Al (RR)-DMPO</b>	34.45	4.921	300	3.28	5.82	4.78
			363.15	3.28	5.59	4.74
<b>Cl<sub>10</sub>K (RR)-DMPO</b>	30.95	4.847	300	3.08	5.59	4.48
			363.15	3.08	5.36	4.45

The proton affinities of the various CI-DMPO adducts in this work were calculated using the Langevin model. This model considers; the long range interaction between a point charge and a polarisable molecule<sup>281</sup>, average-dipole-orientation theory (ADO) which also considers the permanent dipole moment of the neutral organic species, and the refined ADO theory parametrised by Su and Chesnavich<sup>282</sup> to account for the kinetic

energy dependence of the rate constant across a wide range of temperatures. Extensive details on calculating the proton affinities using these theories can be found elsewhere<sup>283</sup>.

### 9.1.4 DFT calculations of Various CI-DMPO Adducts.

An extensive search on the potential energy surface (PES) of these CIs was carried out to identify the relevant minimum energy conformations. It turns out that for  $\text{Cl}_{\text{C}2}$ ,  $\text{Cl}_{\text{C}4}$  and  $\text{Cl}_{\text{C}3\text{AI}}$  the *syn* conformation is more stable than the *anti* one by 1.8, 1.5 and 5.8 kcal mol<sup>-1</sup> respectively. In contrast, the  $\text{Cl}_{\text{C}9\beta\text{pin}}$  *anti* conformer is more stable than the *syn* conformer by about 2 kcal mol<sup>-1</sup>. It is worth noting that these results are in good agreement with previous calculations carried out using *ab initio* highly correlated methods<sup>28,191,284,285</sup>. The addition of CIs with DMPO have been investigated by taking into account both *anti* and *syn* conformers to determine potential differences in the reactivity of the two species.

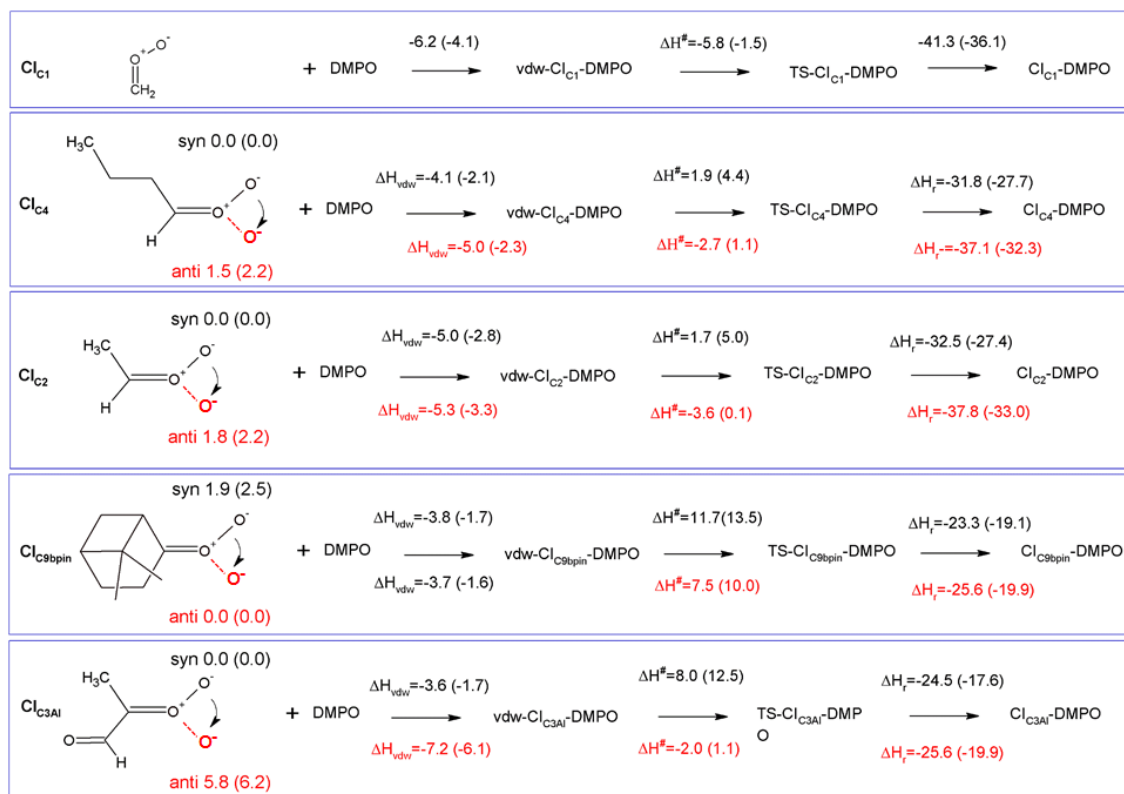


**Figure 9.12** - Schematic representation of the reaction of CIs with DMPO with values of reaction and activation enthalpies. The first step for each reaction is the formation of the van der Waals adduct (vdw-CI-DMPO), the second step is the formation of the transition state (TS-CI-DMPO) and the last step is the conversion to the final adduct (CI-DMPO). All values refer to enthalpy differences calculated with respect to the separated reactants using the B3LYP functional. In parenthesis are the corresponding values calculated using the BP86 functional. The molecular structures define the *anti* (black terminal oxygen) and the *syn* (red terminal oxygen) conformers. The values over (in black) and under (in red) the arrows refer to the reaction of the *anti* and *syn* conformers, respectively.



The cycloaddition of the CIs to the spin-trap DMPO can occur through the attack of the carbon atom of the CI to either the nitrogen or the oxygen atoms of the DMPO nitron group leading to the formation of a 5-membered or a 6-membered ring respectively. DFT calculations show that for all of the compounds investigated the 6-membered ring species is much more stable than the corresponding 5-membered ring species, in agreement with the results obtained from the DFT calculations in Section 3.2.2. Therefore, in the following, only the addition of CIs to DMPO to give 6-membered ring adducts will be considered.

The first step in the reaction of the CIs with DMPO is the formation of pre-reactive van der Waals complexes in which the carbonyl oxide approaches the nitron group of DMPO. The interaction energies of such van der Waals complexes are within -3.6 and -7.2 kcal mol<sup>-1</sup>, with the two extremes given by CI<sub>C3Al</sub> in the *syn* and *anti* conformations (Figure 9.12).

The reactivity of the CIs strongly depends on the number of substituents attached to the carbon atom of the carbonyl oxide, and on the initial conformation of the CI reactants. The reaction of the parent formaldehyde oxide CI<sub>C1</sub> with DMPO is barrierless as the activation enthalpy is lower than the enthalpy of the separated reactants ( $\Delta H^\ddagger = -5.8$  kcal mol<sup>-1</sup>), and only 0.5 kcal mol<sup>-1</sup> higher than that of the van der Waals complex. This reaction is also strongly exothermic with the value of the reaction enthalpy ( $\Delta H_r$ ) as low as -41 kcal mol<sup>-1</sup>. The energy barriers for the addition to DMPO of CI<sub>C2</sub> and CI<sub>C4</sub>, featuring one alkyl substituent bound to the carbon atom of the carbonyl oxide, are slightly larger than that calculated for the CI<sub>C1</sub>, and the reactions are slightly less exothermic.

Indeed, when considering as reactants the most stable *syn* conformers (CI<sub>C2(syn)</sub> and CI<sub>C4(syn)</sub>), the energy barriers for both species are about 2 kcal mol<sup>-1</sup> with respect to the separated reactants, and about 7 kcal mol<sup>-1</sup> with respect to the van der Waals complexes. The reaction enthalpies of these two cycloadditions ( $\Delta H_r$ ) are also very similar and equates to approximately -32 kcal mol<sup>-1</sup>. The reaction is still more favourable when starting from the less stable *anti* conformers (CI<sub>C2(anti)</sub> and CI<sub>C4(anti)</sub>). In this case, the  $\Delta H^\ddagger$  is negative by 3 kcal mol<sup>-1</sup> with respect to the separated reactants, and only 2 kcal mol<sup>-1</sup> higher than the van der Waals complexes. The  $\Delta H_r$  is lower than that of the *syn* conformer ( $\Delta H_r = -38$  kcal mol<sup>-1</sup>) due to the fact that the reactants are higher in energy, and that the

---

ring closure of  $\text{CI}_{\text{C2}(\text{anti})}$  and  $\text{CI}_{\text{C4}(\text{anti})}$  yield the RR/SS diastereoisomers, which are more stable than the RS/SR diastereoisomers formed by the ring closure of  $\text{CI}_{\text{C2}(\text{syn})}$  and  $\text{CI}_{\text{C4}(\text{syn})}$ .

The activation enthalpy calculated for the cycloaddition of  $\text{CI}_{\text{C9}\beta\text{pin}}$  in the most stable *syn* conformation is equal to  $11.7 \text{ kcal mol}^{-1}$ , a value significantly larger than that calculated for the CIs discussed above. Correspondingly, the  $\Delta H_{\text{r}}$  is equal to about  $-24 \text{ kcal mol}^{-1}$ , more than  $10 \text{ kcal mol}^{-1}$  higher than that calculated for the other CIs. The reaction of the less stable *anti* conformer has an energy profile similar to that of the *syn* conformer with  $\Delta H^{\#}$  and  $\Delta H_{\text{r}}$  equal to  $-8$  and  $-26 \text{ kcal mol}^{-1}$  respectively. The difference in reactivity of  $\text{CI}_{\text{C9}\beta\text{pin}}$  compared to the other CIs may be due to the connectivity of the carbon atom of the carbonyl oxide, which in  $\text{CI}_{\text{C9}\beta\text{pin}}$  is bound to two other carbons. It is worth noting that the same trend in activation and reaction energies was observed for the addition of DMPO to the two CIs generated by the ozonolysis of  $\alpha$ -pinene described in Section 3.2.2. The two adducts have one and two alkyl substituents attached to the carbon atom of the carbonyl oxide, and feature energy barriers and reaction energies that differ by more than  $10 \text{ kcal mol}^{-1}$  in favour of the less substituted species.

$\text{CI}_{\text{C3Al}}$  is the species featuring the largest difference in the reactivity of the *syn* and *anti* conformers. Considering the most stable *syn* conformer, the  $\Delta H^{\#}$  and  $\Delta H_{\text{r}}$  are equal to  $8.0$  and  $-25 \text{ kcal mol}^{-1}$ , which are values similar to those calculated for  $\text{CI}_{\text{C9}\beta\text{pin}}$ . Furthermore, considering the less stable *anti* conformer, the energy profile is much more favourable as the barrier is equal to about  $-2 \text{ kcal mol}^{-1}$  with respect to the separated reactants ( $+5.2 \text{ kcal mol}^{-1}$  with respect to the van der Waals complex) and the  $\Delta H_{\text{r}}$  is equal to  $-33 \text{ kcal mol}^{-1}$ , values that fit better those calculated for  $\text{CI}_{\text{C2}}$  and  $\text{CI}_{\text{C4}}$ .

### APPENDIX 3— MATHEMATICA MODEL FOR B-CARYOPHYLLENE MODELLING STUDY

In order to gain further perspective of the gas phase chemistry occurring, and qualitatively describe gas vs particle losses during the reaction of O<sub>3</sub> with β-caryophyllene, a simplified kinetic model was developed using Mathematica (v9.0, Wolfram). The mechanistic information was taken from the Master Chemical Mechanism, MCM v3.2, *via* website <http://mcm.leeds.ac.uk/MCM><sup>218</sup>. Although not entirely explicit, this model provides an estimate of the concentration of products formed in the gas phase in this reaction, and does not consider loss *via* partitioning of low volatile species into the particle phase or particle phase reactions.

A Mathematica model was designed, with rate coefficients taken from the MCM data as opposed to running the model on Atchem. This is because Atchem outputs the data in 1s timesteps. Given the rapid reactivity between β-caryophyllene and O<sub>3</sub>, most of the β-caryophyllene is consumed in < 1s. Therefore, to gain insight into the CI chemistry, it is necessary to run the model with smaller timesteps, to capture the concentration profiles during this rapid gas phase reaction, with a timestep output of 0.01 s. Concentrations of reactants are presented in Section 4.3.5, and the model results are presented in Figure 4.12.

---

```

k = 1.2×10-14;
(* k for reaction of bc w/ o3 *)
kdec = 1×106;
(* rate of decomposition for excited state CI,
given as fractions in the MCM< but this corrects for product distribution*)
kh2o = 2×10-16;
(*rate of reaction between both SCIs and h2o - in the model,
CO/NO/NO2/SO2 neglected as clean system*)
kdec2 = 8×101;
(* rate of decomp of ciaoo to bcsoz*)
kdec3 = 1.2×102;
(*rate of decomp of ciboo to bcsoz*)
m = 3.×1019;

ppm = 1.×10-6;
(*conversion of ppm to molec cm-3*)

vars = {bc, o3, ciooa, cioob, ciaoo, ciboo, h2o};
(*variables in the chemical system*)
header = {"time", "bc", "o3", "ciooa", "cioob", "ciaoo", "ciboo", "h2o"};

(*inits = {bc[0] = 140m ppm,
o3[0] = 18m ppm,
ciooa[0] = 0,
cioob[0] = 0,
ciaoo[0] = 0,
ciboo[0] = 0};*)

inits = {bc[0] = 220 mppm,
o3[0] = 18 mppm,
ciooa[0] = 0,
cioob[0] = 0,
ciaoo[0] = 0,
ciboo[0] = 0,
h2o[0] = 2 mppm};
(* initial conditions *)

eqns = {bc'[t] = -bc[t] o3[t] k,
o3'[t] = -bc[t] o3[t] k,
ciooa'[t] = 0.1 bc[t] o3[t] k - kdec ciooa[t],
cioob'[t] = 0.03 bc[t] o3[t] k - kdec cioob[t],
ciaoo'[t] = 0.435 bc[t] o3[t] k - kdec2 ciaoo[t] - kh2o h2o[t] ciaoo[t],
ciboo'[t] = 0.435 bc[t] o3[t] k - kdec3 ciboo[t] - kh2o h2o[t] ciboo[t],
h2o'[t] = -ciaoo[t] h2o[t] kh2o - ciboo[t] h2o[t] kh2o};
(* loss and production equations for bc, o3 and CIs*)

model = Join[eqns, inits];

```

```

result = NDSolve[model, vars, {t, 10}]
bcr = result[[1, 1, 2]];
o3r = result[[1, 2, 2]];
ciooar = result[[1, 3, 2]];
cioobr = result[[1, 4, 2]];
ciaoor = result[[1, 5, 2]];
ciboor = result[[1, 6, 2]];
h2or = result[[1, 7, 2]];
(*result directory - extracts results from data *)

{bc → InterpolatingFunction[{{0., 10.}}, <>],
 o3 → InterpolatingFunction[{{0., 10.}}, <>],
 ciooa → InterpolatingFunction[{{0., 10.}}, <>],
 cioob → InterpolatingFunction[{{0., 10.}}, <>],
 ciaoo → InterpolatingFunction[{{0., 10.}}, <>],
 ciboo → InterpolatingFunction[{{0., 10.}}, <>],
 h2o → InterpolatingFunction[{{0., 10.}}, <>]}

(*outputbc=Table[{i,bcr[i]},{i,0,10,0.1}];
 outputo3=Table[{i,o3r[i]},{i,0,10,0.1}];
 outputciooa=Table[{i,ciooar[i]},{i,0,10,0.1}];
 outputcioob=Table[{i,cioobr[i]},{i,0,10,0.1}];
 outputciaoo=Table[{i,ciaoor[i]},{i,0,10,0.1}];
 outputciboo=Table[{i,ciboor[i]},{i,0,10,0.1}];

result = NDSolve[model,vars,{t,10}];
bcr=result[[1,1,2]];
o3r=result[[1,2,2]];
ciooar=result[[1,3,2]];
cioobr=result[[1,4,2]];
ciaoor=result[[1,5,2]];
ciboor =result[[1,6,2]];*)

(*result = NDSolve[model,vars,{t,10}];
bcr=result[[1,1,2]];
o3r=result[[1,2,2]];*)

(*ciooar=result[[1,3,2]];
cioobr=result[[1,4,2]];
ciaoor=result[[1,5,2]];
ciboor =result[[1,6,2]];*)

outputbc = Table[{i, bcr[i]}, {i, 0, 10, 0.01}];

```

---

```

outputh2o = Table[{i, h2or[i]}, {i, 0, 10, 0.01}];

ListLinePlot[{outputbc, outputo3, outputciooa,
  outputcioob, outputciaoo, outputciboo, outputh2o},
  PlotLegends → {"BC", "O3", "CIOOA", "CIOOB", "CIAOO", "CIBOO", "h2o"},

  PlotStyle → {{Red, Thick}, {Black, Thick}, {Blue, Thick}, {Green, Thick},
    {Purple, Thick}, {Orange, Thick}, {Yellow, Thick}}, PlotRange → All]

ListLinePlot[
  {outputbc, outputo3, outputciooa, outputcioob, outputciaoo, outputciboo},
  PlotLegends → {"BC", "O3", "CIOOA", "CIOOB", "CIAOO", "CIBOO"},
  PlotStyle → {{Red, Thick}, {Black, Thick}, {Blue, Thick}, {Green, Thick},
    {Purple, Thick}, {Orange, Thick}}, PlotRange → {{0, 1}, {0, 5 × 1015}}]

ListLinePlot[{outputciooa}, PlotLegends → {"CIOOA"},
  PlotStyle → {Blue, Thick}, PlotRange → All]
ListLinePlot[{outputciooa}, PlotLegends → {"CIOOA"},
  PlotStyle → {Blue, Thick}, PlotRange → {{0, 1}, {0, 1 × 1010}}]

outputtable = Table[{i, bcr[i], o3r[i], ciooar[i],
  cioobr[i], ciaoor[i], ciboor[i], h2or[i]}, {i, 0, 10, 0.01}];
outputtablewithheader = Join[Partition[header, 8], outputtable];
(* 8 for number of columns *)
Export["18_ppm_o3_bc.csv", outputtablewithheader];

h2o'[t] == - ciaoo[t] h2o[t] kh2o - ciboo[t] h2o[t] kh2o
h2o'[t] == -  $\frac{ciaoo[t] h2o[t]}{5\,000\,000\,000\,000\,000}$  -  $\frac{ciboo[t] h2o[t]}{5\,000\,000\,000\,000\,000}$ 

outputtable // TableForm

```